



THÈSE

En vue de l'obtention du DOCTORAT DE L'UNIVERSITÉ DE TOULOUSE

Délivré par l'Institut National des Sciences Appliquées de
Toulouse

Présentée et soutenue par

Venkata Bala Varun Kumar YEACHANA

Le 7 janvier 2020

**Mise en oeuvre d'une technique de marquage moléculaire pour la
mesure des champs de température en micro écoulements
gazeux**

Ecole doctorale : **MEGEP - Mécanique, Energétique, Génie civil, Procédés**

Spécialité : **Dynamique des fluides**

Unité de recherche :

Thèse dirigée par

Stephane COLIN et Christine BARROT

Jury

M. Jean-Christophe BATSALE, Rapporteur

M. David NEWPORT, Rapporteur

M. Gian-Luca MORINI, Examinateur

M. Pierre PERRIER, Examinateur

M. Stephane COLIN, Directeur de thèse

Mme Christine BARROT, Co-directrice de thèse

Table of contents

1	Introduction.....	1
2	Basics of gas microflows	8
2.1	Rarefaction at microscale	8
2.1.1	Dilute gas.....	8
2.1.2	Boltzmann equation.....	9
2.1.3	Thermodynamic non-equilibrium	10
2.2	Slip flow regime	12
3	Microscale thermometry and its applications to liquid and gas flows.....	16
3.1	Conventional and contact-based thermometry adopted at microscale	17
3.2	Optical based techniques	18
3.2.1	Interferometry.....	19
3.2.2	Infrared based methods	25
3.2.3	Liquid crystal thermography	28
3.2.4	Raman Thermometry.....	34
3.2.5	Photoluminescence.....	41
3.3	Concluding remarks from literature survey.....	51
4	MTT investigations with first experimental chamber.....	53
4.1	Introduction	53
4.2	Molecular tagging setup	53
4.2.1	Vapour control system	54
4.2.2	Optical system.....	55
4.2.3	Signal acquisition system	61
4.3	Terminology for image acquisition	62
4.4	Design of first experimental chamber	64
4.5	Tracer molecules properties.....	66

4.5.1	Acetone.....	66
4.5.2	Diacetyl	66
4.6	Image analysis	68
4.7	Experiments at room temperature with first experimental chamber	73
4.7.1	Experiments with acetone vapour at 266 nm at room temperature.....	74
4.7.2	Variation of excitation wavelengths with acetone vapour at room temperature	75
4.7.3	Variation of excitation wavelengths with diacetyl vapour at room temperature	80
4.7.4	Excitation at different wavelengths with mixture at room temperature.....	82
4.8	Experiments at higher temperature in the heated chamber.....	86
4.8.1	Heating of experimental chamber	86
4.8.2	Experimental protocol	89
4.8.3	Effect of wavelengths on acetone vapour at $P = 15,000$ Pa and $T = 331$ K.....	90
4.8.4	Behaviour of pure acetone vapour excited at 310 nm in the heated chamber....	91
4.8.5	Behaviour of pure diacetyl vapour excited at 410 nm in the heated chamber ...	94
4.9	Repeatability of the experimental data	97
4.9.1	Reasons for lack of repeatability of data	98
4.10	Experimental study on laser energy	101
4.10.1	Laser energy fluctuations	101
4.10.2	Protocol for studying energy fluctuations	102
4.10.3	Software adjustments on OPO laser.....	107
4.11	Summary.....	109
5	Experimental investigations on second experimental chamber	111
5.1	Design of second experimental chamber.....	111
5.1.1	Initial leakages and outgassing in the second experimental chamber	113
5.1.2	Heating of the second experimental chamber	114
5.2	Basic experimental protocol	116
5.3	Measurement of absorption cross-sections.....	117

5.4	Experimental investigations with acetone in the second experimental chamber	122
5.4.1	Treatment of experimental data.....	122
5.4.2	Image analysis	125
5.4.3	Leakage experiments – influence of air on the phosphorescence signal quenching.....	129
5.5	Influence of laser pulses on acetone vapour composition	133
5.6	Experimental investigation at different conditions of pressure and temperature on pure acetone.....	135
5.6.1	Intensity dependency with temperature.....	136
5.6.2	Intensity dependency with number density	136
5.6.3	Extraction of time constants.....	137
5.7	Modifications to the experimental chamber	143
5.7.1	Elements of the new chamber	143
5.7.2	Numerical simulations.....	144
5.7.3	Experiments.....	146
5.7.4	Image processing.....	146
5.7.5	Experimental images with heated element at 348 K.....	147
5.7.6	Treatment of experimental images.....	148
5.8	Summary.....	154
6	Towards near wall measurements	157
6.1	Temperature prediction near the wall	158
6.2	Total internal reflection and evanescent waves.....	161
6.3	Calculations for our case	163
6.4	Design ideas.....	165
6.4.1	First design idea	165
6.4.2	Second design idea	166
6.5	Fabricated cell.....	167
6.6	Further questions to be addressed.....	167

6.7	Other research directions	169
7	Conclusions.....	172
1	Appendix A.....	175
2	Appendix B.....	178
3	Appendix C.....	183

Roman symbols

Letter	Description	Unit
A	Current	Amp
a	First exponential coefficient	-
b	Second exponential coefficient	-
c_p	Specific heat of gas at constant pressure	$\text{J Kg}^{-1} \text{K}^{-1}$
c_v	Specific heat of gas at constant volume	$\text{J Kg}^{-1} \text{K}^{-1}$
D_l	Laser beam diameter	m
d	Molecular diameter	m
d_p	Depth of penetration of evanescent waves	m
E_{avg}	Average laser energy	J
E_{den}	Average laser energy density	J m^{-2}
E_o	Energy level at electronic ground state for Raman	J
E_{ph}	Energy of photon	J
E_{S_0}	Energy at state S_0	J
E_{S_1}	Energy at state ' S_1 '	J
E_{S_1-0}	Lowest energy level at S_1 state	J
$E_{thermal}$	Thermal energy	J
F	External force	N
G	Gain	-
h	Planck's constant	J.s
I_0	Intensity at the light at wall	w
I_{in}	Energy density of laser beam	J m^{-2}
I_{inlet}	Laser energy measured at inlet of chamber	J
I_{outlet}	Laser energy measured at exit of chamber	w

I_i	Intensity counts along the y-pixel direction for every value of x - pixel	-
$I_{i,j}$	Intensity counts at a particular pixel location	-
i	Pixel in x – direction	-
j	Pixel in y – direction	-
Δt_{IRO}	Gate	s
K_B	Boltzmann constant	J K ⁻¹
k	Thermal conductivity	W m ⁻¹ K ⁻¹
k_{ISC}	Radiative de-excitation rate constant for inter system crossing	s ⁻¹
k_f	Radiative de-excitation rate constant for fluorescence	s ⁻¹
k_{nr}	Non-radiative de-excitation rate constant	s ⁻¹
k_{nr,T_1}	Non-radiative de-excitation rate constant for triplet state	s ⁻¹
k_{ph}	Radiative de-excitation rate constant for phosphorescence	s ⁻¹
k_r	Radiative de-excitation rate constant	s ⁻¹
k_Q	Quenching rate constant per molecular density of quencher	s ⁻¹
Kn	Knudsen number	-
L	Length traversed by laser beam	m
L_{cell}	Thickness of the test cell	m
l	Equivalent mean free path	m
Lc	Characteristic length	m
m	Molecular mass	kg
N	Avogadro's number	mol ⁻¹
N_p	Number of laser pulses	-
N_i	Number of images	-

N_l	Number of laser pulses	-
n	Number density	m^{-3}
n_m	Number of moles	mole
n_Q	Molecular density of quencher	m^{-3}
P	Pressure	Pa
P_{O_2}	pressure of oxygen	Pa
P_{He}	Pressure of helium	Pa
P_{ac}	Pressure of acetone vapour	Pa
P_{air}	Pressure of air	Pa
P_{di}	Partial pressure of diacetyl vapour	Pa
P_{total}	Total pressure	Pa
P_{tr}	Partial pressure of tracer	Pa
\dot{q}	Rate of heat generation	W m^{-3}
R	Universal gas constant	$\text{J mol}^{-1} \text{K}^{-1}$
Ra	Rayleigh number	-
Re	Reynolds number	-
\mathbf{r}	Displacement	m
S	Photons collected by detector	-
S_0	Singlet state '0'	-
S_1	Singlet state '1'	-
S_P	Peak of the Gaussian	-
S_{Pn}	Normalised peak of the Gaussian	-
S_T	Total counts in the image	-
$S_{T,n}$	Normalised total counts	-
S_y	Integrated counts	-
S_λ	Signal intensity value at a particular wavelength	-
s	Direction along the wall	-
T	Temperature	K
T_1	Triplet state	s
T_g	Real gas temperature at the wall	K

T_{jump}	Temperature jump	K
T_s	Temperature of the gas to be considered at the wall	K
T_{S_0}	Temperature at state S_0	K
ΔT	Temperature difference	K
t	time	s
t_{CCD}	CCD exposure time	s
T_{S_1}	Temperature at state S_1	K
u_g	Gas velocity	$m s^{-1}$
u_s	Velocity of gas	$m s^{-1}$
u_{slip}	Velocity slip	$m s^{-1}$
u_w	Wall velocity	$m s^{-1}$
V	Volume	m^3
V_o	Voltage	Volts
v	Velocity	ms^{-1}
v_m	Most probable speed	ms^{-1}
w	Subscript for denoting wall	-

Greek alphabets

Letter	Description	Unit
α	Thermal diffusivity	$m s^{-2}$
α_1	Refractive index of test cell	-
α_2	Refractive index of medium	-
α_{ITO}	Refractive index of ITO layer	-
α_a	Refractive index of material 'a'	-
α_b	Refractive index of material 'b'	-
α_{ac}	Refractive index of acetone vapour layer	-
γ	Ratio of specific heats	-
δ	Mean molecular spacing	m
ζ	Temperature jump distance	m
ζ_T	Temperature jump coefficient	-

η_p	Optics capturing efficiency	-
θ_{ITO}	Angle of incidence of ITO layer	degree
θ_a	Angle of incidence of material 'a'	degree
θ_{ac}	Angle of incidence of acetone vapour	degree
θ_b	Angle of incidence of material 'b'	degree
θ_{crit}	Critical angle	degree
λ	Wavelength of the light used for excitation	m
K	Function of wavelength	$\text{m}^3 \text{kg}^{-1}$
λ_m	Mean free path	m
μ	Dynamic Viscosity	kg m s^{-1}
ξ	Slip length distance	m
ρ	Density	kg m^{-3}
σ	Momentum accommodation coefficient	-
σ_{abs}	Absorption cross-section	m^2
σ_{SD}	Standard deviation	-
σ_T	Thermal accommodation coefficient	-
τ	Characteristic time of the non- radiative de-excitation	s
τ_1	Fast decay time constant	s
τ_2	Slow decay time constant	s
τ_f	Characteristic time of the radiative de-excitation for fluorescence	s
τ_{ph}	Characteristic time of the radiative de-excitation for phosphorescence	s
τ_r	Characteristic time of the radiative de-excitation	s
ϕ	Quantum yield	-
ν	Frequency	s^{-1}
ν_e	Frequency of emission	s^{-1}
ν_m	Frequency difference	s^{-1}
ν_o	Frequency of absorbed photon	s^{-1}

ϕ_f	Fluorescence quantum yield	-
ϕ_{ph}	Phosphorescence quantum yield	-
χ	Normal direction to wall	-
ω_P	Pump frequency	s^{-1}
ω_S	Signal frequency	s^{-1}
ω_I	Idler frequency	s^{-1}

Subscripts

x, y, z	Coordinates	m
-----------	-------------	---

Acronyms

ADU	Analog digital unit
APS	American physical society
AOM	Acousto-optic modulators
BGAS	Ball grid arrays
CARS	Coherent anti-Stokes Raman scattering technique
CCD	Charged coupled device
CFD	Computational Fluid Dynamics
CPF	Circular polarization filtering
DN	Digital unit
DMS	Digital Moiré subtraction
EW	Evanescant waves
FCC	Face centred cubic
G	Gain
HB	Hydrogen bonded
HSD	Heat source density
HIS	Hue, Intensity, and Saturation
ICA	Insitut Clement Ader
ICCD	Intensified charge-coupled device
IR	Infrared

IRO	Intensified relay optics
IRT	Infrared red thermometry
ITO	Indium tin oxide
LIF	Laser induced fluorescence
LIP	Laser induced phosphorescence
LNG	Liquid natural gas
MCP	Micro channel plate
MEMS	Micro Electro Mechanical Systems
MT	Molecular tagging
MTT	Molecular tagging technique
MTV	Molecular tagging velocimetry
NA	Numerical aperture
NHB	Non-hydrogen bonded
OPO	Optical parametric oscillator
OPD	Optical path difference
PCB	Printed circuit board
PCR	Polymeric chain reaction
PDMS	Polydimethylsiloxane
PMI	Phase measurement interferometry
PTU	Programmable timing unit
RGB	Red-Green-Blue
ROI	Region of interest
RSD	Relative standard deviation
RTD	Resistance temperature devices
SHG	second-harmonic generators
SPAD	Single photon avalanche diode
SV	Sampling volumes
TIR	Total internal reflection
TIRF	Total internal reflection fluorescence
TIQSI	Temperature imaging using quadriwave lateral shearing interferometry
TLC	Thermochromic liquid crystals
UV	Ultra violet

ABSTRACT

The technological progress in micro-manufacturing capabilities has resulted in an exponential growth of micro-electro-mechanical systems (MEMS). This has provided an exciting opportunity to the fluid mechanics and heat transfer researchers' community to experimentally observe and measure flow properties at microscale. More specifically, gas flows within microdevices are subjected to rarefaction effects, which are quantified by the Knudsen number. The slip-flow regime is often encountered in most of the usual micro-components involving gas flows. In this rarefaction regime, the flow exhibits local thermodynamic disequilibria in the near-wall regions, leading to a flow velocity slip and temperature jump at the wall. In addition, the behaviour of most of the microfluidic components depends on the accurate control of temperature and heat transfer. In this context, developing new fluidic microsystems working with gases requires a good theoretical and experimental knowledge of temperature fields.

Although the last decades have seen a considerable progress in theoretical and numerical analysis of rarefied gas flows, this is not necessarily the case regarding experimental investigation. This is mainly due to the fact that existing temperature measurement techniques employed at macroscale are generally not suitable for direct application at microscale. Consequently, a very limited number of experimental data is available in this domain, and there is currently no available experimental technique able to provide accurate temperature fields within the gas, especially in rarefied conditions. It is therefore of great interest to develop novel experimental approaches capable of simultaneously mapping local temperature and velocity fields in gas microflows. For this goal, molecular tagging is a potential candidate based on the luminescence phenomenon of tracer molecules, such as acetone, which exhibit fluorescence or phosphorescence when activated by photons. Their tracking can provide velocity data and for temperature measurements, their luminescence lifetime and intensity dependence on the temperature can be exploited. As far as we know, Molecular Tagging Thermometry (MTT) has only been used to measure temperature of liquids in channels of millimetric dimensions.

To gauge the applicability of this technique for gas thermometry in rarefied conditions (that can be reached either by reducing the dimensions of the system or the pressure), an experimental analysis on acetone vapour phosphorescence at low pressures is presented in this thesis. Experiments are carried out to validate the potential of MTT to measure temperature in rarefied conditions. These results are analysed and supported by numerical CFD simulations. It

is concluded that for a temperature ranging from 290 to 350 K, temperature gradients can be indirectly measured from the effect of luminescence dependence with the number density, although the direct influence of temperature is negligible in this range. Additionally, a new experimental setup aimed at simultaneously measuring the wall temperature by Infra-Red Thermography (IRT) and the near-wall fluid temperature by MTT, illuminating only a slice of molecules near the wall by evanescent waves is proposed, with a further objective to measure temperature jump at the wall in the slip flow regime.

In French

Les progrès technologiques récents en micro-fabrication ont entraîné un développement exponentiel des systèmes micro-électro-mécaniques (MEMS). Cela a conduit la communauté des chercheurs en mécanique des fluides et en transferts thermiques à chercher à observer et à mesurer expérimentalement les propriétés des écoulements à échelle microscopique. Plus précisément, les écoulements de gaz au sein de micro-dispositifs sont soumis à des effets de raréfaction, quantifiés par le nombre de Knudsen. Le régime de glissement est rencontré dans la plupart des microsystèmes impliquant des écoulements de gaz. Dans ce régime modérément raréfié, l'écoulement présente des déséquilibres thermodynamiques locaux dans les régions proches de la paroi, ce qui entraîne un saut de vitesse et de température à la paroi. De plus, le fonctionnement de la plupart des composants microfluidiques dépend d'un contrôle précis de la température et des transferts thermiques. Dans ce contexte, le développement de nouveaux microsystèmes fluidiques fonctionnant avec des gaz nécessite une bonne connaissance théorique et expérimentale des champs de température.

Bien que l'analyse théorique et numérique des écoulements de gaz raréfiés ait considérablement progressé au cours des dernières décennies, il n'en va pas nécessairement de même pour la recherche expérimentale. Cela est principalement dû au fait que les techniques de mesure de la température existantes utilisées à l'échelle macroscopique ne conviennent généralement pas pour une application directe à l'échelle microscopique. En conséquence, un nombre très limité de données expérimentales est disponible dans ce domaine et il n'existe actuellement aucune technique expérimentale disponible capable de fournir des champs de température précis dans le gaz, en particulier dans des conditions de raréfaction. Il est donc très intéressant de développer de nouvelles approches expérimentales capables de cartographier simultanément les champs de température et de vitesse locaux dans des micro-écoulements de

gaz. À cet effet, le marquage moléculaire est une technique potentiellement appropriée. Elle exploite le phénomène de luminescence de molécules traceuses, telles que l'acétone, qui émettent un signal lumineux fluorescent ou phosphorescent lorsqu'elles sont activées par des photons. Le suivi de ces molécules peut fournir des mesures de vitesse ; la dépendance de leur durée de vie et de leur intensité lumineuse vis-à-vis à la température peut être exploitée pour des mesures thermométriques. À notre connaissance, la thermométrie par marquage moléculaire (MTT) n'a à ce jour été utilisée que pour mesurer la température d'un liquide dans des canaux de dimensions millimétriques.

Pour évaluer l'applicabilité de cette technique à la mesure de température de gaz dans des conditions raréfiées (pouvant être atteintes en réduisant les dimensions du système ou la pression), une analyse expérimentale de la phosphorescence de l'acétone à basse pression est présentée dans cette thèse. Les résultats sont analysés et appuyés par des simulations numériques de type CFD. Il apparaît que pour une température variant entre 290 to 350 K, des gradients de température peuvent être indirectement mesurés en exploitant la dépendance de la luminescence vis-à-vis de la concentration moléculaire, alors que l'effet direct de la température est négligeable dans cette plage de températures. En outre, un nouveau dispositif expérimental est proposé. Il vise à mesurer simultanément la température de paroi par thermographie infrarouge (IRT) et la température du fluide en proximité de paroi par MTT, en n'éclairant qu'une fine couche de molécules près de la paroi par des ondes évanescentes, l'objectif final étant de mesurer le saut de température à la paroi dans le régime de glissement.

1 Introduction

Microfluidics as a field of study has gained immense prominence in the recent decades. This was, in some sense, predicted by the famous physicist Richard Feynman in his spectacular speech ‘There is plenty of room at the bottom’ addressed at APS (American Physical Society) meeting at Caltech, USA in 1959¹. Many of the ideas suggested by Feynman are being realized, thanks to the recent advances in the fabrication of MicroElectroMechanical Systems (MEMS), and this may be considered as the ushering of the new and exciting field of microfluidics, especially at the experimental front. For example, Figure 1.1 shows an ant holding a nickel microgear². On the other hand, Figure 1.2 shows a design of blood plasma separation micro-device which can revolutionize the way blood tests will be carried out in the future³.

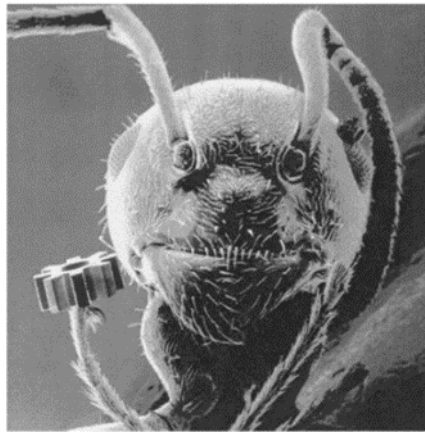


Figure 1.1 An ant holding a nickel microneedle; this image has been generated by electron microscopy at KIT in Germany²

It is difficult to give a simple definition of the field of microfluidics. Depending on their research bend, researchers have given different definitions. However, it is broadly agreed that we deal with the manipulation of fluids in devices with at least one dimension being of the order of few microns to hundreds of microns. The advantage of MEMS is to enhance the possibility to exploit physics at this microscale towards technological progress. Towards this end, a large amount of research, both at theoretical and experimental fronts, has been carried out in microfluidics during the last three decades. Depending on the researcher’s interest and the domain in which the investigation is being carried out, as suggested by Nguyen and Wereley⁴,

several terminologies have cropped up trying to define the field of investigation, with the most prominent being MEMS-fluidics, bio-microfluidics, and microfluidics. In the last few years, with the ability to study fluids in nano-devices, the new field of nanofluidics or nanoflows has also emerged.

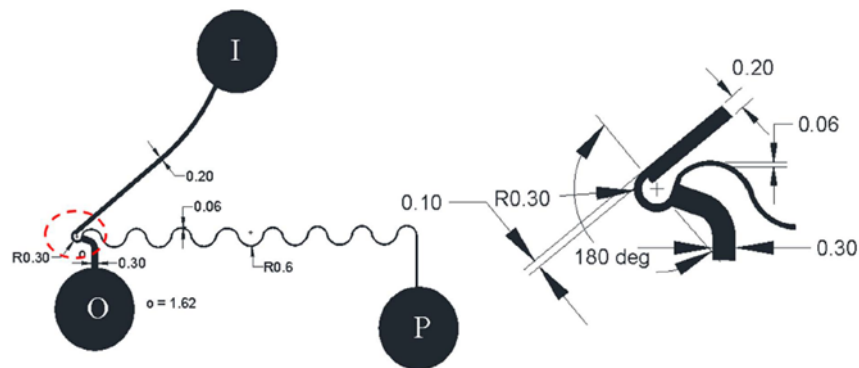


Figure 1.2 Scheme of a micro-device for separation of plasma from human blood (all dimensions are in mm) ³. Design of the microdevice, Zoomed view of junction of microdevice. (I-Inlet, O-outlet, and P-Plasma reservoir). The design has a curvature with an inner bending radius of 0.2 mm, and an outer bending radius of 0.3 mm. Therefore, the zone of constriction has a width of 100 μ m. The bend angle employed in this design is 180°. The microdevice have been fabricated to a depth of 60 μ m

In microdevices, there is a clear difference in the behaviour exhibited by the fluid in comparison with its behaviour at macroscale. When shrinking down the dimensions, the rate of decrease of the role played by properties dependent on the area is slower than that of the properties which depend on the volume – this is sometimes expressed as the ‘square-cube’ law⁵. For example, at microscale, effects of gravity tend to become negligible (as compared to macroscale) and the influence of inertial forces reduces in comparison with that of surface forces. Forces such as surface tension, electrostatic forces and capillary forces begin to play a more important role. The transport of mass, momentum and energy is greatly altered due to a dramatic increase in surface-to-volume ratios at microscale. Consequently, in some case, there is a strong necessity to modify the existing macro boundary conditions or to come up with entirely new models to describe and predict the evolution of the fluids in microsystems.

Broadly, the fluid mechanics investigation at macro and micro domains mainly differs in the following aspects: exhibition of non-continuum effects and increased domination of

surfaces (walls) ⁵. The manifestation of microscale effects is finding various applications. More specifically, for what concerns gas microflows, several practical devices can be cited, such as for example, micronozzles^{6,7}, micro heat exchangers^{8,9}, micro actuators^{10,11}, micro thrusters^{12,13}, micro gas chromatographs^{14,15}, sensors or separators¹⁶, and vacuum micropumps¹⁷. Most of the applications require a control of heat transfer and temperature distributions inside the fluid flow.

Koplik et al.^{18,19} demonstrated the large density fluctuations which occurred in a gaseous or liquid fluid near a wall with Molecular Dynamics (MD) simulations in which a pair of molecules interacts with the 12-6 Lennard-Jones potential. All the dimensional quantities in this paper were made non-dimensional (MD or molecular units) by multiplying with an appropriate combination of distance, energy/Boltzmann constant and mass. The advantages of using these units are: (i) the possibility to work with values of the order of unity instead of the extremely small values at the atomic scale; (ii) the simplification of equations of motion; (iii) a scaling of results for different systems described by the same model. The molecules were initialised in a 3D face centred cubic structural lattice. The spacing of the walls was adjusted to obtain the desired density. The phase diagram shown in Figure 1.3 shows the phase diagram of a 12-6 Lennard-Jones system. Based on this diagram, they adjusted the values of density and temperature to shown in the phase of interest.

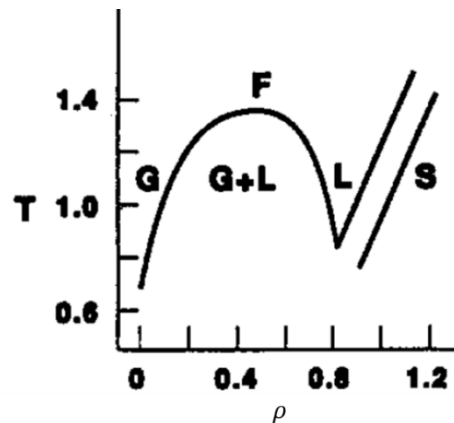


Figure 1.3 The phase diagram 12-6 Lennard-Jones system; G, L, S, F refers to gas, liquid, solid and supercritical fluid respectively. ρ refers to density and T refers to temperature.

For most of their simulations, they utilised 1536 molecules for fluid and 256 molecules for each of the two walls (top and bottom). The size of the FCC structure was adjusted to obtain

a density of 0.8 and the temperature of the system was maintained at 1.2. From the phase diagram, it noted that these conditions correspond to liquid phase. They observed that at the wall, the fluid atoms tend to organize in layers parallel to the atoms of the wall. This phenomenon is referred to as layering effect and the authors demonstrated that this plays a very important role in the large density fluctuations observed near the wall as shown in Figure 1.4. In their study, they were able to demonstrate that this effect of wall-fluid interaction is of the order of a few atomic diameters in liquids, whereas for gases, the effect is significant on much greater distances, this domain can be referred to as the Knudsen layer and has a thickness in the order of the mean free path. This is one of the studies which emphasis the necessity to be careful in modelling gas flow behaviour at micro and nano scales.

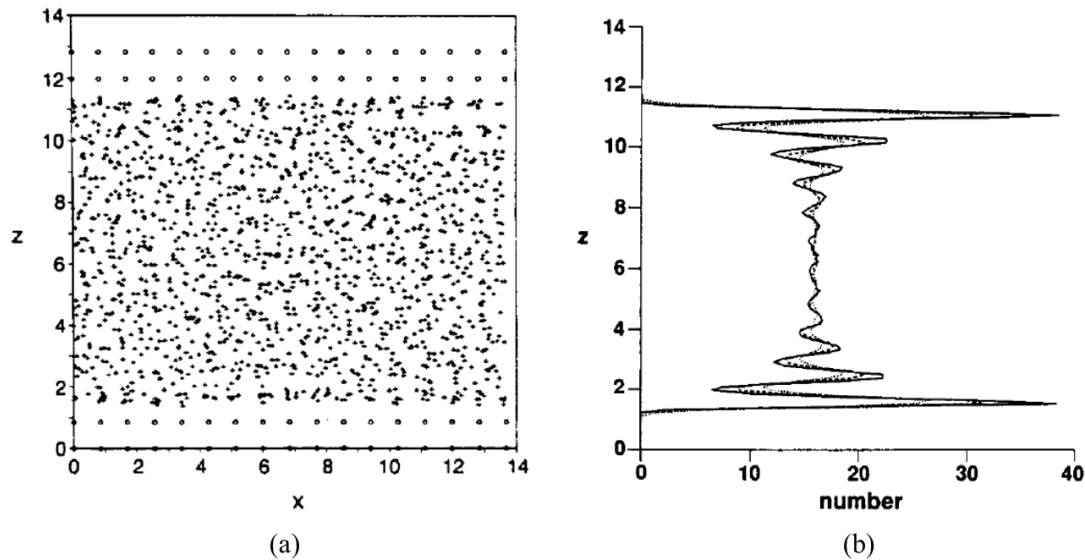


Figure 1.4 (a) Instantaneous molecular positions for a liquid in equilibrium between walls, at $T = 1.2$ and $\rho = 0.8$. (b) The average density profile for (a)^{18,19}

In gas microflows, the Knudsen number Kn , defined as the ratio of the molecular mean free path λ_m to a characteristic dimension of the system L_c (typically the hydraulic diameter in the case of a microchannel), is a dimensionless number quantifying the flow rarefaction, i.e. its deviation from thermodynamic equilibrium. In microsystems with gas microflows, a Knudsen number in the range $10^{-3} - 10^{-1}$ is frequently encountered, and this corresponds to the slip flow regime. In this moderate rarefaction regime, the flow exhibits local thermodynamic disequilibrium in the near-wall region, in the so-called Knudsen layer. Modelling the gas flow

outside this Knudsen layer using a continuum approach is, however, still possible, provided classical boundary conditions are replaced with slip specific boundary conditions that account for a velocity slip and a temperature jump at the wall. Theoretical investigations have revealed a strong influence of the velocity slip and temperature jump at the wall on heat transfer^{4,5,20–22}.

Determining the temperature jump by direct experimental measurements is a very interesting goal in the study of the slip flow regime, especially if experimental data could provide the real distribution of temperature within the Knudsen layer. Very limited experimental data, however, are available in rarefied flows, particularly concerning local measurements of velocity and temperature, especially for what concerns information close to the walls, making the study of heat transfer in gas microflows very challenging. Moreover, the accuracy of different models of velocity slip and temperature jump boundary conditions routinely employed in slip flow analysis must be discussed on the basis of solid experimental evidence, which relies on accurate information of the temperature distribution at the wall and near-wall regions. As suggested in the works of various researchers^{23,24}, there already exists a great deal of literature on the theoretical aspects of gas behaviour at microscale. The knowledge and mastering of temperature distributions at an experimental level is not only of engineering applications interest, but it is also of fundamental importance for validating the theoretical models which are commonly used to predict fluid flow and heat transfer at the microscale level²³. However, due to the difficulties in experimentation, there has been very limited experimental validation of many of these models. Moreover, most of the experiments were carried out to measure some global quantities. Information on local temperature distributions at the near-wall regions is crucial to understand the mechanisms of gas/surface interaction in local disequilibrium conditions. This would allow to enhance the development of new micromechanical systems with optimized properties. It would also be interesting to note that new experimental data will always open the doors to new and more accurate models.

Temperature is a measure of the average translational kinetic energy associated with the microscopic disordered motion of atoms or molecules. It is important to note that the estimation of temperature can only be based on observable temperature dependent effects²⁵. For example, the determination of convective heat transfer coefficients for flows in microchannels is directly related to the knowledge of temperature distribution in these channels²⁴.

At the advent of microfluidics as a new field of study, the first experimental approach towards the measurement of temperature distributions at microscale was to scale down the existing macroscale measurement techniques^{26–29}. However, it was demonstrated that many of

the macroscale temperature measurement techniques were not viable at microscale. This has led researchers to investigate and develop new experimental techniques. The quest for this search is still on, and therefore, it is which makes the field of thermometry at microscale an active area of research nowadays. Reliable experimental data are now available for both hydrodynamics and heat transfers in liquid microflows. However, unfortunately, this is not yet the case for gas microflows.

With the recent advances in the experimental capabilities, it becomes now possible to do experiments on measuring local velocity and temperature in gas microflows. The focus of this thesis is to investigate one such technique based on the phenomenon of photoluminescence to try accessing the temperature of gases in rarefied conditions. This technique presented in this thesis is being referred to as Molecular Tagging (MT). MT is a general reference to the technique of molecules tagging by exciting them with a light source (typically a laser) and extracting relevant informations on velocity, temperature, density or pressure based on either fluorescence or phosphorescence, depending upon the specific requirements of the study. In other words, MT techniques could also be called Laser Induced Fluorescence (LIF) or Laser Induced Phosphorescence (LIP) techniques. The technique in which the interest lies in measuring velocity fields is usually referred to as Molecular Tagging Velocimetry (MTV). If the interest lies in measuring temperature, it is referred as to as Molecular Tagging Thermometry (MTT). This thesis work is built in the continuity of the works of Samouda et al.³⁰, Si Hadj Mohand et al.^{31,32}, and Fratantonio et al.³³ previously developed at Institut Clément Ader (ICA), Toulouse, France. In the theses of the first above-cited authors, it was demonstrated that it was possible to employ MT technique to measure velocity fields in gas microflows. The objective of our work is now to investigate the suitability of this technique MT to measure temperature fields in gas microflows.

Based on the above objective of the thesis, the present manuscript is organised as follows:

- Chapter 2 is an introduction to the theory of gas microflows. A brief introduction to the concepts of rarefaction is presented. The significance of the slip flow regime in gas microflows and a brief outline on the various models available to describe them are presented.
- Chapter 3 is a review of various temperature measurement techniques at microscale with special focus on the measurement of gas temperature. The physical principles of photoluminescence are presented.

- Chapter 4 introduces the molecular tagging experimental setup and is followed by a presentation of the first experimental results and their analysis.
- Chapter 5 presents the details of the design and assemblage of a new experimental chamber. The details on isothermal and non-isothermal experiments carried with this new setup are presented and analysed.
- Chapter 6 presents a possible approach to combine MTT and evanescent waves (EW) that could be developed to measure temperature jump at the wall.
- Chapter 7 provides a conclusion of the different aspects discussed through the thesis and proposes some future perspectives.

2 Basics of gas microflows

In this chapter, a brief discussion on the theory of rarefied gas flows is presented. Basic ideas on dilute gas and rarefied flow regimes are discussed. The concepts of velocity slip and temperature jump are also presented.

2.1 Rarefaction at microscale

2.1.1 Dilute gas

Avogadro's number prescribes the number of atoms/molecules present in a mole of gas (n_m), and this number is a constant: $N = 6.02252 \times 10^{23} \text{ mol}^{-1}$, which does not depend on the kind of gas. Moreover, at given conditions of pressure and temperature, whatever the gas, the volume occupied by a mole of gas is constant. If d represents the molecular diameter and δ represents the mean molecular spacing, then a gas can be approximated as a dilute gas if it satisfies $\frac{\delta}{d} \gg 1$. The molecules of such a gas experience only binary collisions. The ideal gas assumption is a consequence of the dilute gas assumption; it is valid for high temperature at low pressures, above the saturation pressure and below the critical point. An ideal gas can be defined by two state equations: the equation of Boyle Mariotte and equation of Charles law.

Boyle's law:

At constant temperature, pressure (P) of a given mass of an ideal gas is inversely proportional to its volume (V).

$$P \propto \frac{1}{V} \quad (2.1)$$

Charles's law:

At constant pressure, the volume of an ideal gas is directly proportional to its absolute temperature (T).

$$V \propto T \quad (2.2)$$

From Avogadro's law,

$$V \propto n_m \quad (2.3)$$

On combining Equations (2.1), (2.2), and (2.3), we can write,

$$V \propto \frac{n_m T}{P} \quad (2.4)$$

Now putting the proportionality constant as the universal gas constant, R , we get

$$PV = n_m RT \quad (2.5)$$

This ideal gas approximation leads to a significant simplification in modelling the gases. The above equation can be written in terms of Boltzmann's constant, K_B , as $PV = NK_B T$.

2.1.2 Boltzmann equation

Due to the large number of molecules in any physical system and the impossibility of tracking the position and velocity of each molecule at every time, researchers consider the probabilities of molecules to have different positions and velocities. In other words, the focus has been shifted from certainties to probabilities, which is the subject matter of statistical mechanics. The kinetic theory of gases, that is, the statistical mechanics of gas molecules, can be deduced from this assumption of dilute gases along with other considerations, such as the molecular chaos and equipartition of energy. Based on these approximations, from Liouville's equation, we can derive the Boltzmann transport equation³⁴, which can be written in the following manner :

$$\frac{\partial f(\mathbf{r}, \mathbf{v}, t)}{\partial t} + \mathbf{v} \frac{\partial f(\mathbf{r}, \mathbf{v}, t)}{\partial \mathbf{r}} + \mathbf{F} \frac{\partial f(\mathbf{r}, \mathbf{v}, t)}{\partial \mathbf{v}} = Q(f, f^*) \quad (2.6)$$

In Equation (2.6), \mathbf{F} is the external force acting on a molecule and $Q(f, f^*)$ is the collision integral or collision term, which describes the changes in the velocities of the distribution function $f(\mathbf{r}, \mathbf{v}, t)$ following collisions. The solution of the Boltzmann equation can provide the information required to compute the averages of quantities of interest (mass, momentum, and energy) for the gas flow. However, the mathematical complexity of the collision integral is such that even for the simplest case, obtaining an analytical solution is very challenging. The boundary conditions rely on the scattering kernel, which dictates the interactions between the gas molecules and the wall molecules. The dilute gas assumption significantly simplifies its modelling. Researchers have been proposing both physical and

mathematical arguments for modelling this scattering kernel³⁴ (sometimes called as differential cross section). The mathematical description of these aspects are dealt at great length in the works of Cercignani^{34,35}.

2.1.3 *Thermodynamic non-equilibrium*

The concept of thermodynamic non-equilibrium is often discussed in the context of gas microflows and has been detailed in the works of Karniadakis⁵ and Sone³⁶, to name a few researchers. The validity of local thermodynamic equilibrium depends on the degree of intermolecular collisions within the chosen volume of investigation. This chosen volume, or control volume, is divided in small sampling volumes (SV) where macroscopic quantities can be calculated as functions of the microscopic quantities, and determining its size should be done cautiously. This concept of SV is also important as it serves as a bridge between the microscopic fluctuations and macroscopic variations. Researches have suggested that a control volume of 10,000 molecules leads to a statistical fluctuation of 1% in the macroscopic quantity being investigated^{5,22}. For gas at standard conditions, this leads to a sampling volume of $2.7 \times 10^{-22} \text{ m}^3$, which corresponds to a length of 65 nm for one side of a cubic SV³⁷. For a smaller SV, defining macroscopic quantities should not be possible any more.

The notion of mean free path (λ_m) is of fundamental importance in gas microflows. It is defined as the average distance travelled by a molecule from one collision to another, in a referential following the macroscopic movement of the flow. For thermodynamic equilibrium, the intermolecular collision frequency in the chosen SV must be high enough, such that the mean free path should remain small in comparison with the characteristic length of the SV, and a fortiori with the characteristic lengths of the control volume. This idea can be quantified by defining the Knudsen number Kn as the ratio of the mean free path λ_m to a characteristic length L_c of the control volume:

$$Kn = \frac{\lambda_m}{L_c} \quad (2.7)$$

Thermodynamic equilibrium requires $Kn \ll 1$. Slightly depending on the complexity of the geometry being employed, but generally at $Kn > 1$, we tend to get into thermodynamic non-equilibrium and thereby, defining averaged macroscopic values and their variations in time and space becomes questionable. An increase of the Knudsen number, due either to a decrease of L_c or to a decrease of pressure leading to an increase of λ_m , leads to an increase of rarefaction. For $Kn > 1$, mass flow rate, shear stress, heat flux, and pressure drop predicted by continuum

models do not correspond to the values obtained experimentally. This requires assessing the validity of the continuum models, and to use non-continuum appropriate models to predict the experimentally observed behaviour. The value of the Knudsen number at which a model breaks down is not a strict value and is mostly dependent on the problem being investigated, as well as on the choice of L_c .

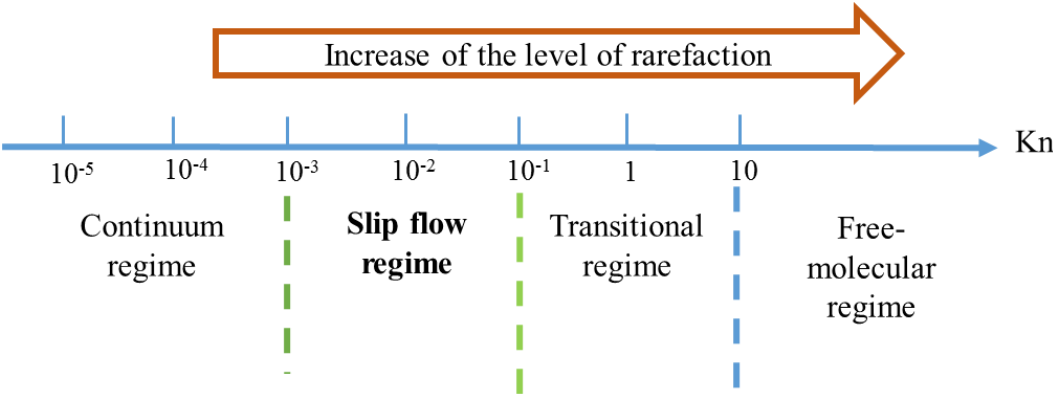


Figure 2.1 Classification of flow regimes based on the Knudsen number

Researchers, based on empirical evidence and theoretical arguments, have come up with different flow regimes based on the value of Kn , as shown in Figure 2.1. Usually, for $Kn < 10^{-3}$, the flow can be treated as a continuum and be modelled by the conventional compressible Navier-Stokes-Fourier equations with the classical no-slip boundary conditions. An interesting flow regime, referred to as slip flow regime, is encountered for $10^{-3} < Kn < 10^{-1}$. Most of the gas microsystems typically lie in the slip flow regime, and also theoretically, this regime leads to lot of interesting analytical and semi-analytical modelling. This regime is of interest in this thesis. In this regime, the flow can still modelled with conventional Navier-Stokes-Fourier equations, provided the boundary conditions are altered to include velocity slip and temperature jump at the wall to take rarefaction effects into account. This underlines the fact that the effects of rarefaction begin to become prominent near the wall, where only a half-space of fluid is present.

Modelling the flow regime for $10^{-1} < Kn < 10$ is rather complicated and this corresponds to the so-called transition flow regime. The constitutive relations defining the heat flux vector and stress tensor break down. The intermolecular collisions still exist and must be considered into analysis. It is possible to analyse this regime, as well as the other regimes, with

the Boltzmann equation (Equation (2.6)). Extended hydrodynamic equations can also be derived to modify the constitutive relations defining the heat flux vector and the stress tensor, resulting for example in the emergence of Burnett equations that can replace the Navier-Stokes equations and extend their range of applicability to Knudsen numbers higher than 10^{-1} . Burnett equations are derived from the Boltzmann equation based on the Chapman-Enskog expansion of the velocity distribution f by including terms of the order of Kn^2 . The free molecular regime with negligible intermolecular collisions between the gas molecules occurs for $Kn > 10$. However, the collisions with the wall should of course be taken into account and properly modelled²².

An additional question that arises in dealing with gas microflows is whether rarefied gas flows due to either low pressures or low dimensions can totally be considered as similar, and if a Knudsen analogy can be fully applied. A theoretical justification to this idea of dynamic similarity is present in the work of Sone³⁶. It is based on the analysis of the Boltzmann equation for low Reynolds and Knudsen numbers. It turns out that two rarefied flows defined by the same value of Kn in an homothetic geometry can be considered as similar if we carefully consider the aspect of onset of statistical fluctuation and wall surface effects²². At microscales, the wall roughness can significantly contribute to the overall dimensions of the channel. Therefore, along with Kn , ratios of $\frac{\delta}{d}$, $\frac{L_c}{\delta}$, and $\frac{L_c}{d}$, should all be taken into consideration to understand the divergences between gas microflows and rarefied flows³⁸.

2.2 Slip flow regime

Many systems commonly encountered in gas microflows are typically in the slip flow regime, which is particularly interesting as some of these flows can be treated by analytical or semi-analytical models with appropriate boundary conditions at the wall. Therefore, this requires further discussion on the kind of boundary conditions to be employed at the wall. The interaction between the wall and the gas molecules is strongly dependent on the wall, and its surface conditions are of utmost importance in dictating the velocity and temperature profiles in gas microflows, thereby the mass flow and heat transfer characteristics³⁷.

For reaching a perfect thermal equilibrium between the gas near the wall and the wall, there should be many molecular collisions in an infinitesimally small duration of time, both between gas molecules and gas and wall molecules, which is practically not possible. Therefore,

irrespective of the Knudsen number, there is always a region close to the wall, where the gas is in disequilibrium with the wall and in non-equilibrium itself due to a lack of intermolecular collisions. This domain is the Knudsen layer (see Figure 2.3) and it can be shown that its thickness is of the order of the mean free path. At low Knudsen number, this Knudsen layer is extremely thin compared to the characteristic length of the flow (such as an hydraulic diameter) and its effect on the bulk flow can be ignored. In other words, the influence of this Knudsen layer is not felt on the experimentally observable macroscopic properties, as we are tending towards continuum approximation in almost all the control volume. However, in the range $10^{-3} < Kn < 10^{-1}$, the effect of the Knudsen layer is to be considered, and it is routinely done by completing the conventional Navier-Stokes-Fourier set of equations with the Maxwell's velocity slip and Smoluchowski's temperature jump conditions at the wall.

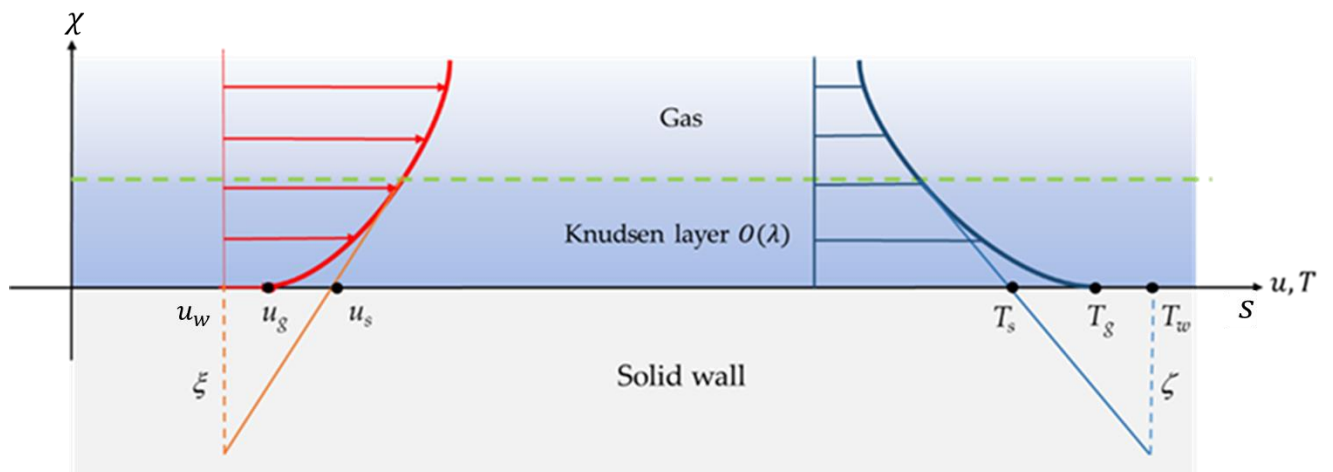


Figure 2.2 Schematic of the concepts of velocity slip (in red) and temperature jump (in blue). ξ and ζ are the slip length and the temperature jump distance, respectively.

In order to better understand the behaviour of the gas in the Knudsen layer, attention should be paid to the reflexions of the molecules at the wall. The realistic reflexions of the molecules at the wall are statistically somewhere in between the limits corresponding to specular and diffuse –i.e. with total accommodation– reflexions (shown in Figure 2.3).

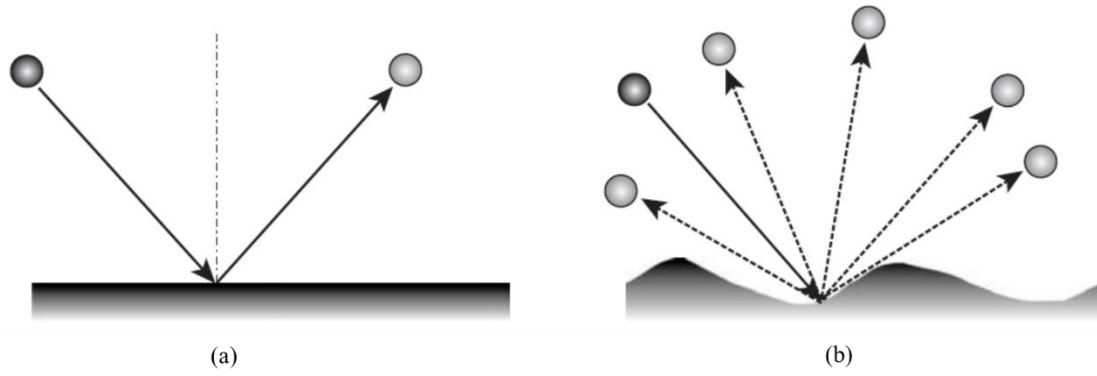


Figure 2.3 (a) Perfect (specular) reflection of a fraction $(1 - \sigma)$ of the molecules. (b) Diffuse reflection of a fraction σ of the molecules²².

Assuming that a fraction σ of the molecules is reflected diffusely and that the complementary fraction $(1 - \sigma)$ is specularly reflected, from a momentum balance at the wall, Maxwell³⁹ came up with the following relation for velocity slip, u_{slip}

$$u_{slip} = u_s - u_w = \frac{2 - \sigma}{\sigma} \lambda_m \left[\frac{\partial u}{\partial \chi} - \frac{3}{2} \frac{\mu}{\rho T} \frac{\partial^2 T}{\partial s \partial \chi} \right]_w + \frac{3}{4} \left[\frac{\mu}{\rho T} \frac{\partial T}{\partial s} \right]_w \quad (2.8)$$

where

$$\lambda_m = \sqrt{\frac{\pi}{2}} \frac{\mu}{\sqrt{P\rho}} = \sqrt{\frac{\pi}{2}} \frac{\mu}{\rho \sqrt{RT}} \quad (2.9)$$

is an expression of the mean free path proposed by Maxwell, assuming hard sphere molecules.

In Equations (2.3) and (2.4), u is the velocity of the gas in the s -direction, u_w is the velocity of the wall, n and s are the normal and tangential directions, μ is the dynamic viscosity of the gas, ρ its density, P its pressure and T its temperature, and R is the specific gas constant. Note that u_s is different from the real velocity u_g of the gas at the wall (see Figure 2.3). It is the value of velocity which provides the boundary condition with a suitable fictitious velocity at the wall for a correct modelling of the velocity out of the Knudsen layer.

In the literature, the second order temperature derivative term in Equation (2.10) is generally ignored, and the resulting equation is presented, without this term, as the classic velocity slip condition. Similarly, a temperature jump condition was proposed by Smoluchowski, assuming a fraction σ_T of the gas molecules with complete energy

accommodation with the wall and a fraction $(1 - \sigma_T)$ reflected with its incident thermal energy. Based on energy consideration, the following temperature jump condition can be identified:

$$T_{jump} = T_s - T_w = \frac{2 - \sigma_T}{\sigma_T} \frac{2\gamma}{\gamma + 1} \frac{k}{\mu c_p} \lambda_m \left(\frac{\partial T}{\partial \chi} \right)_w \quad (2.10)$$

In Equation (2.10), T_s is the temperature of the gas to be considered at the wall to obtain the correct temperature profile out of the Knudsen layer. As in the case of velocity, T_s is different from the actual temperature of the gas at the wall, T_g . In this equation, T_w is the temperature of the wall, γ the ratio of specific heats of the gas, k its thermal conductivity and c_p its specific heat at constant pressure.

It is possible to non-dimensionalise Equations (2.8) and (2.10) with appropriate reference velocity and temperature to better show the role of the Knudsen number, which is the dimensionless form of the mean free path. Coefficients σ and σ_T are the so-called tangential momentum accommodation and temperature accommodation coefficients, respectively. These coefficients give us an indication on the momentum and energy exchanges between the molecules of the gas and the wall. These coefficients are not necessarily equal, and depend upon various parameters, such as the local pressure, velocity, gas and wall temperatures, in addition to the surface nature and roughness⁴⁰.

Researchers have applied these velocity slip and temperature jump boundary conditions at the wall to a variety of flow problems involving circular, annular and rectangular geometries²³. As put forward by various researchers, it is evident that the theoretical understanding of gas microflows is now at an advanced level. On the other hand, there is a clear lack of accurate experimental data, especially regarding the local distribution of velocity and temperature⁴¹. This is true for both steady and unsteady situations in gas microflows. Therefore, there is an urgent need to develop new experimental strategies to address the gap between theory and experimentation.

The need of thermometry at microscale is particularly important, as an increasing number of applications require a precise control of heat transfer⁴². The state of the art on this topic is presented in the following chapter.

3 Microscale thermometry and its applications to liquid and gas flows

The most common method of classifying the temperature measurement techniques in the literature is based on the interaction between the sensing element and the fluid or solid surface which temperature is to be probed or measured⁴³⁻⁴⁶. Contact measurement thermometers such as thermocouples, resistance temperature detectors, etc., or more sophisticated systems, such as atomic force microscopy temperature probes, may be of common use. On the other hand, contactless techniques, such as interferometry, can ensure non-intrusive temperature measurements. Certain techniques, such as molecular tagging, can be classified to lie in between contact and contactless techniques since the molecular tracers which are in contact with the fluid can be considered as intrusive until a certain extent. To summarize, the most general way of classifying the techniques would be contact, no contact, and semi-contact-based techniques.

Another system of classification is based on the calibration procedure used for the technique employed. In primary systems, well-established equations of state are used for directly relating the measured signals to the absolute temperature. In secondary systems, it is necessary for the measured signal to have a reference to a precise temperature (within experimental uncertainties), and in some instances, calibration may pose considerable difficulties.

Lastly, one can also classify the techniques according to the underlying physical principle exploited to map temperature. The techniques are classified as based on: thermal expansion, thermo-electric effect, and thermo-optic effect, as shown in Table 3-1. Thermo-optic techniques based on the implementation of an optical system can be sub-classified as luminescent and non-luminescent measurement techniques.

Techniques based on thermal expansion are hardly applicable to microscale as they require using a non-negligible additional volume of gas, liquid or solid. Micro-sensors exploiting a thermo-electric effect are briefly described in Section 3.1 and less intrusive techniques based on thermo-optic effects are analysed with more details in Section 3.2.

Table 3-1 Classification of various temperature measurement techniques according to the underlying physical principle exploited.

Thermal expansion	Thermo-electric effect	Thermo-optic effect
<ul style="list-style-type: none"> ➤ Gas <ul style="list-style-type: none"> • Gas bulb thermometer • Gas pressure thermometer ➤ Liquid <ul style="list-style-type: none"> • Liquid bulb thermometer ➤ Solid <ul style="list-style-type: none"> • Bi-metallic thermometer 	<ul style="list-style-type: none"> ➤ Thermocouple ➤ Resistance temperature detector (RTD) ➤ Thermistor ➤ Semiconducting sensor 	<ul style="list-style-type: none"> ➤ Non-luminescent techniques <ul style="list-style-type: none"> • Interferometry • Infrared (IR) techniques • Thermochromic liquid crystals (TLC) • Raman thermometry • Temperature sensitive paints ➤ Laser based techniques <ul style="list-style-type: none"> • Laser induced fluorescence (LIF) • Laser induced phosphorescence (LIP) • Molecular tagging (MTT)

3.1 Conventional and contact-based thermometry adopted at microscale

In this section, we briefly present the conventional contact-based temperature measurement techniques adopted to measure temperature at microscale. These techniques were conventionally used for measuring temperature at macroscale, and subsequently with modern fabrication techniques, sensors have been miniaturized for microscale temperature measurement.

Thermocouples are based on the Seebeck effect. A thermocouple is essentially formed by joining two dissimilar metals with two junctions. On imposing a temperature difference between these two junctions, one of which being at a reference temperature, an intrinsic Seebeck voltage is produced. The temperature response with voltage is almost linear, resulting in simple calibration curves. Thermocouples are among the most common devices used for temperature detection at macroscale. With the advances in microfabrication, it has become common to fabricate micro-thermocouples using different methods⁴⁷. For instance, Zhang et al.⁴⁸ provided the design, fabrication and characterization of metal embedded thin film thermocouples with various film thicknesses and junction sizes. Thiery et al.⁴⁹ have carried out temperature profile measurements of near-field optical microscopy fiber tips by means of sub-micrometric thermocouples. Recently, researchers have been able to fabricate gold-nickel (Au-Ni) thermocouples with 2.5- μm -wide electrodes on a 30-nm-thick silicon nitride (Si_3N_4) membrane, using electron beam lithography⁵⁰.

The disadvantages of thermocouples are their low lifetime and robustness. Sometimes they are very sensitive to external sources of temperature and may be prone to corrosion. During operation of a thermocouple, there are many potential sources of error (noise, drift, etc.). In case of micro-thermocouples, additional challenges come into picture: especially the difficulties in forming a junction using thin wires and thereby making a useful and reliable device. The micro-thermocouple itself has some thermal inertia influencing its temporal response and can pose difficulties to be implemented inside microsystems.

Other contact-based techniques, such as micro resistance temperature detectors (μ RTD)⁵¹⁻⁵⁴, thermistors⁵⁵⁻⁶⁰ and semiconducting sensors⁶¹⁻⁶⁴ are employed in various studies in the literature. All these techniques allow a measurement of temperature only at discrete locations. Therefore, there is no direct information about the continuous spatial distribution of temperature, making it difficult to obtain temperature profiles within a system. In addition, these sensors do not allow temperature measurement within the bulk flow without a strong perturbation of the flow and heat transfer. Therefore, though the above mentioned methods may be easy to use, they are mainly limited to provide local data at the walls and do not really serve the requirements of temperature distribution analysis in a flow, necessitating the development of further sophisticated, optical based, techniques.

3.2 Optical based techniques

In this section, various optical based techniques applied to measure temperature of fluids at microscale are examined. Optical techniques have been widely employed at microscale due to their unique characteristic of non-destructiveness and the ability to provide superior spatial and temporal resolutions⁶⁵. Each sub-section is introduced by a brief description of the physical principles, followed by applications to liquid and gas microflows. Some techniques, such as the liquid crystal thermography, can provide the wall temperature, and based on this information, the fluid temperature can be inferred. On the other hand, techniques based on molecular tagging can provide a signal within the gas, more or less directly linked to the gas temperature. For each technique, a table summarizing the pros and cons is presented.

3.2.1 Interferometry

3.2.1.1 Principle

Interferometry has been widely used in applications of thermal and fluids engineering. A real-time recording of the interference patterns can be carried out using this technique. In division of amplitude interferometry, a change in optical paths (phases) between two or more coherent light beams is measured. But, in most of the interferometers light issued from one single laser is divided into only two beams. One beam passes through the experimental test cell (phase object) and the other beam follows a reference path with uniform non temperature and physical properties. The experimental test section experiences certain temperature and density or pressure distributions. The variation of several physical quantities, such as density or concentration, can result in the modification of the refractive index, n , in the test section. Therefore, there is a variation δ_0 in the phase of the optical beam:

$$\delta_0 = \frac{2\pi L_{cell}}{\lambda} (\alpha_1 - \alpha_2) \quad (3.1)$$

In equation (3.1), $(\alpha_1 - \alpha_2)$ is the refractive index change between the reference medium and the test cell, the thickness of which is L_{cell} , and λ is the wavelength of the laser beam. For the specific case of gases, the refractive index, α_1 , in the test cell is linked to the density, ρ , according to the Gladstone-Dale equation:

$$\alpha_1 - 1 = K\rho \quad (3.2)$$

Where the Gladstone-Dale constant, K , is a function of the wavelength. Finally, n , can be linked to the pressure and temperature, following the gas law for a perfect gas, as in Equation (2.5), modified to be written in terms of density:

$$P = \rho RT \quad (3.3)$$

Where R is the specific gas constant. When pressure P is known and uniform in the test section, δ_0 provides an indirect measurement of temperature T .

After crossing the reference and test sections, the two light beams are recombined, resulting in the emergence of interference patterns of white and dark fringes (interferograms). In case the interference pattern which has emerged is due to a two-dimensional temperature field at uniform pressure, each fringe represents an iso-density, and consequently, an isothermal region. There is a variety of methods by which the temperature at each fringe can be evaluated⁶⁶, providing thereby a distribution of the temperature field. In measurements involving

interferometry, there are two principal set of instruments^{67–69}. The first one regroups the various optical instruments to generate an interference pattern. The second one is dedicated to the observation and processing of interferograms.

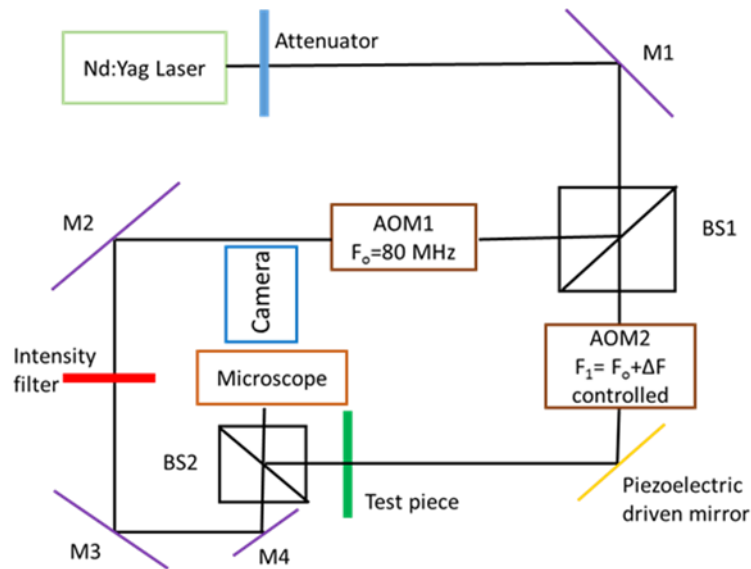


Figure 3.1 Typical interferometry setup for microfluidic applications, adapted from Garvey et al⁶⁹

Figure 3.1 shows a typical interferometric setup for microfluidic measurements. There are a wide variety of interferometric configurations available, and for the purpose of illustration, we present a Mach-Zehnder type. A Nd:YAG laser source provides the laser beam. Mirrors M1, M2, M3 and M4 reflect the laser beam in appropriate directions and the beam splitter, BS1, separates the initial beam into a reflected component and a transmitted component. The beam splitter, BS2, recombines these beams. A piezoelectric driven mirror can introduce phase-stepping in the transmitted beam. Acousto-optic modulators, AOM1 and AOM2, can introduce signal heterodyning, which is a process to create interferences between two signals from the same source shifted by a frequency difference, $\Delta\nu$. The control of the signal phase or frequency is used for applying the phase measurement interferometry (PMI) technique, which allows to measure from multiple intensity patterns the phase shift produced by the change in the optical path distance. The beam recombined by BS2 passes through a microscope lens to magnify the interference pattern, and it is captured with a camera. The interferometric setup shown in Figure 3.2 was developed by Garvey et al.⁶⁹ and has been used to compare phase stepping and

heterodyne retrieval techniques for extracting the phase change between the reference beam and the beam crossing the test section. It was demonstrated that the heterodyne phase retrieval technique allows six times higher resolution than the classic phase-stepping retrieval technique.

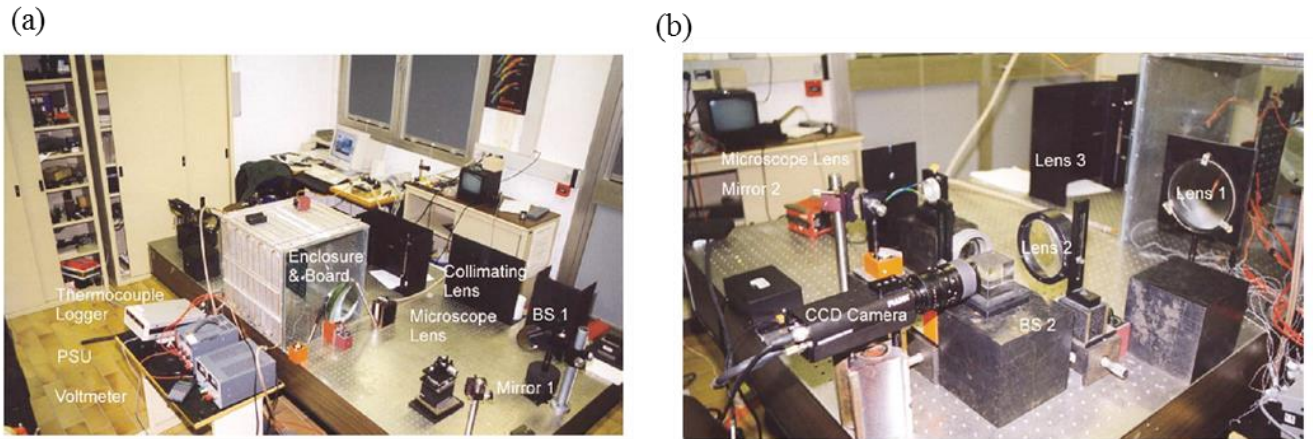


Figure 3.2 Interferometric setup utilised by Newport et al.⁷⁰ in the study of heat transfer in enclosures, (a) Front view of the interferometric setup. (b) Rear view of the interferometric setup

3.2.1.2 Applications to liquid microflows

In the work of Garvey et al⁶⁹, the set up shown in Figure 3.1 was implemented to analyse mixing of water with a 0.2 mol/L NaCl solution in a T-junction of $500 \times 500 \mu\text{m}^2$ square microchannels, and provided concentration profiles along the microchannel with a spatial resolution of $8.9 \mu\text{m}$. They found a rather good agreement with theoretical predictions. Although the study was dedicated to concentration field analysis, a short discussion about the possible use of this setup for measuring temperature fields in a liquid suggested that a resolution of 0.1 K could be reasonably achieved with a heterodyne technique.

Bon et al.⁷¹ developed an interferometry technique, abbreviated as TIQSI (temperature imaging using quadriwave lateral shearing interferometry). With this technique, they measured the three-dimensional temperature distribution around a heated gold microwire with 40 nm thickness, $1 \mu\text{m}$ width and $80 \mu\text{m}$ length, immersed in a thin water layer. The experimental arrangement is shown in Figure 3.3a and b. A water droplet was deposited on the top of the gold wire sample. The heating of the gold microwire induced a variation in the refractive index of the water. A numerical approach based on Green's function was developed to evaluate the 3D temperature distribution. The ambient temperature in this study was $23 \text{ }^\circ\text{C}$, and the heated wire had a temperature of about $60 \text{ }^\circ\text{C}$. The optical path difference (OPD) due to thermal

induced variation of the surroundings refractive index was measured with the wavefront analyzer, the image is shown in Figure 3.3c. The corresponding heat source density (HSD) images, and the temperature distribution at various heights from the microwire are shown in Figure 3.3d and Figure 3.3e, respectively.

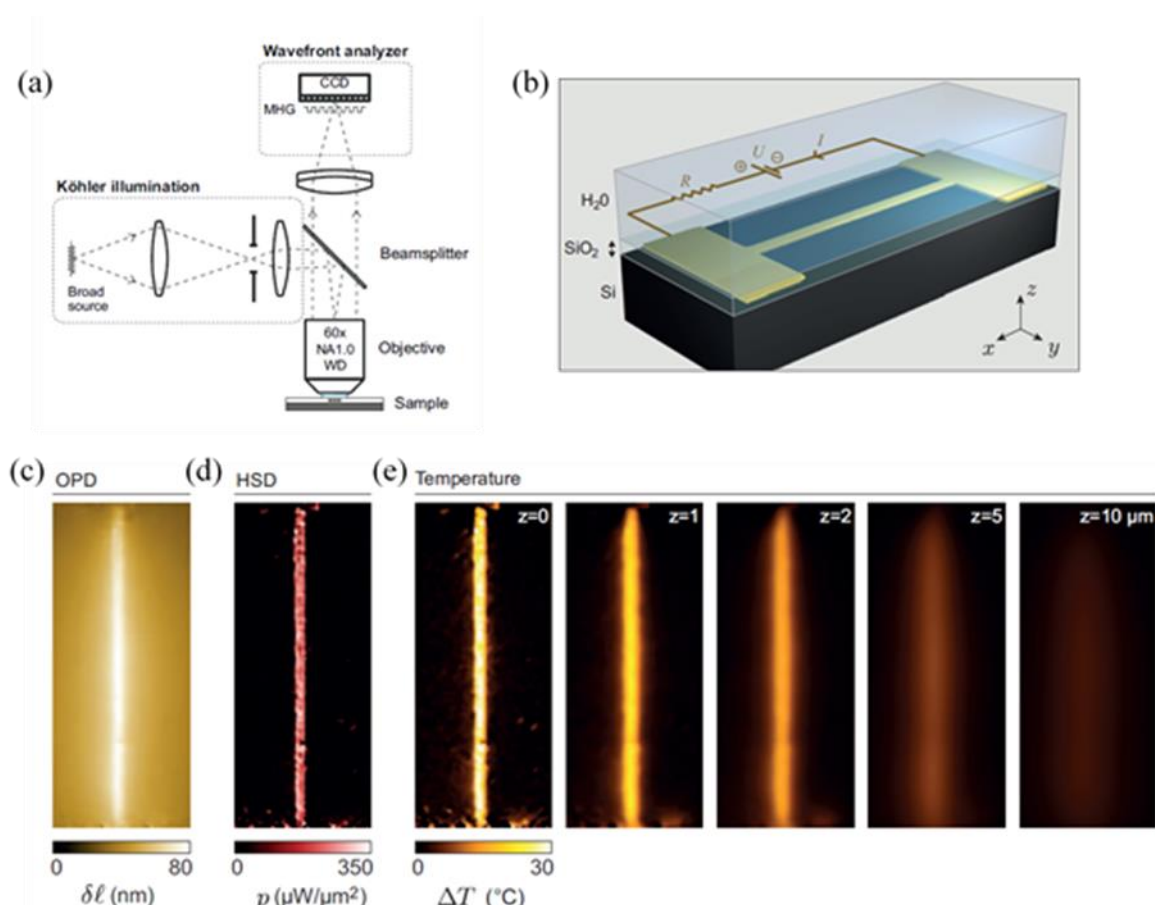


Figure 3.3 a) Schematic of the experimental setup. b) The gold microwire is embedded in a layer of SiO_2 and is connected to two gold electrodes. c) Optical path difference (OPD) image. d) Heat source density (HSD) obtained from the OPD. e) Microwire at $z = 0$, temperature distribution at various heights from $z = 0$ obtained from the HSD images (all images are from Bon et al⁷¹).

Newport et al.^{67–69} have carried out a series of studies to develop a micro-interferometry technique based on the conventional Mach-Zehnder interferometer. A T-shaped microchannel of $500 \mu\text{m}$ width and $500 \mu\text{m}$ depth was employed in one of their studies⁶⁹. Water was flowed through one junction and 0.2 mol/L NaCl was flowed through another junction. They could successfully map the concentration of NaCl in water as a function of the Reynolds number.

Even though their approach had the potential to map temperatures, issues of small phase angle and conduction by device material served as obstacles to measure temperature.

3.2.1.3 *Applicability to gas microflows and current limitations*

Interferometry has been applied to study various phenomena involving gases, such as combustion heat transfer, sometimes in transient conditions, but most of these studies were at macroscale. as it is possible to relate the pressure and density changes with the variation in the refractive index⁷².

Researchers have expressed concerns over the high cost involved in successful implementation of interferometry technique. This is usually due to the requirement of high quality optics. To tackle this aspect, researchers have employed a technique known as Digital Moiré Subtraction (DMS)⁷³. In this process, the optical aberrations are corrected. The process of moiré refers to the process of combining intensity distributions of two dissimilar grid patterns. A moiré fringe pattern represents the local differences between the spatial frequencies of the grids. This approach puts less demand on the high-quality optics and provides an improved field of view for measurements.

Newport et al.⁷⁰ studied the free convection heat transfer temperature fields in enclosures with DMS interferometry. Figure 3.2 shows their experimental setup to study the thermal interaction between 2D components representing ball grid arrays (BGAs) on a vertical printed circuit board (PCB). Their objective was to study electronics cooling in enclosures. Interferograms were taken around a 20 mm in diameter and 305 mm long aluminium isothermal cylinder, which was suspended in the centre of a 470 mm sided water cooled cubical aluminium enclosure. Figure 3.4 shows the DMS interferograms of the above isothermal cylinder at different Rayleigh numbers (Ra), defined as $Ra = \left(\frac{\rho^2 g \beta D^3 (T_{cyl} - T_e) c_p}{\mu k} \right)$, where ρ is the density, g is the gravitational acceleration, β is the volume coefficient of expansion, D is the cylinder diameter, T_{cyl} is the cylinder temperature, T_e is the enclosure temperature, c_p is the specific heat capacity, μ is the dynamic viscosity, and k is thermal conductivity. The uncertainty in their data was at most 0.7 °C.

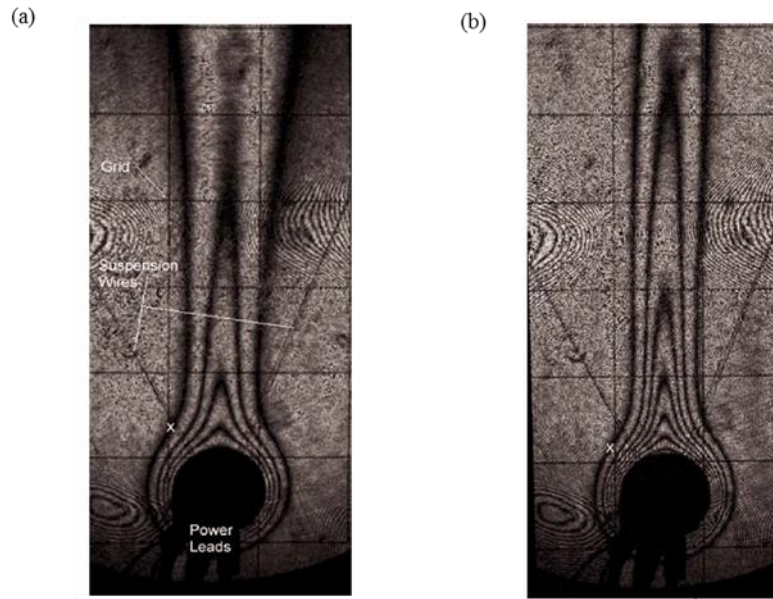


Figure 3.4 (a) DMS interferograms at $Ra = 6.8 \times 10^3$, (b) at $Ra = 1.04 \times 10^4$, from Newport et al⁷⁰.

Newport et al.⁶⁷ carried out a detailed study to assess the factors limiting the wide applicability of interferometry to gases at microscale. They based their study on noise and error analysis to assess the limitations of an interferometric approach to measure the temperature in different channels with varied dimensions employing gases and liquids as working fluids. Temporal noise, identified as one of the limiting factor at microscale, is defined as the variation in the system's phase with time⁶⁷. Temporal noise is an independent variation in the pixel values from one image to another, even under the conditions of constant illumination. This may be due to device noise, supply and substrate noise⁷⁴. Conduction by device materials significantly affects the temperature and velocity fields in the region external to the boundary layer. Therefore, conduction within the device must be considered in a design of the prototype or numerical models, to avoid unwanted phase accumulation⁷². Walsh and Davies⁷⁵ discusses this for minisystems. In order to quantify the temperature gradients in the transparent fluid, it is necessary to quantify the gradients in the channel material because the interferometer will detect the total phase change in the system. That is, the phase change in the solid plus the phase change due to the heat transfer in the fluid⁶⁹. Phase accumulation and additional path length in microfluid device materials must be accounted for if temperature data is to be obtained.

Other factors, such as small phase shift signal also serve as obstacles in fully exploiting interferometry⁶⁸. Additionally, for gas flows, issues linked to low density (compared to liquids) also come into picture. Roughly, there is a thousand-fold difference between the density of

gases and liquids and this difference in density increases with rarefaction, thereby complicating the task of temperature measurements. Newport et al.⁶⁷ reveal that for a microscale length of about 1 μm , temperature resolution of 1 K cannot be achieved in gas microflows designed by them. Table 3-2 summarizes the main characteristics of interferometry.

Table 3-2. Thermometry by interferometry

Method	Principle	Resolution	Advantages	Disadvantages	Gas microflows
Optical interferometry	Variation of refractive index with density that can be linked to temperature through the state equation of the gas	Spatial ⁷⁶ $\sim 1 \mu\text{m}$ Temperature ⁷⁶ $\sim 10^{-1}$ K	Possible to integrate with remote detection systems ⁴⁵	At micro-scale, issues linked to temporal noise, small phase angle, conduction by device materials	Theoretically possible

3.2.2 Infrared based methods

3.2.2.1 Principle

A body, whose temperature is above absolute zero, emits thermal radiation. The total emissive power is a function of temperature and varies roughly as the fourth power of temperature. Planck's law, under the assumption of black body, is used to determine the temperature of the body by measuring either its spectral or total emissive powers. However, some bodies may have a radiative behaviour far from the blackbody one. Therefore, the analysis should consider the role of factors such as spectral emissivity of the considered body. Also, great care must be taken to include additional issues in analysis, such as reflection of thermal radiation from nearby sources, to ensure reliable estimate of temperature. As a rule of thumb, it can be argued that, low reflectivity materials due to their high emissivity are better suited for infrared (IR) imaging.

3.2.2.2 Applications to liquid microflows

Infrared techniques have been widely used in evaporation studies. For instance, Buffone and Sefiane⁷⁷ used this technique to measure the temperature distribution along the meniscus of volatile liquids in capillaries. The diameters of their channels were ranging from 600 to 1630

μm . Hetsroni et al.⁷⁸ applied the IR technique to measure the external surface temperature of small capillaries of inner and outer diameters of 1007 and 1500 μm , respectively. Their working fluid was water at a temperature of about 60 °C, and they explored a Reynolds number ranging from 10 to 400. Patil and Narayanan⁷⁹ employed the IR technique to measure the wall and near-wall temperatures of water flowing through a silicon microchannel. They worked at a temperature of about 45 °C. They were able to determine the local temperatures with an uncertainty of 0.60 °C and 1.33 °C for a Reynolds number of 297 and 251, respectively. Their IR camera had a spatial resolution of 10 μm .

Haber et al.⁸⁰ studied the temperature profiles by IR imaging in a stainless steel rectangular microchannel. The lowest hydraulic diameter of the cross section was 150 μm . The microchannel was designed as a microreactor to study fast and exothermic reaction of tetraethoxysilane hydrolysis. Thanks to a calibration, Haber et al. were able to estimate the temperature profiles in the microreactor during the hydrolysis of tetraethoxysilane at different flow velocities and time intervals, as shown in Figure 3.5. The reported accuracy of their temperature measurements was about 1 °C, with a spatial resolution of 200 μm . They consider the temperature variation only in the axial direction, and try to measure temperature at the centre of the channel. They averaged the temperature values for two pixels (400 microns) along the direction of the diameter and used it as the temperature value at every axial location. They ignored the pixels and the temperature variation near the walls as they report that they did not have confidence on the accuracy of pixel information near the walls

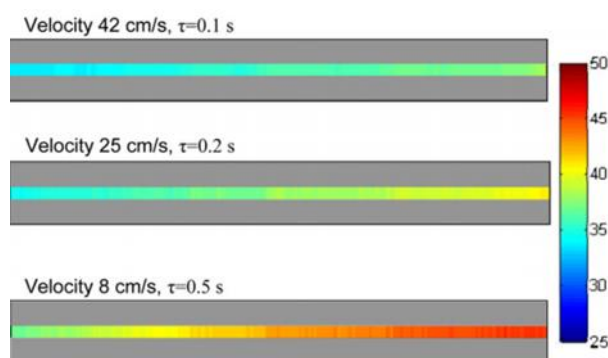


Figure 3.5 Temperature profiles in a capillary reactor during the hydrolysis of tetraethoxysilane at different flow velocities and times⁸⁰.

3.2.2.3 *Applicability to gas microflows and current limitations*

IR imaging technique has been employed in gases for leak detections and to measure temperature. For example, Safitri⁸¹ has detected the leak and studied temperature by directly measuring the IR signal of methane gas, which is the major constituent in liquefied natural gas (LNG). The aim of this study was to determine the concentration and temperature of LNG vapour plumes generated by spills of LNG on concrete and water (in an open environment). Initial experiments were carried out to study the emissivity of methane in the range of 110-350 K. Subsequently, temperature of methane gas was measured in this range in an LNG pit of length 3 m, width 3 m and depth 1.2 m. Their IR camera had a spatial resolution of 5 μm . The uncertainty in the measurements has not been explicitly reported.

Researchers at Bell Labs, Ireland, have developed thin Indium Tin Oxide (ITO) coated sapphire sensors with the objective of non-intrusive surface temperature measurements involving gas microflows. They were able to quantify the apparent emissivity of ITO layer in the temperature range of 5 to 75 $^{\circ}\text{C}$ above the ambient (private communication). This sensor can be employed at the wall of microchannels involving gas microflows, and then provide the wall temperature, but not directly that of the gas.

The main issue in IR studies is the signal dependency on the surface or fluid emissivity, which itself is a function of temperature and is not always known with a great accuracy. In general, only certain gases can emit energy in the infrared spectrum, but this emission is restricted to a very narrow range of spectrum, especially at room temperature⁸². Moreover, temperature differences in a gas induce a change in the local density, thereby, changing the apparent emissivity of gases. This augments the problem of connecting the infrared signal to the emissivity. IR signal is also affected by other factors, such as ambient temperature, humidity, atmospheric content, optical path length, and reflectance. There is a lack of comprehensive mathematical model to take all these factors into account.

In experiments, usually the IR camera is placed at a distance from the source whose temperature is of interest. Certain gases, such as CO_2 and H_2O vapours, are reported to absorb IR wavelengths. The presence of these gases in the measurement path will alter the IR signal, resulting in an error in the estimation of temperature. Also, the concentration of H_2O vapour in the atmosphere between the observed sample and the camera, i.e. the ambient hygrometry, will modify the signal. However, other gases, such as N_2 , O_2 , and Ar are reported to have no

absorption in the IR range, therefore the presence of these gases along the IR signal path would make the temperature measurements more reliable^{83,84}.

Table 3-3 summarizes the features of the IR technique for measuring temperature. To summarize, in principle, the IR technique can be employed to measure temperature of gases. However, some of the parameters (especially, emissivity), based on which we can estimate the temperature, are functions of temperature and it is not straightforward to take this aspect into account. These factors have considerably restricted the usage of IR techniques to measure temperature in gases, particularly in gas microflows.

Table 3-3. Summary of IR based technique

Method	Principle	Resolution	Advantages	Disadvantages	Gas microflows
Infrared thermography	Measurement of emissive power linked with temperature	Spatial ⁴⁵ ~ 10 μ m Temperature ⁴⁵ ~ 10 ⁻¹ K	Commercially available cameras. Successfully tested for liquid flows. Provides temperature fields	Difficult to generate calibration curves as emissivity is a function of temperature	Possibility to measure IR spectrum for gases is limited

3.2.3 Liquid crystal thermography

3.2.3.1 Principle

From the last few decades, thermochromic liquid crystals (TLC) have found a place in temperature measurement. Recently, researchers have tried to employ TLC for microscale thermometry. TLC are basically highly anisotropic (for optical properties) liquids, which are a complex arrangement of cholesteric mesophase (CN) and chiral-nematic mesophase (CL) liquid crystals. Liquid crystal phase is called as mesophase. The terms CN and CL (are sometimes used interchangeably). The difference is that CN are derived from non-sterol chemicals such as phenyl-benzoate esters, while CL are derived from cholesterol esters. CN and CL are characterised by formation of helical structures, referred to as helics. This is due to the distinctive shape of the nematic molecules containing chiral centres. Nematic molecules possess high oriental order (direction of molecules is oriented towards one direction) and low positional order⁸⁵. The detailed chemical structures of TLC is beyond the scope of this thesis, and the interested reader to refer to other works dedicated to this subject^{86,87}.

These crystals exist somewhere between the crystalline solid phase boundary (for optical behaviour) and the isotropic (conventional) liquid phase (for mechanical behaviour)⁸⁸. TLC molecules are highly sensitive to temperature. In other words, the molecular structure of TLC, in terms of twist and position, varies with temperature, resulting in a temperature-dependent reflectivity. On illuminating the TLC by a white light, depending on temperature, they reflect visible light at different wavelengths, i.e. with different colours. Therefore, a relation can be established between the colour reflected by the crystals and their temperature.

Depending upon the temperature and the viewing angle between the observer and the incident light, TLC exhibit apparent colour (or hue). TLC require calibration to relate hue values to temperature. During calibration, certain important factors such as the background surface reflectivity, colour, transparency, liquid crystal film thickness, measurement and image processing techniques, must be taken into consideration. A detailed information on these factors has been presented in various studies^{86,88,89}. Different combinations of commercial TLC mixtures provide a working range from -30 to 120 °C, with 0.5 to 20 K band widths⁸⁶. Band width is the temperature range in which a TLC can actively reflect visible light, also referred to as colour play interval.

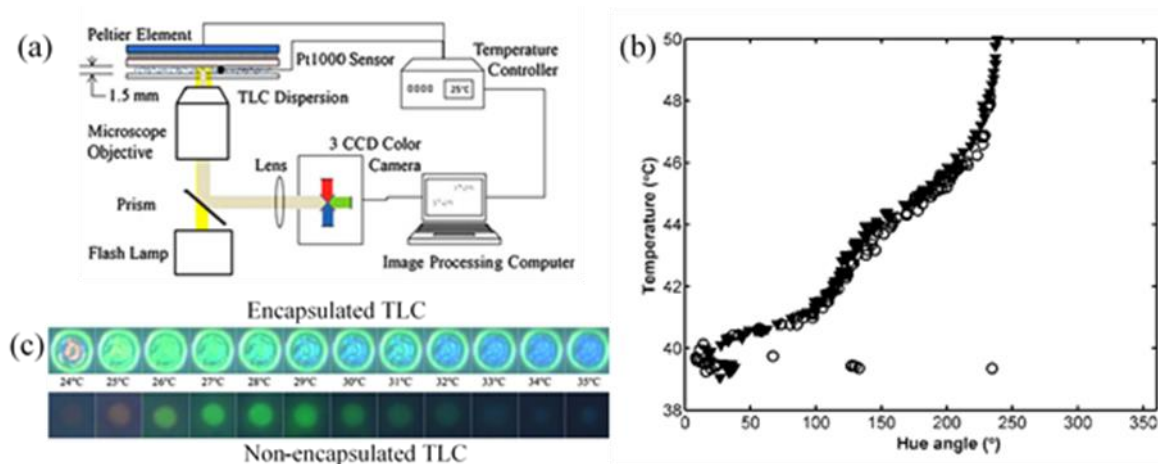


Figure 3.6 a) Schematic of experimental setup adopted for TLC temperature measurement⁹⁰, b) Typical calibration curve of TLC, adapted from Muwanga et al.⁹¹, and c) raw colour images of encapsulated TLC particles (top) and non-encapsulated TLC particles (bottom) at various temperatures, adapted from Segura et al.⁹⁰.

Figure 3.6a shows a typical experimental setup adopted for TLC measurements in microchannels, consisting of the microfluidic device, a flash lamp for light, optical elements for focusing and recording the images, temperature controllers, and an image processing unit.

Figure 3.6b shows a calibration curve obtained with TLC. The hue angle in this figure is defined as $Hue\ angle = \arctan\left(\frac{\sqrt{3}(G-B)}{2R-G-B}\right)$, where RGB (red, green, and blue) are the colours (intensity) captured by the camera.

Broadly, TLC can be classified into two types: encapsulated and non-encapsulated. In the encapsulated version of TLC, an external polymer coating is present around the TLC droplets. Therefore, they can form particles or protective microcapsules whose size can vary from the order of micrometre to millimetre and is usually in the range of 5 to 10 μm . The polymer shell causes aberrations and distortions that introduce an error in the detected colour, which increases the uncertainty on the temperature measurement. In non-encapsulated TLC, there is no such external polymer coating. Some research studies have shown that, due to the absence of an external coating, they exhibit better colour response with higher signal to noise ratio (excellent colours)⁹². However, because of the absence of an external coating, non-encapsulated TLC can be contaminated by dust and solvent, which alter their light response and reduce their lifetime. Moreover, the exposure to UV-light deteriorates in time the luminescence properties of the particles, which may result in a colour difference between the calibration step and the actual temperature measurement.

Figure 3.6c shows the colour response of encapsulated and non-encapsulated TLC, adapted from Segura et al.⁹⁰.

Park et al.⁹³ analysed the uncertainty on the temperature measurement inferred from a single particle. The authors pointed out that the main uncertainty is due to the low repeatability in manufacturing TLC particles. Even for the same temperature and illumination conditions, the reflected light varies from particle to particle. Moreover, in the case of encapsulated TLC, the polymer shell causes a refraction of the reflected light that depends on the thickness of the coating. Park et al.⁹³ estimated an uncertainty of 5-20%, depending on the range of working temperature, when the temperature measurement is based on a single particle. For this reason, the authors proposed a procedure of particle averaging for increasing the accuracy of the measurement. Because the smallest diameter of TLC particles reported in the literature is about 1 μm ⁹⁴, the number of particles in microscale flows is quite limited, and the temperature

measurement cannot be carried out but on single particles. While the spatial resolution of the technique requires particles that are as small as possible, the TLC droplet needs to be large enough to exhibit colour play, which represents a continuous changing of colour of the crystals with temperature. The average size of the TLC is around 5 to 10 microns to exhibit difference in colour with temperature.

3.2.3.2 Applications to liquid microflows

Researchers have adopted TLC to study polymerase chain reactions (PCR) at microscale^{92,95}. For instance, Chaudhari et al.⁹² adopted encapsulated TLC to measure temperature in microfabricated PCR vessel arrays. Temporal and spatial temperature variations in the range of 55 to 95 °C, and with a resolution of 0.1 K, were measured in their study. Hoang et al.⁹⁶ demonstrated dynamic temperature measurement, i.e. reported temperature versus time in microfluidic devices for PCR using microencapsulated TLC. This was achieved by analysing reflected spectra of TLC as a function of time. However, it should be noted that the biological activity in the microsystem may be influenced by the presence of TLC, as it must be suspended in the fluid for measuring temperature.

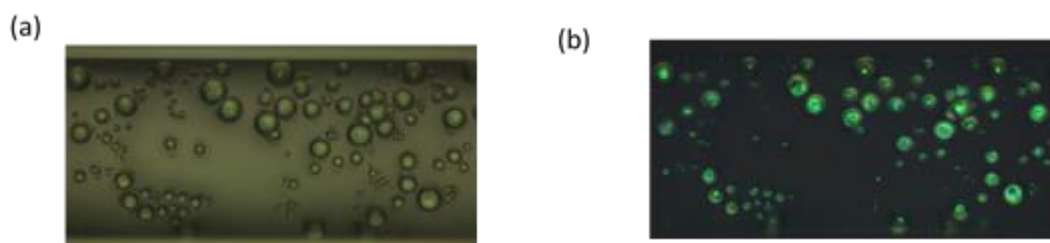


Figure 3.7 TLC particles in a microchannel with water as the working fluid, a) at standard illumination, b) with circular polarization filtering, adapted from Basson and Pottebaum⁹⁷

Basson and Pottebaum⁹⁷ studied the temperature of water at rest using encapsulated TLC by imposing a linear temperature gradient along a microchannel with a $100 \times 100 \mu\text{m}^2$ cross-section. The slurry of particles was properly filtered in order to retain only TLC droplets with diameter between 1 and 10 μm . To improve the signal to noise ratio in their study, Basson and Pottebaum⁹⁷ adopted circular polarization filtering (CPF), as shown in Figure 3.7a and b. For an electromagnetic wave, circular polarization refers to the condition in which the magnitude of the electromagnetic field vector remains constant, but its direction rotates at a constant rate in a plane perpendicular to the propagation of the wave. This rotation can be right-

hand (RCP) or left-hand sensed (LCP) with respect to the direction of propagation. CPF exploits the circular dichroism of TLC, i.e. differential absorption of right and left circularly (RCP, LCP) polarised light. This helps to distinguish reflections from TLC particles and reflections from other surfaces. In their study, illumination is with LCP light. The light reflected by TLC particles remain LCP, and light reflected by the wall surfaces changes to RCP light. Thus CPF was used to discern between wall surface and TLC reflections. The working temperature range was 36.3 to 43.7 °C, and the authors reported an uncertainty between 0.4 and 2.4 °C.

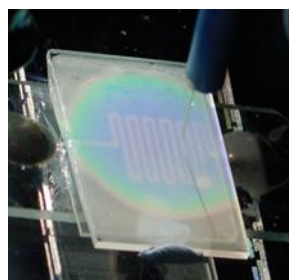


Figure 3.8. Microheater for studying Reimer-Tiemann reaction, using TLC in the study of Iles et al.⁹⁸

Iles et al.⁹⁸ used encapsulated TLC for thermal optimization of the Reimer-Tiemann reaction⁹⁹, for the preparation of phenolic aldehydes by the action of chloroform on phenols, and is highly exothermic reaction. Therefore, it is essential to design and control the heat removal system to prevent overheating in alkaline medium (system). In this study, this reaction was studied in a serpentine structure as shown in Figure 3.8. The resistive heating elements were fabricated with a thin film of Nickel–gold on a glass substrate by evaporative deposition. TLC bead layer sandwiched between two glass slides was placed onto a microheater. TLCs changed colour according to local temperature distribution. The temperature in this study was ranging from 60 to 65 °C, and they could resolve the temperature to about 0.4 K. Segura et al.⁹⁰ employed non-encapsulated TLC produced with Shirasu porous glass membrane emulsification approach, which resulted in a narrow size particle distribution¹⁰⁰. The colour response of individual non-encapsulated TLC was carried out in this study with a field of view of $400 \times 300 \mu\text{m}^2$. Their calibration involved all RGB and HIS (hue, intensity, and saturation) colour components. Therefore, low uncertainty levels (0.65 K) were achieved in the temperature measurement range from 24 to 37 °C.

To address the issue of shear stress in non-encapsulated TLC, experiments in controlled temperature and flow conditions were carried out by Puccetti et al.¹⁰¹. The objective of these experiments was to study influence of mechanical stress on the colour response (optical properties) and the reliability of measurements of non-capsulated TLC. To study this, they performed experiments in liquid flows. Three different types of TLC materials with a temperature ranging from 20 to 30 °C were studied. Experiments were carried out in a microchannel of 500 µm in width, 200 µm in height, and 25 mm in length. The study revealed no observable colour change up to shear stress value of 0.4 Pa. Non-encapsulated TLC subjected to strong shear stress will deform and consequently can change their optical properties and reliability. This flow-induced mechanical stress might alter the colour response of the crystals, which are, in this configuration, in direct contact with the fluid. In their study, on increasing the shear stress values to 4 Pa, some particles were destroyed. Nevertheless, the authors showed that the colour response remained reliable.

3.2.3.3 Applicability to gas microflows and current limitations

TLC must be seeded in the fluid to map the temperature profile within the flow. Therefore, the difference in density between gas and TLC is a strong limitation for its applicability in a gaseous environment, as the seeding cannot be neutrally buoyant as in a liquid phase.

As a consequence, regarding gas flows, TLC have only been employed by researchers to study the wall surface temperature. In addition, some studies have demonstrated the possibility of making simultaneous velocity and temperature measurements by adopting TLC^{102,103}. Few research studies have also shown surface shear stress measurements with liquid crystals^{104,105}. For these studies, it is necessary to coat the surface whose temperature should be measured. At macroscale, researchers have adopted non-encapsulated TLC to measure temperature on gas turbine blades^{106,107}. At microscale, Muwanga and Hassan⁹¹ adopted distilled water as the fluid in their study. Even though they employed water as the working fluid, their approach has potential even in temperature measurement of gas microflows. The authors coated the walls of microchannels with non-encapsulated TLC to measure local heat transfer coefficients and obtained wall surface temperature at a spatial resolution of 183 µm with an uncertainty of 0.1 °C. However, it should be noted that coating is not a trivial task. Researchers have reported practical problems, such as i) the difficulty to obtain a continuous coating on the surface of interest as well as a contaminant free area, ii) erosion of coating with time, iii) formation of air

pockets etc⁹¹. Moreover, non-encapsulated material does not solidify, and tends to be in an oily state⁹¹.

Also, due to the presence of TLC, the initial surface conditions and physical properties of the wall will change. In addition, the temperature information provided by the TLC with this approach will be neither the wall nor the near wall gas temperature. Therefore, extraction of the gas temperature near the wall from this TLC data would require further theoretical analysis. Table 3-4 summarizes the technique of liquid crystal thermography. The size of the TLC particles generally limits the spatial resolution.⁹⁷ TLC were also applied in visualization of internal electrical behavior at microscale in very large scale integrated systems (VLSI) circuits. The heating in these systems can result in localised hot spots, which may result in the alteration of electrical signals and lead to subsequent failure of the VLSI systems. Temporal resolution of the order of $10^2 \mu\text{s}$ has been reported¹⁰⁸ in these studies. Temperature resolution of $\sim 0.1 \text{ K}$ have been reported with TLC^{97,98}.

Table 3-4. Summary of thermochromic liquid crystals technique

Method	Principle	Resolution	Advantages	Disadvantages	Gas microflows
Liquid crystal thermography	Phase transition (molecular twist and position) with temperature	Spatial ⁸⁶ ~10 μm Temperature ⁸⁶ ~ 10^{-1} K	<ul style="list-style-type: none"> • Wide variety of commercially available TLC • Successfully tested for liquid flows 	<ul style="list-style-type: none"> • Difficult to work with • Hysteresis, • Difficult to calibrate 	<ul style="list-style-type: none"> • Not feasible with encapsulated TLC • Possible information at the walls only

3.2.4 Raman Thermometry

3.2.4.1 Principle of Raman and Rayleigh scattering

The basis of the Raman technique is the exploitation of inelastic scattering of light. In this technique, the sample is exposed to an intense monochromatic light (laser). The energy provided by the laser is partially absorbed by the sample which can “jump” to a non-stable virtual higher energetic state. After a short delay, the energy is re-emitted in the form of radiation with a frequency shift in respect to the frequency provided by the laser. This frequency

shift can be associated to the different vibrational and rotational modes of the concerned molecule.

Therefore, the inelasticity of the light scatter depends on the faculty of the molecule after remitting radiation to: i) permanently absorb part of the laser energy in order to increase its vibrational energy in respect to its initial equilibrium state (Stokes scattering) or ii) permanently give away part of its vibrational energy in order to decrease its vibrational energy in respect to its initial equilibrium state (Anti-Stokes scattering), as shown in Figure 3.9.

In particular, the vibrational normal modes of a molecule can attribute a specific frequency shift to the remitted light signal. Therefore, by measuring this signal, one can obtain particularly sensitive information on the vibrational and rotational modes of the sample. More specifically, the inelastic Raman scattering is a consequence of the change of polarizability of the molecule due to the vibrational and rotational motion of the atoms¹⁰⁹. This motion changes the shape and dimension of the electron cloud of the molecule. If the electron cloud oscillates periodically between two antisymmetric configurations, the polarizability of the molecule changes as a function of the atomic relative displacement. The intensity and the spectrum of the scattered light informs on the vibrational and rotational characteristics of the molecule. In order to acquire the light signal, a high-resolution Raman Spectrometer is needed. This technique can be employed only for molecules which exhibit non-zero polarizability¹⁰⁹.

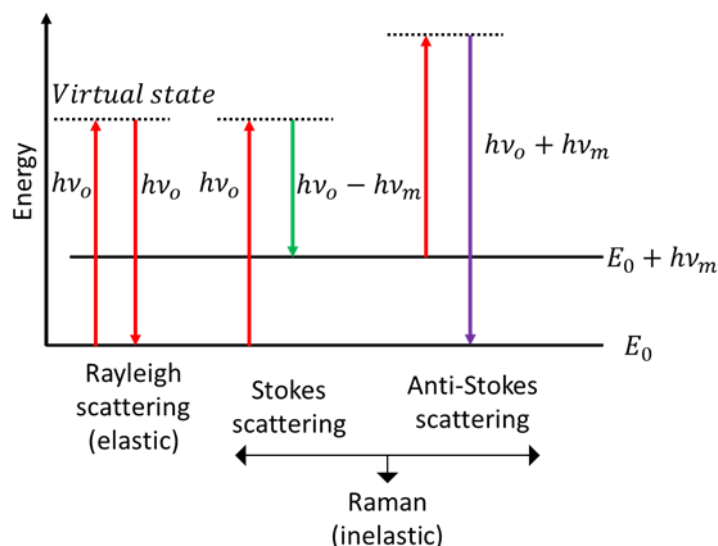


Figure 3.9 Illustration of Rayleigh and Raman (Stokes and anti-Stokes) scattering¹¹⁰.

Differently from Raman scattering, in the Rayleigh or elastic scattering phenomenon, the sample, after reaching a “virtual state”, reemits radiation at the same frequency as the monochromatic laser used for excitation, and thus it returns to its original energy level. The photon is reemitted almost instantaneously from the ‘virtual state’ and it is the most probable kind of scattering. That is why a Rayleigh signal is more intense than a Raman signal (Figure 3.10). On the contrary, the Raman inelastic scattering is a rare occurrence (about 1 in 10^6) and the Stokes and anti-Stokes scattering depend on the initial state of excited molecule. During a Stokes shift, the molecule is initially in the ground state, making this type of Raman scattering the most probable one, and it can thus provide the strongest signal. This is due to the fact that at low temperatures the population of molecules is higher at the ground energy level. Nevertheless, even if the obtained signal intensities are substantially different, Stokes and anti-Stokes lines provide the same kind of information in regards to the vibrational and rotational modes of the molecule.

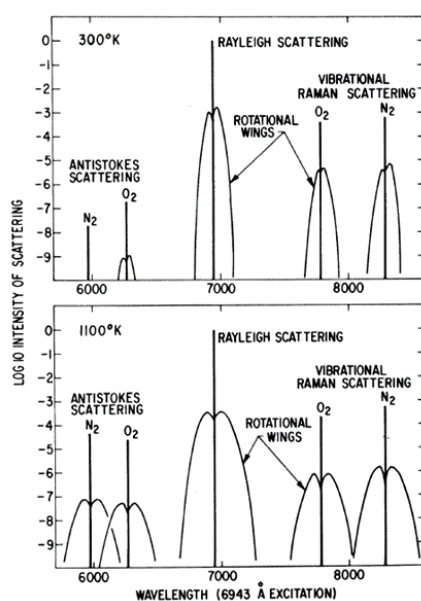


Figure 3.10 Raman and Rayleigh scattering for air, drawn roughly to scale, at room temperature and 1100 K¹¹¹

This inelastic scattered light of arbitrary wavelength is spectrally resolved. Depending on the type of probed molecules and temperature, a unique ‘signature’ of the scattered light can be detected. Thus, by observing the relative amplitudes of the peaks of Stokes and anti-Stokes lines, the temperature can also be deduced. A temperature shift has an influence on the Raman

spectra, i.e. it affects the frequency, lifetime, and population of the phonon modes¹¹². Therefore, the shifts of peak positions, and the broadening of the linewidth are the other means by which temperature can be measured. This can be readily seen from Figure 3.10 where air is investigated at different temperatures. It is possible i) to see how the signal differs as a function of the molecular signature; for example dioxide and dinitrogen reemit at different wavelengths (contrarily to the Rayleigh signal that is reemitted at the same wavelength of the laser); ii) to differentiate the information received in respect to the rotational and vibrational modes of the molecule; iii) to associate the signal response to gas temperature variations (which affect the vibrational and rotational modes). As it is the case for many other thermometry techniques, Raman thermometry also requires prior calibration of the signals in respect to the temperature measurements.

Nowadays, Raman applications for microfluidics have started to become more common since the equipment is more accessible in terms of reduction in the cost. However, to the best of our knowledge, until now this technique has been applied only to liquid flows.

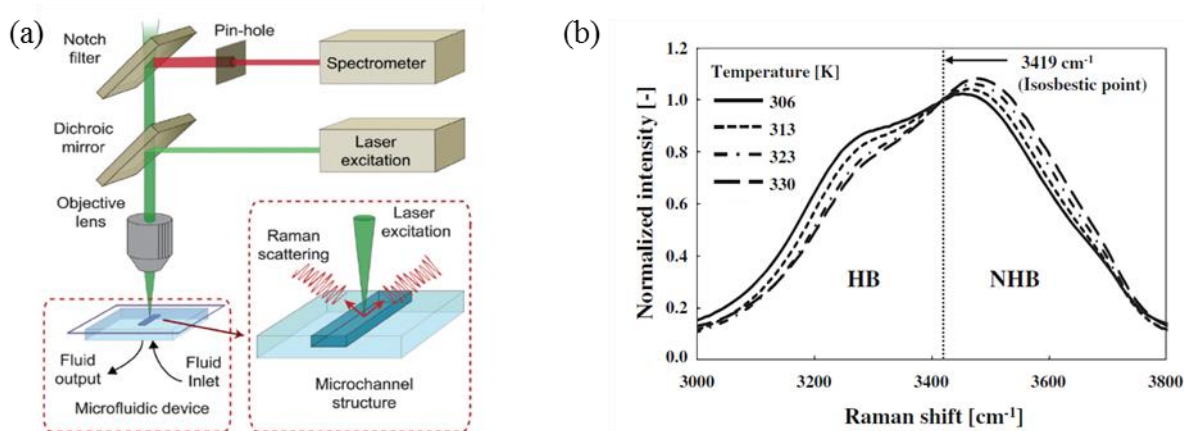


Figure 3.11 a) Schematic of a typical Raman spectroscopy system with a microfluidic device¹¹³, b) water Raman spectra of OH stretching mode at different temperatures (HB hydrogen-bonded OH stretching mode, NHB non-hydrogen-bonded OH stretching mode)¹¹⁴.

In Raman microfluidics, a laser beam is focused into the microsystem through the use of a microscope. The microscope also collects the light, which is scattered from the probe, and passes it through a dichroic filter to the spectrometer (see Figure 3.12a). Before entering the spectrometer, the strong elastically scattered Rayleigh wavelength is removed by the filter,

while the in-elastic Raman components are transmitted¹¹¹. Raman microscopy can offer submicron spatial resolution with very high sensitivity and selectivity. As an example, Figure 3.11b shows the typical water Raman spectra in a microfluidic system as a function of different water temperatures. OH represents a hydroxy or hydroxyl group, and it contains oxygen bonded to hydrogen. The anion, OH⁻ is referred to as hydroxide. OH stretching band of liquid water is composed of hydrogen bonded (HB) and non-hydrogen bonded (NHB) OH stretching modes. In particular, it is possible to see the great sensitivity of the OH, hydroxy or hydroxyl group, stretching vibrations of H₂O with respect to temperature. Molecules of water that are hydrogen-bonded (HB) have a different wavelength shift than non-hydrogen-bonded (NHB) water molecules^{114,115}.

The isosbestic point corresponds to the wavenumber at which the Raman intensity does not vary with temperature. The Raman intensity of the NHB mode (where frequency is higher than that of the isosbestic point) increases with a rise in temperature, whereas the opposite effect occurs with HB mode. Heating breaks the hydrogen bonds, and thus this alters the ratio between bonded and non-bonded water molecules, resulting in a dependency with temperature¹¹⁴, i.e. the higher the temperature, the higher the NHB population and therefore the Raman signal intensity at a certain frequency.

Shifting away from fluidic samples, Raman thermometry has also been applied in steady and transient surface temperature measurements on semiconductor micro devices^{116,117}, micro membranes^{118,119}, micro thermal actuators¹²⁰, and on simultaneous temperature and stress measurements¹²¹. To improve the sensitivity and spectral resolution of Raman spectroscopy, there are certain variations of conventional Raman spectroscopy. These techniques are referred to as surface-enhanced Raman spectroscopy, resonance Raman spectroscopy, surface-enhanced resonance Raman spectroscopy, coherent anti-Stokes Raman spectroscopy, stimulated Raman scattering, or tip-enhanced Raman spectroscopy. Details on each technique are presented in the review of Chrimes et al.¹¹³.

3.2.4.2 Applications to liquid microflows

Kim et al.¹²² adopted a micro-Raman spectroscopy system to study temperature distribution within a liquid in a microchannel (width 600 μm, length 13 mm, volume 1 μL) in their research on PCR with a microfluidic approach. Calibration of Raman measurements was done by TLC and thermocouples. Depending on the location in the microchannel, the temperature, controlled at 55 °C, varied from 53.6 to 54.8 °C. However, the spatial resolution

within the microchannel volume was not specified. Ewinger et al.¹²³ measured the temperature of water in microchannels of 400 μm width, 200 μm depth, and 32 mm length. The temperature was ranging from 30 to 58 $^{\circ}\text{C}$. The uncertainty in the temperature measurement was ± 1.2 K with a spatial resolution of 15 μm and 25 μm , in the plane and the depth, respectively.

Kuriyama and Sato^{114,124} studied the two-dimensional temperature distribution of water for a temperature ranging from 20 to 60 $^{\circ}\text{C}$ by a one-wavelength imaging system. Raman scattering of OH stretching vibrations of water was employed in this study due to its high sensitivity with temperature variations, as shown in Figure 3.11b. The steady-state temperature distribution inside a T-shaped microchannel made up of Polydimethylsiloxane (PDMS) and borosilicate glass, with hot and cold water flowing from either side, was investigated in a measurement area of $819 \times 819 \mu\text{m}^2$, with a spatial resolution of $12.8 \times 12.8 \mu\text{m}^2$. The uncertainty of temperature measurement was high: 3.7 K with a 95 % confidence level. In their later study, Kuriyama and Sato¹²⁵ developed a two-wavelength technique to measure transient temperature fields in water. This technique reduced the uncertainty to 1.43 K, with a 95 % confidence level, and the temperature sensitivity was 0.28 K. Experiments were carried out on a Y-shaped millichannel in the temperature range of 20 to 70 $^{\circ}\text{C}$. The height of the channel was 2 mm and the width was 8 mm. They captured the temperature distribution at the junction of the Y-channel until 650 seconds after the initialisation of the heating. .

3.2.4.3 Applicability to gas microflows and current limitations

In general, Raman spectroscopy can be applied for direct gas temperature measurement. For instance, Lutch et al.¹²⁶ measured the temperature of air from frequency-spread dephasing of the Raman coherence using femtosecond coherent anti-Stokes Raman scattering technique (CARS). Three different temperatures of 300, 600 and 940 K were measured. Also, N_2/Ar mixtures, with varying concentration of nitrogen, were studied. Temperature was assessed by studying the CARS signal as a function of probe-delay time.

To the best of our knowledge, Raman technique has not been directly applied for the measurement of temperature in gas microflows. Low sensitivity of gases to Raman spectroscopy, fewer number of molecules in a given volume (compared to liquids), low scattering cross-section are some of the issues pertaining to this technique for gas flows¹¹⁰. In gas microflows, and especially in rarefied scenarios, these issues tend to escalate. Generally, high powered lasers and special long path length sample cells are necessary for measurement in gases¹¹⁰.

Chrimes et al. showed that it is possible to achieve a lateral and depth resolutions of approximately 0.25 and 1.7 μm by a 633 nm laser source with a pinhole of 50 μm in radius. A 60 \times / 1.2 numerical aperture objective was used¹¹³. They used a pin-hole with a controllable diameter. This can reduce the beam diameter and also allows only the strong signal from the centre of the beam to pass through the region of investigation. Given the significant advantages of Raman thermometry in terms of non-intrusiveness, capability in hazardous environments, sub-micron spatial resolution, high optical sensitivity, and good development in other applications, this technique has the potentiality of being applicable for studying gas microflows if further research is carried out to overcome some of the above discussed aspects. Therefore, it will be of great interest to note the developments of this technique and its applicability to gas microflows in the future. Table 3-5 summarizes the features of Raman technique for temperature measurement.

Table 3-5 Summary of Raman thermometry features

Method	Principle	Resolution	Advantages	Disadvantages	Gas microflows
Raman thermometry	Inelastic scattering of incident monochromatic light	Spatial ¹¹⁰ ~ 1 μm Temperature ¹¹⁰ ~ 1 K	<ul style="list-style-type: none"> • Successfully tested for liquid flows • Possible to probe very small sample volumes • Cost is also reducing 	<ul style="list-style-type: none"> • Raman effect is very weak, low scattering sensitivity, making it difficult to measure at low concentrations • Serious issues can arise when large background signals or from fluorescence of impurities in the sample itself can arise¹¹¹ 	Theoretically possible, but issues of low sensitivity, low scattering cross-section for gases, and is about 5 times lower than that of liquids ¹²⁷ .

3.2.5 Photoluminescence

3.2.5.1 Principle

Eilhardt Wiedemann in 1888 was the first to introduce the word luminescence (as *luminescenz*), and he described it as “all those phenomena of light which are not solely conditioned by the rise in temperature”, as opposed to incandescence. Out of the myriad varieties of luminescence, such as radioluminescence, cathodoluminescence, electroluminescence, etc., we are interested in what is referred to as photoluminescence, which includes the phenomenon of fluorescence, phosphorescence and delayed fluorescence¹²⁸, as shown in Figure 3.12.

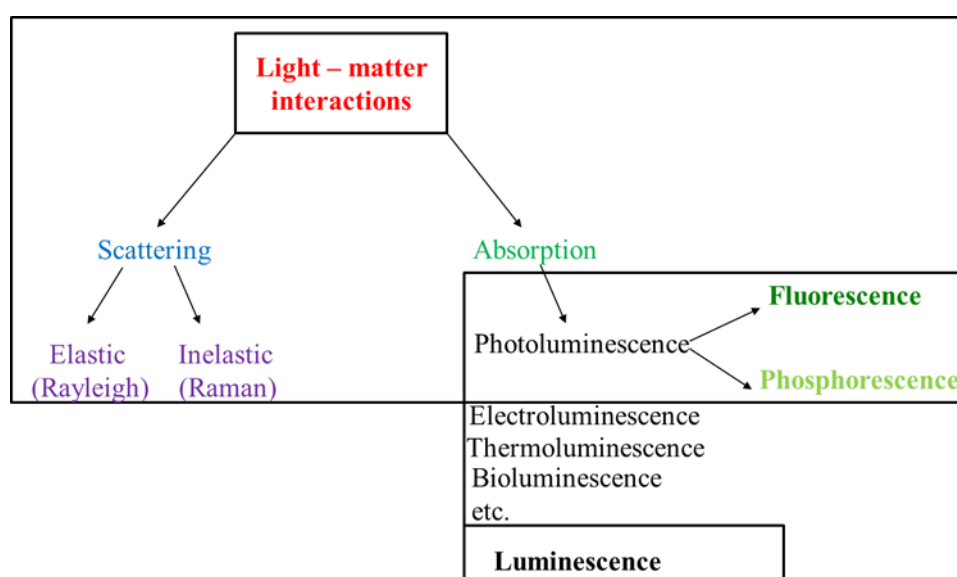


Figure 3.12 Diagram showing the position of photoluminescence in the broad area of light-matter interactions¹²⁸.

Photoluminescence has been widely exploited to measure temperature in fluids. Certain molecules, once excited with a light, usually in the ultraviolet (UV) spectrum, exhibit photoluminescence. Following absorption of photons at a specific wavelength, these molecules are excited from a ground state to higher energy states or levels. In this intramolecular phenomenon, a valence electron is excited to an outer orbital level. The energies involved in this electronic transition are much higher than those related to vibrational/rotational mode excitations that occur in the IR or Raman spectroscopy. Molecules at higher energy levels are generally unstable, and they de-excite to the lower energy state. During this de-excitation

process, the absorbed photon is emitted. Depending upon the kind of de-excitation, the process can be classified as fluorescence or phosphorescence. Fluorescence occurs rapidly after the excitation of the molecule and lasts for about few nanoseconds, and this de-excitation does not involve spin change of the electron. In contrast, to exhibit phosphorescence, the molecule must undergo a change in the electronic spin. With respect to fluorescence emission, phosphorescence lasts longer and has a higher lifetime, which can vary from a hundreds of microseconds to a few milliseconds, depending on the molecule, the laser wavelength excitation, and the thermodynamic conditions.

A classical Quantum mechanical principle referred to a Pauli Exclusion principle states that no two electrons in an atom cannot have the same four quantum numbers (principal quantum number, the orbital angular momentum quantum number, the magnetic quantum number, and the electron spin quantum number) and only two electrons can occupy each orbital where they must have opposite spin states. These opposite spin states are called spin pairing. Because of this spin pairing, most molecules do not exhibit a magnetic field and are diamagnetic i.e., in these molecules there is no force of attraction or repulsion in the presence of a static electric field. On the other hand, free radicals are paramagnetic because they contain unpaired electron, have a magnetic field and experience a force of attraction or repulsion in the presence of an electric field and magnetic field.

Figure 3.13 shows a schematic of the electrons spin in the singlet and triplet states. Singlet state is defined when all the electron spins are paired in the molecular electronic state and the electronic energy levels do not split when the molecule is exposed into a magnetic field. In an excited singlet state, the electron which has moved to the higher energy level, conserves its spin orientation (as it was in the ground state, when it was paired). On the other hand, in a triplet excited state, the excited electron changes its spin orientation (now it has the same spin orientation as that of the other unpaired electron).

The spin of an electron is represented in this section as "*spin*". A spin up of an electron has a value of $+\frac{1}{2}$ and the opposite spin down has a value of $-\frac{1}{2}$. The spin multiplicity equation in Quantum mechanics, we can estimate the multiplicity of an energy state, which is given by $2\Lambda + 1$, where Λ is the total spin angular momentum, which is nothing but the sum of the electrons spins.

For a ground state and excited singlet state, we would be getting, the multiplicity as $2\left(\frac{1}{2} - \frac{1}{2}\right) + 1$, which is equal is 1, which can provide an indication of the state being represented

by the term singlet. On the other hand, for a triplet state, the multiplicity is $2\left(\frac{1}{2} + \frac{1}{2}\right) + 1 = 3$. The difference between singlet (ground and excited) state and triplet state is that the molecules is diamagnetic in the singlet state and paramagnetic in the triplet state.

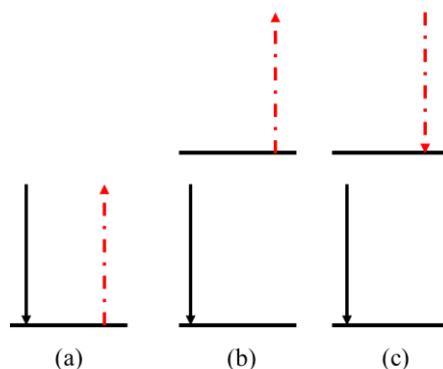


Figure 3.13 Schematic representations of electron spin orientations (a) ground state singlet, (b) excited singlet state, (c) excited triplet state

To further elaborate on these ideas, we can take the aid of Jablonski energy-level diagram. Figure 3.14 is a schematic representation of the Jablonski energy-levels for the phenomena of fluorescence and phosphorescence. It is a simplified representation of the transitions encountered by a molecule absorbing a photon of specified wavelength capable of exciting the molecule to a higher energy level. The bottom black line indicates the electronic singlet ground state S_0 of the molecule. The red lines represent the different vibrational levels at an electronic state. The ground state energy level can be expressed as

$$E_{S_0} = E_{S_{0-0}} + \Delta E_{thermal}(T_{S_0}) \quad (3.4)$$

where $E_{S_{0-0}}$ refers to the lowest energy level of the ground state, T_{S_0} is the temperature at level S_0 . The presence of various vibrational levels is due to the average thermal energy of each level, $\Delta E_{thermal}(T_{S_0})$. Therefore, the energy level at state S_0 of the molecule is a sum of $E_{S_{0-0}}$ and $\Delta E_{thermal}(T_{S_0})$. Similar argument can be made about the excited state S_1 . The difference in energy between S_0 and S_1 is $h\nu_m$.

$$E_{S_1} = E_{S_{1-0}} + \Delta E_{thermal}(T_{S_1}) = E_{S_{0-0}} + h\nu_m + \Delta E_{thermal}(T_{S_0}) \quad (3.5)$$

A valence electron in the state S_0 on absorbing a photon of specific wavelength, gets excited to a higher singlet S_1 electronic state (or S_2 , not shown in Figure 3.14). This process of excitation is very rapid, and usually occurs in the order of 10^{-15} sec or 10^{-6} ns. Usually, the excited electron lands in one of the higher levels of vibrational energy levels. From there, it undergoes vibrational relaxation. Thereafter, the electron de-excites from S_1 to S_0 by spontaneous emission and this process is referred to as fluorescence. The timescale at which this process occurs is of the order of few nanoseconds.

Figure 3.14 also shows other possible phenomena that can occur during the photoluminescence process. Another possibility which exists for the electron excited to the state S_1 is to undergo intersystem crossing, ISC, (radiation less transition from singlet to triplet), which results in the transition to a triplet state T_1 . In fact, this intersystem crossing is largely responsible for the limited fluorescence signal and thereby, poor quantum efficiency or yield, which is the ratio between number of photons emitted to the number of photons absorbed. The direct transition $S_0 \rightarrow T_1$ is not allowed according to quantum mechanical analysis, as it would require a change in the electron's spin. This requirement for the conversion in spin state from singlet to triplet the transition from singlet to triplet (or vice versa) is highly improbable than the singlet-to-singlet transitions. In other words, this would involve a change in multiplicity and is referred to as 'forbidden transitions'. The de-excitation from state $T_1 \rightarrow S_0$ results in phosphorescence. Due to the requirement of change in electron's spin (ISC), as explained above, the rate of this occurrence is lower than that of fluorescence. On the other hand, this phenomenon has a relatively higher lifetime of about 10^{-4} to 10 sec (varies for different molecules).

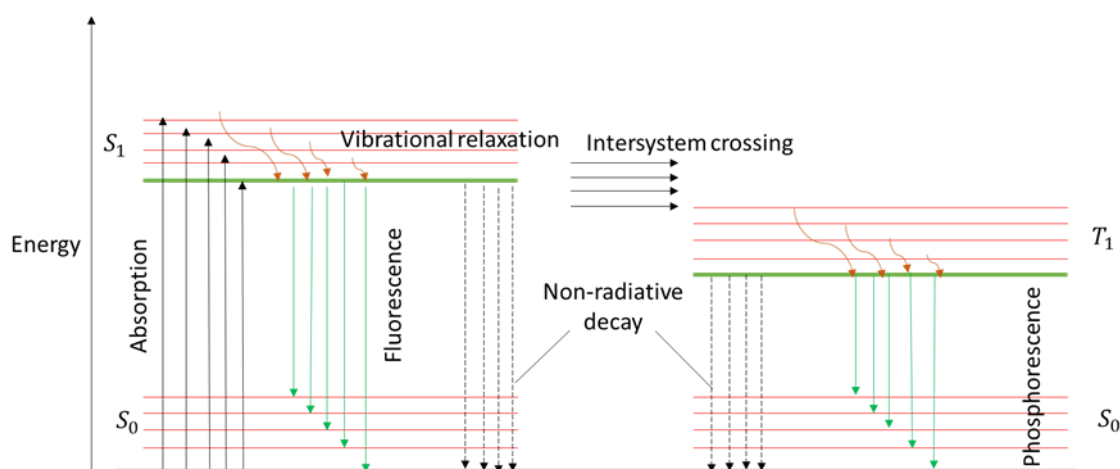


Figure 3.14 Jablonski's diagram and schematisation for the phenomenon of fluorescence and phosphorescence.

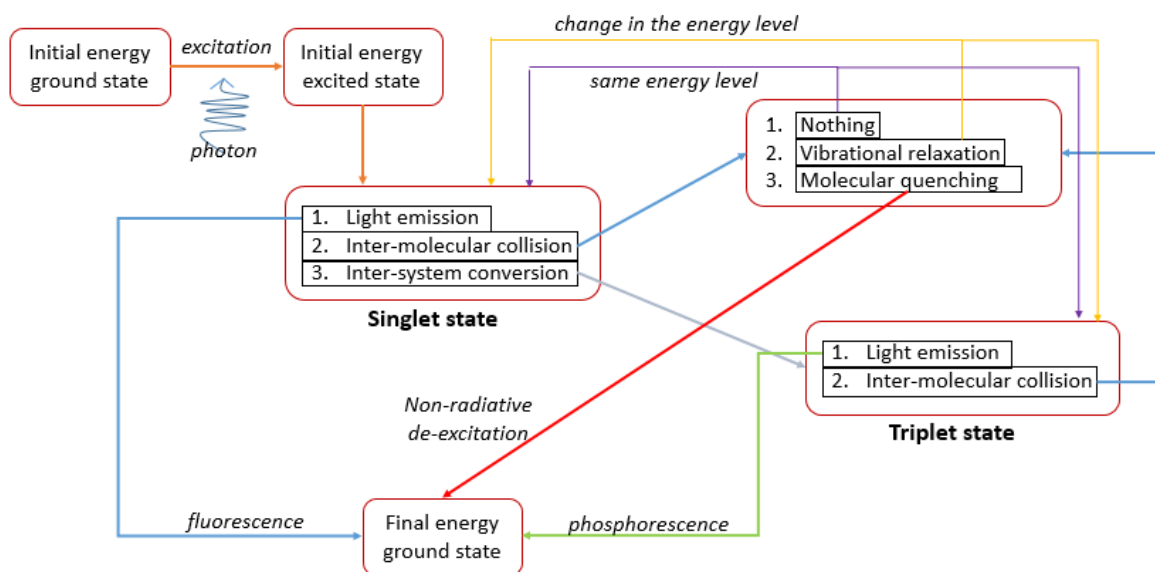


Figure 3.15 Scheme of the possible path that a molecule can go through, from the absorption of light to the de-excitation to the ground state

The discussion in the preceding paragraphs talks only about radiative de-excitation with the emission of a photon. However, the de-excitation can also occur non-radiatively in the form of electron returning to the ground state by colliding with a quencher species and transferring the energy to the quencher molecule. The phenomenon of quenching is more pronounced for molecules in the triplet state, i.e. its effect is more visible for phosphorescence than for fluorescence.

To put all the diverse ideas of the preceding paragraphs of this section succinctly, a flow chart is presented in Figure 3.15, which shows the journey of an molecule/ atom from the state of being excited by a photon until it reaches back to its initial ground state. It shows the outcome of an excited electron, which can undergo fluorescence, radiation less de-excitation, or change its multiplicity, and exhibit phosphorescence.

For a photoluminescence phenomenon, the number of photons collected by a photo detector (S) from a volume ΔV of molecules excited by a laser beam of energy density I_{in} , can be estimated as^{129, 130},

$$S = \eta_p \frac{I_{in} \sigma_{abs}(\lambda, T)}{E_{ph}(\lambda)} n \phi(\lambda, T, P) \quad (3.6)$$

Where σ_{abs} is the absorption cross section and is a representation of the ability of a molecule to absorb a photon having a particular wavelength. E_{ph} is the energy of a photon, λ is the wavelength of the light used for excitation, T is the temperature and P is the pressure, n is the molecular concentration of the emitting molecules, and η_p is the capturing efficiency of the detecting optics. ϕ refers to the quantum yield of photoluminescence = $\frac{\text{number of photons emitted}}{\text{number of photons absorbed}}$, and it can also be expressed in terms of rate constants as follows¹²⁹

$$\phi = \frac{k_r}{k_r + k_{nr} + k_Q n_Q} = \frac{\tau}{\tau_r} \quad (3.7)$$

Here, k_r is the radiative de-excitation rate constant, k_{nr} is the non-radiative de-excitation rate constant, k_Q is the quenching rate constant per molecular density n_Q of quencher. τ refers to the characteristic time of the non-radiative de-excitation, and τ_r refers to the characteristic time of the radiative de-excitation. It is possible to derive Equation (3.7) based on Beer-Lambert's law coupled with the differential equations governing the time decay of the singlet and triplet state of the molecule. In the specific case of fluorescence, the expression of the quantum yield (ϕ_f) takes the following form¹²⁹

$$\phi_f = \frac{k_f}{k_f + k_{ISC} + k_Q n_Q} = \frac{\tau}{\tau_f} \quad (3.8)$$

where k_{ISC} is the rate constant for inter system crossing. Similarly, for phosphorescence the quantum yield (ϕ_{ph}) can be written

$$\phi_{ph} = \frac{k_{ph}}{k_{ph} + k_{nr,T_1} + k_Q n_Q} = \frac{\tau}{\tau_{ph}} \quad (3.9)$$

where k_{nr,T_1} is the non-radiative de-excitation rate constant for triplet state. The characteristic times and the rate constants are functions of the kind of excited molecule. The primary interest of this thesis is to study acetone molecule, and the values of these constants for this molecule are as follows¹²⁹: $\tau_f = \frac{1}{k_f} = 2 \mu\text{s}$ and $\phi_f = 0.2 \%$. The low value of the fluorescent quantum efficiency of acetone indicates the important role of non-radiative de-excitations during the fluorescence. The high characteristic time indicates the rapidity of the process, and thereby, the

high intensity of signal achieved in relatively low time. Similarly, for phosphorescence of acetone¹²⁹, $\tau_{ph} = \frac{1}{k_{ph}} = 0.1$ s and $\phi_{ph} = 1.8$ %.

Generally, the rate constants are dependent on the temperature. From Equation (3.7), if the molecular density remains constant, there is a variation in the σ_{abs} and (or) the quantum yield $\phi(\lambda, T, p)$ of the emission with temperature. Depending on the wavelength at which the molecule has been excited, these factors may lead to the temperature dependency of photoluminescence.

3.2.5.1.1 Laser induced fluorescence (LIF), Laser induced phosphorescence (LIP), and Molecular tagging thermometry (MTT)

In this section, we discuss about the various techniques which exploit the above described properties for the measurement of temperature. The focus will be on LIF, LIP and MTT. Laser induced fluorescence (LIF) has been widely employed by researchers to map temperature profiles. As the name implies, this technique is based on the fluorescence exhibited by certain molecules. Depending on the excited molecule, emission intensity and lifetime can be function of temperature. As in the case of LIF based techniques, one can also map the relevant temperature information based on phosphorescence exhibited by the tracer molecule, and this technique is referred to as laser induced phosphorescence (LIP). However, since fluorescence lifetime is usually very short to be accurately measured, LIF-thermometry is mainly based on the light intensity sensitivity to temperature. Differently, LIP can exploit the signal intensity and its evolution with time, which can be both function of temperature.

Molecular tagging is a general reference to the technique of tagging molecules by a laser and extracting relevant information on velocity/temperature based on either fluorescence or phosphorescence. The technique in which the interest lies in measuring velocity fields is usually referred to as ‘Molecular tagging velocimetry (MTV)’. If the interest lies in measuring temperature, it is referred to as ‘Molecular tagging thermometry (MTT)’. The term MTT has come into usage from the work of Thomson¹³¹.

The molecules used to measure temperature fields are referred to as ‘tracer molecules’. The usual tracers in this technique for liquid flows are rhodamine B (fluorescein - RhB) and rhodamine 110 (Rh110). The widely used tracer molecules in study of gases are acetone and diacetyl. In addition to these molecules, studies have also been conducted on toluene, tert-butyl nitrite, sodium, strontium, OH, O₂, etc., to name of few¹³². These tracer molecules are

sometimes generated thanks to reactions occurring in the system. In other cases, they are not a part of the process, and must be added to the fluid to map the temperature field.

3.2.5.2 *Applications to liquid microflows*

Fogg et al.¹³³ measured void fraction and liquid temperature in microchannel flow boiling. The experiments were carried out in a microchannel of 500 μm width, 100 μm depth, and 2.5 cm length. Fogg et al. adopted laser induced fluorescence thermometry (LIFT). As mentioned previously, LIFT uses fluorescent intensity to carry out temperature analysis. This intensity is influenced by a variety of factors, such as the laser intensity distribution, the variation in the dye concentration and photo bleaching, which refers to the phenomenon of permanent destruction of fluorescence at higher intensity of illumination, thereby, reducing the signal emitted. Therefore, to minimize these effects, researchers generally employ two tracers – temperature sensitive and temperature insensitive tracer. The calibration curves are generated by normalization of the intensity of temperature sensitive dye with that of temperature insensitive tracer, and this approach is referred to as ratiometric approach. The ratio of fluorescent emissions of Rh110 and RhB was used to generate the calibration curves in a temperature range from 40 to 100 $^{\circ}\text{C}$. This approach was able to obtain local liquid temperature within an uncertainty of ± 3 K.

In a similar approach, Chamrathy et al.^{134,135} carried out studies on temperature measurements using these tracers. For instance, they measured the temperature in a T-junction at the mixing plane of hot and cold deionized water. RhB was the temperature dependent dye and Rh110 was the temperature independent tracer. A typical calibration curve and an experimental image from this study are shown in Figure 3.16a and Figure 3.16b, respectively. They studied with this technique the non-uniform temperature profiles generated by the flow maldistribution in a silicon microchannel heat sink of a series of 76 parallel microchannels, each 110 μm wide and 9 mm in length. The average depth of the channels was 371 μm . Their approach demonstrated an uncertainty in the range of ± 0.6 to 1.25 K for single-pixel measurements in the temperature range of 20 to 50 $^{\circ}\text{C}$.

Kim et al.¹³⁶ carried out temperature measurements of water in the range of 20 to 60 $^{\circ}\text{C}$ for laminar Poiseuille flow through a PDMS-glass channel, heated on one side and having a square cross section of width 1 mm and a length of 28 mm. The fluorophores were RhB and Sulforhodamine B, and Kim et al. observed a temperature sensitivity depending on the temperature being measured. The uncertainty in temperature measurements was estimated to be about 0.3 K for a spatial resolution of 30 μm .

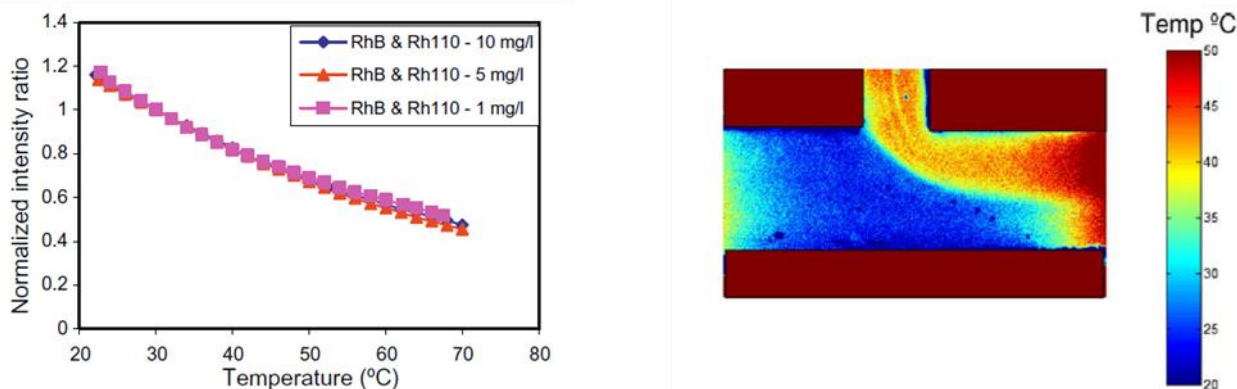


Figure 3.16 a) Normalized intensity (RhB/Rh110) for different concentrations of the tracers, b) temperature measurements in a T-channel¹³⁵.

Hoera et al.¹³⁷ developed an integrated microfluidic chip to measure surface temperature in microflow reactors. The addition of fluorescent dyes to the fluid is employed in many experimental studies. However, this approach is sometimes not appropriate due to the issues of the dye effect on the chemical reaction. Therefore, Hoera et al. presented a fabrication procedure for the integration of thin polymer layers with optical sensing functionality (to detect fluorescence) in microchannels of glass-PDMS chips of 150 μm width and 29 μm depth. These microchannels allowed them to investigate wall temperature in the range of 25 to 65 $^{\circ}\text{C}$, and a resolution of 0.07 K was reported.

LIP-based thermometry technique is referred as Molecular tagging technique by the research group of Hu and Koochesfahani¹³⁸. They have widely exploited this approach in liquid flows to measure temperature. The main tracer in their study studies was 1-BrNp . M β -CD . ROX triplex, which exhibits dependency of phosphorescence lifetime with temperature. Hu and Koochesfahani studied diverse problems, such as the thermal effects on the wake instabilities behind a heated cylinder¹³⁹, unsteady heat transfer and phase changing process within micro-sized icing water droplets pertinent to aircraft icing phenomena¹⁴⁰, spray flows¹⁴¹, etc.

3.2.5.3 Applicability to gas microflows and current limitations

As in LIPT, temperature measurement is dependent both on the intensity values and lifetime of the tracer, this makes temperature measurements relatively more difficult to extract. In the other hand, the information is richer than with the LIFT technique because one can base their estimations just on the intensity signal and there is no need to consider the signal evolution with time . In the literature, however, there is a clear lack of experimental data on the exact

dependency of intensity and lifetime with temperature for the widely employed tracer molecules, such as acetone and diacetyl (or biacetyl).

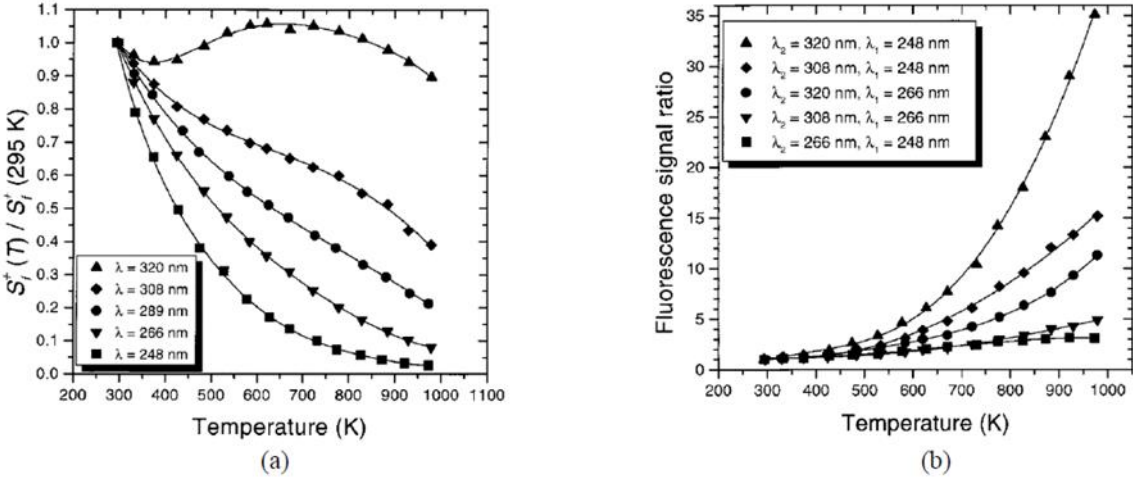


Figure 3.17 a) Fluorescence signal per acetone mole and per unit laser energy normalized to the room temperature and at atmospheric pressure as a function of temperature. b) Fluorescence ratio $S_{\lambda_2}/S_{\lambda_1}$ for the dual-wavelength excitation normalized to the room temperature and at atmospheric pressure as a function of temperature, where S_{λ_2} and S_{λ_1} are the fluorescence intensity values.

In the literature, studies have demonstrated a dependency of fluorescence emission intensity of acetone with temperature. For instance, Thurber et al.¹⁴² carried out investigations on acetone fluorescence at atmospheric pressure and temperature varying from room temperature to 1,000 K by exciting acetone vapour at wavelengths varying from 248 to 320 nm, as shown in Figure 3.17a) and b). Table 3-6 summarizes the features of photoluminescence for temperature measurement.

Table 3-6 Summary of Photoluminescence features

Method	Principle	Resolution	Advantages	Disadvantages	Gas microflows
Photoluminescence	Temperature dependence with lifetime/intensity	Spatial $\sim 1 \mu\text{m}$ Temperature $\sim 10^{-1} \text{ K}$	Local information of temperature and velocity distribution.	Expensive, challenging in non-circular geometries.	Possible and is the objective of this thesis to demonstrate the challenges.

3.3 Concluding remarks from literature survey

This chapter presented the various techniques currently available to map temperature, especially the optical based techniques. Based on the underlying physical principle, the existing measurement techniques have been classified into different categories and their applications at microscale have been discussed. The feasibility and the factors hindering/promoting the applicability of every technique for gas microflows has been brought about.

Though the contact-based techniques are relatively simple to implement, their applicability at microscale poses certain disadvantages: these sensors are generally invasive in nature; their effect on the temperature distribution is non-negligible especially at microscale; temperature is obtained only at discrete locations, and at microscale; incorporating them can strongly influence the fluid flow and heat transfer characteristics; considering this effect during analysis is not a trivial task. Moreover, in practical applications, they are limited to the measurement of wall temperature. However, due to their relative ease of operation and not requiring expensive optical equipment as in case of luminescent-based approaches, the conventional techniques of temperature measurement are still being widely used in gas microflows.

Interferometry based techniques have been limited at microscale gas temperature measurements by issues of temporal noise. Infrared-based measurement techniques are limited by the signal dependency on the surface emissivity, which in turn is a function of the temperature. Raman thermometry is an interesting alternative technique for gas microflows. However, due to issues of low sensitivity of gases to Raman spectroscopy, low density and low scattering cross-section of gases – this technique is yet to reach its full potential for temperature measurement in gas microflows.

TLC is interesting to measure the wall temperature. However, at microscale, wall characteristics play a very important role in heat transfer. TLC might alter the thermal conductivity and heat capacity of the ‘real’ wall. The temperature information would be of ‘modified’ wall. In addition, there will be a variation of the surface roughness and this have a consequence on the measured momentum and thermal accommodation coefficients. Therefore, this is can be argued to be an intrusive technique that modifies the properties of the walls.

The semi-intrusive techniques based on photoluminescence seem to be interesting candidates for thermometry in gases. The advantages stem from the following: to generate local temperature profiles; possibility to map near wall fluid temperature – exploring temperature

jump experimentally; possibility of simultaneous mapping of velocity and temperature distributions with the same set of images; technique has been successful in liquid flows.

However, for temperature measurements in gases at microscale/ rarefied conditions (with photoluminescence), there is still a significant amount of research to be done. The main issue is the quantifying of the photoluminescence of the suitable tracers (acetone and diacetyl) in these rarefaction conditions. The experimental conditions presented in literature do not represent those of rarefied conditions. Moreover, there is limited information in these studies about phosphorescence of acetone vapour. In this regard, it would be necessary to study the temperature dependent behaviour of these tracer molecules at low pressures and to generate data on photoluminescence. Therefore, the next chapters in this thesis focus towards this objective of studying these tracers at low pressure conditions and to comment upon its potential for measuring temperature in gas microflows.

In chapter 4, an introduction of the molecular tagging technique and the modifications carried out on the existing experimental facility at ICA Toulouse to adapt it for temperature measurements are presented. The initial experiments were carried with the existing experimental chamber in the lab, and we term this chamber as the first experimental chamber. These experiments helped us to identify the optimal excitation wavelengths for acetone and diacetyl vapour. The subsequent analysis of the experimental data provided us with the possible factors which can influence the reproducibility of the experiments. These experimental analyses paved the way for the design of a new experimental chamber, which is termed as second experimental chamber. The experiments and analysis on this chamber are presented in the Chapter 5 of the thesis. Different image analysis procedures and the subsequent experimental analysis is shown in this chapter. The details on isothermal and non-isothermal experiments carried with this new setup are presented.

4 MTT investigations with first experimental chamber

4.1 Introduction

The research carried out at Institut Clément Ader (ICA) during the last few years resulted in the development of an experimental setup capable of carrying molecular tagging studies^{30,31,33}. The experiments were mainly carried out at continuum flow conditions and with Nd:YAG Quantel twins laser capable of 266 nm UV excitation wavelength. The focus of this existing set-up was to measure velocity fields in gas-micro flows. The initial goal of the present thesis was to identify and carry out necessary modifications on the existing experimental facility to adapt it for temperature measurements. The focus was to study the luminescence intensity of tracer molecules at different conditions of pressures and temperatures, and to analyse the possibility of molecular tagging thermometry in gases in rarefied regimes.

Initial studies of this thesis were devoted towards understanding the optimal conditions, (such as excitation wavelengths and laser energy) to achieve the highest intensity signal of phosphorescence for the tracer molecules, acetone and diacetyl. The work described in the initial part of this chapter, until the identification of optimal excitation wavelength(s), was carried out collaboratively with D. Fratantonio, whose thesis focused on studying molecular tagging velocimetry in rarefied and confined gas flows³³.

In this chapter, in the initial sections, we describe the molecular tagging setup and the physical equipment required to capture photoluminescence signal of tracer molecules. Thereafter, different photoluminescence lifetime curves and their analysis are presented. Experiments are performed to discuss the repeatability of the experimental data and the corresponding factors are identified and analysed. In the final sections of the chapter, we present a detailed analysis of the laser energy fluctuations.

4.2 Molecular tagging setup

The primary components of molecular tagging set-up can be categorised into three groups (shown in Figure 4.1):

1. Vapour control system
2. Optical system
3. Signal acquisition system

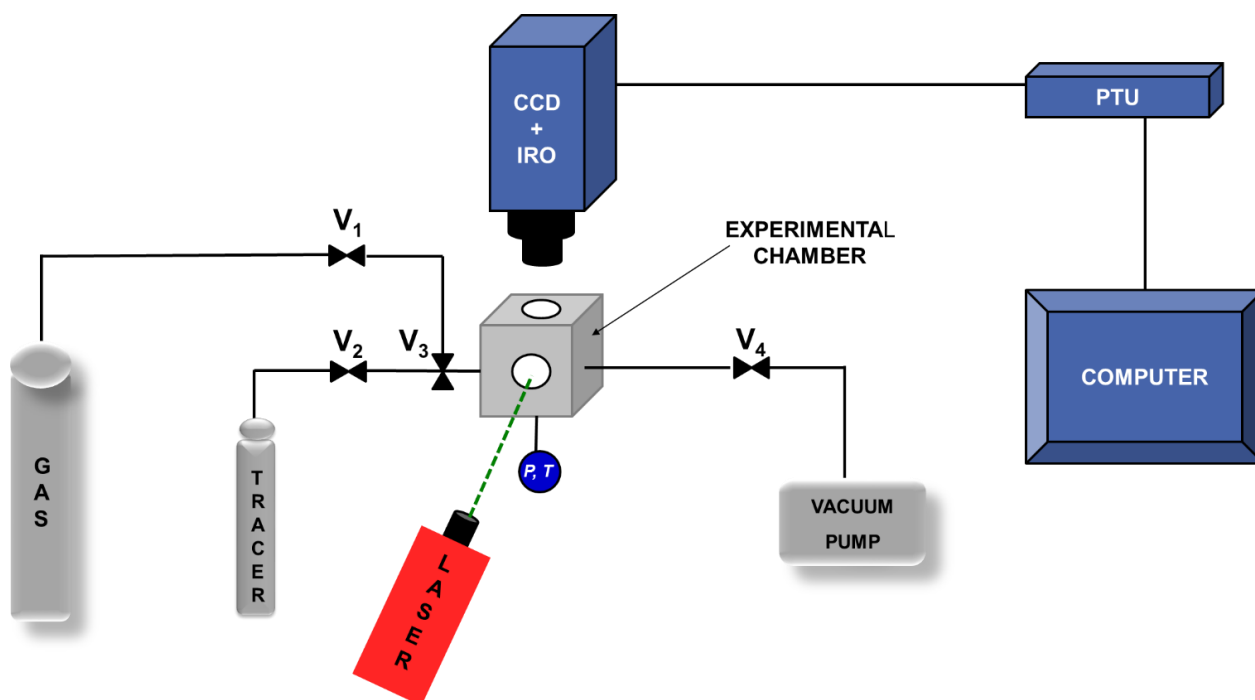


Figure 4.1 Schematic of the molecular tagging experimental setup. Components in Grey represent the vapour control system, in red represents the optical system, and in blue represent the signal acquisition system. V_1 to V_4 represent different valves by which we can control the pressure of gas and tracer in the system.

4.2.1 Vapour control system

This system consists of a tracer liquid bottle, valves for controlling the flow into the experimental cell or chamber, valves for vacuuming, pressure gauges, thermocouples, heating elements, and vacuum pump. This part of the setup is mainly for flow seeding and controlling the operating conditions of the experiments.

In this study, we used CDG025D Capacitance Diaphragm pressure gauges provided by Inficon®. Three different types of gauges with capacity of 10, 100 and 1,000 Torr, i.e. 133, 1,333 and 13,332 Pa are used. Table 4-1 shows the general characteristics of all these gauges.

Table 4-1 Characteristics of the pressure gauges used in this study

Precision	0.2 % of the reading
Resolution	0.0015 % of the full scale reading
Operation (ambient)	+5 to 50 °C
Bakeout at flange	≤ 110 °C

4.2.2 Optical system

In this subsection, we provide details on the components composing the optical system. Two lasers, with different technical specifications, have been used separately.

4.2.2.1 Nd:YAG Quantel Twins laser

LASER is the acronym for ‘Light Amplification by Stimulated Emission of Radiation). The Q-switched Nd:YAG laser provided by Brilliant® is shown in Figure 4.2, and is based on the stimulation of the Nd:YAG crystals, which generates a laser beam at 1064 nm. Two sequential second-harmonic generators (SHG) i.e., frequency-quadrupling modules, allow to convert the laser beams to 266 nm. Table 4-2 provides the technical specifications of this laser.

Q-switching is a method for generating intense short pulses of light with a laser, generally used for the generation of pulsed laser beams. A simplified description of the laser cavity (or resonator) is shown in Figure 4.3. Energy is provided to the Nd:YAG crystals by triggering the flash lamp. This process excites the crystals, and subsequently there is a stimulated emission of light. Due to the optical arrangement of the mirrors, this light beam bounces to and fro in the resonator, and its intensity amplifies with time. On actuating the Q – switch, which can either be an acousto-optic or electro-optic modulator, the laser pulse is released as an output pulse. The energy of the laser beam output can be adjusted by controlling the timing of flash lamp trigger and Q – switch trigger. Due to the resonator losses, the laser energy in the cavity decreases with time. If the activation of Q – switch is delayed with respect to flash lamp triggering, we can have a lower energy in the output laser pulse.

In the laser system of our lab, a mechanical attenuator placed at the exit of the second SHG can reduce the energy of the laser pulses at the exit, and generates beams with low and stable energy. This approach is preferable compared to the approach of reducing the laser energy by increasing the Q-switch delay with respect to the flash lamp. This usually results in the reduction of the stability of the laser beam energy. A mechanical arm at the exit of the laser beam deflects the laser beam towards the region of interest (the experimental chamber) in the experimental setup.

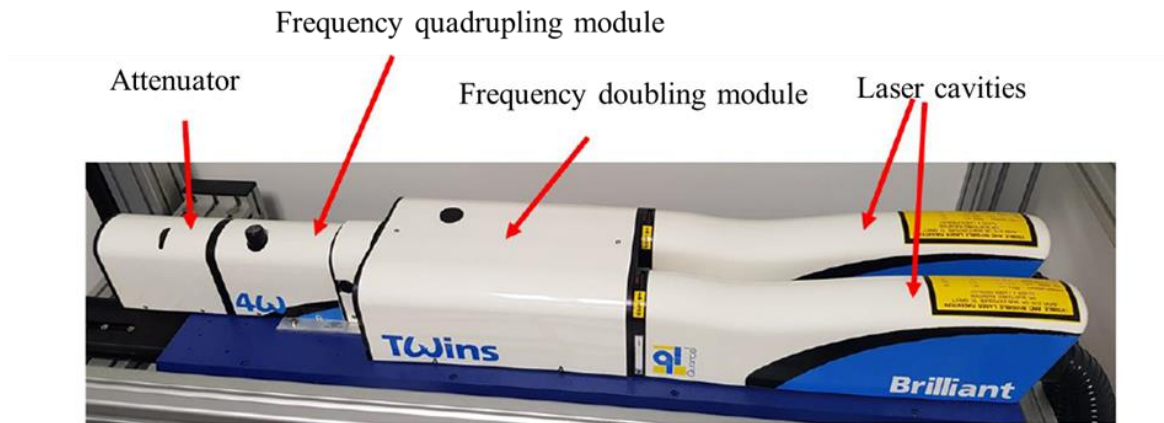


Figure 4.2 Nd :YAG laser provided by Brilliant

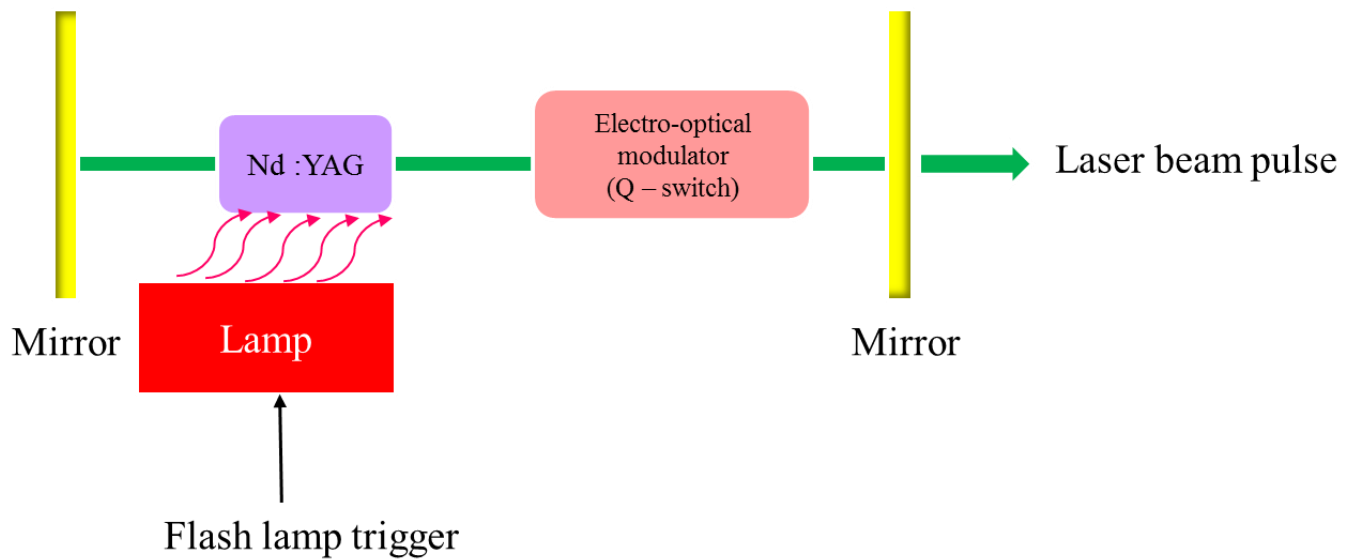


Figure 4.3 Schematic of laser cavity (with Q – switching)

Table 4-2 Specifications of the Nd:YAG Quantel Twins laser.

Wavelength (nm)	266
Pulse duration	9 ns
Repetition rate	10 Hz
Beam diameter at the exit	7 mm
Highest energy per pulse	30 mJ
Beam quality factor (M^2)	4
Beam divergence	< 0.7 mrad

4.2.2.2 OPOlette laser

In this study, unless stated otherwise, the experiments have been performed with a tunable laser system from Opotek Inc®, which utilizes a patented Optical Parametric Oscillator (OPO) technology to generate wavelengths in the ultraviolet (210-410 nm), visible and near infrared (410-2400 nm) ranges.



Figure 4.4 Simplified schematic of the working principle of OPO laser

The basic working of an OPO laser is as follows: an input photon (pump) of certain energy (and thus frequency, ω_p) is transformed into two output photons (signal and idler) with respectively higher and lower energies (total energy is equal to the energy of input photon). The output photon with higher frequency (ω_s) is referred as signal, and the other photon with lower frequency (ω_l) is referred as idler. During the process of conversion, the energy of the input photon is conserved, resulting in $\omega_p = \omega_s + \omega_l$. The conversion is achieved through a nonlinear optical interaction through an OPO crystal. Some input photons are not converted and lead to a residual pump frequency ω_p . In the case of non-conversion, the frequency of the photons after passing through the OPO will remain the same as that of inlet pump, and these photons are called as residual pump. In our system, we do not have these unconverted photons in the output beam as they are blocked by the system. The schematic in Figure 4.4 shows the principle of the OPO laser.



Figure 4.5 OPO laser used in our study

Figure 4.5 shows the OPO laser used in our study. The model is OPOlette HE355LD UV12. It is a highly portable system with the laser head occupying a footprint of only 7x12". The laser

can be operated and triggered with the software provided by the manufacturer. However, for the purpose of our experiments, we must establish a synchronisation between laser pulse triggering and image capturing. This was achieved by operating the laser with an external triggering software provided by La Vision. Table 4-3 presents the salient technical features of the laser.

Table 4-3. Technical specifications of OPO laser used in our study

Wavelength (nm)	210-355 and 410-2200
Peak duration	7 ns
Repetition rate	10 or 20 Hz
Beam diameter at the exit	4 mm
Highest energy per pulse	8 mJ at 450 nm
Beam quality factor (M^2)	3.94
Beam divergence	< 0.5 mrad

4.2.2.3 Power meter

The optical system includes a UV optical beam generator, i.e. a laser in our experiments. A power meter used to measure the energy of this laser beam. The model used in our study is QE12LP-S-MB-QED-D0, fabricated by Gentec Electro-Optics (Figure 4.6).

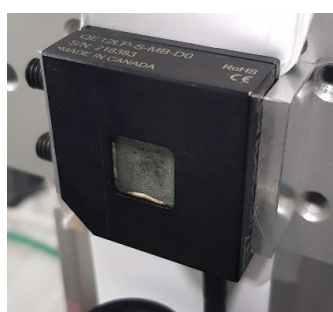


Figure 4.6 Schematic of the power meter

The energy detector sensitivity is 103 V/J at 1064 nm, with an energy calibration uncertainty of $\pm 3\%$ (of reading), with 95% confidence level. The maximum admissible energy density varies from 8 to 1 J cm⁻² at 1064 and 266 nm, respectively. Other specifications of the power meter are presented in Table 4-4.

The energy densities (E_{avg}) in this study, varied between of 0.04 to 0.08 J cm⁻². These values ensure that we are within the permissible limits to avoid damage to the optical access windows (Suprasil), which were calculated by previous researchers¹⁴³. They estimated that that $E_{avg} > 0.2$ J cm⁻² could lead to cracks in the Suprasil and further higher values, may lead to a creation of hole in the material³⁰. These values are much lower than the maximum energy to which we can subject the power meter.

Table 4-4 Specifications of the powermeter

Spectral range for measurement	193 to 2100 nm
Maximum repetition frequency (for pulsed lasers)	300 Hz
Energy sensitivity	103 V/J at 1064 nm
Energy calibration uncertainty	± 3% of measured value
Maximum energy density	8 to 1 J cm ⁻² at 1064 and 266 nm, respectively
Aperture width of sensor	9 mm
Aperture height of sensor	9 mm

Power meter is an essential component in the molecular tagging setup. It provides us with the information energy of the laser beam, based on which we can adjust the laser energy. Also, in the later stages of the thesis (See section 4.10.1), we performed a detailed analysis on the laser energy fluctuations and the power meter provided us with a measure of energy in these experiments.

4.2.2.4 Beam focalisation

The beam generated by the OPO laser is about 5 mm in diameter. An optical arrangement consisting of a diaphragm valve, a beam expander and a Plano-convex lens is used to modify the beam. The beam expander increases the diameter of the laser beam, which allows higher focusing of the beam by the plano-convex lens as the beam diameter at its entrance is larger. This arrangement is positioned at outlet of the laser beam from OPO, as shown in Figure 4.7.

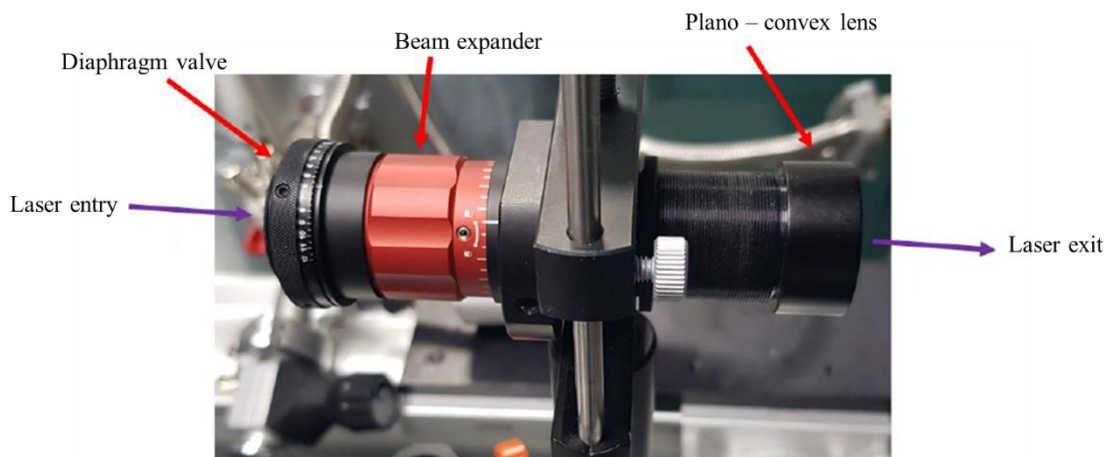


Figure 4.7 Optical system for focusing the laser beam

The beam diaphragm can be mechanically adjusted by the markings designated as D1 to D9, which varies the diameter of the opening for the laser beam, with the lower number corresponding to the lower diameter.

4.2.2.5 Optical lenses



Figure 4.8 Optical lenses arrangement placed before the IRO

The optical lenses are placed in front of the IRO and transmit to the camera the light emitted by the molecules in the experimental chamber. We used two associated objectives in our studies. The first one is an inverted 28 mm f: 2.8 Nikkor objective and the second one is a 105 mm f: 2.8 Nikkor objective. The configuration is shown in Figure 4.8. Both objectives are set to infinity

with their maximum aperture (f/2.8). For this configuration of lenses, the experimental calculated focusing distance is about 38 mm.

4.2.3 Signal acquisition system

The signal acquisition system consists of an intensified charge-coupled device (ICCD), which is a combination of 12-bit LaVision® Imager Intense progressive scan charge-coupled device (CCD) coupled with a 25-mm intensified relay optics (IRO). The ICCD is connected to the previously described dual objective. The IRO gate is controlled by a trigger signal generated by an IRO controller. A programmable timing unit (PTU) with a precision of 5 ns is used to synchronise the laser trigger, the camera shutter trigger, and the IRO trigger. The acquisition system is shown in Figure 4.9. The IRO principally consists of a S20 photocathode, a microchannel plate (MCP), a P46 phosphor screen, and internal lenses, as shown in Figure 4.10.

The conductivity of the S20 photocathode allows minimum gate times of 100 ns. This photocathode converts the incident photons into electrons. The MCP amplifies the electron flux generated by the photocathode and the phosphor plate allows the reconversion to photons. The lens coupling system collects the light emitted by the phosphor plate. The CCD accumulates the electrical charges proportionally to the light received. The final step in the acquisition process is the digitalisation of the accumulated electrons on the CCD cell. The accumulated electrons in each photosite are represented in units of DN (Data number) or ADU (Analog Digital Unit) or ‘counts’. The conversion of the measured counts to the photons per photosite can be obtained from the curves of photocathode sensitivity and signal amplification.



Figure 4.9 Image acquisition system.

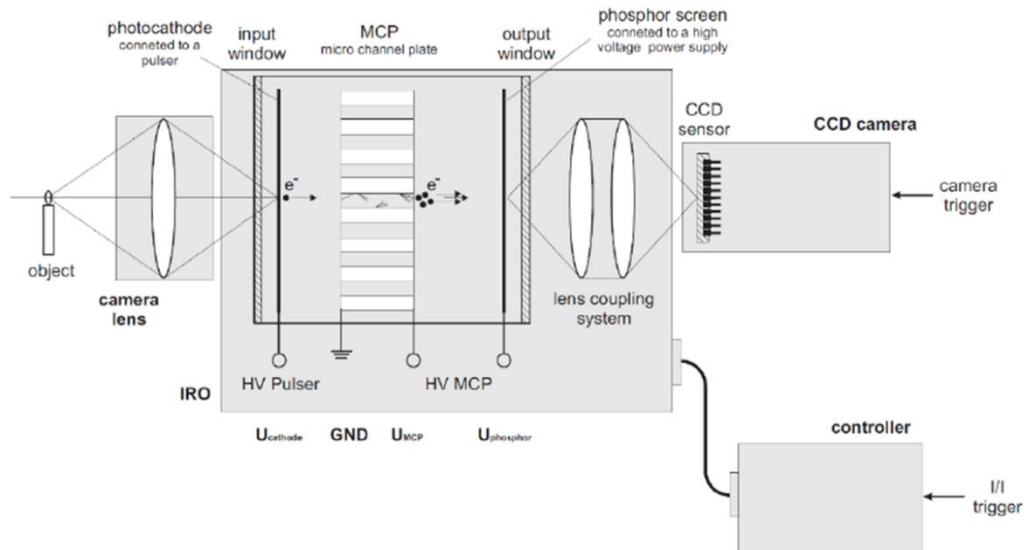


Figure 4.10 Schematic of the ICCD internal structure. The orientation is the inverse from the one in Figure 4.9.

The parameters of the IRO and of the CCD sensor are controlled via the Davis® interface: this software provides the triggering of the camera, duration of exposure, number of images to be acquired, the method to process and saving the image, various image transformation options (rotating, mirroring, etc.), intensity corrections, etc. The captured light of photoluminescence is saved in the form of numerical data. The resolution of the CCD imager intensifier is 1376 (horizontal) \times 1040 (vertical) pixels, with a pixel size of $6.45 \times 6.45 \mu\text{m}^2$ (physical size of the photosite). Binning refers to the procedure of grouping pixels into one mega pixel to increase the signal intensity. This results in a decrease in the spatial resolution. All the images in this study were captured with 4×4 binning, leading to a dimension of the image matrix of 344×260 pixels.

4.3 Terminology for image acquisition

Before getting in the details of the experiments, it would be essential to present the terminology for an acquisition of an image. The same set of terms have been used in the entire thesis. Every image captured in this study can be identified by the following information, represented in Figure 4.11.

- ‘Delay (t)’ refers to the time of capturing the image after the laser shot
- ‘IRO Gate (Δt_{IRO})’ refers to the time for which the camera and IRO were open to capture the information, i.e., the light integration time
- ‘IRO Gain (G)’ is a measure of signal amplification
- ‘ N_l ’ is the number of laser shots per recorded image
- ‘ N_i ’ is the number of recorded images which are averaged to deliver the final image

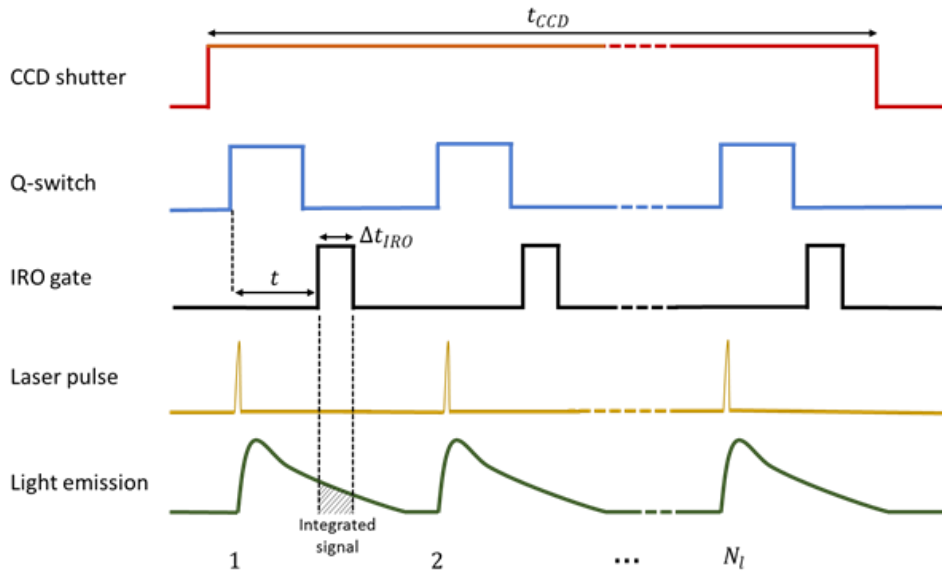


Figure 4.11 Sequence of operations for image acquisition.

In general, photoluminescence emission signal of excited molecules at low pressure conditions is weak and it is necessary to enhance the signal. For achieving this enhancement, we adopt an approach referred as on-chip integration technique, and is described in the following paragraph.

Final image of every acquisition by this technique is an average of N_i images. In addition, every single image of this N_i images are the result of the integration of N_l laser pulses. Every image at a particular delay t in this study can be identified by specifying it as follows: $P_{ac} = 10,000 \text{ Pa}$, $N_l = 100$, $N_i = 10$, $G = 100\%$, $\Delta t_{gate} = 100 \text{ ns}$. If there is no energy normalisation, we have to additionally specify the average energy (E_{avg}) or average energy density (E_{den}). The above conditions show that the pressure of tracer in the system was 10,000 Pa, and every image had 100 pulses, and we averaged 10 such images. Therefore, the total

number of pulses for this acquisition are 1,000. For a 20 Hz pulsed laser, this indicates 50 seconds of CCD exposure (t_{CCD}) to capture all the images. The other parameters, $G = 100\%$, shows that we used maximum signal amplification (the minimum is 60%), and $\Delta t_{IRO} = 100$ ns shows that time duration for which the emission was integrated.

4.4 Design of first experimental chamber

In this thesis, two different experimental chambers were employed to study the photoluminescence of acetone vapour. In the present chapter, the experimental results on the first chamber will be presented. In the next chapters, the attention is devoted towards the second experimental chamber. The schematic of the first experimental chamber is shown in Figure 4.12, and a cross-sectional view is presented in Figure 4.13.

The visualization chamber was made up of anodized aluminium. The chamber consisted of two optical accesses. The optical access for the laser beam (laser entry) was made up of Suprasil, a specific grade of fused silica, and the optical access for the visualisation system (camera access) was made up of Borofloat. The choice of Suprasil was based on the experimental observations of previous researchers³⁰. Care must be exercised in choosing the material of the glass window so that it is transparent to UV and has negligible fluorescence compared to the tracer molecule in the chamber. If the window emits significant light, this signal can overshadow, or at least add noise to, the signal of gas luminescence in the chamber. Table 4-5 shows the properties of these materials used in the chamber.

Table 4-5. Temperature limits of the various materials of the first experimental chamber.

Material (place in the chamber)	Maximum temperature
Suprasil (windows)	1223 K (1473 K for short-term)
Kalrez O-rings	600 K
Inficon CD025 Pressure gauge	≤ 383 K (Bake out at flange)
Aluminium (chamber)	873 K

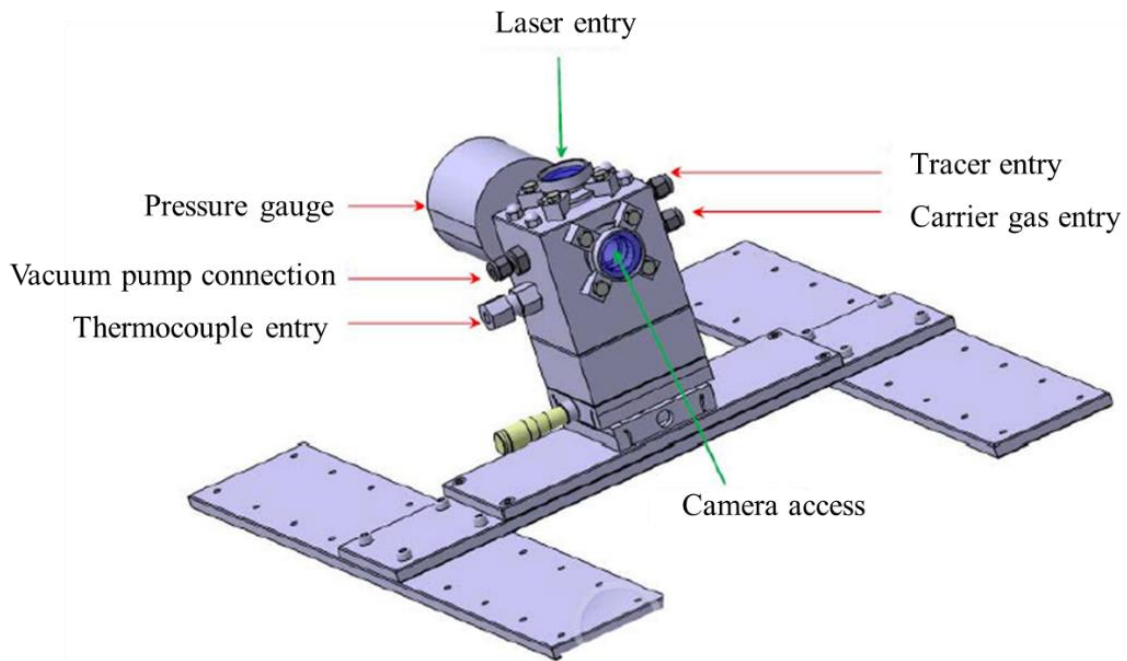


Figure 4.12 Schematic of the experimental setup; adapted from Samouda et al.¹⁴³

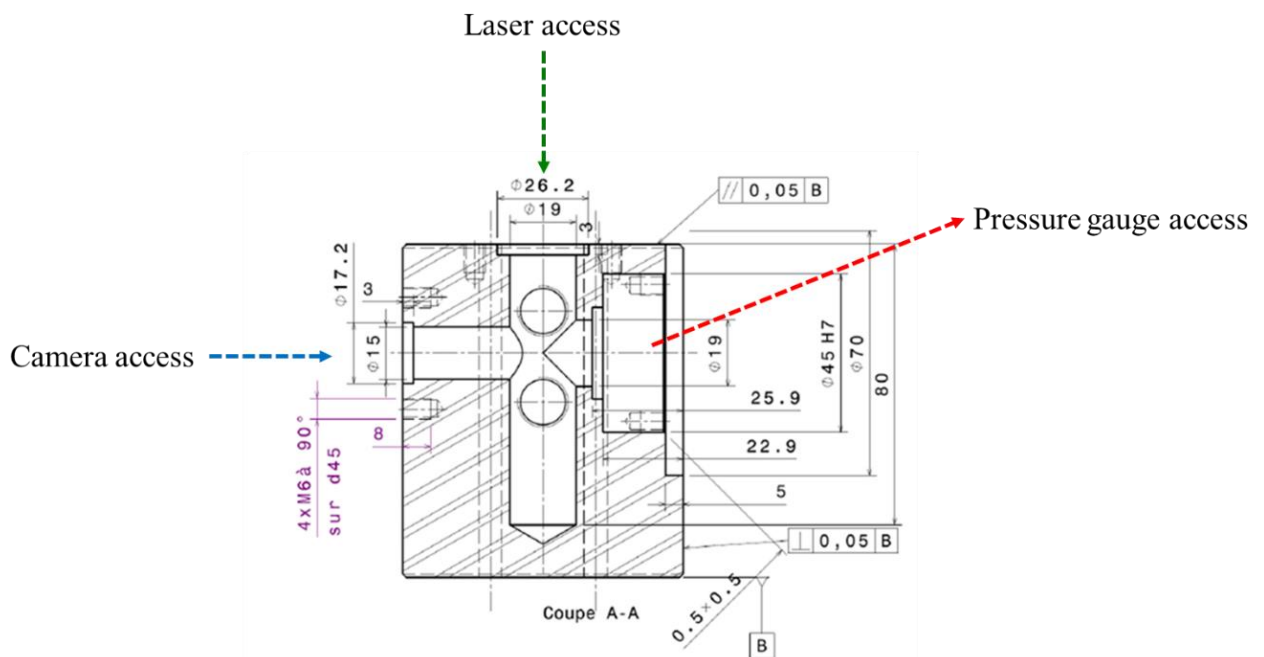


Figure 4.13 Cross-sectional view of the experimental chamber

4.5 Tracer molecules properties

4.5.1 Acetone

CH_3COCH_3 is the chemical formula of acetone, also called 2-propanone, with a molar mass of 58.08 g mol^{-1} and saturation pressure of around 25.3 kPa at $20 \text{ }^\circ\text{C}$. It is a highly transparent liquid, with high volatility and flammability. The toxicity depends on the level of inhalation; however, it is generally quite safe to handle. There is a possibility of irritation of eyes, upper respiratory tract, and mucous membranes, headache and nausea with prolonged exposure¹⁴⁴.

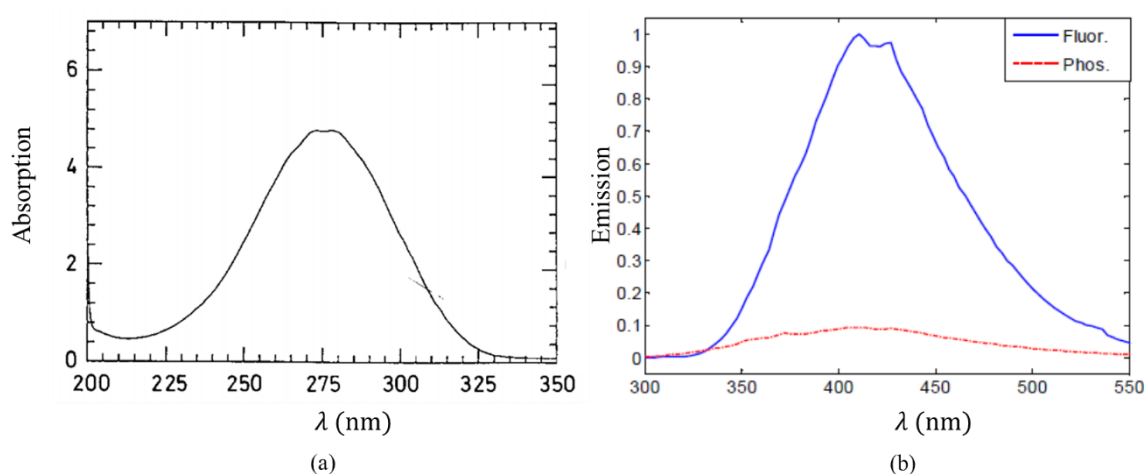


Figure 4.14 a) Absorption wavelengths of acetone¹⁴⁵, b) emission wavelengths of acetone (fluorescence and phosphorescence)¹⁴⁶.

The absorption spectrum of UV light is between 225 to 320 nm with a peak absorption around 275 nm (Figure 4.14a). These experiments have been repeated in our thesis and are presented in the later parts of the thesis. The emission spectrum is between 350 to 550 nm, i.e. mainly in the visible spectrum (Figure 4.14b). During the initial months of the thesis, we had only the Nd:YAG laser (Section 4.2.2.1) which could provide UV laser beam only at 266 nm to excite acetone. Therefore, we performed the initial experiments at this wavelength. Thereafter, we were able to procure OPO laser (see section 4.2.2.2), which enabled us to experiment in the entire absorption spectrum of acetone.

4.5.2 Diacetyl

The chemical formulae of diacetyl (or biacetyl) is $\text{CH}_3\text{COCOCH}_3$. It is also referred to 2, 3-butanedione. It has a molar mass of 86.10 g mol^{-1} . It is slightly yellowish in colour with a very strong odour, even when present in very minute concentrations. Also, diacetyl is highly

inflammable. It should be handled with care and it is preferable to have a dedicated inlet and exit for diacetyl in the system, so that the user is not in physical contact (breathing fumes) with this tracer, especially if one is exposed for prolonged duration. It can be absorbed by the skin and can result in headache, nausea, irritation to the skin, eyes, and mucous membranes. Moreover, prolonged exposure to diacetyl vapour can result in permanent, severe, and potentially lethal lung diseases.

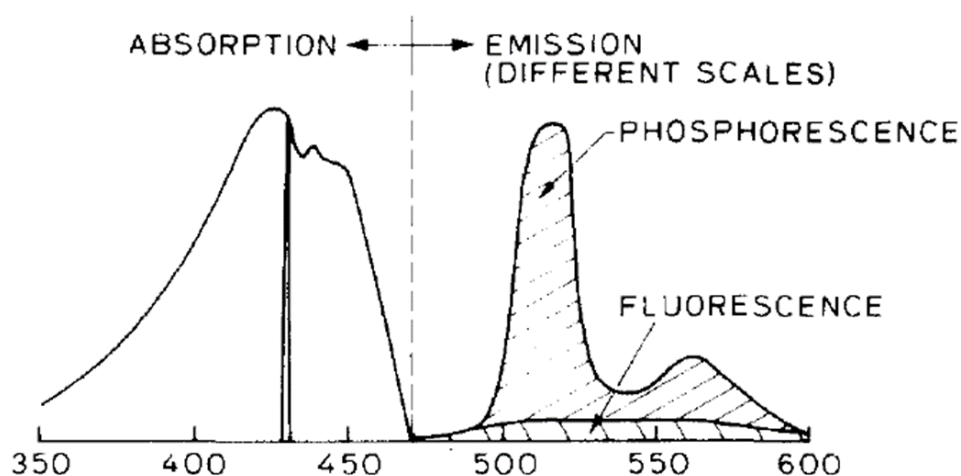


Figure 4.15 Absorption and emission spectrum of diacetyl¹⁴⁷

The optical properties of diacetyl are close to that of acetone, especially the emission spectrum. However, diacetyl generally provides an intense signal of fluorescence and phosphorescence compared to acetone vapour (at similar conditions of pressure and temperature). This aspect has also been studied and verified in the experiments presented in this chapter.

Figure 4.15 shows the absorption and the emission spectrum of diacetyl. Diacetyl absorbs from about 350 nm to around 470 nm, and the emission spectrum is between 450 to 600 nm. Since the OPO laser used in our study could not provide wavelengths between 355 to 410 nm, we could not investigate this part of the spectrum for diacetyl. Therefore, the photoluminescence study with diacetyl vapour was restricted from 410 to 470 nm. However, these are the first experimental results on diacetyl vapour with our experimental facilities at ICA.

4.6 Image analysis

A typical image generated in our study is shown in Figure 4.16. Once the experimental image is obtained, the data provided by it has to be treated in an appropriate manner to generate utilisable data. The image analysis carried out in this thesis is based on the work of previous investigators^{30,31,33,143,148}.

The following image treatment was carried out to analyse the data in this chapter: the image generated is a simple matrix containing a certain number of counts for every pixel. Let $x_{i,j}$ represent the pixel in the i^{th} line in the x -direction, and in the j^{th} line in the y -direction. Let $I_{i,j}$ be its intensity value (i.e. the number of counts measured at this pixel). In our case, $1 \leq i \leq 344$ and $1 \leq j \leq 260$. For every line i corresponding to a value of x , we sum up all the intensity values along the y -direction: $I_i = \sum_{j=1}^{260} I_{i,j}$.

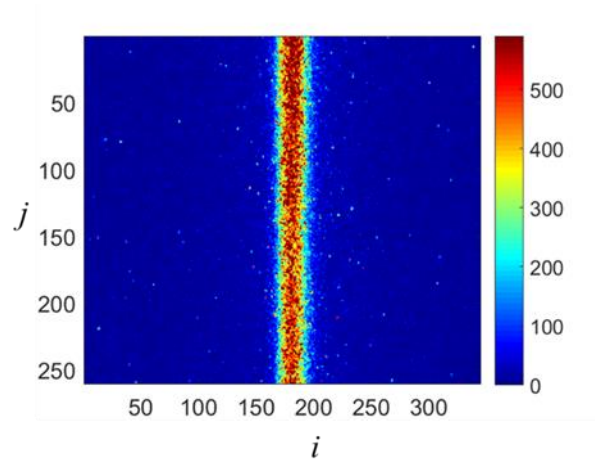


Figure 4.16 Typical experimental image. The experimental conditions are the following:

$$P_{ac} = 5,000 \text{ Pa}, t = 5000 \text{ ns}, \Delta t_{IRO} = 100 \text{ ns}, G = 100, N_l = 100, N_i = 10$$

Once we obtain I_i , a Gaussian is fitted to the raw experimental data. The reason for fitting the data with a Gaussian is due to the energy distribution of the laser beam, which closely resembles a Gaussian. Therefore, the interesting point to analyse from this Gaussian curve is the value of the peak of the Gaussian.

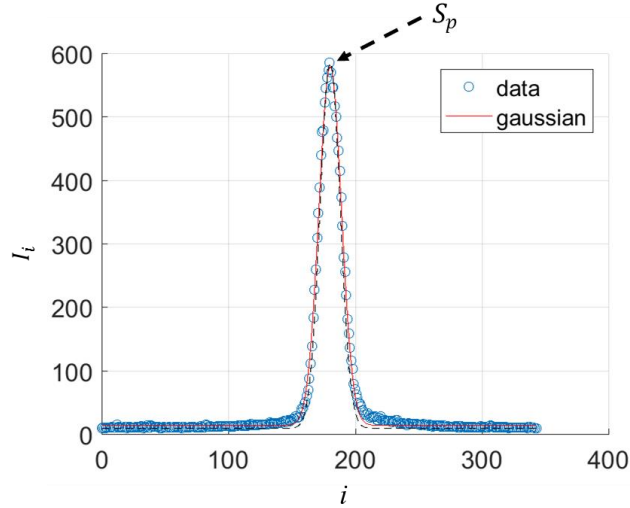


Figure 4.17 Gaussian fit of I_i extracted from Figure 4.16, S_p is the peak of this fitted Gaussian.

From the Gaussian shown in Figure 4.17, we can extract the peak value S_p of the Gaussian. The total number of counts in the image is $S_T = \sum_{i=1}^{344} \sum_{j=1}^{260} I_{i,j}$. This information of S_p and S_T for an image would correspond to the delay at which this image was captured. Therefore, to generate the lifetime curves, we have to repeat the same process of image analysis (for images at different delays). Here, we illustrate the manner in which we generate the lifetime curves.

Consider an experiment performed with pure acetone vapour, P_{ac} at 10,000 Pa and $T = 298$ K. The other experimental conditions are $N_l = 100, N_i = 10, G = 100\%, \Delta t_{gate} = 100$ ns, $E_{den} = 0.04$ Jcm⁻². The delay, t , to obtain lifetime curve for this particular experiment varied as follows: 500 to 3,000 ns, in steps of 500 ns; 5,000 to 100,000 ns in steps of 5,000 ns. Since the t in this example starts at 500 ns, the lifetime curve in this case would be that of phosphorescence. In the case of fluorescence, in general, we start capturing the images from 5 ns.

For illustration, Figure 4.18 shows the sequence of images at three different delays, $t = 500, 10,000,$ and $50,000$ ns. From these images, we notice that at $t = 500$ ns, we get the highest $S_p = 2062$. This is due to the fact that we are at the beginning of the phosphorescence. At $t = 10,000$ ns, we still notice a strong signal, but S_p value decreases to 500. Similarly at $t = 50,000$ ns, S_p value further decreases to 107. In this manner, we can note the peaks of all the Gaussians fitted at different t . Once we have this information, we can generate the lifetime curve based on S_p . For the data given in this example, the lifetime curve is as shown in Figure

4.19. On fitting an decay function to this curve, we can estimate the time constants. Usually an exponential decay fits the curve. A detailed study on fitting exponentials and the corresponding evaluation of time constants at different conditions of pressure for acetone vapour is presented in Chapter 5 (section 5.6.3).

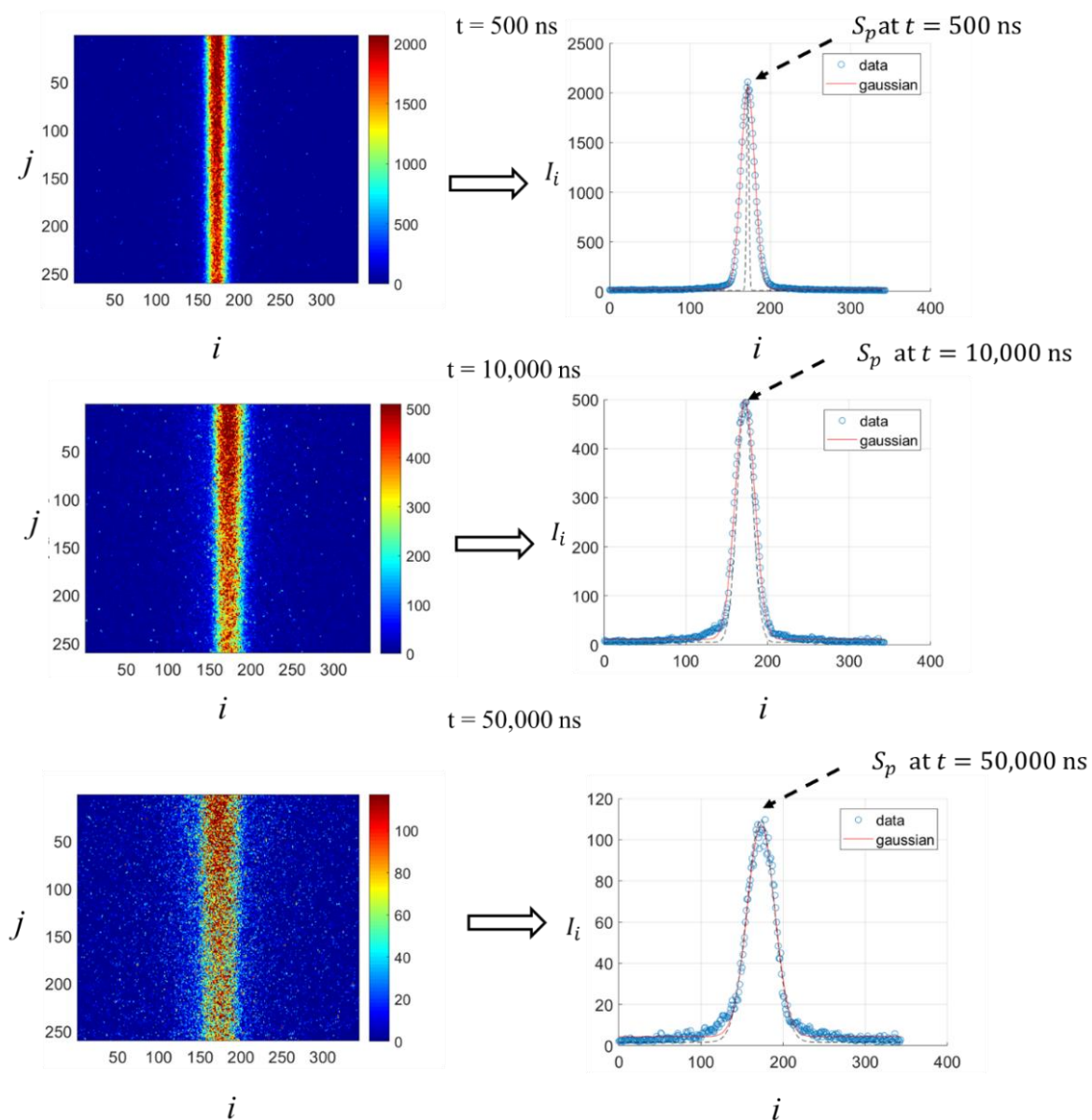


Figure 4.18 Sequence of images at different delays.

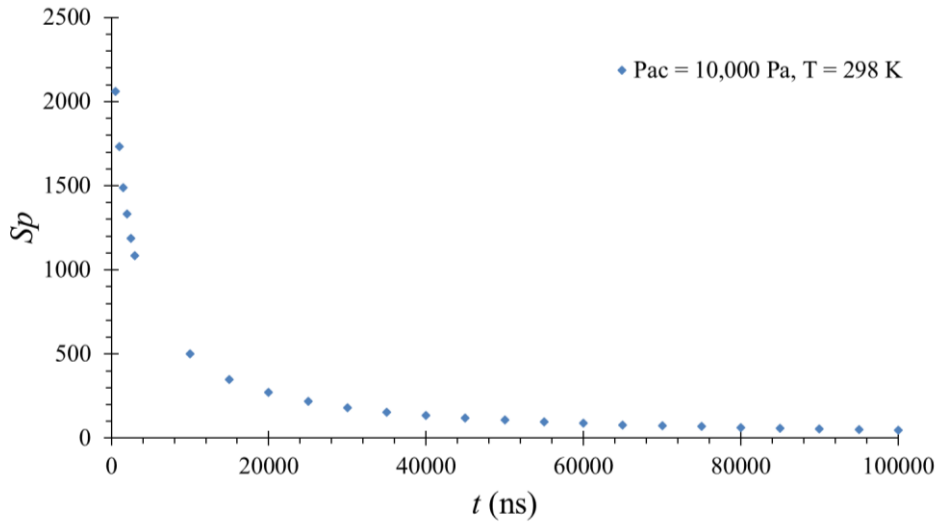


Figure 4.19 Lifetime curve based on S_p for pure acetone vapour

For the data S_p , the normalised values are represented as S_{pn} . Depending on the pressure and energy used in the experiments, different experiments would be having different scale. Therefore, the purpose of normalisation is to homogenise the scale of different experiments, so that it lies between 0 and 1. This is usually done by dividing S_p and S_T at different delays with the highest value on that particular curve, and this would normally be at the lowest delay in that particular curve. To illustrate, as mentioned in the preceding paragraph, for the Figure 4.19, the highest S_p is at 500 ns and is equal to 2062. We can normalise all the values of S_p with this value and plot the lifetime curve with S_{pn} , as shown in Figure 4.20. This information would help us to compare experiments at different conditions of pressure, or experiments performed with experimental configurations.

Similarly, we can plot the value of total number of counts in the experimental image, S_T , as shown in Figure 4.21. This is another manner to analyse the experimental data. But this data are influenced by the presence of background noise, and these aspects are discussed in Section 5.4.1.1, when we study the aspect of background images. We notice from Figure 4.21 that the trend of decay is still exponential, but the scale of the figure is very high ($\sim 10,000$ times higher than the scale of S_p), and this is due the way in which S_T is evaluated. As we sum up all the intensity counts in the entire pixels of the image, this explains the very different scale of S_T .

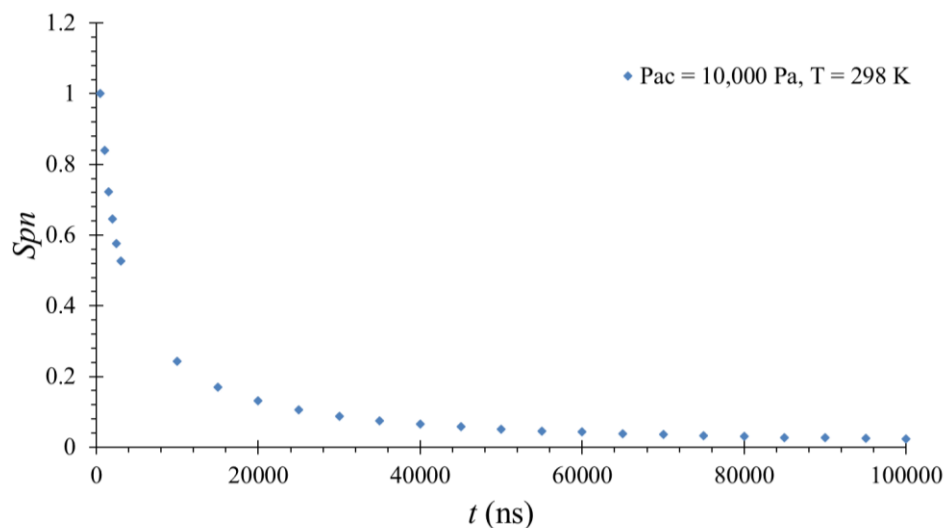


Figure 4.20 Normalised lifetime curve S_{pn} for the data shown in Figure 4.19

In a similar manner, we can normalise the Figure 4.21 with the highest intensity counts for this figure, $S_T = 13630080$ at $t = 500$ ns, and the corresponding normalised values are defined as S_{Tn} . This information is shown in Figure 4.22.

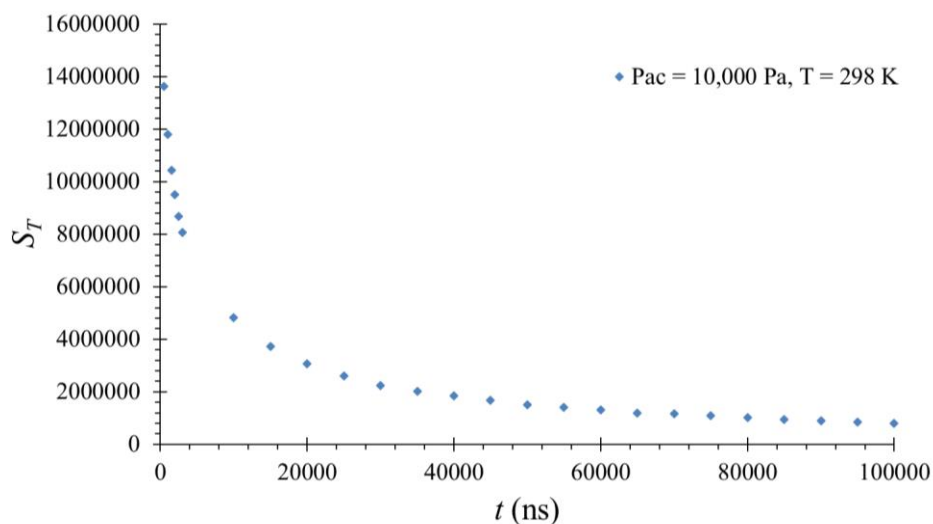


Figure 4.21. Lifetime curve based on S_T for pure acetone vapour

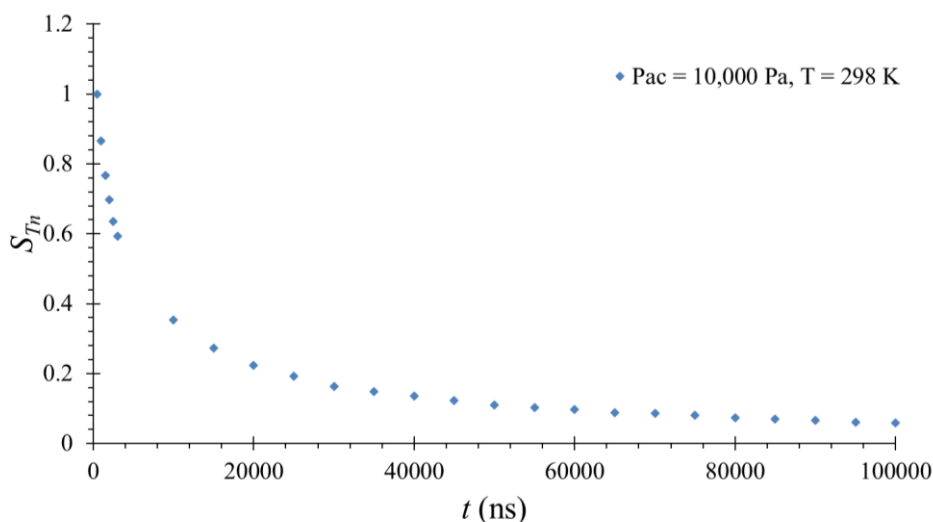


Figure 4.22 Normalised lifetime curve (S_{Tn}) for the data shown in Figure 4.21

With the availability of new experimental data, improvements were made in the image analysis and other manners to treat the data were developed. The details of these methods will be shown in the next chapter (sections 5.4.2). The main improvement is the following: during the phase of investigation presented in this chapter (at this point in the investigation), we were yet to understand the role of background image (apart from the dark noise image) and subsequent corrections to improve the image processing. However, as demonstrated in later chapters, the additional background image subtraction, though is an improved way to analyse the data, does not significantly alter the results if we do not make those corrections. Therefore, the conclusions drawn from this chapter still hold good.

The Gaussian peaks are further plotted as a function of delay time, generating the lifetime curves presenting in next sections.

4.7 Experiments at room temperature with first experimental chamber

Before presenting the details of the protocol for the experiments, it must be emphasised that it evolved over time, especially based on the gaps in our previous experimental protocols. Analysis of every experimental investigation with subsequent data analysis aided us in improving the manner to generate and analyse the experiments.

The protocol for the experiments from Sections 4.7.1 to 4.7.4 was as follows:

- Vacuuming the experimental chamber;
- Introduction of acetone vapour at required pressure;
- Adjusting the laser to the desired wavelength and energy;
- Noting the laser energy at the front of the chamber before starting the experiment;
- Capturing the images at various delays (t), gain (G) and gate (Δt_{IRO});
- Vacuuming and repeating the experiments.

4.7.1 Experiments with acetone vapour at 266 nm at room temperature

These particular experiments were carried out at 266 nm with a Nd:YAG laser. The objective of these experiments was to understand the intensity of signal (S_p) at different t . By analysing the results, we can comment on the maximum t until which we can get an exploitable phosphorescence signal with acetone vapour excited at 266 nm. The signal can be said be exploitable if S_p is not close to zero or if S_T is not just the sum of background noise, i.e. the excited molecules are still phosphorescing at the time instant when the image is being captured. With increase in t , the number of molecules de-exciting decreases, which is reflected in the reduction of S_p and S_T . Therefore, if these values are close to zero, this would imply that almost all the excited molecules (at a particular P , T and λ) have de-excited and we cannot further exploit the signal.

Figure 4.23 shows the time evolution of phosphorescence emission of acetone vapour excited at 266 nm at a laser energy intensity of about 0.08 Jcm^{-2} . The abbreviation ‘ac’ has been used in the legend to refer to acetone vapour (also, in all the subsequent graphs). The figure plots the peak of the Gaussian count value, S_p , obtained for different experimental conditions as a function of delay time t . The experimental were done with pure acetone vapour at room temperature by varying the pressures from 10 to 2.5 kPa.

At $P_{ac} = 10,000 \text{ Pa}$, $S_p = 4320$ at $t = 550 \text{ ns}$, and $S_p = 294$ at $t = 50,000 \text{ ns}$, and the ratio of S_p is ~ 14.6 . This shows that with increasing t , there is a strong reduction in S_p . Also, we expect that with a decreased in P_{ac} , there should be a reduction in S_p . This can be seen from the data at $P_{ac} = 5,000 \text{ Pa}$, shown in Figure 4.23. At $P_{ac} = 5,000 \text{ Pa}$, $S_p = 597$ at $t = 550 \text{ ns}$, and $S_p = 55$ at $t = 50,000 \text{ ns}$, and in this case, the ratio of S_p is ~ 10.8 . At $P_{ac} = 2,500 \text{ Pa}$, $S_p = 8.6$ at $t = 50,000 \text{ ns}$, thereafter S_p decreases further and is close to zero at $t = 100,000 \text{ ns}$. The ratio of S_p at $P_{ac} = 10,000$ and $P_{ac} = 2,500$ is ~ 34 . Therefore, compared with higher P_{ac} , S_p for P_{ac}

= 2,500 Pa is very low compared to the other higher pressures, but still exploitable (greater than zero) until 50,000 ns.

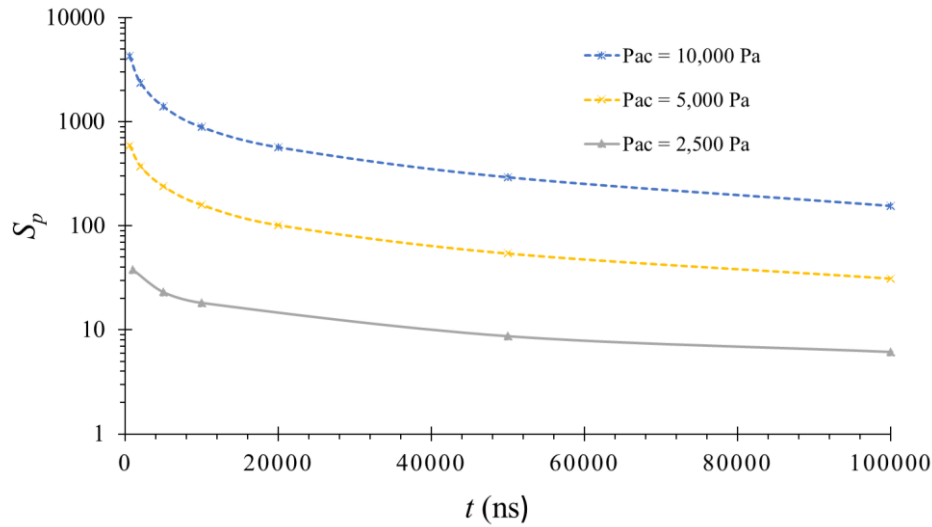


Figure 4.23 Phosphorescence signal of acetone vapour excited at 266 nm at different conditions of pressure

In the literature, the information on the de-excitation behaviour of acetone phosphorescence as a function of different wavelengths is sketchy^{142,145,147}. Therefore, it is interesting to investigate the acetone emission at different wavelengths. Until this point of investigation, we were limited by the Nd:YAG laser which could only provide with a single wavelength (266 nm) in the absorption spectrum of acetone. However, acetone has a wide absorption spectrum and it would be interesting to study the emission behaviour at different wavelengths (see Figure 4.14 for absorption spectrum of acetone). This investigation was done after procurement of the OPO laser and is provided in the subsequent sections.

4.7.2 Variation of excitation wavelengths with acetone vapour at room temperature

In this section, the experiments with acetone vapour at room temperature for different conditions of pressure and excitation wavelength are presented. Later, experiments involving a mixture of tracer and helium were performed (see section 4.7.4). E_{avg} at the entry of the chamber was adjusted to 30 μ J for a beam diameter of 310 nm. This corresponds to $E_{den} =$

0.04 μJcm^{-2} . Table 4-6 presents the experimental conditions at which the experiments were conducted. The absorption and emission were studied at $P = 15$ and 1.5 kPa. The excitation wavelength was varied from 250 to 340 nm in steps of 10 nm .

Table 4-6. Experimental conditions for understanding the influence of wavelength on intensity.

$$N_i = 100, N_t = 10, G = 100\%, \Delta t_{gate} = 100 \text{ ns}, E_{den} = 0.04 \text{ Jcm}^{-2}.$$

Tracer	P_{ac} (Pa)	λ (nm)
Ac	15,000; 1,500	250 to 300, varied in steps of 10; 300, 305, 310; 310 to 340 in steps of 10

Figure 4.24 shows the intensity counts for acetone vapour at $P = 15,000$ Pa as a function of excitation wavelength at different delays. It can be observed from the figure that S_p increases with wavelength, reaches a maximum, and then decreases. Irrespective of the delay, the highest intensity counts is always recorded for excitation wavelengths in the range of 300 to 320 nm.

At, $t = 5,000$ ns, at $\lambda = 300$ nm, $S_p \sim 684.4$; $\lambda = 305$ nm, $S_p \sim 681.9$; $\lambda = 310$ nm, $S_p \sim 711$. We observe that S_p at $\lambda = 300$ nm is slightly higher ($\sim 0.3\%$) than S_p at $\lambda = 310$ nm. This shows that there is a double peak at $t = 5,000$ ns. This difference can be due to the laser energy fluctuation during this experiment or could be a contribution from the background counts. As mentioned in Section 4.6, at this point of investigation we were yet to study the influence of above contributions on the intensity peak. So, we could not make corrections to the data. However, at other t in Figure 4.24 we do not notice this difference in trend. The objective of these experiments was to identify the excitation wavelength at which we were obtaining highest emission counts, and this was at $\lambda = 310$ nm, and S_p at this wavelength was higher ($\sim 4\%$) than $\lambda = 300$ nm and $\lambda = 305$ nm.

Figure 4.25 shows the same information as that of Figure 4.24 by normalising the data with highest intensity counts obtained for every delay. From this, it can be understood that irrespective of the delay time, the highest normalised intensity, S_{pn} , is also around 310 nm.

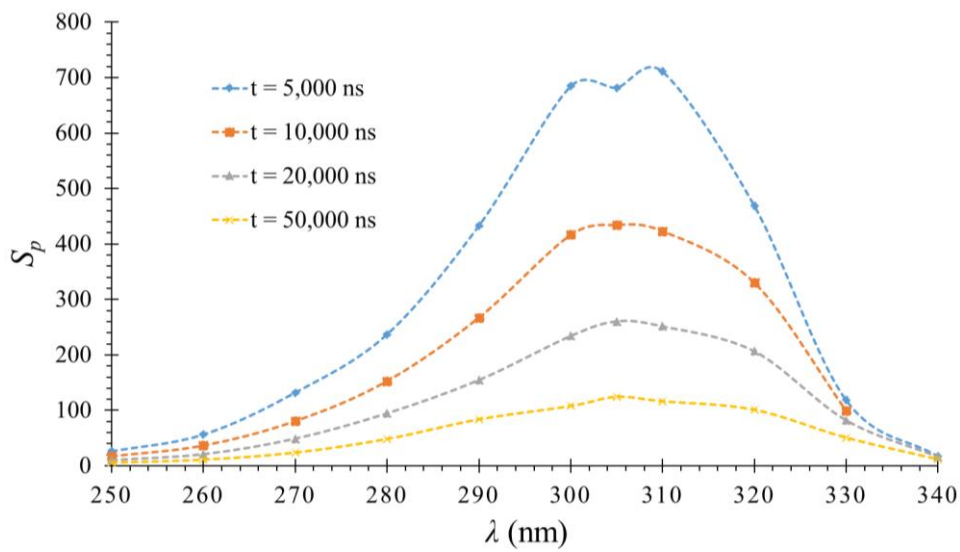


Figure 4.24 Phosphorescence of acetone vapour at $P_{ac} = 15$ kPa and room temperature at different delays by varying the excitation wavelengths.

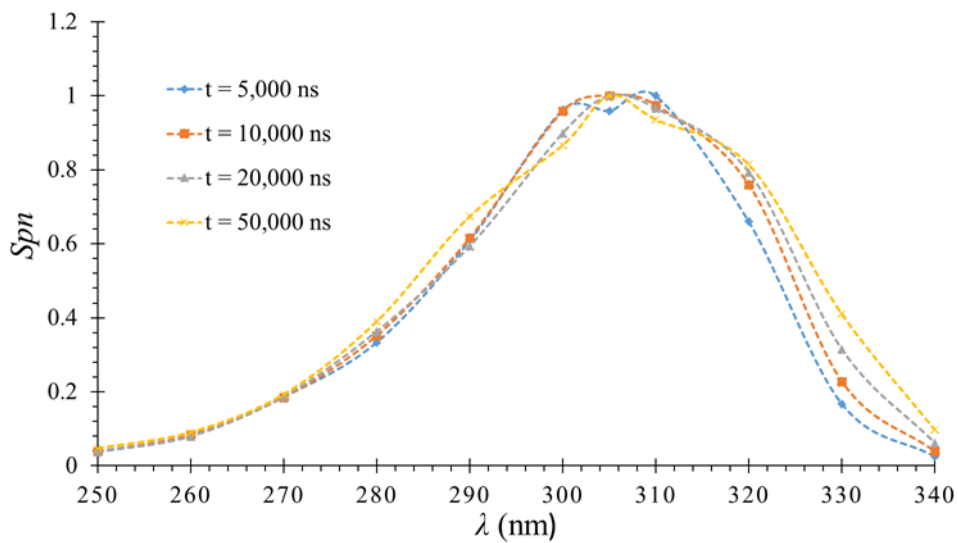


Figure 4.25 Same information as in Figure 4.24 after normalising (S_{pn}) every point of a particular delay curve with the highest intensity on the corresponding curve.

Similar behaviour was observed at $P = 1,500$ Pa, as can be seen from Figure 4.26. Figure 4.27 shows the same information as that of Figure 4.26 by normalising the data with highest intensity counts obtained for every delay

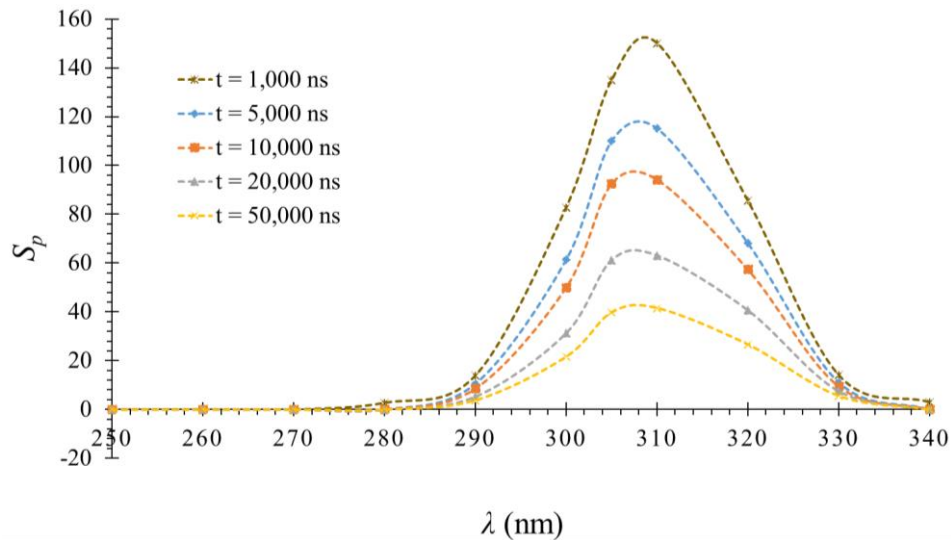


Figure 4.26 Phosphorescence of acetone vapour at $P_{ac} = 1.5$ kPa and room temperature at different delays by varying the excitation wavelengths.

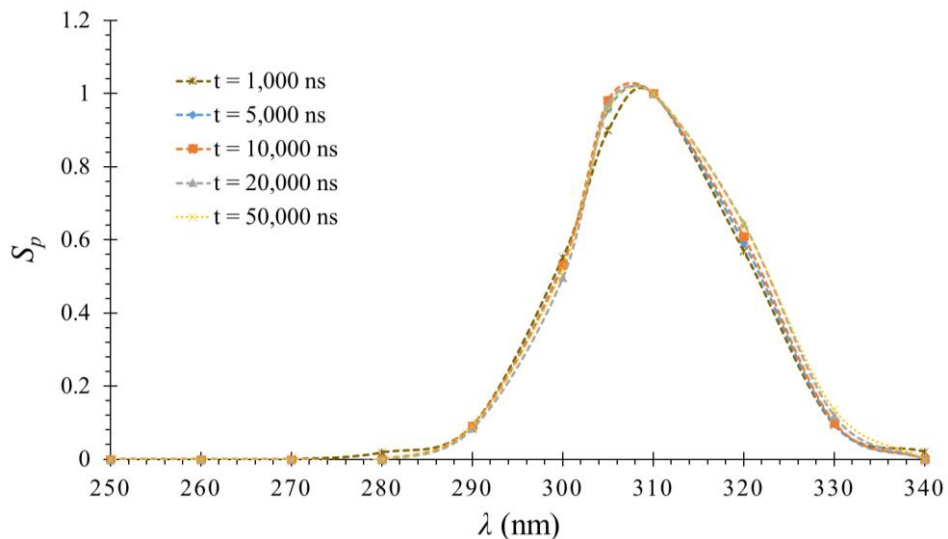


Figure 4.27 Same information as in Figure 4.26 after normalising every point of a particular delay curve with the highest intensity on the corresponding curve.

From Table 4-6, we have the information about the intensity values at two different pressures of acetone vapour differing by approximately an order of magnitude. For both these pressures, if we observe the data shown in Figure 4.24 and Figure 4.26, we note that irrespective of t , the highest emission intensity seems to be at 310 nm. Since the volume in our system is constant, and the temperature is constant at room temperature, changing pressure in the system would be equivalent to changing n in the system. From these observations, we have to estimate

if highest S_p at 310 nm would hold true for conditions of pressure other than those experimented. One approach would be to experiment further at different conditions, and the other approach can be based on the emission intensity dependency shown in Equation (3.6), shown below:

$$S = \eta_p \frac{I_{in}\sigma_{abs}(\lambda, T)}{E_{ph}(\lambda)} n\phi(\lambda, T, P)$$

In our case, the temperature is remaining constant. We have to evaluate how this equation would behave at different pressures at a particular wavelength. The P in the above equation can be written in terms of n from Ideal gas equation, $P = nK_B T$. Since K_B and T are constants, the above equation can also be written as

$$S = \eta_p \frac{I_{in}\sigma_{abs}(\lambda, T)}{E_{ph}(\lambda)} n\phi(\lambda, T, n) \quad (4.1)$$

S_p represents the peak of the Gaussian and S is the photoluminescence signal, and these two values would be proportional to each other. In our case, also the optics remain the same, so η_p does not change. When we were performing experiments at a particular wavelength and changing the pressure (or number density) in the system, we were maintaining energy density of laser beam I_{in} as constant. Similarly, $E_{ph}(\lambda)$ would remain constant at same wavelength. σ_{abs} is independent of pressure or number density in the system (see Section 5.3). Therefore, the above equation further reduces to

$$S_p = C(\lambda)\sigma_{abs}(\lambda, T)n\phi(\lambda, T, n) \quad (4.2)$$

In the above equation, $C(\lambda)$ is a constant. The behaviour of S_p as a function of λ for different t is shown in Figure 4.24 and Figure 4.26. If we have information of $S_p, C(\lambda), \sigma_{abs}(\lambda, T),$ and n we can evaluate $\phi(\lambda, T, n)$. At a particular λ , for two different number densities, n_1 and n_2 , the above equation can be written as

$$\frac{S_{p2}}{S_{p1}} = \frac{n_2\phi(\lambda, T, n_2)}{n_1\phi(\lambda, T, n_1)} \quad (4.3)$$

For the sake of discussion, assume $n_2 > n_1$. Now we have observe the behaviour of ratio $\frac{\phi(\lambda, T, n_2)}{\phi(\lambda, T, n_1)}$. If we recall the definition of ϕ From Equation (3.7), we can note that ϕ represents the number of photons emitted to the number of photons absorbed. In our assumption, since $n_2 > n_1$, we can infer that number of molecules absorbing photons would be higher in case of n_2 than the case with n_1 . This higher absorption of photons would translate into higher number

of emitted photons. Therefore, for $n_2 > n_1$, the ratio $\frac{\phi(\lambda, T, n_2)}{\phi(\lambda, T, n_1)}$ has to be greater than if λ and T remains constant. This would imply that S_{p2} has to be greater than S_{p1} .

From Equation (4.2), we notice that with a change in n and λ , S_p value changes. For different P_{ac} (or n), the variation of S_p with λ is presented in Figure 4.24 and Figure 4.26. For any particular λ , by changing n , we have shown in the preceding paragraph that S_p has to change. With increasing n , the value of S_p has to increase, for every λ . If we consider n to lie between the two extremities shown in Figure 4.24 and Figure 4.26, then we can see that for any particular λ , the S_p value is an extremity. Therefore, for any other value of n , S_p values would lie between these extremities. And, the trend of S_p as a function of λ for any particular n should be similar to that of Figure 4.24 and Figure 4.26.

From this discussion, we can infer that the highest S_p values obtained from these two curves should be representative of the highest S_p that can be obtained at any other value of n , which was not experimented. There is no particular reason for choosing the n values in Figure 4.24 and Figure 4.26 as the extremities, they could be different from those experimented in Table 4-6, but still the arguments presented will hold. For the curves shown in Figure 4.24 and Figure 4.26, the peaks are at 310 nm. Therefore, it can be concluded that 310 nm seems to be the optimal wavelength to achieve the most intense signal at any condition of pressure in the system.

4.7.3 Variation of excitation wavelengths with diacetyl vapour at room temperature

After studying acetone vapour, we shifted our attention towards another tracer molecule, diacetyl. Due to limitations of the OPO laser employed in this study, which cannot provide wavelengths in the range of 355 nm to 410 nm, the experiments were carried out with an excitation wavelength varying from 410 to 470 nm, in steps of 10 nm. The average energy and recording parameters for these images were similar to that of previous investigation on acetone and are as follows: $N_l = 100$, $N_i = 10$, $G = 100\%$, $\Delta t_{gate} = 100 \text{ ns}$, $E_{den} = 0.04 \text{ Jcm}^{-2}$.

Table 4-7 Experiments on diacetyl vapour

$$N_l = 100, N_i = 10, G = 100\%, \Delta t_{gate} = 100 \text{ ns}, E_{den} = 0.04 \text{ Jcm}^{-2}.$$

Tracer	P_{di} (Pa)	λ (nm)
<i>di</i>	5,000	410 to 470, varied in steps of 10

Table 4-8. Values of S_p at $\lambda = 410$ and 420 nm for $P_{di} = 5,000$ Pa

λ (nm)	S_p at $t = 5,000$ ns	S_p at $t = 10,000$ ns	S_p at $t = 25,000$ ns
410	1274.2	836.2	474.9
420	1205	830.5	495.7

Figure 4.28 shows the experimental data generated for pure diacetyl vapour at 5,000 Pa. average energy of $30 \mu\text{J}$, beam diameter of 310 nm, implying an average energy density. It can be noted from the Figure 4.28 that, S_p in general decreases with increases with increase of λ from 410 to 470 nm. However, this behaviour of S_p is not the same at $t = 25,000$ ns. Therefore, it would be interesting to note the variation of S_p so as to choose λ which provides highest S_p . Table 4-8 shows the values of S_p for $P_{di} = 5,000$ Pa at $\lambda = 410$ and 420 nm. It can be noticed from this table that at $t = 5,000$ and $10,000$ ns, S_p is higher at $\lambda = 410$ nm compared to $\lambda = 420$ nm. Especially at $t = 5,000$ ns, this difference in S_p is 70 counts. At $t = 10,000$, S_p values are rather close, and at $t = 25,000$ ns, S_p at 420 nm is higher than the value of 410 nm by about 20 counts.

In order to choose the excitation wavelength, we can put forth the argument that with increase in t , there is a reduction in the emission intensity due to the reduction in the number of molecules de-exciting with time, and also there is a diffusion of the tagged molecules with time. Also, the images were not corrected by the subtraction of a background image. In other words, with increase in t , the signal of emitted molecules becomes appreciable with that of the background noise. All these factors would influence the fitted Gaussian from which the peak S_p is extracted. These factors are not pronounced at lower t , as the molecules are still strongly emitting and do not have sufficient time to undergo strong diffusion. Taking this factors into consideration, we can make a choice of λ at which diacetyl provides a strong emission signal. Out of the different t studied, the strongest signal will be at $t = 5,000$ ns, and here the highest

S_p is at 410 nm. Therefore, we can choose this value of λ as the optimal wavelength of excitation for diacetyl vapour in the future experiments.

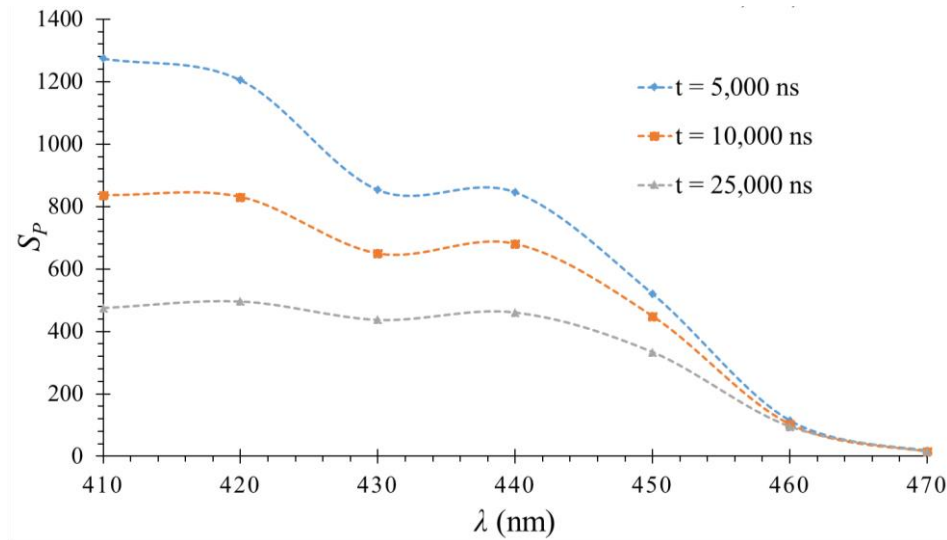


Figure 4.28 Phosphorescence of diacetyl vapour at $P_{di} = 5,000$ Pa for different delays by varying the varying the excitation wavelength

4.7.4 Excitation at different wavelengths with mixture at room temperature

The investigations carried out in sections 4.7.1 to 4.7.3 were on pure acetone and diacetyl vapours. However, many applications of this technique will involve situations in which the interest will be to investigate gas flows seeded with tracer molecules. Therefore, it is imperative to study the behaviour of seeded tracer molecule in a carrier gas. We then carried out experiments by choosing acetone/diacetyl as the tracer molecule and helium as the carrier gas. The experimental conditions are shown in Table 4-10.

The partial pressures of tracers, i.e. acetone vapour and diacetyl vapours, were 50 and 20 Pa, respectively. The tracers are introduced in the chamber at these pressures, thereafter, the tracer valve is closed. The carrier gas (helium, in this case) is introduced by turning on the carrier gas valve, and the carrier gas is introduced in the chamber until the total pressure reaches the intended value. In this way, we evaluate the partial pressure of acetone/ diacetyl and the partial pressure of carrier gas. These values are at least two orders of magnitude lower than the values in the previous sections.

For the conditions shown in Table 4-10, we can evaluate the Knudsen number assuming these conditions would exist in a channel. The mean free path (λ_m) for a two species gas mixture can be estimated as³⁸:

$$\lambda_m = \sum_{i=1}^2 \left(\frac{X_i}{\sum_{j=1}^2 n_j \pi d_{ij}^2 \sqrt{\frac{m_i + m_j}{m_j}}} \right) \quad (4.4)$$

Where X is the mole fraction, evaluated as n_i/n ; n_i is the number density of species i and n is the total number density of the species; m is the molecular mass; $d_{ij}^2 = \frac{1}{2}(d_i + d_j)$, d is the molecular diameter.

From ideal gas equation (in terms of Boltzmann constant), we have, $P = nK_B T$. In a two-gas mixture, the total pressure in the system will be equal to sum of partial pressure of tracer and helium.

$$P = P_{tr} + P_{He} = n_{tr} K_B T + n_{He} K_B T \quad (4.5)$$

Since we know the partial pressures of tracer and helium, we can evaluate the number density of tracer and helium. In our case, we have tracer as acetone (or diacetyl) and the carrier gas as helium gas, and the corresponding diameter are provided in Table 4-9.

Table 4-9 Diameter and molecular mass of acetone, diacetyl, and helium

Molecule	$d (\times 10^{-12} \text{ m})$	$m \text{ (g/mol)}$
Acetone	730	58.08
Diacetyl	590	86.09
Helium	233	4.00

From Equation (2.7), we can evaluate Knudsen number based on a channel having a characteristic dimension of 1 mm. The conditions shown in Table 4-10 would correspond to tracer molar fractions are 5% and 2%, for acetone and diacetyl, respectively. For these conditions, we will obtain Knudsen number in the order of 0.01 corresponding to slip flow regime.

Table 4-10. Experiments on acetone and diacetyl vapour in the presence of helium gas

$$N_l = 500, N_i = 10, G = 100\%, \Delta t_{gate} = 500 \text{ ns}, E_{den} = 0.08 \mu\text{Jcm}^{-2}$$

P_{tracer} (Pa)	P_{He} (Pa)	P_{total} (Pa)
Acetone, $P_{ac} = 50$	950	1,000
Diacetyl, $P_{di} = 20$	970	1,000

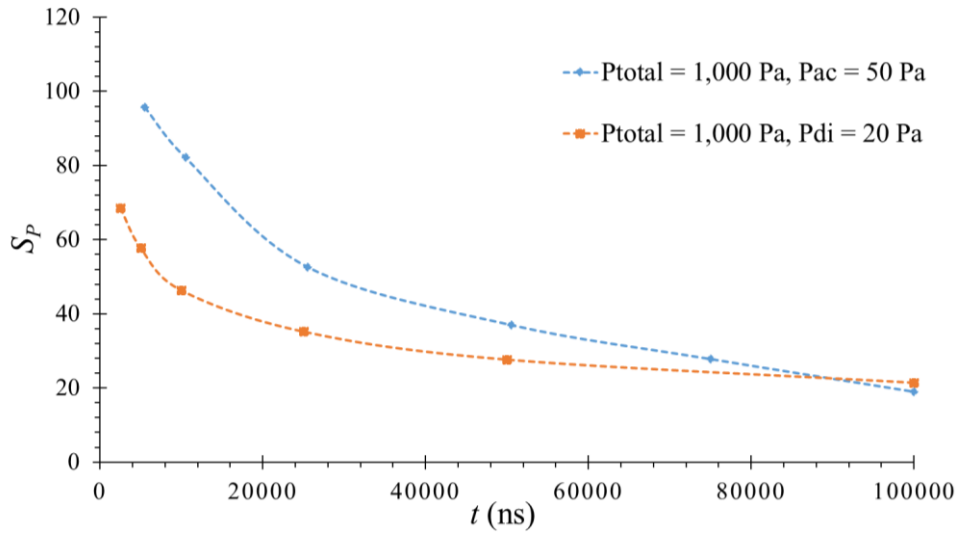


Figure 4.29. Phosphorescence of acetone and diacetyl vapour in helium mixtures for the conditions shown in Table 4-10

The purpose of these experiments was to understand if we can achieve an exploitable signal even at such lower concentrations of tracers, given that we now possess the information on the best wavelengths for intensity. Due to the low concentration of tracers, there was a requirement to change some of the image acquisition parameters for the experiments shown in Table 4.3 as follows: increase the number of laser pulses per image, the gate, and the intensity of laser energy. Therefore, the following were the experimental parameters at which the images were acquired: $N_l = 500, N_i = 10, G = 100\%, \Delta t_{gate} = 500 \text{ ns}, E_{avg} = 60 \mu\text{J}, D_l$ of 310 nm, implying $E_{den} = 0.08 \text{ Jcm}^{-2}$. Figure 4.29 shows the lifetime curves for the experimental conditions presented in Table 4-10. The intensity obtained from diacetyl and helium mixtures are rather close, even though the pressure of diacetyl was ~ 2.5 times lower than that of acetone. To further investigate these observations, we studied the de-excitation characteristics of

diacetyl-helium mixture at the conditions shown in Table 4-11, for lower total pressure of 500 Pa, but for higher tracer concentrations.

Table 4-11. Diacetyl – helium mixture

$$N_l = 500, N_i = 10, G = 100\%, \Delta t_{gate} = 500 \text{ ns}, E_{den} = 0.08 \text{ Jcm}^{-2}.$$

P_{di} (Pa)	P_{He} (Pa)	P_{total} (Pa)
50	450	500
100	400	500

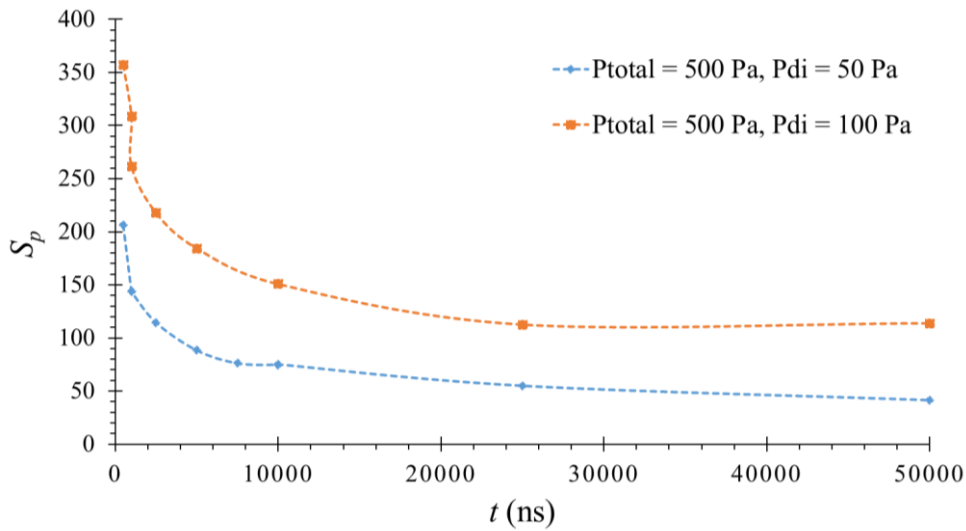


Figure 4.30. Phosphorescence of diacetyl vapour in Helium mixture for the conditions shown in Table 4-11

The image acquisition parameters for these experiments were: $N_l = 100, N_i = 10, G = 100 \%, \Delta t_{gate} = 500 \text{ ns}, E_{den} = 0.08 \text{ Jcm}^{-2}$. The results are shown in Figure 4.30, where the partial pressure of diacetyl vapour is equal to and twice that of acetone vapour in Figure 4.19. Even though the number of laser pulses employed were 5 times lower for the curves of Figure 4.31, we can observe that for the same partial pressure of tracer, S_p for diacetyl (Figure 4.30) is almost twice the value for acetone (Figure 4.29). Evidently, on increasing the number of laser pulses, we could enhance the phosphorescence intensity.

In this section, details on the experimental campaign to obtain the optimal excitation wavelength for acetone and diacetyl vapour have been presented. Further analysis on this experimental data, in terms of extracting diffusion coefficients to propose corrections to the

velocity profile, can be carried out. However, the studies on diffusion coefficients are not of immediate concern to this thesis. To summarise, we have shown the following: if the objective of an experiment is to achieve the highest possible exploitable signal, i.e., highest number of intensity counts at any delay time, the appropriate choice of excitation wavelengths are 310 nm and 410 nm for acetone and diacetyl, respectively. These observations can imply that in applications where one is restricted to have lower concentration of the tracer molecule, diacetyl may be a more suitable choice.

Having said that, there are safety concerns with diacetyl vapour. Prolonged exposure to diacetyl vapour can result in permanent, severe, and potentially lethal lung diseases¹⁴⁹. Since there was no dedicated exit for diacetyl vapour after vacuuming from the chamber, the diacetyl vapour was present in the experimental room. However, masks were worn to reduce exposure during our experiments. Since the experimental investigation would have been carried out for three years, and every experiment will involve at least few hours of handling diacetyl, this prolonged exposure might have some long-term implications on the health¹⁴⁴. Therefore, also considering these aspects, we chose to work with acetone, which is safer to handle than diacetyl.

4.8 Experiments at higher temperature in the heated chamber

In this section, we will present the experiments carried out on acetone and diacetyl vapour by heating the experimental chamber. Before starting the experimentation with heating the chamber, it was necessary to understand the temperature limits of various materials of the experimental chamber. This can be read from Table 4-5 presented in section 4.4, and we observe that the chamber is made up of different materials with varying degrees of temperature limits. Certain materials, such as Sapphire, could be subjected upto 2073 K. However, we would be limited by the material with lowest temperature limit, which turned out to be pressure gauges, which can withstand maximum of 383 K.

4.8.1 Heating of experimental chamber

The next step was to find suitable elements to heat the chamber. The first chamber was heated with simple surface spot heating elements as shown in Figure 4.31. They were provided by OMEGA company and were compact, easy to arrange via flange and could be subjected to a maximum Heater Temperature of 443 K. The temperature distribution on the surface of the chamber was measured by thermocouples placed at different locations. One of the thermocouple was placed on the front top end of the chamber, and the other was placed at the

bottom back end of the chamber. Also, few infrared camera measurements were carried to observe the temperature distribution on the chamber (see Figure 4.32). The infrared camera was not calibrated and these images were just used to assess if the heat is well distributed and leads to a uniform temperature of the chamber, and to note the distribution of temperature with time. From the infrared image, we can notice that there is an increase in the temperature of the chamber on heating, and the temperature distribution of the chamber is uniform.

Initial experiments were carried out on heating and noting the power requirements for experimental chamber. The intention of these experiments was to optimize the power input to the heating elements and to have an estimate regarding the time required to obtain a steady state with uniform temperature distribution of the chamber.

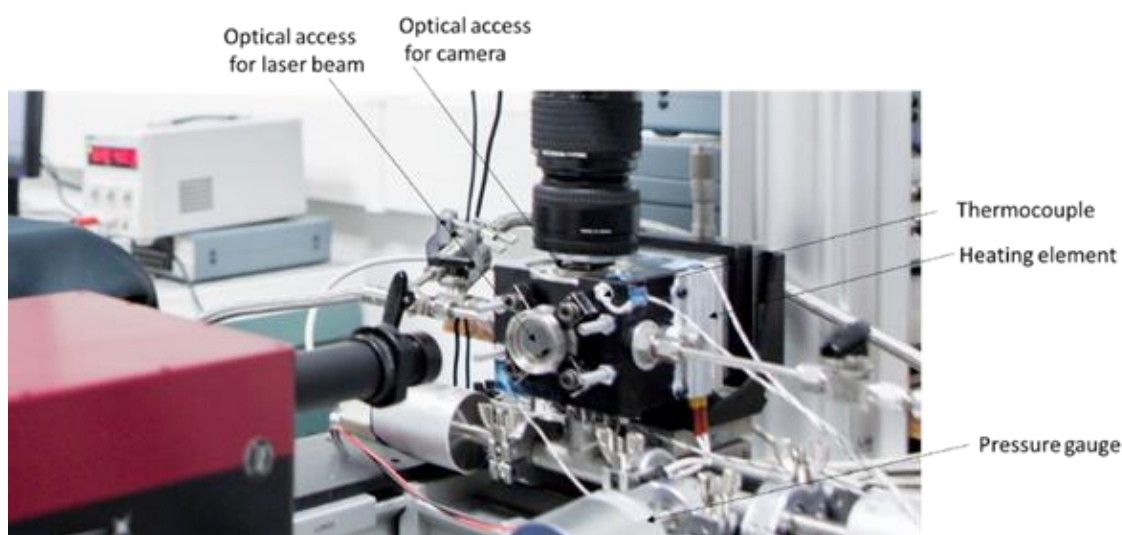


Figure 4.31. Modified experimental chamber for temperature

The heated chamber was tested and could reach a maximum temperature of about 368 K. During the experiments, it was observed that depending on the temperature required, the time to obtain steady state varied. For instance, temperature of the order of 310 K can be reached in about 10 min. However, to reach a temperature about 323 K, it took about an hour. It is to be noted that the experiments were not carried out immediately after the chamber reached the specified temperature. Instead, about 30 min were allowed for observing the variation of temperature and ensuring that the steady state was reached, prior to conducting experiments. Table 4-12 shows some of the details of the experiments carried out.

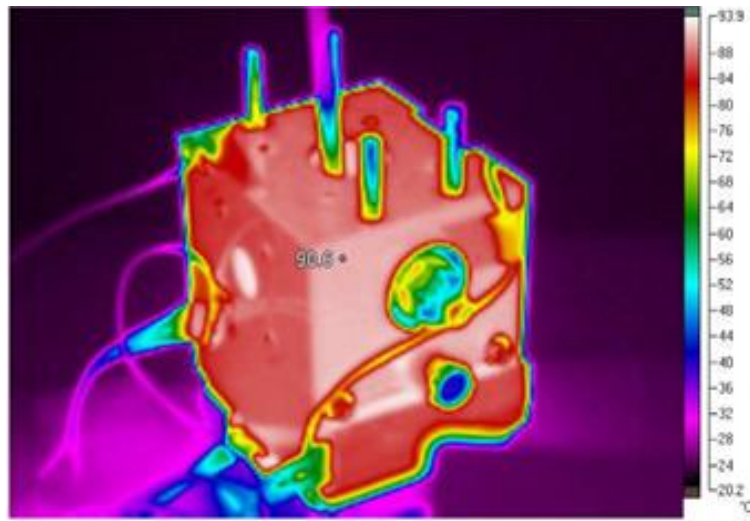


Figure 4.32. Infrared camera image of the temperature distribution on the heated chamber.

Table 4-12. Current – voltage settings to obtain desired temperature on the chamber.

V_o (Volts)	A (amps)	T (K)
4.22	2.56	309
4.57	2.84	314
5.83	3.64	323
6.35	4.02	329
8.41	5.10	343

The experiments discussed in the previous paragraph were performed before the assemblage of the chamber in the setup. On integrating the chamber with the other optical elements, another factor related to the distance between the optical lens and the heated chamber had to be considered. As it can be noted from Figure 4.31, this distance was about 10 mm (exact distance could not be measured, because of the physical constraint of accessibility). The temperature of the lens was being monitored with a thermocouple when the chamber was being heated. At 331 K, we could notice that the temperature of the lens was about 315 K, which is slightly above the recommended temperature to operate the lens (313K). Therefore, even though it was possible to heat the chamber to ~ 373 K, the aforementioned physical constraint

limited our ability to carry out experiments at this temperature. The maximum temperature to which the chamber was heated and the experiments were carried was at 331 K.

In the following sections, we present the experiments performed to study the dependency of intensity and lifetime with temperature. These experiments are preliminary in nature and due to some difficulties encountered during this investigation (enumerated in later parts of the section), it was not entirely possible to come up with reliable conclusions. This necessitated the design of an improved experimental chamber for temperature measurements, which will be discussed in the Chapter 5.

4.8.2 Experimental protocol

The experimental protocol was the following:

For experiments at room temperature:

- (a) Vacuuming the experimental chamber;
- (b) Introduction of acetone or diacetyl vapour at room temperature at required pressure;
- (c) Adjusting the laser to the desired wavelength and energy. The average laser energy was maintained at 30 μJ with a beam diameter of around 310 nm for the experiments with acetone and 410 nm for experiments with diacetyl, unless otherwise stated explicitly;
- (d) Noting the laser energy at the front of the chamber before starting the experiment;
- (e) Capturing the images at various delays, gains and gates;
- (f) Vacuuming (and repeating the experiments if needed).

For experiments at heated temperature:

(g) If experiment is planned with heating, turn on the power supply and heat the experimental chamber;

(h) Introduction of acetone or diacetyl vapour (initially at room temperature) at required pressure and waiting for 10 min for the vapour to heat and achieve the desired temperature;

Thereafter, repeat steps from (c) to (f).

Due to the constraints of experimental facilities at the time of performing these experiments, the pressure and temperature were noted manually during these experiments. However, later in the thesis, the necessary hardware required for continuous monitoring of temperature and pressure were procured and the process of recording the temperature and pressure was automated.

4.8.3 Effect of wavelengths on acetone vapour at $P = 15,000$ Pa and $T = 331$ K

In Section 4.7, we had demonstrated that acetone vapour excitation at 310 nm provided phosphorescence with the highest intensity at any delay. These conclusions were based on experiments carried out at room temperature. It should be investigated to see whether these observations hold good even with acetone at higher temperature. Therefore, experiments in the heated chamber with acetone vapour at $T = 331$ K and $P = 15,000$ Pa were performed with excitation wavelengths varying from 250 to 340 nm, in steps of 10 nm. The acquisition parameter were: $N_l = 100, N_i = 10, G = 100 \%$, $\Delta t_{gate} = 100$ ns, $E_{den} = 0.04 \mu\text{Jcm}^{-2}$.

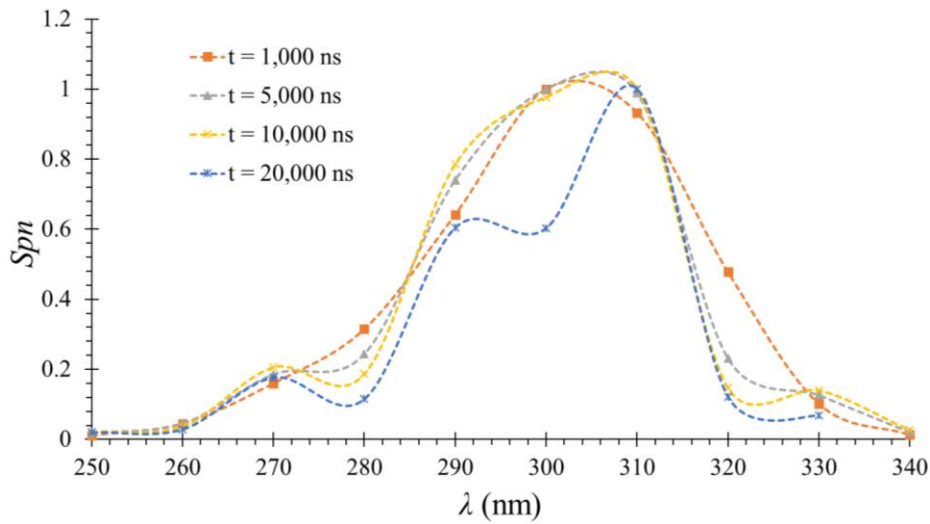


Figure 4.33. S_{pn} shown as a function of time for varying excitation wavelengths at $P_{ac} = 15,000$ Pa and $T = 331$ K

The results of this investigation are shown in Figure 4.33. We notice that the data points are more uniform in the case of the experiments at room temperature for similar condition of pressure (Figure 4.24), whereas for the case of heating, there is a spreading of the data, which is especially pronounced at $t = 20,000$ ns. This can be due to the combined effects of diffusion and laser energy fluctuations in the system. Also, at wavelengths between 250 to 280 nm and 320 to 340 nm, where S_{pn} is pretty low, there is a slight dispersion of the data, which is pronounced for $t > 1,000$ ns. This can arise due to the problems of diffusion combined with the low signal intensities. Therefore, the fitting of Gaussian and extractign the peak S_p is not very accurate and this is reflected in the dispresion of the data. However, at other wavelengths, especially when S_{pn} is high, the data seems to be more uniform. This is a reflection of the

strength of emission intensity. It can be noted from the figure, even with the heated chamber, for different delays, the highest intensity is obtained at an excitaiton wavelength of around 310 nm. Therefore, this wavelength was chosen even for further investigation. We can compare this experimental data with the normalised data at expeirmental data carried out with room temperature at the same pressure (Figure 4.25).

4.8.4 Behaviour of pure acetone vapour excited at 310 nm in the heated chamber

The heating of the chamber was achieved by adjusting the current and voltage values of the power source based on Table 4-12. Depending on the experiment, the temperature of the chamber was varied and experiments were predominantly carried out at 293, 307, 314, and 323 K (with an uncertainty of ~ 1.5 to ~ 3 K). The pressure of pure acetone vapour in the chamber was varied from 1,000 to 15,000 Pa. Table 4-13 shows the details of the experiments. The acquisition parameters were: $N_l = 100, N_i = 10, G = 100 \%, \Delta t_{gate} = 100 \text{ ns}, E_{den} = 0.04 \text{ Jcm}^{-2}$. Regular monitoring of the temperature distribution and pressure variation was carried out manually during experimentation.

Table 4-13. Experimental conditions for pure acetone luminescence analysis

$$N_l = 100, N_i = 10, \quad G = 100 \%, \Delta t_{gate} = 100 \text{ ns}, E_{den} = 0.04 \mu\text{Jcm}^{-2}$$

λ (nm)	P_{ac} (Pa)	T (K)
266	10,000	293; 307; 317; 327
266	15,000	293; 307; 325
310	15,000	293; 307; 325
310	10,000	293; 307; 314
310	5,000	293; 307; 314; 325
310	2,500	293; 307; 314
310	1,000	293; 307; 325

Experimental results for $P_{ac} = 15,000$ and $5,000$ Pa at $\lambda = 310$ nm are shown in Figure 4.34 and Figure 4.36, respectively. In these figures, each point is a representation of the peak S_p of the Gaussian. The graphs at other experimental conditions are presented in the Appendix A. Also, the normalised images are plotted by normalising the intensities at different

delays of the entire curve(s) with the highest value of that corresponding curve(s), which is chosen to be at 500 ns in all our cases. The corresponding images for Figure 4.34 and Figure 4.36 are shown in Figure 4.35 and Figure 4.37.

It can be readily noted from these figures that with decrease in pressure, there is a reduction in the phosphorescence intensity. For example, at 500 ns, for $P_{ac} = 15$ kPa, $S_p \sim 1400$ counts, whereas, for $P_{ac} = 5$ kPa, $S_p \sim 500$ counts. As the volume of chamber is constant for every experiment, the number density decreases with the reduction of pressure in the system, and this reflects in the intensity. During this preliminary investigation, especially at certain delays after 5,000 ns, it appears that there is a difference in the emission intensity for various temperatures, at same conditions of pressure. However, as elaborated in the last section of this chapter, the differences cannot be attributed completely to the temperature effects.

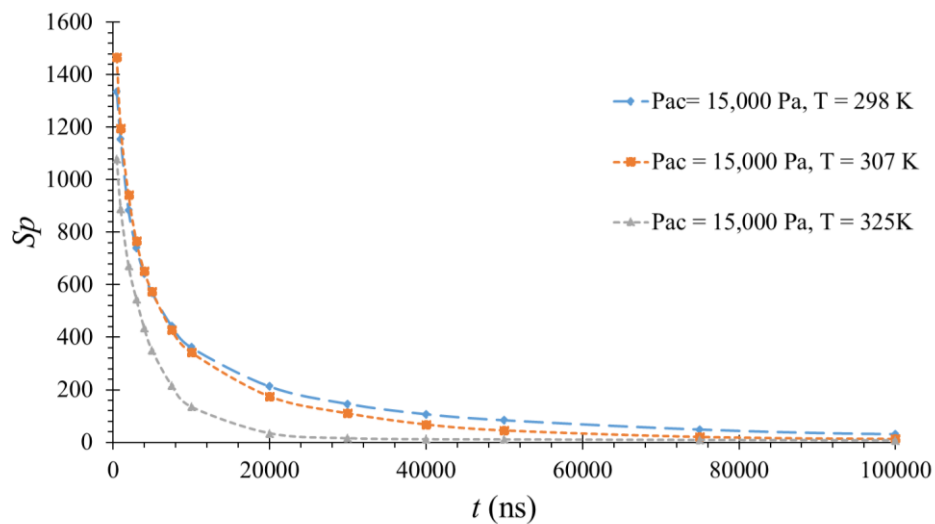


Figure 4.34. Phosphorescence of acetone vapour at $P_{ac} = 15,000$ Pa at different temperatures

Figure 4.34 shows that with increase in temperature, there is a reduction in S_p , and this seems to be more pronounced at $T = 325$ K. At 500 ns, $S_p = 1335$ and 1078 for $T = 298$ and 325 K, respectively. The ratio of these temperatures gives a value of ~ 1.09 . The inverse of it would be the number density ratio, which is ~ 0.91 . The ratio of S_p is 0.80, which is lower than the number density ratio. Therefore, the signal is closer to the number density, but will not be exactly equal because there should be multiplicative factors arising from absorption cross sections and quantum yield (see Section 4.7.2).

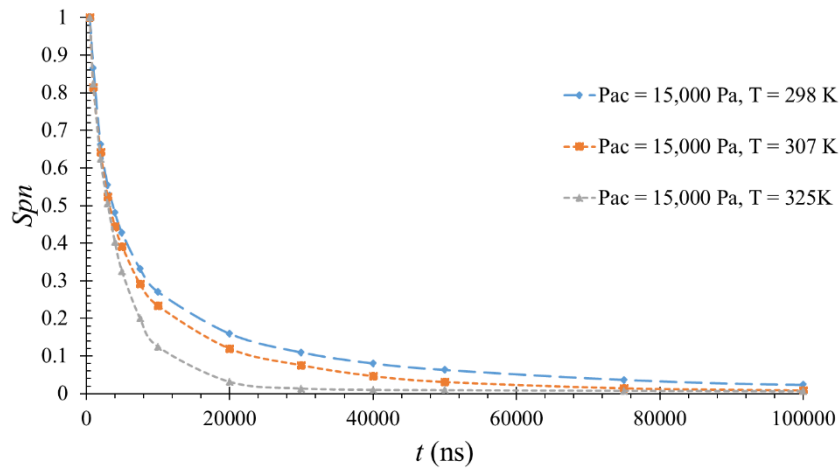


Figure 4.35. Data shown in Figure 4.34 normalised with the intensity value at 500 ns for every curve

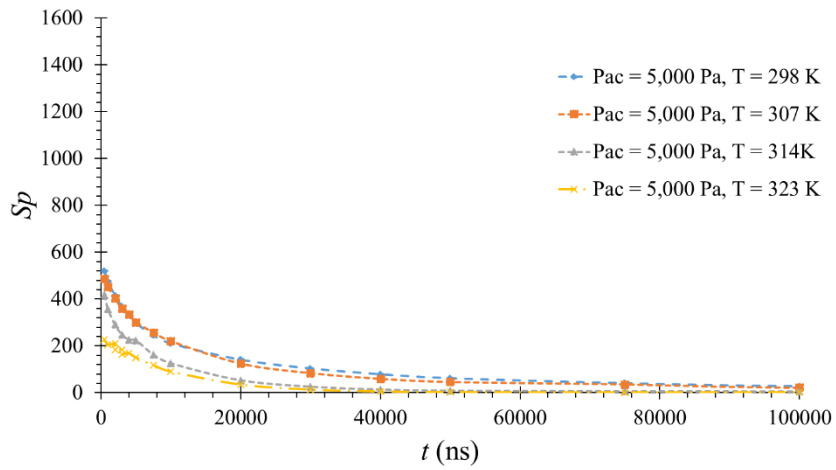


Figure 4.36. Phosphorescence of acetone vapour at $P_{ac} = 5,000$ Pa at different temperatures

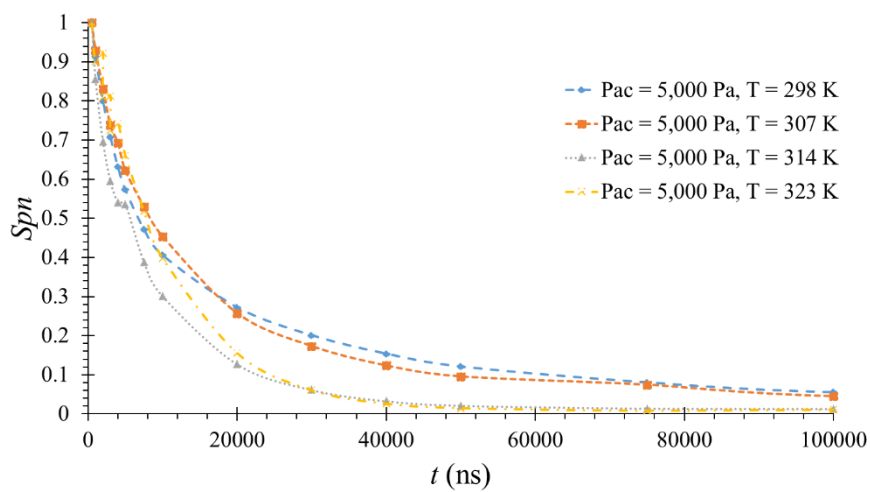


Figure 4.37. Data shown in Figure 4.36 normalised with the intensity value at 500 ns for every curve

For the experiments shown in this section, it is not explicitly possible to isolate the effect of temperature on the intensity signal. When we are heating the acetone vapour, we are maintaining the pressure constant. Therefore, there will be a reduction in the number density with increase in temperature to maintain a same pressure (in a constant volume). Therefore, due to the reduction in the number density, there will be a decrease in the intensity counts. To isolate the effect of temperature itself, we have to maintain the number density constant so that if there is a change in intensity, it can be attributed to temperature. Due to the problems encountered in these experiments, which are detailed in Section 4.9.1, we had to modify the setup and the experiments of isolating the temperature effect by maintaining constant density in Chapter 5 (see section 5.6).

4.8.5 Behaviour of pure diacetyl vapour excited at 410 nm in the heated chamber

In addition to acetone vapour, pure diacetyl vapour was studied for the conditions shown in Table 4-14 for an excitation wavelength $\lambda = 410$ nm. The excitation wavelength is chosen based on the experiments of section 4.7.3. Figure 4.38 shows the results at $P_{di} = 1,750$ Pa. In this figure, experimental conditions at $T = 298$ and 323 K are presented. The observation made in Sections 4.7.3 and 4.7.4 regarding the higher intensity signal of diacetyl vapour compared to the acetone vapour is also noticed here. In section 4.7.4, the experiments were done with mixture of acetone-helium, and diacetyl-helium. In this case, we noticed that S_p value for diacetyl was closer to acetone case, even though the pressure of diacetyl was ~ 2.5 times lower than that of acetone.

Table 4-14. Experimental conditions for pure diacetyl phosphorescence analysis.

$$N_l = 100, N_i = 10, G = 100\%, \Delta t_{gate} = 100 \text{ ns}, E_{den} = 0.04 \text{ Jcm}^{-2}, \lambda = 410 \text{ nm}$$

λ (nm)	P_{di} (Pa)	T (K)
410	4,000	298; 323
410	1,750	298; 323

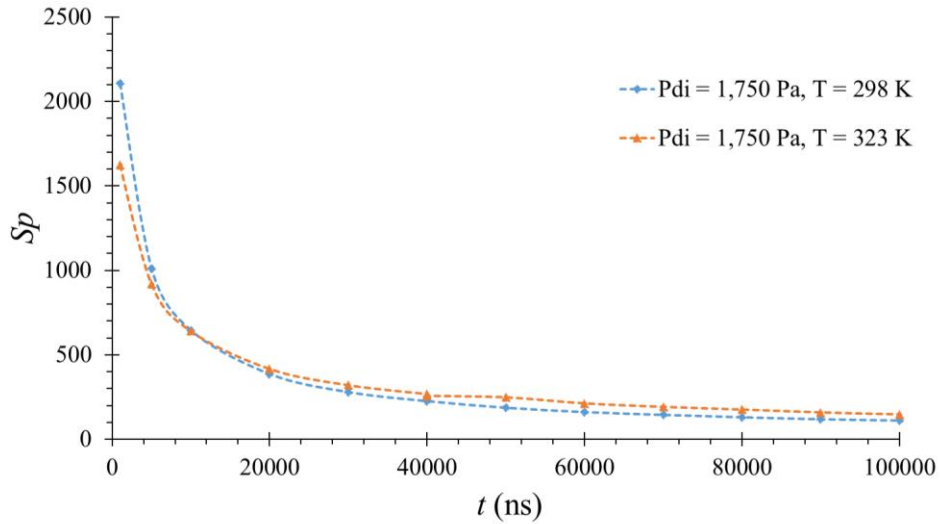


Figure 4.38. Phosphorescence of pure diacetyl vapour at $P_{di} = 1,750$ Pa and at different temperatures

In this section, S_p values obtained for $P_{di} = 1,750$ Pa, are closer to the case of acetone vapour at $P_{ac} = 15,000$ Pa (see section 4.8.3). In other words, similar signal intensity is observed even though the pressure of diacetyl is ~ 8.5 times lower than that of acetone. In section 4.7.4, the experiments were conducted with a mixture, whereas, in this section, the experiments are conducted with pure diacetyl vapour. Therefore, there is a possibility that the de-excitation phenomenon of the molecules in the gas-mixture case was influenced by the collisional interaction of the tracers with that of helium molecules. For the experiments with pure tracer (either diacetyl and acetone), there are collisions only between the molecules of the same species (due to absence of carrier gas). Therefore, we seem to obtain similar S_p with pure acetone and pure diacetyl, even though the pressure of pure diacetyl is almost three lower than the case in which there is a mixture of diacetyl and helium.

This observation will have some implications in the experiments in which we would require to evaluate the temperature or pressure of the carrier gas with tracer gas. Because there is an influence on the signal decay with the presence of carrier gas in the system. This also leads to the fact that it is slightly difficult to perform experiments with gas mixtures as the signal can be influenced not only the tracer, but also due to the interaction with the tracer and the carrier gas molecules.

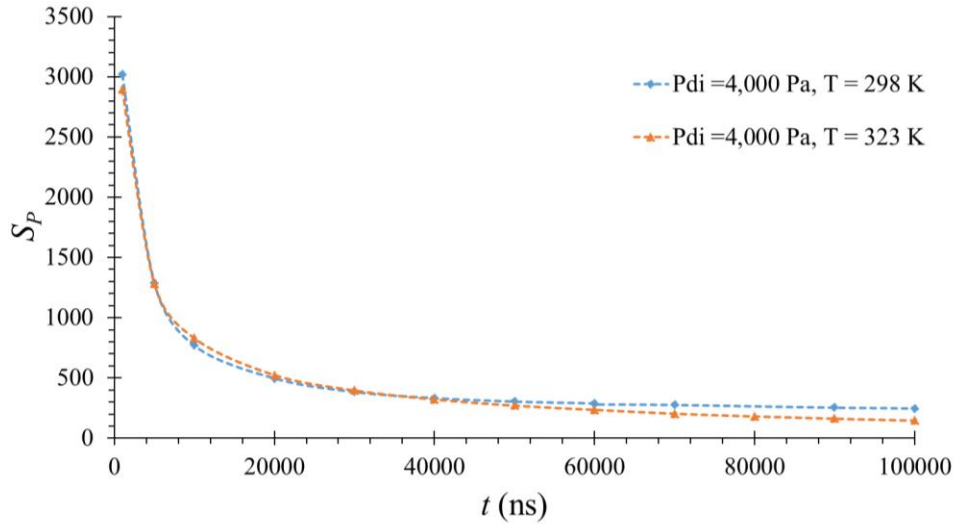


Figure 4.39. Phosphorescence of pure diacetyl vapour at $P_{di} = 4,000$ Pa and at different temperatures

From Figure 4.38, we can compare the values of S_p for $T = 298$ and 323 K. At $t = 1,000$ ns, we observe that S_p at $T = 323$ K is ~ 1624 and is lower than that of $T = 298$ K, where $S_p \sim 2107$. This difference is ~ 480 counts between the heated and the unheated case. This might give the impression that there is a strong difference between the heating and unheated case. However, we find that for both these cases, especially from $t = 5,000$ to $100,000$ ns, we find that S_p values are very close to each other. Therefore, the difference in S_p at $t = 1,000$ ns can be due to the fluctuations in laser energy caused during the capturing of images. At this point of investigation, we were not able to incorporate corrections for the laser energy. Later, in section 4.10 we did a detailed study to investigate this point. However, at this stage of investigation, we carried out another experiment shown in Figure 4.39 at $P_{di} = 4,000$ Pa. As mentioned in section 4.7.4, there are health risks associated with diacetyl, so we sought to generate experimental data at a different condition of pressure. Therefore, we chose to not repeat the experiment at the same pressure of $P_{di} = 1,750$ Pa. In this figure, at $t = 1,000$ ns, we notice that $S_p \sim 3020$ and 2900 , for the cases at $T = 298$ and 323 K, respectively. Here, we can notice that these values of S_p are close to each other and have a difference of only ~ 120 counts. Therefore, we can notice that there seems to be no strong dependency of S_p for the conditions investigated in Table 4-14.

4.9 Repeatability of the experimental data

The validity of any experiment is based on the ability of the data to be reproducible and repeatable under similar experimental conditions. Therefore, experiments were carried out to test the repeatability of the experiments presented in the previous sections with acetone vapour. Acetone vapour was introduced at 15,000 Pa in a heated chamber at $T = 325$ K. The lifetime curve was obtained by repeating the experiments on four different days. If all the conditions were similar, the curves obtained should be similar. The acquisition parameters were similar to those of Figure 4.34 and are as follows: $N_l = 100, N_i = 10, G = 100 \%, \Delta t_{gate} = 100$ ns, $E_{den} = 0.04$ Jcm⁻².

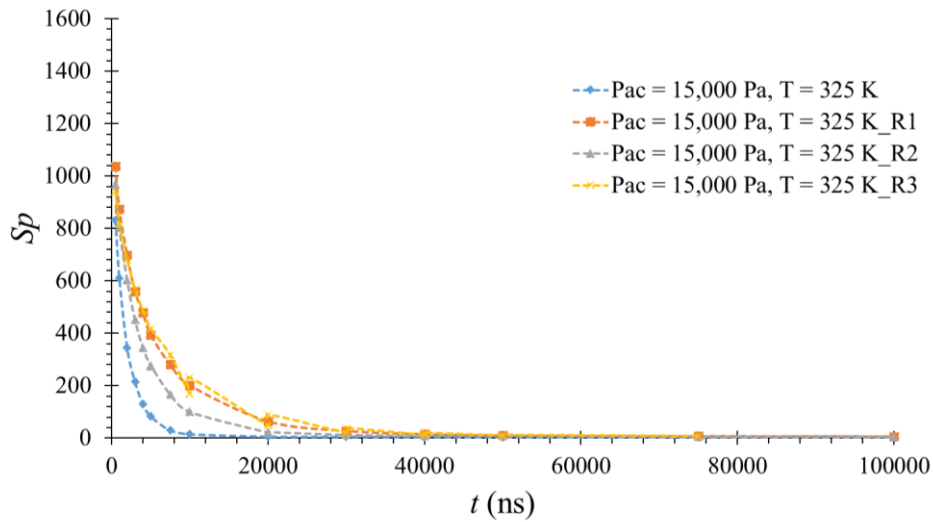


Figure 4.40. Phosphorescence of acetone vapour at $P = 15,000$ Pa at different temperatures to understand the repeatability of the experimental data. Suffixes R1, R2, and R3 refer to the number of repetition

Figure 4.40 and Figure 4.41 show the findings. It can be clearly observed that there is a significant deviation of data from one experiment to another experiment, purportedly to be at similar experimental conditions. Similar observations were made on repeating the experiments even by varying the pressure and temperature in the system. Therefore, it was evident that the data are not satisfactorily reproducible. In these experiments, even though the number density (due to constant pressure and temperature) is same for every experiment, there is not reproducibility of the data. This is probably due to the signal quenching by oxygen leaking into the system. A detailed investigation on oxygen quenching is presented in Section 5.4.3.

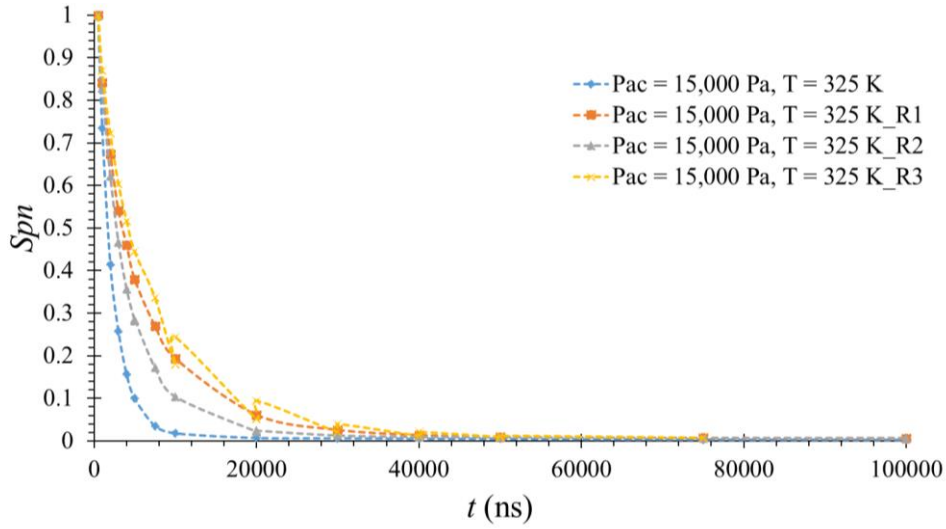


Figure 4.41. Data shown in Figure 4.40 normalised with the intensity value at 500 ns for every curve. Suffixes R1, R2, and R3 refer to the number of repetition

4.9.1 Reasons for lack of repeatability of data

In this section, possible reasons underlying the lack of repeatability in the experimental data are discussed. A critical analysis on all the probable factors, which can conceivably influence the signal, are identified. Major part of this thesis focused on trying to rectify these factors and to achieve a reproducible and reliable experimental data.

4.9.1.1 Laser energy fluctuations

The average laser energy was maintained approximately at 30 μJ at the beginning of the experiments. This value of energy was obtained by placing the power meter at the front of the optical access. The experimental images for the heating experiments shown in Section 4.8.4 were acquired at the following conditions: $N_l = 100$, $N_i = 10$, $G = 100\%$, $\Delta t_{gate} = 100 \text{ ns}$, $E_{den} = 0.04 \mu\text{Jcm}^{-2}$. For these conditions, it takes about 50 seconds to finish an acquisition at a particular delay. Let us assume that we would be needing about 40 delay times to have a lifetime curve for phosphorescence; this would correspond to an experimental duration of $\sim 2,000 \text{ s}$ or $\sim 34 \text{ min}$.

As mentioned, the energy was recorded at the front of the chamber at the beginning of the acquisition. Similarly, energy was recorded at the end of the acquisition. The energies

recorded at the beginning and the end of the experiment were always different. In general, it was noticed that the energy tends to decrease with time. An approach to overcome this problem would be to assume a linear behaviour in the decrease of energy with time during one life curve measurement and make corresponding normalizations to the measured intensity values to eliminate the influence of energy. However, this approach would result in erroneous results. The linear energy variation is not necessarily the case in reality. These observations were studied at a greater depth and the corresponding results and analysis are presented in Section 4.9.1.1. Another approach might have been to place a beam splitter at the entry of the beam and measure the energy. However, even this approach was limited by the following constraint: sometimes even on operating the laser at 100% energy, we noticed that the level of energy was just at the threshold level to obtain images. Having said this, experiments in which we are able to have sufficient energy to capture the images, we can use a beam splitter to measure energy continuously during the experiments. Experiments of this kind can be carried out in the future.

Due to the absence of an exit optical access (for exiting the laser beam which entered the chamber), it was not possible to know the level of energy exactly at the instant of capturing the images. Therefore, the best possible solution to eliminate the problem of energy fluctuations would be to continuously monitor the laser energy at the exit of the chamber and make corresponding normalization to the intensity counts. This idea has been incorporated in the second design of the chamber presented in Chapter 5.

4.9.1.2 Leakages

On heating the chamber, we noticed that there was a steep rise in the leakage rate of air into the system. The leakages can be due to uneven expansion of different materials with the chamber is made, providing a source for air to enter into the system. Oxygen in air is known to quench the luminescent signal of acetone vapour. Therefore, it is very important to have a leakage free environment in the experimental chamber. This would ensure that any differences noted in the lifetime curves and intensities can be attributed to pressure and temperature differences, and not due to quenching by oxygen. Table 4-15 shows the leakage rates measured in this chamber at vacuum conditions.

Table 4-15. Leakage rates measured in the chamber

T (K)	Pressure rise due to leakages (Pa/hr)
Room	~ 60
325	~ 400

It should be emphasised that this chamber was initially intended to perform experiments at room temperature and not at elevated temperatures. However, we proceeded with heating experiments on this chamber to get a preliminary idea on temperature dependency. The experimental chamber was quite bulky and it took considerable amount of time to heat (See section 4.8.1). It can be clearly noted from Table 4-15 that the leakage increased on heating the chamber. Even at room temperature, the leakage in the chamber was not negligible. Especially, given the experimental time required for capturing a lifetime curve (~ 35 min) in this study, there is an influx of air during the experiment and this can quench the phosphorescence signal of acetone. This was one of the reasons for the data to be not reproducible. Therefore, it was important to have leakage free chamber. In the next chapter after obtaining a leakage free chamber, we were able to experimentally demonstrate the influence of oxygen on quenching the phosphorescence signal (see section 5.4.3).

4.9.1.3 Gaps in experimental protocol

Another problem can be attributed to the protocol followed during the course of experimentation. The tracer were being replaced for every experiment, i.e., if we carried out the experiment with acetone vapour at 10,000 Pa and room temperature, then we were not heating the same vapour; instead, we were heating the chamber and then introducing fresh acetone mixture at the same pressure. This makes the comparison between different experiments complicated, because with this approach, not only are we changing the temperature but also the number density. Therefore, the intensity differences can result due to temperature as well as the number density. Moreover, when we increased the temperature, we have adjusted the pressure to maintain the pressure as that of room temperature. This means that when we have carried the experiments at higher temperature, the number density is already lower than that of the room temperature values (to have the same pressure). Therefore, this decrease in the molecules also manifests as the difference in the curves between the room temperature and the higher temperature, and therefore, is not exactly a representation of the temperature dependency of the molecule.

Though the results from this experimental chamber seemed to be encouraging; they must be improved as there is a lot of uncertainty with the obtained results and there was a dire necessity to improve the protocol of the experiments. To summarise, the intensity of phosphorescence is a function of the number density, excitation wavelength, energy of the laser pulse, presence of a quencher in the medium, pressure and temperature of the mixture.

Therefore, theoretically, a change in anyone of the above parameters would result in a different intensity. It was imperative to redesign the chamber and to rethink the strategy to carry the experiments, as done in Chapter 5.

4.10 Experimental study on laser energy

4.10.1 Laser energy fluctuations

To establish a reliable set of experimental data which are repeatable and reproducible, a *laser operating protocol* was developed and rigorously followed during experiments with OPO laser. The objective of this protocol is to understand, minimise and normalise the energy fluctuations of laser energy. The laser beam can be triggered internally or externally. OPO software provided by the company is the internal triggering mechanism. The laser beam every time after turning on the power supply has to be initialised with internal triggering. Thereafter, if needed, we can adjust the laser beam by external triggering.

To synchronize laser with the camera (via the Programmable Timing Unit - PTU), so as to capture images during experiments, we require an external triggering mechanism (DAVIS in our case). This indicates that an external source generates both the flash lamp trigger and the Q-Switch trigger (refer section 4.2.2.1). In fact, the second approach of controlling the laser beam with DAVIS software was employed for capturing all the images in this thesis. However, to assess if there is any influence of the triggering mechanism on the energy fluctuations, the triggering of laser beam was controlled by DAVIS software for some experiments, and OPO for some other experiments.

The wavelength of the laser beam was adjusted to 310 nm, as this wavelength was the best one for our experiments with acetone. Depending upon the experiment, the number of recorded laser pulses varied from 20,000 to 100,000. The real value of laser beam energy for every pulse is highly fluctuating. However, the average energy for about 1,000 pulses is fairly constant. 1,000 pulses corresponds to the minimum number of pulses over which we generally obtained an exploitable integrated image in our experiments. Therefore, the average energy for every 1,000 pulses was plotted.

The beam generated by the OPO laser is about 4 mm in diameter. The beam diaphragm can be mechanically adjusted from D1 to D9, which varies the diameter of the opening for the laser beam (refer section 4.2.2.4). In the following experiments, as the interest was to study the

fluctuation of the laser energy, the choice of this diaphragm valve position is of no importance. Adjusting the diaphragm valve to a different position would only alter the beam diameter. It has no bearing on the quantity of interest for these experiments, i.e. the fluctuation of energy. The beam diaphragm was kept at D2 for all sets of experiments shown in Table 4-16 and Table 4-17.

4.10.2 Protocol for studying energy fluctuations

Table 4-16 and Table 4-17 shows the details of the experiments carried out with DAVIS and OPO triggering, respectively. As it can be noted from these tables, some experiments were with DAVIS triggering and the others with OPO triggering. For every experiment, laser energy was continuously monitored by recording the energy by the power meter. The parameters being varied were the trigger energy and number of recorded pulses.

Table 4-16. Trigger energy and repetition of experiments with DAVIS software

Davis trigger energy (%)	Repetitions
75	15
77	15
79	15
81	5
83	5
87	5
89	5
91	5
93	2
97	2
100	15

Table 4-17. Trigger energy and repetition of experiments with OPO software

OPO trigger energy (%)	Repetitions
75	5
85	5
100	15

The following was the protocol for the experiments on energy fluctuations: For these set of experiments, laser and power meter, are the only equipment required. The camera is not used in these measurements. Therefore, for these set of experiments, the question of adjusting t , G , and Δt_{IRO} are irrelevant.

For OPO internal triggering experiments:

- (a) Warming up the laser by turning on the power supply half an hour before starting the OPO software;
- (b) Adjusting of wavelength to 310 nm;
- (c) Turning on the OPO software, which is internal triggering.
- (d) The power meter was positioned directly in front of the experimental chamber and the laser beam was directly shot on the detector of the power meter. Adjusting the laser energy (depending on experiment) and recording the intended number of pulses and the laser energy of every pulse by the power meter.

For DAVIS, external triggering experiments:

Steps from (a) to (c) remain the same as above.

- (a) Adjusting the software from OPO, internal to DAVIS, external triggering;. After this adjustment, perform step (d) as above.

Based on the above protocol, we carried out about 90 experimental measurements on laser energy with DAVIS triggering, and about 25 experiments with OPO triggering.

A typical curve obtained during the experiments is shown in Figure 4.42, with Davis trigger set at 100%. Np represents the number of laser pulses. All the four experiments shown in Figure 4.42 were performed on different days, but with the same parameters. For the sake of clarity, only 4 experimental data are presented in this figure, but the differences shown here were a common observation during all the different experiments. All data from these experiments are provided in Annex B

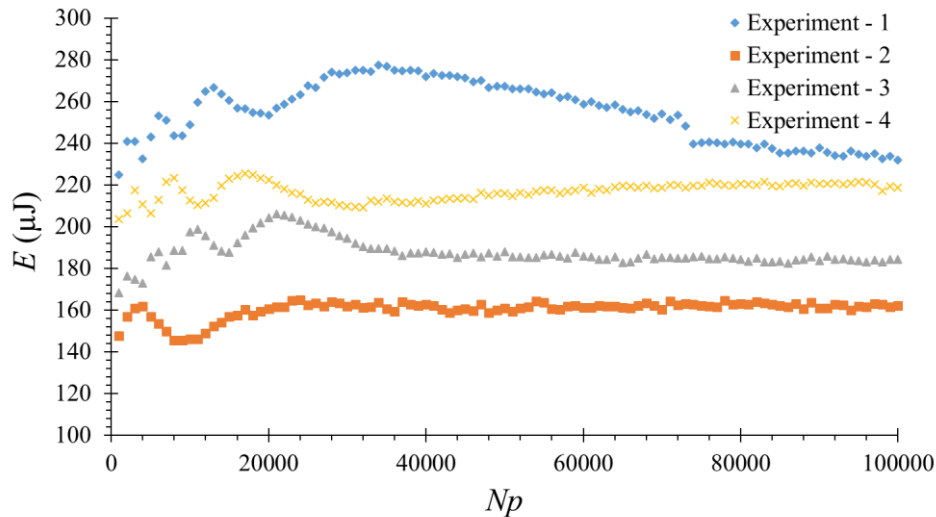


Figure 4.42. Laser energy fluctuations as a function of number of pulses, for Davis trigger set at 100%.

It can be noted that all curves seem to show a similar behaviour of fluctuation until the beam roughly stabilises: the laser energy seems to be almost stable around 50,000 pulses for Experiments 3 and 4. For example, in Experiment 3, the average energy during the first 50,000 pulses is $190.69 \mu\text{J}$. The maximum and minimum energies during this interval are 206.21 and $81.59 \mu\text{J}$, respectively. This leads a fluctuation in energy to be about 12.9 % of the average value. However, the average energy from 50,000 to 100,000 pulses is $184.73 \mu\text{J}$. The maximum and minimum energies during this time interval are 182.82 and $187.62 \mu\text{J}$, respectively. This gives a maximum fluctuation in energy of about 2.5 %. Therefore, these values clearly demonstrate relative stabilization of the beam around 50,000 pulses for Experiments 3 and 4, and to a lower extend for Experiment 2. However, this was not the case for Experiment 1, which tends to stabilise around 75,000 pulses. The laser pulse frequency is 20 Hz. Therefore, it took about 2,500 s (~ 42 min) for the laser energy to stabilize in Experiments 2, 3, and 4. In Experiment 1, this would be about 3,750 s (~ 62 min).

Figure 4.42 shows that the scale of energy level is very different (~ 270 , ~ 220 , ~ 180 , and $\sim 160 \mu\text{J}$) in the four experiments, and the energy scale did not show any discernible trend. In the experiment, every phosphorescence image captured is based on the average of 100 pulses. Further, ten such images are averaged, which corresponds to a total of 1,000 pulses. Therefore, it is interesting to note the average energy for every 1,000 pulses and note its deviation from the total average, since these number of pulses would correspond to the real experiments.

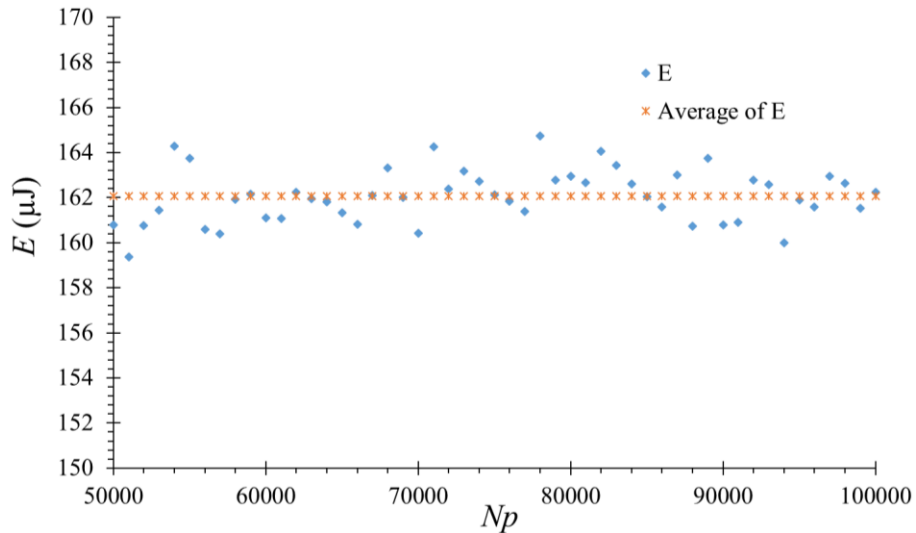


Figure 4.43. Fluctuation of the OPO laser energy from 50,000 until 100,000 pulses, from Experiment 3 in Figure 4.42

Figure 4.43 shows the variation of the energy for Experiment 3, from 50,000 pulses until 100,000 pulses. In this interval, the average energy corresponds to 162.07 μJ , and the standard deviation (σ_{SD}) is 1.18 μJ . This would correspond to a relative standard deviation (RSD) of 0.72%. These values suggest that, in this case, after 50,000 pulses, we consider the laser beam to be stable.

Figure 4.42 shows the laser energy when the laser beam is generated at 100% energy. According to the manufacturer, the laser has to be operated at 100% energy until the stability of the beam is achieved. After the beam stabilises, we can reduce the energy in the range of 30-60 μJ , depending on our experimental requirements. Therefore, it was required to observe the behaviour of the laser on reducing the energy level.

Figure 4.44 shows the variation of laser energy at lower values of energy of the order of 60 μJ . The experiments in Figure 4.44 have been carried out immediately after the laser energy has stabilized. In this interval, the average energy corresponds to 60.03 μJ , and the σ_{SD} is 0.64 μJ . This would correspond to a RSD of 1.06%. These values suggest that, in this case, after 50,000 pulses, even with a reduction of the laser energy, the average energy seems to be constant.

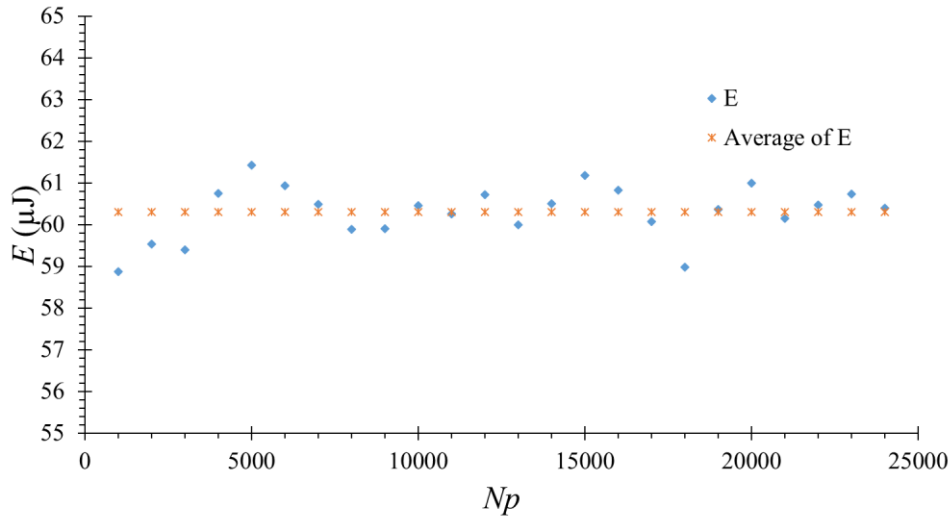


Figure 4.44. Example of laser energy fluctuations at 60 μJ .

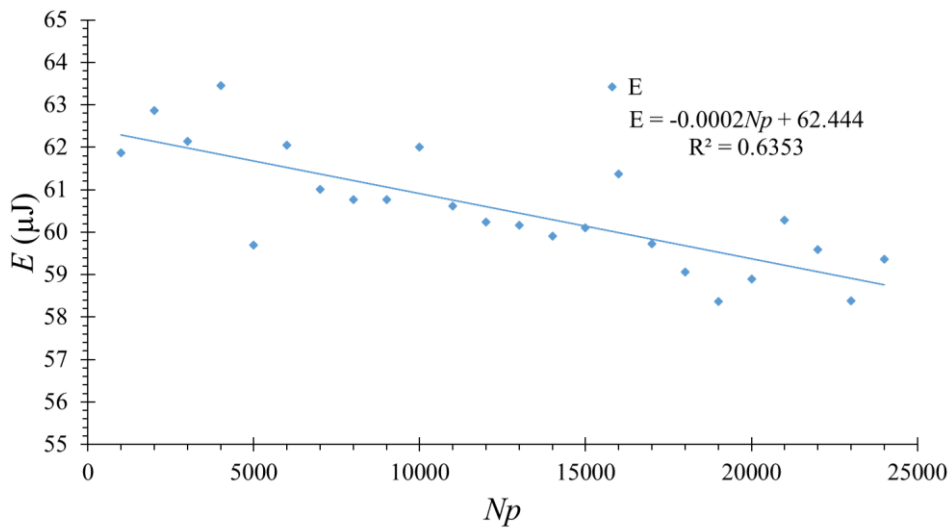


Figure 4.45. Other example of laser energy fluctuations at 60 μJ

However, this observation of constant energy seems to be not true for all the experiments carried out. For instance, Figure 4.45 shows the variations of laser energy for another experiment performed on a different day. As previously, the laser beam energy was stable at 100% energy. Thereafter, the energy was reduced to 60 μJ . The average energy seems to be close to 60 μJ , but the overall trend seems to suggest that there is a slight decrease in the energy with the number of pulses. The average energy for this data is 60.52 μJ , and σ_{SD} is 1.36 μJ , corresponding to a RSD of 2.24%. To avoid this error which can be introduced by assuming that the energy remains constant during the entire image acquisition, we had captured the energy

for every pulse. Thereafter, we averaged the pulses for the time taken for the acquisition of data for every delay. Subsequently, the real values of the energy averages were used to normalise the experimental data.

4.10.3 Software adjustments on OPO laser

Based on the above experimental results, the influence on the laser energy stability of other laser parameters, such as adjusting the ‘JOG’ and ‘harmonic optimization’, were studied. These software options generally adjust the OPO doubling wavelengths by adjusting the UV crystals. UV Jog function allows the user to make small corrections to the signal/idler wavelengths. JOG control Harmonics are the unwanted higher frequencies that are superimposed on the frequency of interest, and this may distort the wavelength of interest. Therefore, it may be interesting to adjust this to reduce this influence on higher frequencies. In our model of OPO, the software provides this adjustment.

In general, the Opolette is a hermetically sealed system but it can be somewhat affected by ambient lab temperatures, especially when using the system without first warming it up. For systems that experience significant 'energy drift', it is recommended to optimize the harmonics if the energy is not close to optimal after the warm up (harmonic optimization). This implies that when we measure the maximum energy at 100%, it would not be in agreement with the values provided by the manufacturer.

The OPO crystal module is controlled by a rotation stage driven by a stepper motor. UV wavelengths are generated by special UV tuning crystals in the laser, and this involves the process of OPO doubling or mixing wavelengths. On initiating the UV software, the stepper motor is started, technically referred to as ‘homing’, which involves the movement of stepper motor until the triggering of a photo-sensor. When the photo-sensor is triggered, the position of the motor is found and assigned a value. Thus, based on the number of steps required for the movement of motor from this ‘home’ position, the wavelength tuning is done automatically. The phase match angle of the UV doubling or mixing crystals are factory calibrated to generate maximum pulse energy. The UV crystals are also a bit temperature sensitive, so it may be necessary to 'JOG' the UV motor to optimize the UV output as well. This motor allows the positioning of the UV crystals to generate laser beam. The UV Jog control allows the user to make small corrections to the factory calibrated phase matching angle (maximum pulse energy). Phase matching refers to a group of techniques, such as birefringent phase matching, for achieving efficient nonlinear interactions in the laser crystals¹⁵⁰. When tuning to the UV wavelength, we should get >70% of optimal output (based on the pulse energy vs wavelength

curves provided by the manufacturer). To recover the remaining 30%, it might be necessary to jog the UV motor.

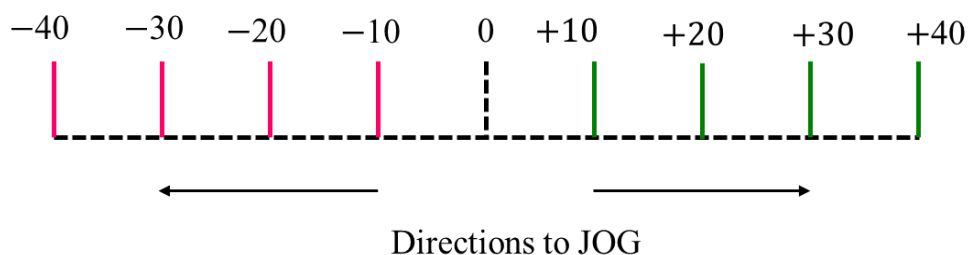


Figure 4.46 Schematic of the JOG positions

Table 4-18. Experimental conditions for adjustment of JOG

Np	JOG	E (μJ)	σ_{SD} (μJ)	RSD (%)
0 – 10,000	–10	103.32	0.83	0.80
10,001 – 20,000	–20	101.46	0.97	0.96
20,001 – 30,000	–30	102.60	0.90	0.88
30,001 – 40,000	–40	104.85	1.13	1.08
40,001 – 50,000	0	103.18	0.51	0.49
50,001 – 60,000	+10	104.09	0.87	0.83
60,001 – 70,000	+20	102.92	0.92	0.89
70,001 – 80,000	+30	103.08	0.51	0.49
80,001 – 90,000	+40	101.65	1.18	1.16

On turning on the software, the position of JOG is set to the factory calibrated value (let us call this position as zero position). The UV JOG function of the software allows the user to jog the motor with a minimum step of 10. This adjustment in step value can be done on the either side of the zero position as shown in Figure 4.46. If we make 50 steps in either direction of zero, this would correspond to change of one nanometre and the wavelength might change. For instance, 310 nm can change to 309 or 311 nm, depending on the direction of the JOG. Since we wanted to experiment at 310 nm, we restricted our step size to 40 in either direction. The software was turned and the laser wavelength was adjusted to 310 nm. The first reading was taken by shifting the JOG position by –10, and then –20, until –40. Thereafter, the JOG

position was returned to zero and energy measurements were taken. Similarly reading were taken from + 10 to + 40. These values are shown in Table 4-18.

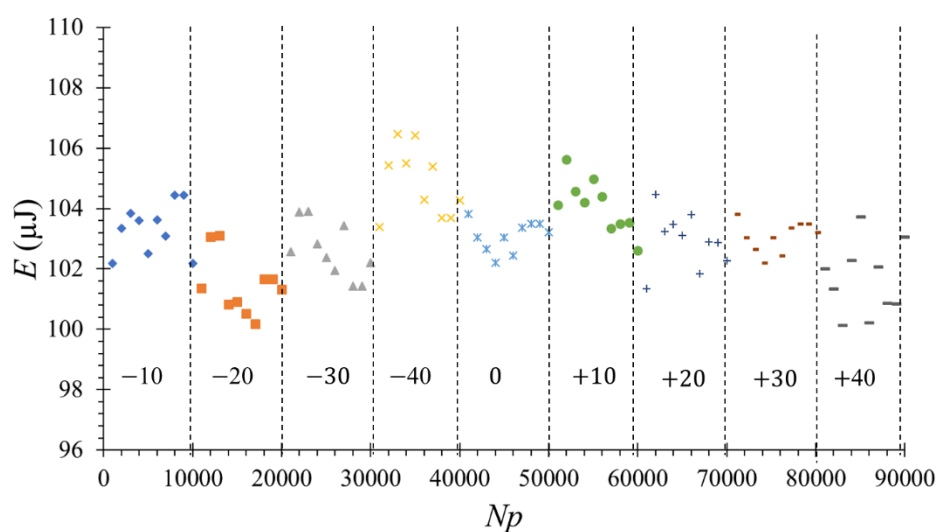


Figure 4.47. Variation of energy with JOG function on OPO software. The values from -40 to $+40$ represent the JOG steps moved from the factory calibrated setting (zero).

Figure 4.47 shows the variation of laser energy by varying the values of JOG. For every value of JOG, the laser energy was recorded for 10,000 pulses (every point in the graph represents an average of 1,000 pulses). Therefore, in Figure 4.47, there are nine different values of JOG (each corresponding to 10,000 pulses), represented by different symbols in the figure. Table 4-18 shows the variation of the average value for every 10,000 pulses with the JOG function. The table also provides the information on the σ_{SD} and the RSD for every 10,000 pulses. As it can be noted from this table, the average value of energy doesn't seem to vary much by altering the JOG function. We note that the lowest and highest values of the average energy for every 10,000 pulses are about 101.46 and 104.85 μJ , which corresponds to a difference of 3.39 μJ . Also it can be clearly observed from this table that the σ_{SD} is no more than 1 % for any combination of 10,000 pulses. Therefore, it can be concluded that the JOG function doesn't seem to have any noticeable influence on the laser energy variation.

4.11 Summary

This chapter commenced with a detailed description of the various components in our molecular tagging experimental setup. A description of the existing experimental chamber

before this thesis has been presented, and this chamber was referred as the first experimental chamber. Initial experiments on this chamber we focused on understanding the delay until which we could notice phosphorescence on exciting acetone vapour at 266 nm. The analysis of the results suggests that the signal intensity was very weak after a few thousand nanoseconds delay time. Therefore, it was necessary to investigate acetone vapour by exciting at different wavelengths.

The existing Nd:YAG laser was replaced by OPO laser and a detailed experimental investigation was carried out on both acetone vapour by exciting it from 250 to 340 nm. Similarly, we investigated the excitation behaviour of diacetyl vapour between 410 to 470 nm. The data analysis suggested that around 310 nm for acetone vapour and 410 nm for diacetyl vapour, we could achieve highest emission signal.

Thereafter, the study shifted towards temperature measurements. The initial experiments on acetone vapour luminescence in the temperature range of 298 to 323 K and pressure range of 1,000 to 15,000 Pa seemed to indicate a dependency of temperature. However, this experimental data was not reproducible. Therefore, a careful investigation was done to identify the parameters influencing the experiments and leading to non-repeatability. During the experiments, we noticed that the laser energy was not stable and since the laser beam intensity would affect the number of molecules being excited, and thereby the intensity signal, it was crucial to investigate these fluctuations. A large number of experiments were carried out by controlling the laser with the internal (OPO) and external (DAVIS) triggering. Certain software adjustments, such as varying UV motor JOG were done. These experiments suggested that the laser energy tends to be highly unstable during the first 50,000 pulses, and thereafter tends to stabilise. These experiments helped us to develop and standardise the protocol to control and minimise laser energy fluctuations.

Another important factor which could influence the signal intensity was the presence of oxygen. Moreover, the first experimental chamber was bulky and possessed some connections (for instance, the hole to provide a thermistor), which were not essential and were sources of leakages. Therefore, there was definitely a need to redesign the experimental chamber. In Chapter 5, we present the design and the experiments performed with this new experimental chamber, which is referred to as second experimental chamber.

5 Experimental investigations on second experimental chamber

In this chapter, we present the details of the design of the second experimental chamber. After a brief description of this new setup, experiments on measurements of σ_{abs} of acetone vapour at different excited wavelengths and temperatures are presented. Based on the experimental findings of Chapter 4, the experimental protocol was improved and is presented. An investigation on the influence of oxygen on photo luminescence quenching is presented, and is followed by a study on the influence on laser pulses on acetone vapour composition. An improved image analysis of the experimental data by taking into account background subtraction is discussed.

An investigation of acetone vapour emission at different conditions of pressure and temperature are presented. The approach to estimate the time constants from the lifetime curves obtained will be presented by fitting a single and bi-exponential functions to the data. Finally, the experimental chamber will be further modified to incorporate a heating element. Experimental technique and the data analysis to observe the difference in the number density induced near the heating element are discussed.

5.1 Design of second experimental chamber

To address the leakage issues, incorporate the optical access to monitor energy, to improve the heating of chamber, and to create a temperature gradient in the chamber - it was essential to redesign and build a new experimental chamber. The design was conceived as shown in Figure 5.1.

Modifications were made to reduce the number of connections (from six to four), and this automatically reduced the risk of leakages. Two side faces of the chamber were made available for mounting Peltier heaters, as shown in Figure 5.2a. The new design possesses an optical access at the back end of the chamber (Figure 5.2b) to monitor energy by placing the power meter as shown in Figure 5.2c. The design of this chamber is symmetrical with a symmetrical heating. This ensures better uniformity in the distribution of heat, and therefore, it is simpler to achieve isothermal conditions in the zone tagged by the laser. Based on the above design considerations, we fabricated the chamber as shown in Figure 5.2.

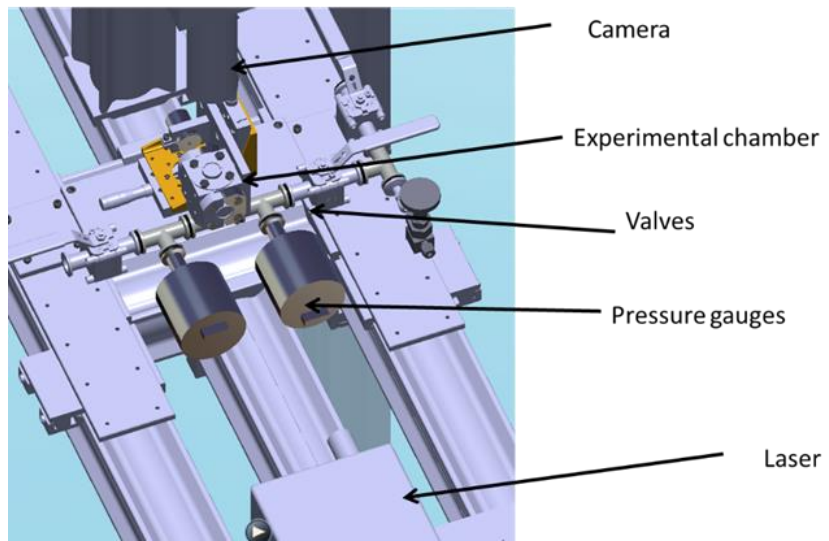


Figure 5.1. Schematic of the experimental design

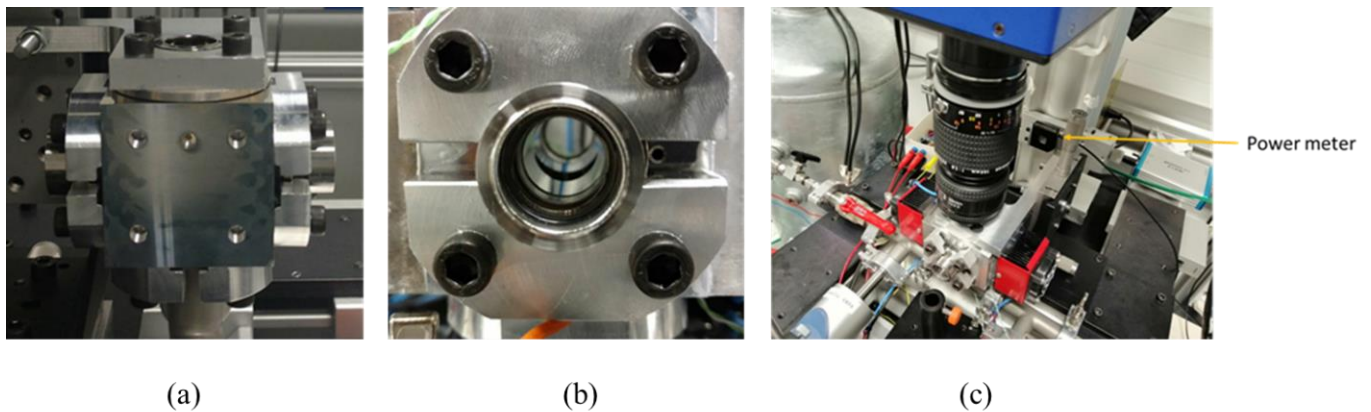


Figure 5.2. Fabricated chamber: (a) side face to place the Peltier heaters, (b) back end of the chamber to monitor laser energy, and (c) position of the power meter

This new chamber was fabricated with aluminium and the main components for the assembled setup shown in Figure 5.3 can be broadly listed as follows:

- Connections required for tracer (acetone or diacetyl vapour) and carrier (helium or nitrogen) gases: valves, clamps and T-junction, adapters for Swagelok fittings;
- Connections to pressure gauges: clamps and T-junction;
- Connections to vacuum pump: valves, clamps and hose pipe;
- Optical accesses: Suprasil (special grade of fused silica) for laser beam access; glass for camera and exit beam access;

- Heating elements and temperature measurement devices: Peltier heaters, power supply sources, pressure gauges and thermocouples.

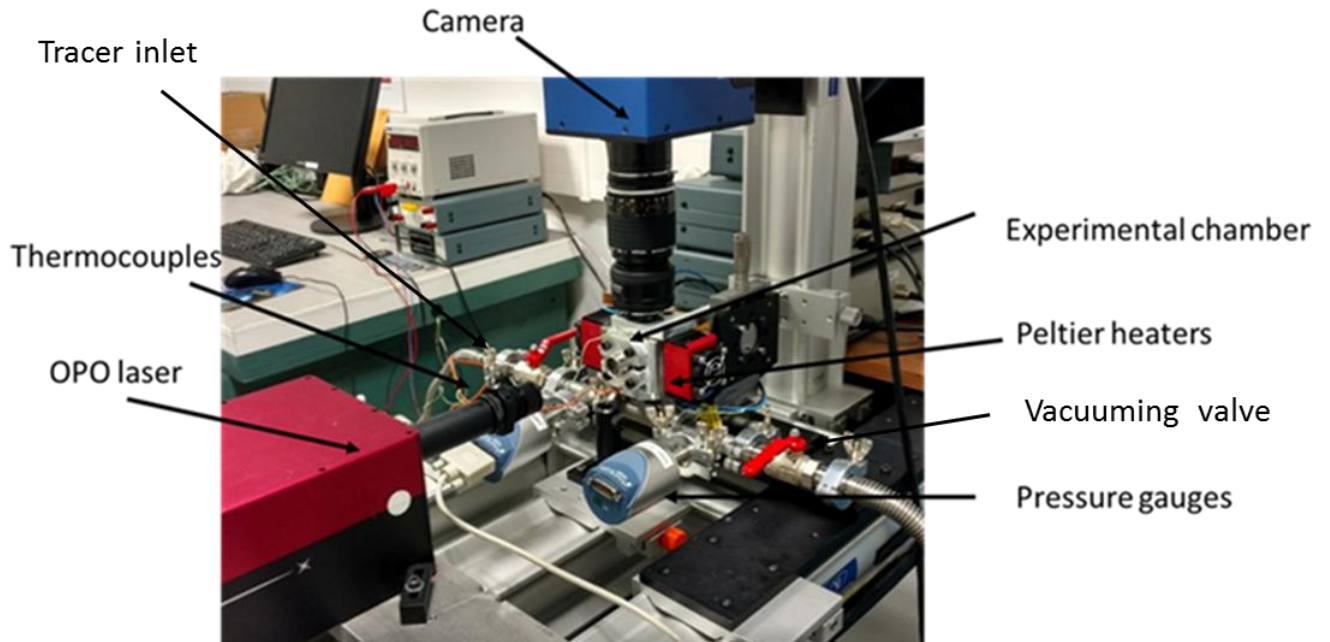


Figure 5.3. Assembled new experimental chamber

5.1.1 Initial leakages and outgassing in the second experimental chamber

After assembling all the components, leakage tests were carried out at room and higher temperatures. The procedure for leakage tests was as follows. The vacuum pump was turned on for vacuuming the entire system for at least 12 hours. Thereafter, the valve of the vacuum pump was turned off to measure the rise in pressure (with two pressure gauges). Figure 5.4. shows the pressure rise experiment carried out as soon as the experimental chamber was assembled. For these data, the trend of pressure rise is almost linear and is about 30 Pa/h. This initial leakage rate itself is lower than the rates which were observed with the old chamber (~ 60 Pa/h). However, after continuously vacuuming the entire setup for few days, and tightening all the components to limit possible leakages, the pressure increase was considerably reduced. The experimental chamber was then brought to atmospheric pressure. Once again, it was vacuumed, and the pressure rise was measured; and it was about 4 Pa/h. The process of vacuuming and noting the leakage rates was repeated for several days. One such experimental measurement of pressure rise due to leakage/outgassing as a function of time is shown in Figure 5.4.

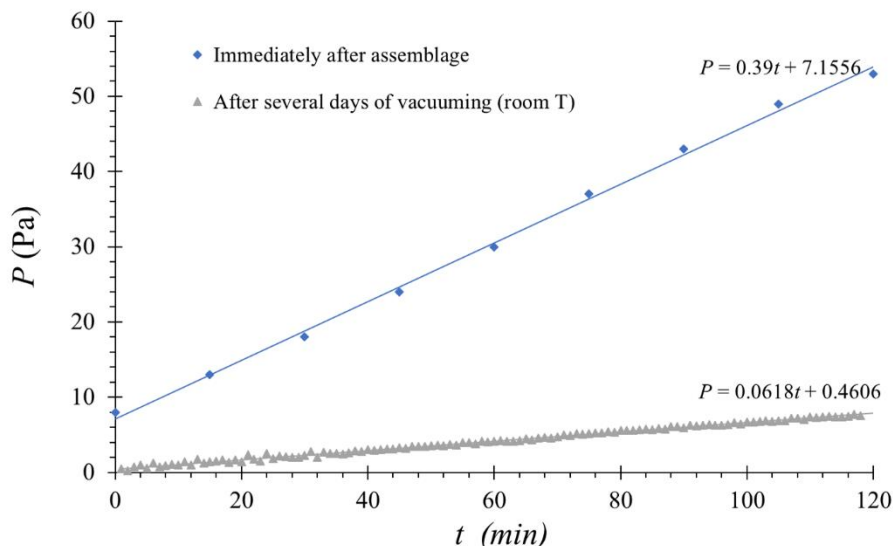


Figure 5.4. Initial leakage/outgassing rate experiments showing the pressure rise as a function of time

The leakages play an important role in diminishing the photoluminescence signal, and this is one of the reasons which led to the non-repeatability of the experiments presented in Chapter 4 (see Section 4.9). To demonstrate the influence on oxygen on signal quenching, a detailed section devoted to the influence of leakages on photoluminescence signal quenching is presented in later part of this chapter (see Section 5.4.3).

5.1.2 Heating of the second experimental chamber

The next stage of experimenting on the new chamber was to establish the relationship between the power requirements to establish required temperature on the chamber. The heating of the chamber was achieved with Peltier heating modules, which were placed on the two sides of the chamber. Two thermocouples were permanently fixed on the experimental chamber. One of them was placed on the top end of the chamber and the other at the bottom end of the chamber. With these fixed thermocouples and another thermocouple which was not fixed, temperature was being monitored at different locations. The temperature of the chamber was varied from 287 K to 353 K. The temperature distribution on the chamber was almost uniform, with less than 0.5 K difference between the fixed thermocouples on the chamber, as shown in Figure 5.5. A slight increase of ~ 0.1 K in 20 min is seen in this figure, indicating that the chamber is tending to reach a steady state temperature.

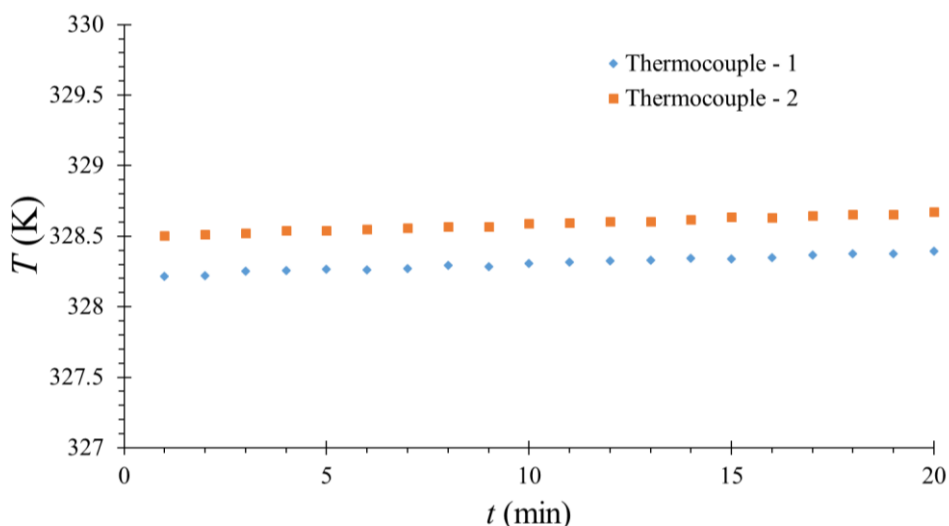


Figure 5.5. Typical curve of temperature evolution with time shown by thermocouples on the chamber.

Experimental observations, obtained by measuring the pressure rise in the heated chamber, show an increase of the pressure rise with temperature. This can be due to an increase of the leakage and outgassing rates. As the chamber is made up of different materials, on heating, the rate of expansion for every material will be different, and this could result in an enhancement in the leakage rate. A temperature increase can lead to more desorption of molecules from the walls and an increase of outgassing. Therefore, it was expected that the pressure rise would increase when heating. The average pressure rise varied from about 20 Pa/h at 287 K to about 100 Pa/h at 353 K immediately after assemblage. After continuously vacuuming the entire setup for few days, and tightening all the components to limit possible leakages as done in the case without heating, the pressure rise reduced to ~ 10 Pa/h, see Figure 5.6.

An important point to be noted is that these pressure rises in Figure 5.6 correspond to values when the system is at complete vacuum. Therefore, there is the highest possible pressure difference between the chamber and atmosphere and the leakages and outgassing rates should be at their maximum possible values. During the course of experimentation, after introduction of tracer and stabilisation of pressure in the system (after achieving the required pressure at which the experiment is to be done), we did not notice any measurable pressure rise due to leakage or outgassing in the chamber.

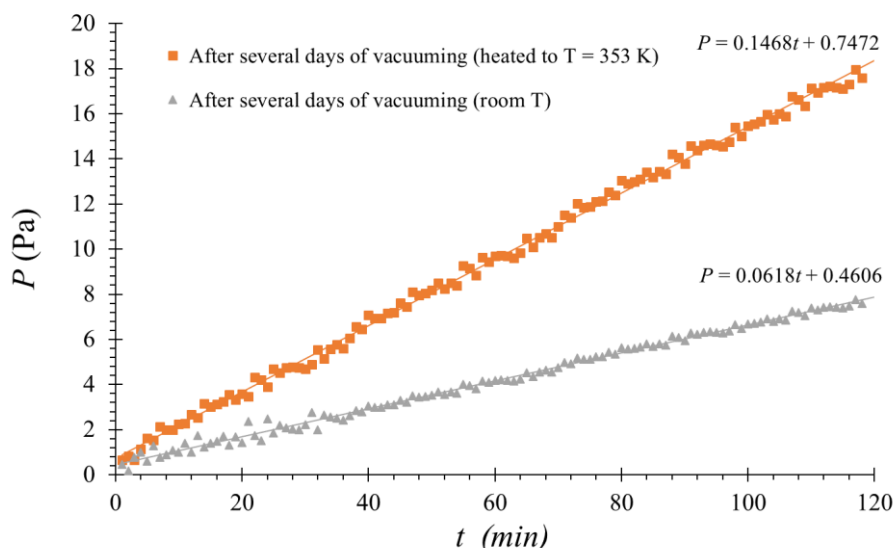


Figure 5.6. Leakges before and after heating the experimental chamber

At the cost of repetition, it must be emphasised that it is crucial to have a chamber with the least possible leakages, or preferably leakage free, at least within the duration of experimentation. Therefore, apart from this observation of pressure rise to assess leakages, a variety of experiments focusing on the lifetime and intensity of acetone vapour phosphorescence were conducted to assess the leakages. These experiments and corresponding results are discussed at length in the later sections of this chapter (see Section 5.6).

5.2 Basic experimental protocol

In this section, the protocol followed during the experiments is presented. Based on the previous experimental results and the laser energy stabilisation experiments, the procedure to conduct the experiments was finalised. However, slight improvements were made at every stage of experimentation by further identifying the possible sources of errors. Nonetheless, a summary of the basic protocol followed during the experimental investigation can be presented. Wherever we have made some changes to this protocol, we will highlight them in the discussions.

- The experimental chamber is vacuumed for at least 12 hours before the start of the experiments. This ensures that the chamber is free from the presence of air (thereby, oxygen).

- At time $t = 0$, the power supply of laser is turned on. It is recommended by the manufacturer to warm up the laser power source for about 20 minutes before turning on the laser beam. The OPO software is turned on after this step.
- At $t = 20$ min, acetone is introduced in the chamber as follows: introduction of acetone at saturation pressure, followed by vacuuming. This step is carried out for about 20 times to ensure that if there is any air left in the system, it will be replaced by acetone molecules.
- At $t = 25$ min, the laser beam is turned on, adjusting the wavelength to 310 nm. Our previous experiments (Section 4.10.1) on laser beam stability have shown that it takes about 50,000 pulses for the laser beam to stabilise. Therefore, the laser beam power is turned on at 100 % and allowed to operate until the laser energy stabilizes.
- At $t = 55$ min, once again, acetone vapour is introduced at saturation pressure and then vacuumed. The process is repeated 20 times.
- At $t = 60$ min, acetone is introduced at desired pressure and temperature. The acetone vapour is allowed to stabilise its temperature and pressure.
- At $t = 75$ min, the laser energy is reduced to the required value and acquisitions are started.

5.3 Measurement of absorption cross-sections

In this section, we present the absorption cross-sections (σ_{abs}) of acetone vapour excited at different excitation wavelengths. This is an important information in the study of vapour (acetone in our case), as it can provide information on the absorption spectrum. σ_{abs} is an indication of the molecules ability to absorb a photon having a particular wavelength. Technically, the higher the value of σ_{abs} , the easier it is to photo excite the molecule. Moreover, these values give an indication whether we can ignore the effects of absorption of laser energy by the molecules and consider the field of investigation as optically thin. Moreover, these values provide a means of converting the counts provided by the experimental images into number density, as shown below by Equation (5.1). σ_{abs} can be used to evaluate the quantum yield (see section 4.7.2), which can serve to be of fundamental importance to understand the photo physics of tracers.

σ_{abs} can be calculated from Beer-Lambert's law, which is represented in equation (5.1):

$$\sigma_{abs} = -\frac{1}{nL} \ln\left(\frac{I_{outlet}}{I_{inlet}}\right), \quad (5.1)$$

where σ_{abs} is the absorption cross-section, n is the number density of acetone vapour, L is the length traversed by the laser beam in the acetone vapour, I_{outlet} is the laser energy intensity at the exit of the chamber, and I_{inlet} is the laser energy intensity at the entry of the chamber. In the present experimental study, a single power meter was used (Figure 5.3), and the ratio $\frac{I_{outlet}}{I_{inlet}}$ was measured by comparing its signal obtained at the exit of the chamber for a chamber filled with acetone and for an empty chamber. The procedure to measure σ_{abs} is as follows:

- Vacuuming the experimental chamber to ensure that there is no gas in the chamber;
- Generating the laser beam at the desired wavelength and measuring the energy at the chamber exit, $I_{exit\ without\ acetone}$;
- Introducing acetone vapour and measuring the energy at the exit, $I_{exit\ with\ acetone}$;
- Vacuuming the mixture, and repeating the process for different wavelengths and temperatures of the system.

Table 5-1. Excitation wavelengths and operating temperatures used in measuring σ_{abs} of acetone vapour

λ (nm)	248, 266, 276, 282, 289, 300, 308, 310, and 320
T (K)	298 and 328.5

It should be noted that the σ_{abs} is independent of pressure and number density in the system and are only varying with temperature and excitation wavelength¹³⁰. This independency with pressure was verified at 310 nm, which is the wavelength of interest in this study. An experiment at $P_{ac} = 5,000$ Pa was carried out and σ_{abs} obtained was similar to the value obtained at 10,000 Pa. However, on reducing the pressure in the system, the number density reduces, and this results in a weak difference in the values of $I_{exit\ with\ acetone}$ and $I_{exit\ without\ acetone}$. Therefore, for the measurements, the important aspect to be taken into account is that number of molecules must be sufficiently high to enable sufficiently strong detection of energy differences with and without acetone in the system. The pressure at which we carried out measurements was 10,000 Pa and this was sufficient to observe and accurately

measure energy differences. The experiments were carried out at the conditions shown in Table 5-1.

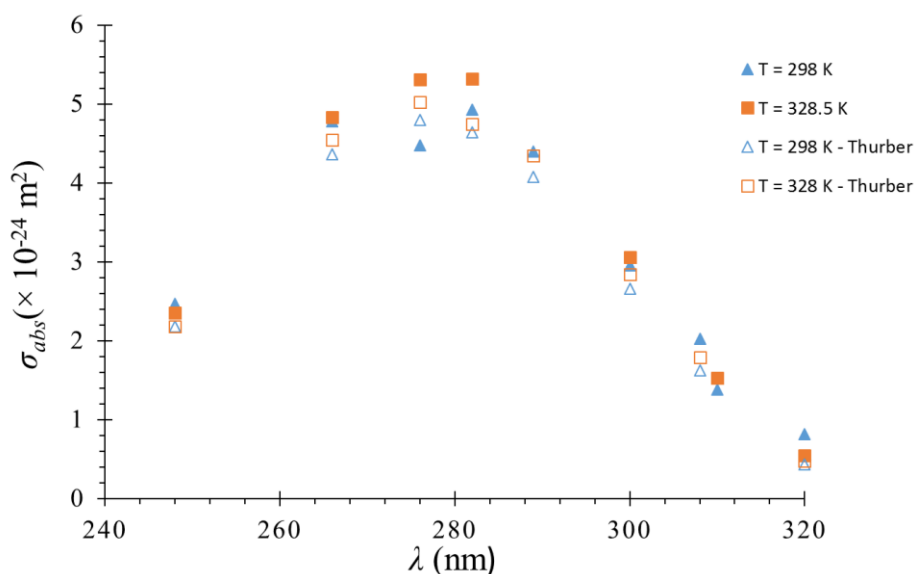


Figure 5.7. σ_{abs} of acetone vapour for the data shown in Table 5-1. The figure also shows a comparison with the values measured by Thurber et al¹²⁹.

Table 5-2. Comparison of data in this study with Thurber et al¹²⁹

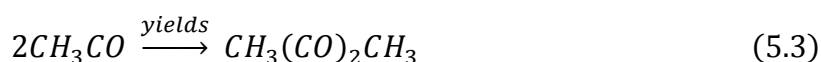
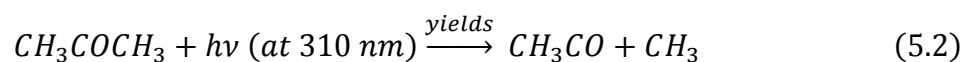
λ	Relative change (%) at $T = 298$ K	Relative change (%) at $T = 328.5$ K
248	11.74	7.62
266	8.78	5.79
276	- 7.14	5.46
282	5.88	10.71
289	7.27	NA
300	10.13	7.18
308	19.70	4.27
310	Not available	Not available
320	46.19	12.36

Figure 5.7 shows the variation of σ_{abs} as a function of wavelength at two different temperatures, measured in this thesis and compared to measures published by Thurber et al¹²⁹. The σ_{abs} increases with the excitation wavelength, reaches a maximum around 280 nm and then decreases. We observe that the σ_{abs} obtained at 298 K and 328.5 K are quite close. Table 5-2 shows the relative change percentage (referenced with this data) with data provided by Thurber

et al¹²⁹. In general, the values predicted by our experiments seem to be 5 to 10% higher than those provided by Thurber et al. At 320 nm, there is a very high difference of 46.19 %. This can be due to the very low absorption by acetone vapour at this wavelength. To improve the accuracy of this reading, the number density of molecules in the system has to be increased, which will result in an increased absorption by the molecules and this will reflect in an increase in accuracy. The general trend was, at every wavelength, an increase in σ_{abs} with temperature. However, at $\lambda = 248$ and 320 nm, there appears a decrease in σ_{abs} with temperature. The same argument of very low absorption holds good for these cases also. As the interest of this thesis was to experiment at $\lambda = 310$ nm, this aspect was not further investigated.

Since the dependency itself is very weak with temperature, further experiments at higher temperature would be needed to clarify if this is the case even on further increase of temperature. From our experiments, at $\lambda = 310$ nm, we calculated $\sigma_{abs} (\times 10^{-24})$ at 298 K and 328.5 K as 1.42 and 1.55, respectively (data not available in literature at $\lambda = 310$ nm). These values seem to be in agreement with the general trend of σ_{abs} showing an increasing with temperature.

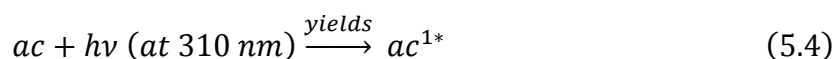
Quantum yield or efficiency (ϕ) indicates the probability of absorption and the efficiency of fluorescence emission respectively. Even though σ_{abs} are highest around 280 nm, the λ at which highest emission intensity for phosphorescence is not necessarily at this λ , but rather around 310 nm, as previously shown in Figures 4.16 and 4.23. In other words, even though less number of photons are absorbed by acetone vapour at 310 nm, there may be a variation in the chemical decomposition of acetone molecules around this wavelength into diacetyl molecules. This is a probable explanation of this behaviour. Fratantonio et al³³ have elaborated on this point. Few decades back researchers have noted a ‘green’ phosphorescence emitted by acetone molecules excited at 313 nm and were similar to the emission bands of diacetyl^{151,152}. There were also reports of presence of diacetyl in acetone. One hypothesis for the absorption of higher emission signal at 310 nm was linked to the following chemical reaction¹⁵³ shown in Equations (5.2) and (5.3).



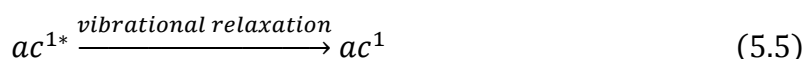
Some acetone molecules (CH_3COCH_3) on absorption of photons at 310 nm could decompose and free acetyl radicals (CH_3CO). Two of these free radicals could potentially

recombine to produce diacetyl in the system ($CH_3(CO)_2CH_3$). Researchers in the past were trying to link the higher emission intensity at 310 nm to the presence of these diacetyl molecules formation. However, diacetyl cannot be excited at 310 nm, and therefore question of direct emission of these diacetyl molecules by observing laser energy at 310 nm does not arise.

The above set of chemical reactions are followed by another set of chemical reactions, which could possibly be the reason for higher emission.



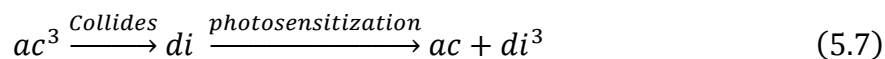
Equation (5.4) shows the absorption of a photon by acetone molecule and excitation into single state, ac^{1*} . The star mark represents the excitation of vibro-rotational states of the molecule. The journey of an excited molecule from the state of excitation to de-excitation has been detailed in Section 3.2.5.1. The excited singlet state molecules, now undergoes vibrational relaxation and reaches the lowest energy level in the excited singlet state, ac^1 . This is shown in Equation (5.5).



If there is fluorescence, the above singlet state molecules will directly reach the ground state. Else, one of the other possibilities is that, there can be an inter system crossing, which results in the transformation from excited singlet to excited triplet state, ac^3 as shown in Equation (5.6).



From Equation (5.3), we have already seen that there is a possibility to have diacetyl molecules in the presence of acetone. For these diacetyl molecules (di) to undergo phosphorescence, they have to be excited into triplet states, di^3 . This excitation of the ground state diacetyl molecules into excited triplet state is possible by the interaction with excited acetone molecules. Through inter molecular collisions, there can be an energy transfer to diacetyl, and this process is referred as ‘photosensitization’¹⁵⁴. After this transfer of energy, excited triplet state acetone molecule returns to ground state. The corresponding conversion is shown in Equation (5.7).



These excited triplet state molecules now might undergo de-excitation, thereby contributing to the strong emission signal of acetone vapour excited at 310 nm. From Equation

(5.8), it can be seen that the excited triplet state diacetyl is de-excited and it emits a photon of frequency ν_e . This diacetyl formation shown in Equations (5.2) and (5.3) reduces as the excitation wavelength is not close to 310 nm. At other wavelengths, there is increase of photodecomposition, and thereby hindering the formation of diacetyl, which can potentially aid to enhance phosphorescence of acetone¹⁵⁵.

5.4 Experimental investigations with acetone in the second experimental chamber

In this section, we will present the investigations carried on the second experimental chamber. All the experiments presented in this chapter were performed with pure acetone vapour. Experiments were conducted at different conditions of pressure and temperature. A large number of experiments was studied to develop the experimental protocol and improve the repeatability of the data. The focus has been to understand the variation of intensity and lifetime dependency as a function of pressure and temperature, considering the influence of air/oxygen on phosphorescence, forward and reverse cycling at same temperature, and cycling with temperature variation. Single exponential and bi-exponential functions have been used to fit the experimental phosphorescence lifetime curves and the corresponding time constants have been evaluated.

5.4.1 Treatment of experimental data

A brief discussion on the image analysis has been presented in Chapter 4. In this section, we expand this discussion by providing various manners in which the experimental image can be treated.

The experimental image of photoluminescence is a matrix (see section 4.2.3) with a particular count assigned to every pixel. From the manual provided by LaVision, we gather that the dark noise of ICCD can be due to the shot noise of photocathode, the CCD dark noise, the photocathode dark noise, and the readout noise. Therefore, there is always some unnecessary information generated due to this dark noise, that must be subtracted from the captured images. This process can be automatically done with the camera software. This subtraction was always carried out in all the experiments in the study (both in the first and second experimental chamber).

However, during image analysis, we noticed that in spite of removing this dark noise, the images being captured still had ‘some noise’ which is a source of unnecessary information. This noise is different from the dark noise and we refer to it as ‘background noise’. The camera captures all the light within its field of view; it doesn’t make a distinction between the light from background sources and the photoluminescence of molecules. Even though the experimental arena is isolated from other sources of unnecessary light by covering with a thick black cloth, there are still ‘some gaps’ through which the light will pass and this information is recorded in the images captured. Therefore, this unnecessary source of background information has to be removed by capturing a ‘background image’, generated in the same conditions than the experimental image of interest, and subsequently subtracted to the this image of interest.

5.4.1.1 Noise from background image

To understand the influence of the background image and the corresponding counts generated in these images, an investigation was carried out. For every image captured for phosphorescence analysis, immediately after finishing the acquisition, a background image was captured at the same experimental conditions. Therefore, for capturing the background image, the laser was continuing to emit light, but the laser beam was blocked by thick sheets of papers and black cloth. This ensured that no laser beam energy was reaching the integration zone of the camera.

Figure 5.8 shows the level of intensity of the background images captured. For this discussion, we show 5 typical experimental repetitions. The background image is taken at the usual delays t at which we had captured experimental images, and the other parameters of image acquisition were: $N_l = 100$, $N_i = 5$, $G = 100\%$, $\Delta t_{gate} = 100$ ns. The total intensity counts (S_T) of all the pixels (344×260) for every image are summed up and are plotted as a function of delay t . As it can be observed from these images, even though the ‘dark noise’ has been subtracted and there is no laser beam passing through the chamber, there are still counts in the image.

Also, it can be observed from Figure 5.8 that there is a variation in the scale of noise from one experiment to another. To estimate an average value of counts per pixel, we divide S_T by the total number of pixels (344×260). Experiment 3 has the highest number of counts for all pixels (275141), and the average value per pixel in this case is 3.07, and RSD of S_T is 6.03%. Experiment 2 has the lowest number of counts for all pixels (183956) and the average

per pixel in this case is 2.08. Thus the average counts per pixel is close to zero. The values of RSD for other experiments are presented in Table 5-3.

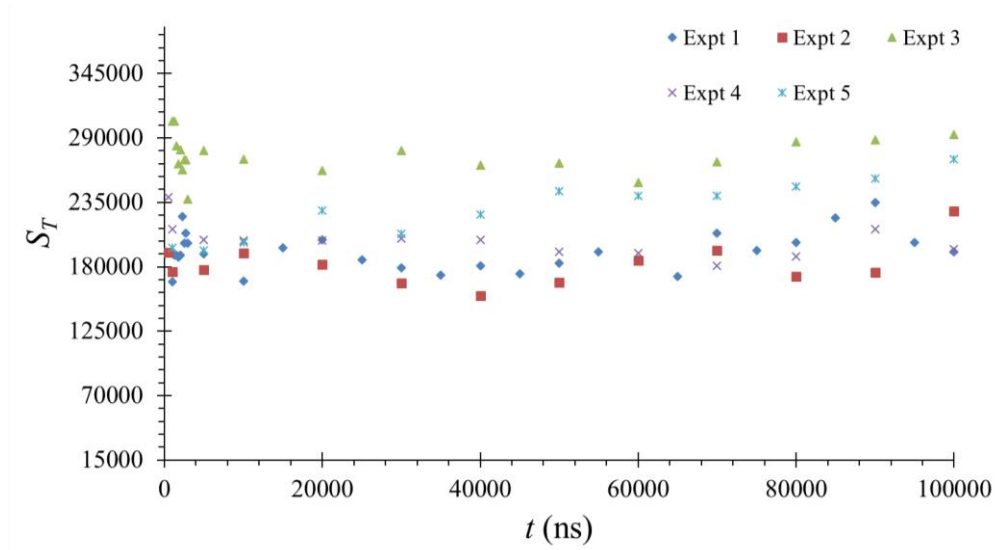


Figure 5.8. Total number of counts of all pixels for the background image noise

This suggested that it would be necessary to capture a background image for every delay time to make the corresponding subtraction. This implies that the time duration of capturing the images would considerably increase. For a 20 Hz laser with image acquisition parameters of $N_l = 100$, $N_i = 5$, $G = 100\%$, $\Delta t_{gate} = 100$ ns, the time of acquisition for 25 delay time images would be ~ 625 sec or ~ 10.5 min. The covering of exit of laser beam at every delay time to capture the background image (in a real experiment) has to be done manually. We required about 60 sec every time we performed this step, and this would further add 10.5 min. Thereafter, with the same image acquisition parameters, we have to capture background image and this would take ~ 10.5 min. Therefore, with background image capturing, the same experiment would take ~ 31.5 min. Therefore, there is a threefold increase in the time of experimentation with this method of capturing background images. To avoid this, a practical approach must be found to perform and reduce time of experiments. This increase of experimental duration can be avoided by just taking background images at regular intervals. This change in the procedure would not result in the alteration of the experimental conclusions, but would result in considerable gain in the time of experimentation. The following paragraph demonstrates the validity of this approach.

Table 5-3 Variation of S_T , average counts per pixel, and relative standard deviation for the experiments shown in Figure 5.8

Experiment	S_T	Average counts per pixel	RSD of total counts (%)
1	193,923	2.15	7.86
2	183,956	2.05	8.78
3	275,141	3.07	6.03
4	199,400	2.22	7.91
5	235,920	2.63	11.42

It can be noted from Table 5-3 that the relative standard deviation of the total number of counts varied from a maximum value of $\sim 11\%$ to a minimum value of $\sim 6\%$. The typical contribution from the background counts is only about 3 to 19 % of the total intensity counts in the image (see section 5.4.2.1.1). Therefore, we can capture images at regular intervals (one background image for every four acquisitions) and make an average of these images to generate one ‘average background image’. In this way, for 25 delay times, 6 background images would be required, and this will bring down the experimental duration from 32.5 minutes to 20.5 min. Then we can make the subtractions of this average background image to the main image. As mentioned, the relative standard deviation of the counts for the background images varied between 6 to 11 %. Therefore, this would not result in any discernible difference between the approaches of having a background image for every delay and carrying subtraction; or taking an average background image and carrying subtraction with this image. Therefore, the approach of averaging by capturing the images at regular intervals can be applied in our analysis.

5.4.2 Image analysis

In this section, we present the details on the different manners in which an image can be processed for subsequent analysis.

5.4.2.1 Analysis by Gaussian fitting

Let x_i represent the pixels in the x -direction, and y_j represent the pixels in the y -direction. Let $I_{i,j}$ be the intensity value at a particular location. In our case, i varies from 1 to 260 and j from 1 to 344. For every pixel in the x -direction, we sum up all the intensity values

in the y -direction, and then make an average value. This is of interest if the beam is parallel to y -direction and there is no variation of phosphorescence intensity along the beam. This process is repeated for every pixel in the x -direction. Once we obtain this information, a Gaussian curve is fitted to the obtained data. In our initial experiments shown in Chapter 4, we were yet to understand the process of subtracting background information.

5.4.2.1.1 Analysis after subtraction of background image

The background image in this case has been obtained by averaging blank images obtained at regular intervals, as described in Section 5.4.1.1. We carried out a pixel-by-pixel correction with this background image and then fit a Gaussian to the generated data as mentioned in 5.4.2.1. The process is detailed with an image obtained at the following experimental conditions: pure acetone vapour at $P_{ac} = 5,000$ Pa, $t = 500$ ns, $N_l = 100$, $N_i = 5$, $G = 100\%$, $\Delta t_{gate} = 100$ ns

The approach of background subtraction is as follows: for every pixel in the main image (Figure 5.9a) and background image (Figure 5.9b), the number of counts is measured. We subtract the counts of the background image for each pixel from the corresponding pixel counts in the main image. The final image after background pixel-by-pixel subtraction is shown in Figure 5.9c.

Figure 5.9d shows the Gaussian fitted to the data of Figure 5.9a. From this image, the peak of the Gaussian is identified with a value of 891.1 counts. Figure 5.9e shows the y – averaged intensity values of the background image and it can be seen that for every pixel, the average counts is ~ 2.2 . Figure 5.9f shows the Gaussian fitted to the data of Figure 5.9c, and the peak of the Gaussian in this case is identified as 888.9. This background subtraction doesn't significantly change the peak of the Gaussians. Similarly, the total number of counts in each of these three raw experimental images for Figure 5.9a, b, and c, are 6065089, 193049, and 5872040, respectively.

The background image is subtracted for every value of delay time t to get a corrected image. The ratio of the total background counts over the total number of counts of the initial image (before subtraction) is shown in Figure 5.10 as a function of t . It can be noted from this figure that for delay times below 10,000 ns, the background contribution is lower than 5%. This implies that the signal is strong in comparison with the background. At higher delays until 50,000 ns, it is lower than 12%. At 100,000 ns, the contribution is around 19%. This analysis shows that the influence of the background effect increases with higher delays. At higher t

phosphorescence signal decreases, but the noise level of the background counts remains same. Therefore, there is an increase in the background contribution to the total counts. Thus, there is also an increase in the noise over signal ratio.

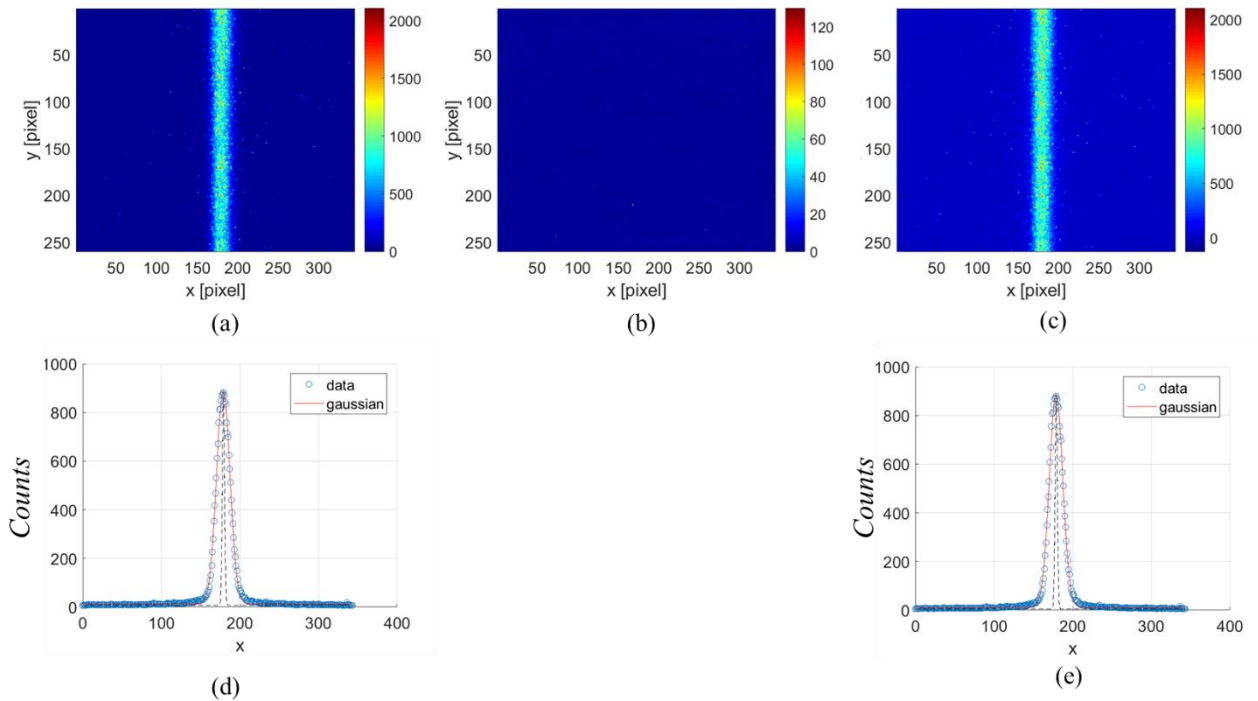


Figure 5.9. (a) pure acetone vapour at $P_{ac} = 5,000$ Pa and $t = 500$ ns, $N_l = 100$, $N_i = 5$, $G = 100\%$, $\Delta t_{gate} = 100$ ns (b) corresponding background image, (c) subtracted image, (d) Gaussian fitting for image a, (e) Gaussian fitting for image c.

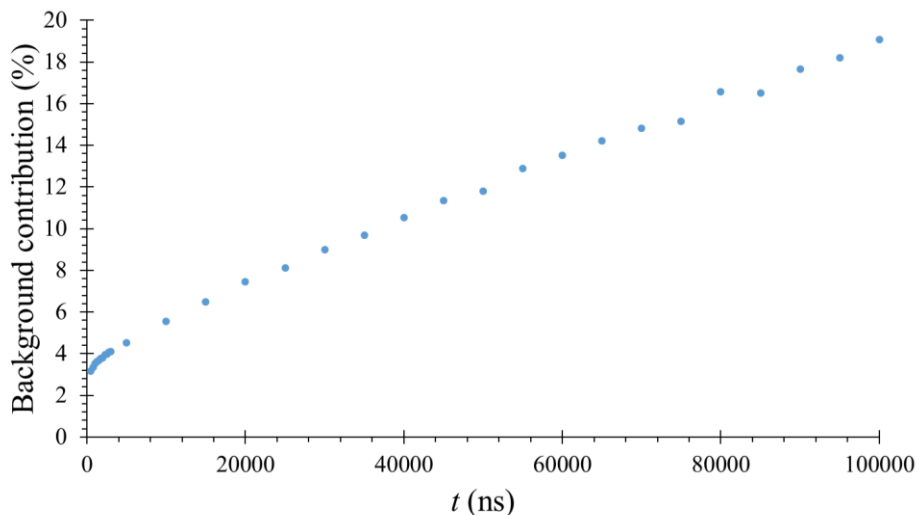


Figure 5.10. Background contribution to the total number of counts in the image

Figure 5.11 shows the lifetime curves obtained for pure acetone vapour at $P_{ac} = 5,000$ Pa, from the total number of counts and from the Gaussian peaks, with and without background subtraction. Without taking background correction into account, we overestimate the intensity values, and this overestimation is a function of delay and can be up to 19% at the highest delay considered in this study (100,000 ns).

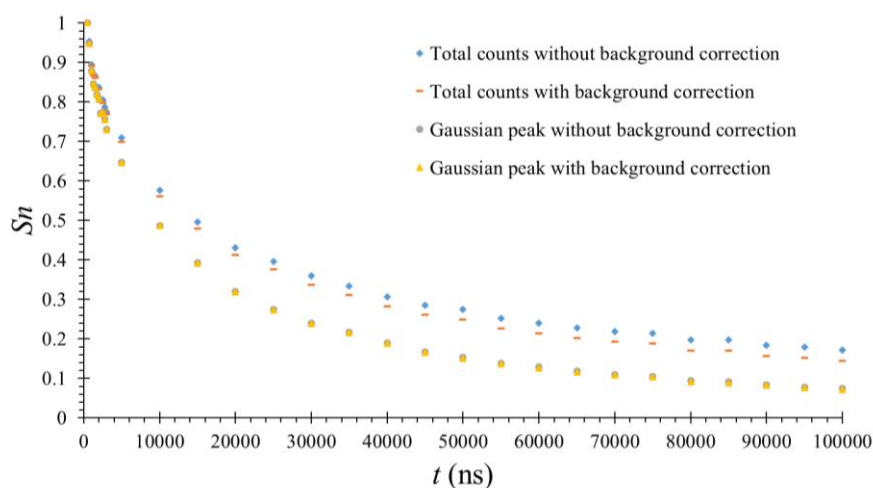


Figure 5.11. Lifetime curve at $P = 5,000$ Pa. The figure shows the different manners to analyse the experimental image.

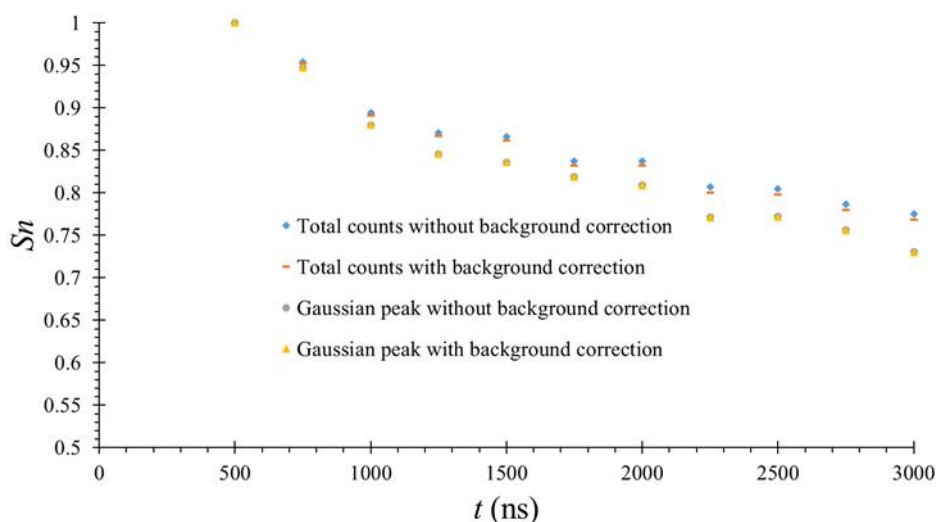


Figure 5.12. Zoomed portion of Figure 5.11

Another approach consists of considering the intensity value of the peak of the fitted Gaussian as the representative point of interest, and observe its evolution with time. Since the scale is different between these two approaches, results are normalised by the highest intensity (obtained at 500 ns). For the shortest delays, during the first 3,000 ns, the normalised signal is very close with and without background correction, considering total numbers of counts as well as Gaussian peaks. This information is shown in Figure 5.12. Therefore, if the interest of analysis lies in the first 3,000 ns, both kinds of analysis would yield similar results. Thereafter, at higher delays, considering the total number of counts requires taking into account the background noise.

For next figures, we will only consider lifetime curves based on the Gaussian peaks, which are naturally much less sensitive to the background noise.

5.4.3 Leakage experiments – influence of air on the phosphorescence signal quenching

In chapter 4 (see section 4.9.1.2), we argued the need for a leakage free chamber. Previous researchers have shown that oxygen quenches the photoluminescence signal^{129,130}. However, those studies were not focusing on acetone vapour at low pressure conditions. Therefore, we have carried out an investigation on signal quenching. Modifications were made by creating an additional volume in the experimental configuration, as shown in Figure 5.13. The volume of air introduced in the experimental chamber was controlled as follows:

Step 1. All valves A_0, A_1, A_2, A_3, A_4 are closed. Valve A_2 is connected to the vacuum pump, which is always turned on. Valve A_0 is connected to the acetone vapour.

Step 2. Valve A_4 is opened. This will introduce air in the volume between A_3 and A_4 .

Step 3. Valve A_4 is closed and Valves A_1 and A_3 are opened. The other valves are still closed. This will introduce air in the entire network.

Step 4. Valve A_1 is closed and Valve A_2 is opened. The other valves are closed. This will vacuum the region between A_1 and A_2 .

Step 5. Valve A_2 is closed and Valve A_1 is opened. The other valves are still closed. This will allow the air between A_0 and A_1 to expand, resulting in the reduction of pressure in the entire system. We repeat steps from 1 to 5 until the desired pressure of air is achieved in the system. The pressure read at this instant corresponds to the air pressure in the system.

Step 6. Valve A_1 is closed and Valve A_0 is opened. This will introduce acetone in the system. During this step, there is a possibility of air removal from the system due to diffusion. However, the pressure in the acetone pipeline is the saturation pressure of acetone vapour at room temperature (~ 24 kPa at room temperature), and the pressure of air in the chamber is much lower than this value, as shown in Table 5-4. Also, due to the rapidity of this step of introducing acetone (~ 10 seconds), we supposed that this effect of diffusion was negligible. Valve A_0 is closed when the desired total pressure is achieved. From the total pressure P_{total} and the partial air pressure P_{air} , the acetone partial pressure $P_{ac} = P_{total} - P_{air}$ is calculated.

All the experiments were carried out at room temperature and excitation wavelength of 310 nm. The energy was continuously monitored during the experiments. We maintained the partial pressure of acetone $P_{ac} \sim 5,000$ Pa and varied the partial pressure of air, P_{air} , from 163 to 3,320 Pa. Table 5-4 shows the experimental conditions. It can be noted that the ratio of partial pressures of acetone and air, $\left(\frac{P_{air}}{P_{ac}}\right)$, varied from 0.0340 to 0.6574. Air is a complex mixture of various gases. However, for the purpose of this study, we can assume air to be only a mixture of nitrogen and oxygen, with the later contributing to 21% of partial pressure. Therefore, the partial pressure of acetone and oxygen, $\left(\frac{P_{O_2}}{P_{air}}\right)$, varies from 0.0071 to 0.1380.

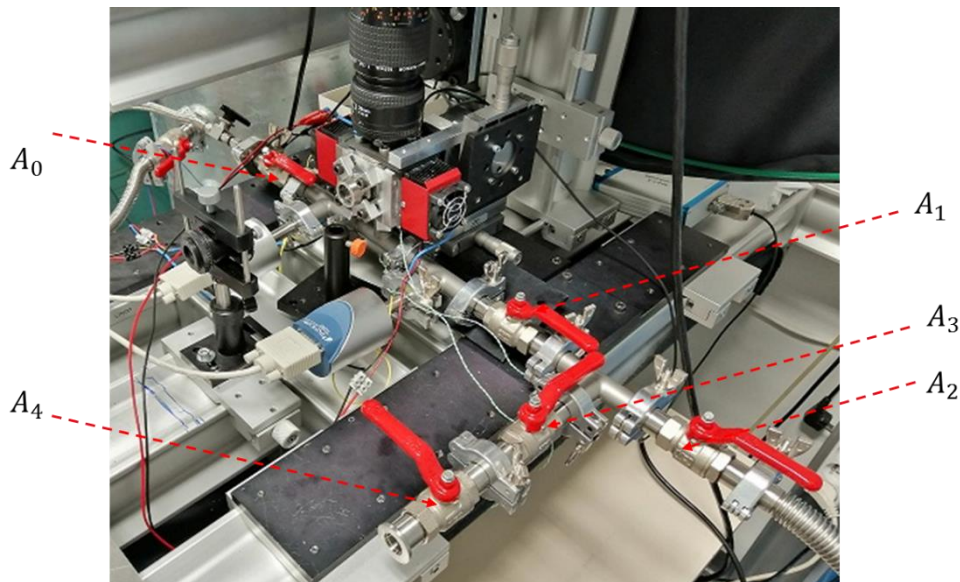


Figure 5.13. Experimental apparatus for determining the influence of oxygen on photoluminescence

Table 5-4. Variation of ratio of partial pressures of air/oxygen over acetone vapour to study quenching

P_{ac} (Pa)	P_{air} (Pa)	P_{O_2} (Pa)	P_{total} (Pa)	$\frac{P_{O_2}}{P_{ac}}$	$\frac{P_{air}}{P_{ac}}$
4,781	163	34.23	4,944	0.0071	0.0340
4,800	320	67.2	5,120	0.0140	0.0666
4,985	565	118.65	5,550	0.0238	0.1133
4,992	788	165.48	5,780	0.0331	0.1578
5,080	1,110	233.1	6,190	0.0458	0.2185
5,040	1,630	342.3	6,670	0.0679	0.3234
5,100	2,320	487.2	7,420	0.0955	0.4549
5,050	3,320	697.2	8,370	0.1380	0.6574

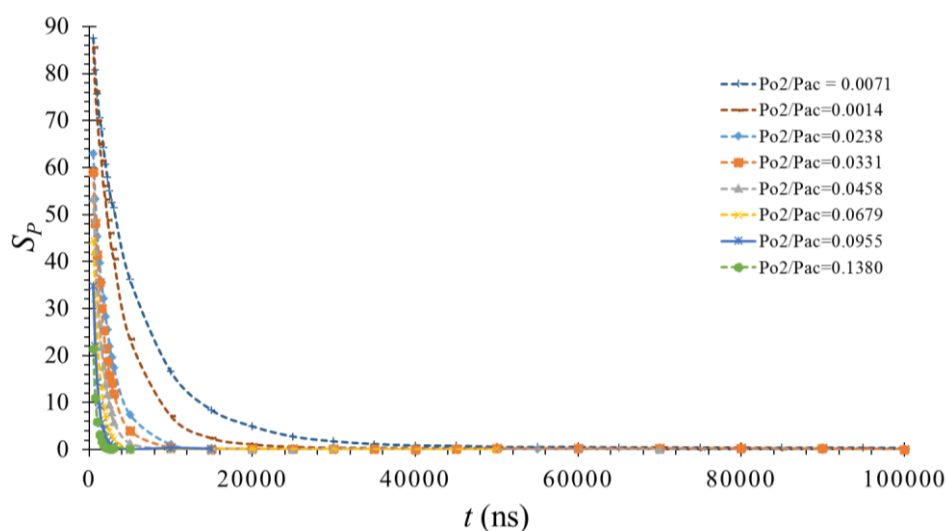


Figure 5.14. Signal quenched by the presence of oxygen in the system

Figure 5.14 shows the evolution of the signal intensity with time for different values of the ratio $\frac{P_{O_2}}{P_{air}}$ described in Table 5-3. The images have been analysed as discussed in Section 5.4.2. For every curve, the number density of acetone was aimed to be kept constant (with a variation of $\sim 5\%$). Therefore, it can be observed that an increase in the number density of oxygen drastically reduces the lifetime luminescence. For instance, for $\frac{P_{O_2}}{P_{ac}} = 0.0071$, which corresponds to only 0.7% of oxygen in the system, the signal is significantly quenched, and close to zero at 30,000 ns. On increasing the oxygen percentage, the phosphorescence signal is

dramatically lost, which is particularly observable for delays less than 10,000 ns, as shown in Figure 5.15. In this figure, we can observe that the signal for $\frac{P_{O_2}}{P_{ac}} = 0.1380$ is close to zero within the first 1,500 ns.

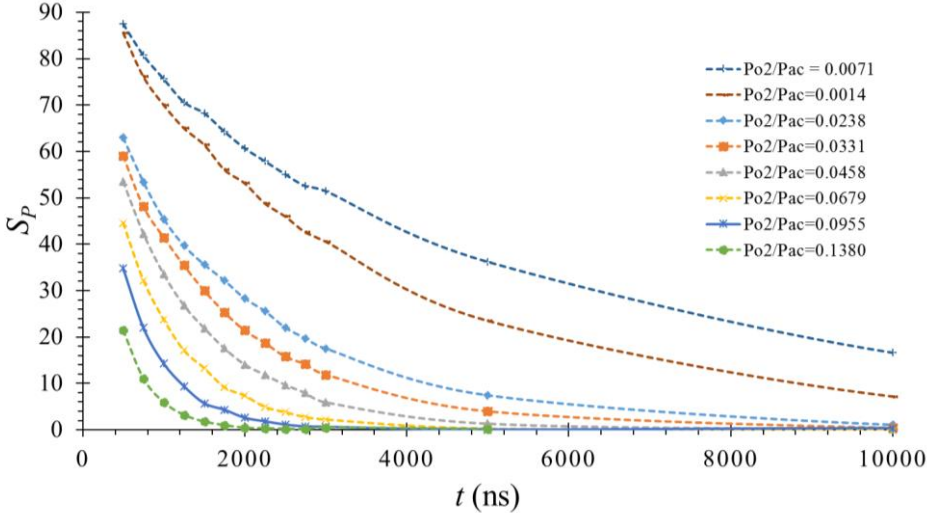


Figure 5.15. Zoom on Figure 5.14 for delay up to 10,000 ns

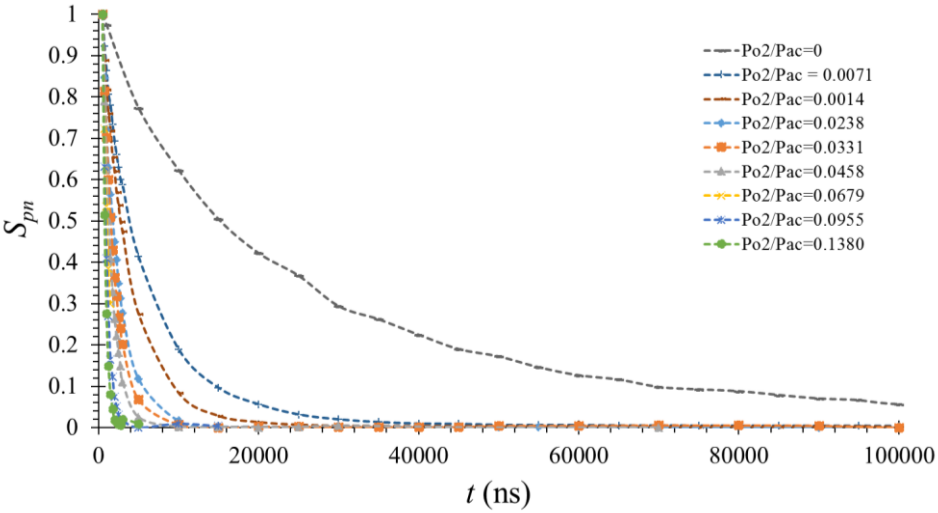


Figure 5.16. Comparison of normalised data

These results are compared with the case in which there are no leakages. The additional data point, $\frac{P_{O_2}}{P_{ac}} = 0$, is at $P_{ac} = 5,000$ Pa for pure acetone vapour at room temperature and compared to the other data in Figure 5.16. If the experiments would be conducted by a different

research group or even with our setup by altering the acquisition parameters, then the absolute values of S_p shown in Figure 5.14 would differ. Therefore, it is interesting to compare the data $S_{pn} = S_p/S_{pmax}$ normalised with the highest number of counts S_{pmax} obtained in our case at 500 ns. Every change in the experimental configuration would result in the alteration of the scale of the image, but as the physics of the investigated problem remains the same, the normalised values should yield similar trends. This comparison is shown in Figure 5.16.

In Figure 5.16, we can notice that whatever the delay, normalised intensity values are much higher in the absence of oxygen. Until 100,000 ns, a signal can clearly be observed, which is not the case even with the presence of oxygen. This study demonstrates the importance to have a leakage free environment during the experiments as even a small percentage of oxygen in the mixture rapidly quenches the signal.

5.5 Influence of laser pulses on acetone vapour composition

In this section, the influence of the laser pulses on the possible alteration of chemical properties of acetone is discussed. Photolysis refers to the breakdown of acetone molecules on repeated excitation with laser at UV wavelengths. If this occurs in the system, the mixture is no longer pure acetone vapour, and there is a reduction in the number density of the acetone vapour. This would result in erroneous conclusions regarding the dependency of intensity and lifetime with temperature or number density. Therefore, it is of interest to investigate possible photolysis for the experimental conditions at which acetone vapour is used in the setup. Thurber et al¹²⁹. carried out similar kinds of studies. In their study, the authors studied the acetone vapour photolysis at 10,000 and 5,000 Pa, subjected to 12,000 pulses at wavelengths of 248, 266 and 308 nm. They employed energy densities of the order of 50 mJcm^{-2} , and could notice a decrease in normalised intensity up to 10 % in some experiments at 266 nm. However, in the present study, we performed experiments at much lower pressures of the order of 1,000 Pa and at 310 nm. As far as we know, information about photolysis in these conditions is not available in the literature. Therefore, experiments were performed to analyse photolysis studying the influence of number of pulses on the acetone chemical structure.

Considering 500 pulses per averaged image and 30 images for a lifetime curve experiment, the acetone vapour is subjected to 15,000 pulses (for each experiment). The average energy density in our study was in the range 0.04 to 0.08 Jcm^{-2} . Therefore, it has been investigated if subjecting the acetone vapour to a large number of pulses at this energy density

might alter its chemical structure. For this, we carried out experiments with pure acetone vapour at 1,000 and 5,000 Pa. The results at 1,000 Pa are presented below. We introduce acetone vapour at time $t = 0$ and wait for pressure stabilisation in the system. The lifetime curve is captured by varying the delay time from 500 to 100,000 ns in increasing steps. Then, with the same acetone vapour, the same experiment is repeated in decreasing steps of delay time.

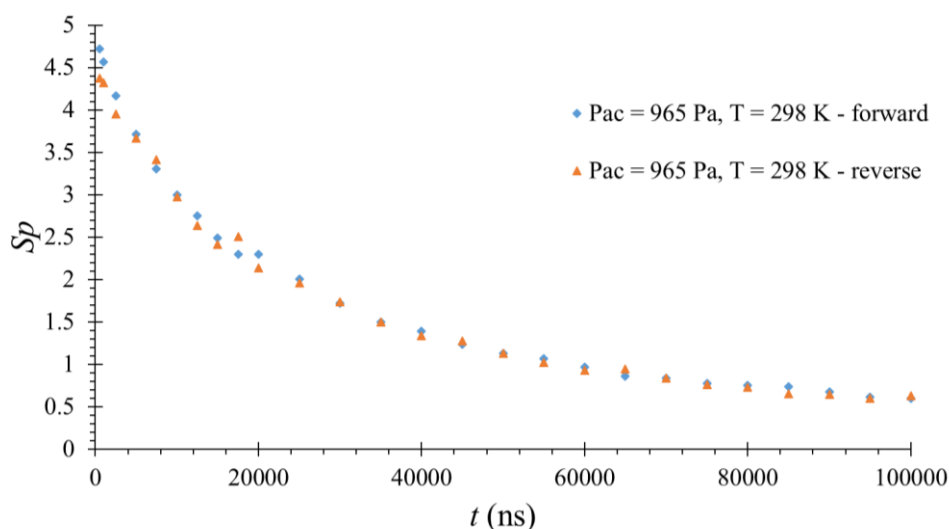


Figure 5.17. Experiment with pure acetone vapour at $P = 965$ Pa and $T = 298$ K

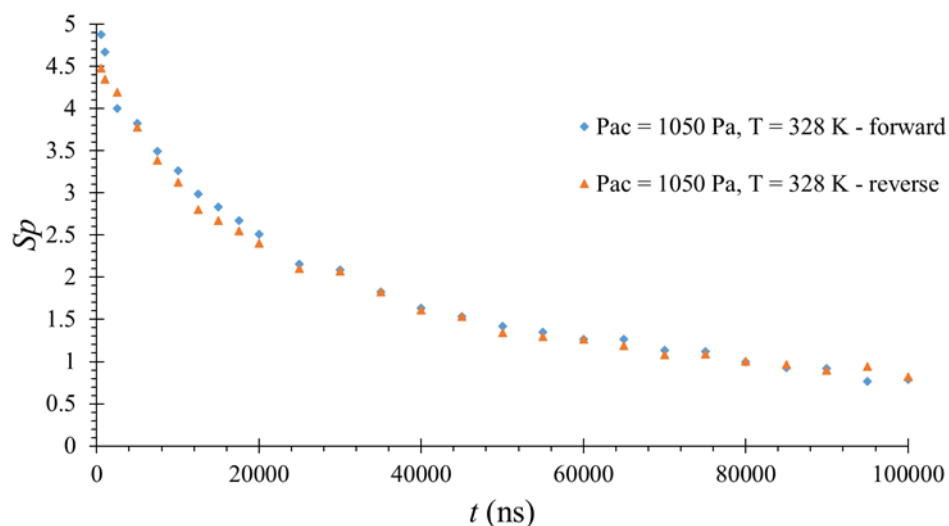


Figure 5.18. Experiment with pure acetone vapour at $P = 1050$ Pa and $T = 328$

Figure 5.18 and Figure 5.17 was about one hour (half an hour for each curve). As it can be noted from these figures, similar curves are obtained in both forward and reverse experiments. The experiments shown in this section prove that the chemical structure of acetone vapour was not being altered due to repeated exposure with the laser pulses. The observations of little variations can be attributable towards changes in pressure and temperature, and are not

due to the alteration of chemical structure in the system. Similar conclusions could be drawn from the experiments done with acetone vapour at 5,000 Pa.

5.6 Experimental investigation at different conditions of pressure and temperature on pure acetone

The next set of experiments focused on understanding the influence of pressure and temperature on intensity and lifetime. The experimental investigation was carried out following the protocol of Section 5.2 with the laser wavelength set to 310 nm. The image acquisition parameters were: $N_l = 100, N_i = 5, G = 100\%, \Delta t_{gate} = 100 \text{ ns}$. The energy was continuously recorded at the exit of the laser beam in the chamber. Table 5-5 shows the experimental conditions at which the experiments were carried out. In these experiments, the main objective was to isolate the effect of temperature from that of number density. Therefore, acetone was introduced at pressures shown in Table 5-4 at room temperature. Thereafter, the same acetone vapour was heated to higher temperatures, namely 328 and 343 K. As the volume of the chamber is constant, heating changes the pressure in the system. However, the number density remains constant. In this manner, we can see the influence of heating on the acetone vapour luminescence. These experiments are different from those presented in Chapter 4, where we were changing the mixture to keep the pressure constant. Therefore, there was a combined effect of heating and change in number density, which was affecting the signal. The experiments presented here have been repeated at least 4 times for every experimental condition.

Table 5-5. Experimental conditions with pure acetone vapour excited at 310 nm.

Pressure at 298 K (Pa)	Heated temperatures (K)	Repetitions
1,000	328; 343	6
3,000	328; 343	4
5,000	328; 343	4
10,000	328; 343	4

5.6.1 Intensity dependency with temperature

In this section, we present the experimental results obtained at $P_{ac} = 5,000$ Pa. The results of the other pressures are in Annex C. All the values of Gaussian peaks at different delays have been normalised with the value of the highest intensity, obtained at delay $t = 500$ ns, which is the first delay time for these sets of experiments. This normalises the scale in the range 0 to 1, and we can see the decay behaviour with change in temperature. From Figure 5.19, it can be seen that there is no discernible difference in the lifetime curve with modification of temperature from 298 K to 343 K.

Similar observations were noticed for the experiments at other conditions of pressure (see Annex C). There was no significant dependency in the intensity nor any significant variation in the lifetime curves with the temperature for the range investigated in Table 5-5.

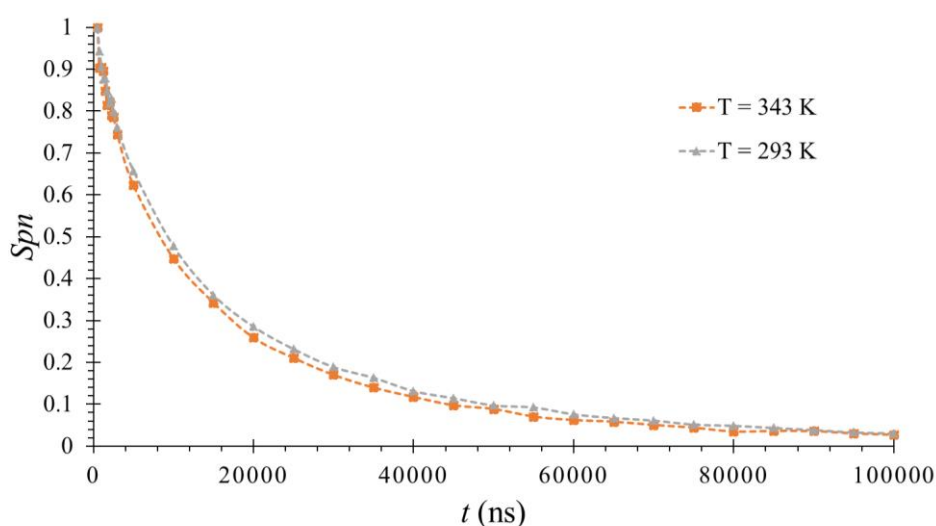


Figure 5.19. Lifetime curve of pure acetone vapour at $T = 298$ and 343 K.

The pressure at $T = 298$ K is $P_{ac} = 5,000$ Pa

5.6.2 Intensity dependency with number density

In this section, we present the dependency of intensity on number density. The previous sections have shown that for the temperature range exploited in our experiments, acetone does not exhibit a strong dependency with temperature. However, changing the pressure in the system, we could observe that there is a difference in the intensity counts as shown in the Figure

5.20. As the volume and temperature were constant for all these experiments, different pressures correspond to different number densities.

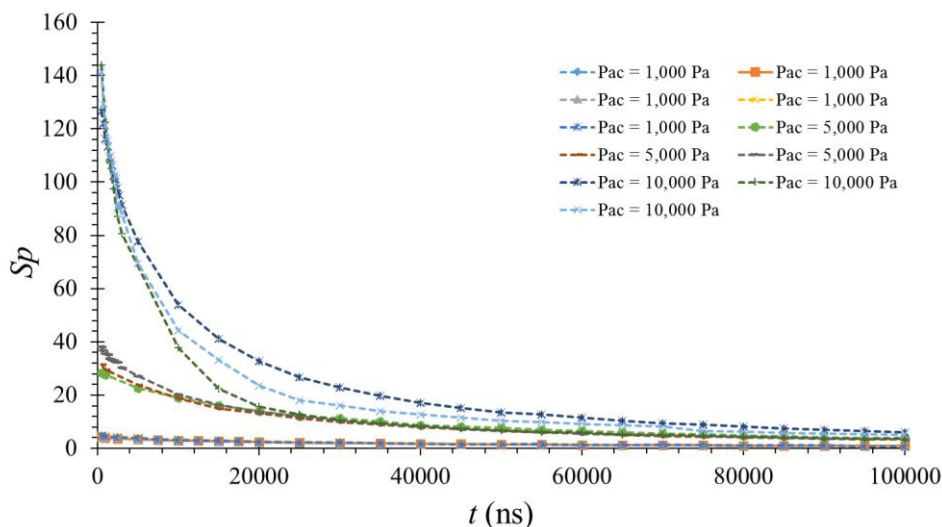


Figure 5.20. Figure showing the lifetime curves obtained at different pressures in the system. It can be seen that there is a difference in the intensity counts with pressure

The highest intensity in the order of 140 counts is obtained at $P_{ac} = 10,000$ Pa. Thereafter, about 35 counts are obtained at $P_{ac} = 5,000$ Pa. The lowest number of counts (about 4) is obtained at $P_{ac} = 1,000$ Pa. As it can be observed from this figure, there is a significant difference in the intensity counts due to the variation of the pressure caused by the changes in the number density of acetone vapour. As explained in Section 4.7.1, the peaks S_p are not just proportional to number density, but also there are other factors, such as absorption cross-sections and quantum yield.

5.6.3 Extraction of time constants

The experimental analysis of Section 5.6.1 revealed that at a fixed number density, for the temperature range investigated in our study, there is no significant variation of intensity with temperature. However, we were noticing intensity dependency with number density. Therefore, further investigations were done to study if the time constants would exhibit number density dependency. The time constant is the amount of time that an exponentially decaying quantity takes to decay by a factor of $1/e$. Since the volume of the chamber is constant, at a given temperature (room temperature for this study), a change in number density implies the

pressure has changed. So, the ratios of pressures in our case, would be also a representation of the ratios of number densities.

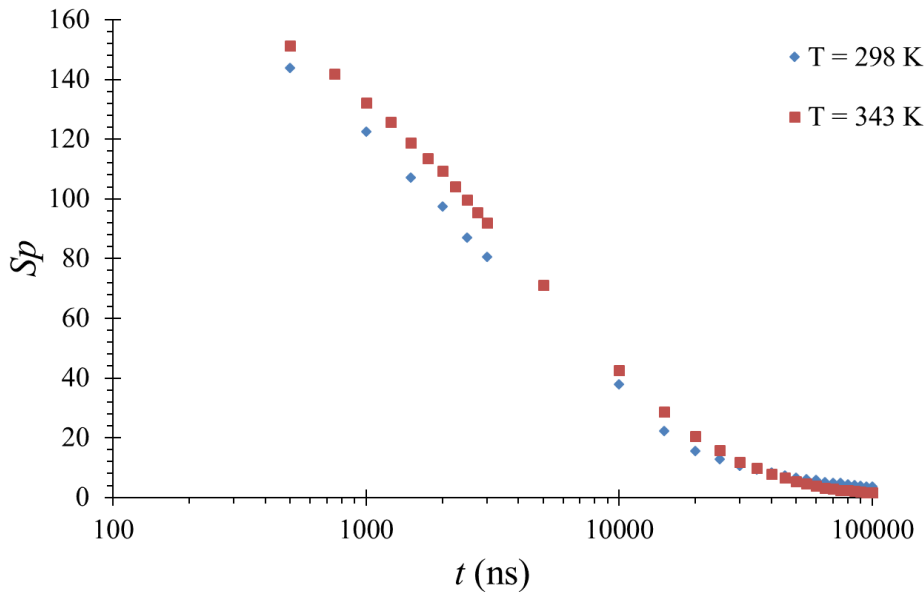


Figure 5.21. Lifetime curve (on logarithmic scale) for acetone vapour at initial conditions of $P_{ac} = 10,000$ Pa and $T = 298$ K. The same acetone vapour was heated to $T = 343$ K.

The decay of acetone vapour phosphorescence closely approximates an exponential behaviour, which is very typical in photoluminescence processes. This fitting of exponential can be done in two ways, either by a single exponential or by a bi-exponential^{130,146}. However, a simple exponential curve does not fit the experimental observations. After a delay of 10,000 ns, the slope of the curve tends to change. This may imply that a double exponential decay curve would be a better fitting function for the experimental data. This observation can be made when we plot the lifetime curve on a logarithmic scale. As an example, the data at $P_{ac} = 10,000$ Pa are shown in Figure 5.21

The rapid decay components describe the early, strong emission. The slow decay components describe the late, weak emission. For the lifetime curves, a bi-exponential of the following form is fitted and the time constants are extracted.

$$f(t) = ae^{\frac{-t}{\tau_1}} + be^{\frac{-t}{\tau_2}} \quad (5.1)$$

Here, a and b are the fitting coefficients, τ_1 and τ_2 are the fast and slow decay components. In case of a single exponential fitting, coefficient b is zero.

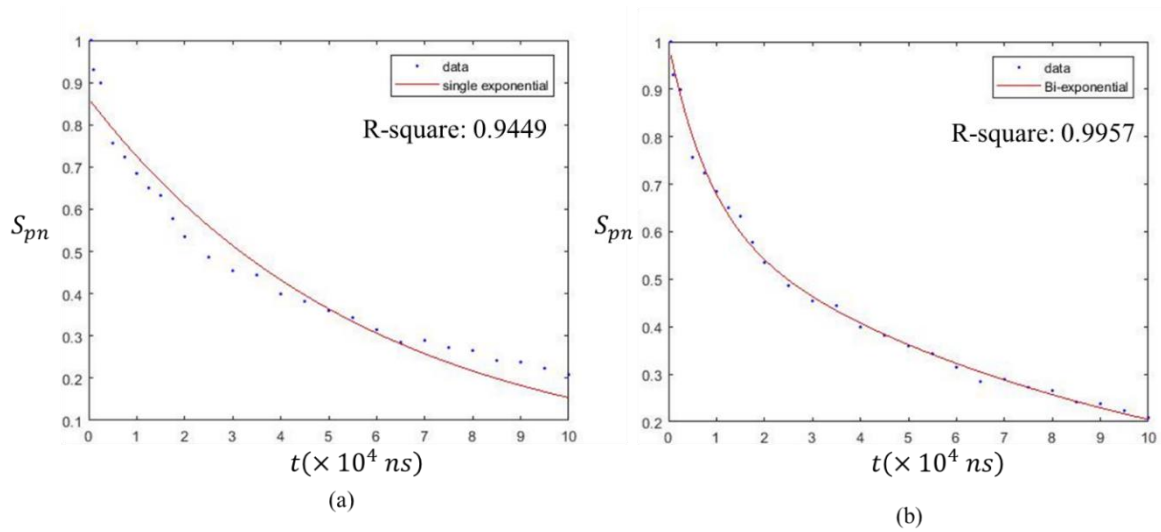


Figure 5.22. Normalised data of Gaussian peaks intensity at $P = 1,000$ Pa.

(a) Single exponential fitting, (b) Bi-exponential fitting

Figure 5.22a and b shows the single exponential fitting and bi-exponential fitting of normalised data of Gaussian peaks obtained at $P_{ac} = 1,000$ Pa. It can be clearly observed that the second order fitting is much better as it improves the coefficient of determination to $R^2 = 0.99$ from $R^2 = 0.94$ for the simple exponential fitting. The time constant estimated for this data from a single exponential fitting is $58.02 \mu\text{s}$, whereas, for the bi-exponential fitting, τ_1 and τ_2 are $8.48 \mu\text{s}$ and $88.12 \mu\text{s}$. Therefore, the bi-exponential fitting is a better representative of our experimental data, as it can capture the two distinct kinds of decaying behaviour. In the further analysis, we will then fit our experimental data with the bi-exponential.

Acetone vapour emission having a better fit with a bi-exponential function can be related to the fact that there is an evolution of phosphorescence signal with time due to the reduction in the triplet states with time (see Section 3.2.5.1). Initially, the populated triplet states are rather high, and there is a strong emission signal due to high number of de-excitations from these triplet states. With time, the triplet population decreases, and thereby, there are lower number of de-excitations and the signal is weaker and the process gets slower. As we have already shown in previous Sections 5.6.1 and 5.6.2, there is no significant dependency of luminescence intensity and lifetime with temperature, but rather with number density.

Therefore, we can focus on data at room temperature to represent the decay curves and estimate their time constants.

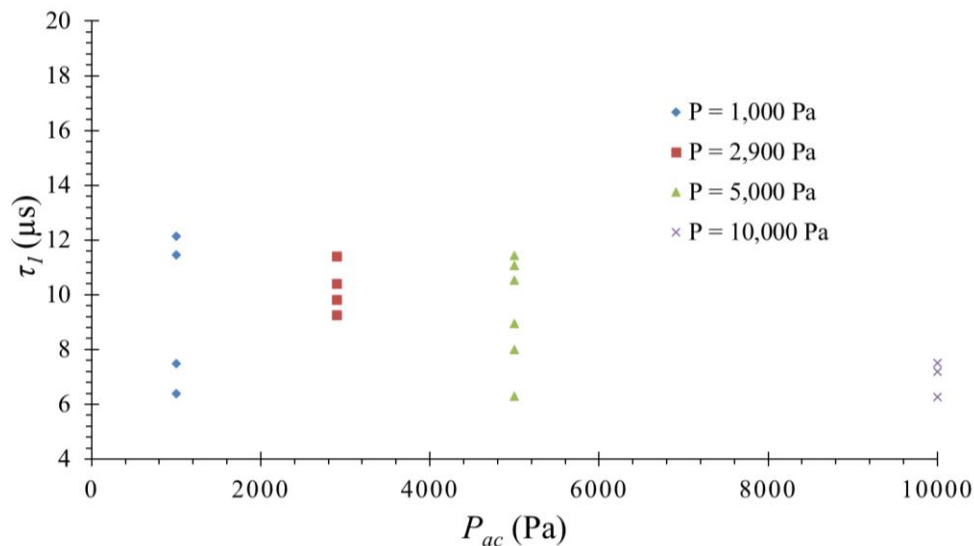


Figure 5.23. Fast decay time constants (τ_1) based on total number of counts, data at $T = 298$ K.

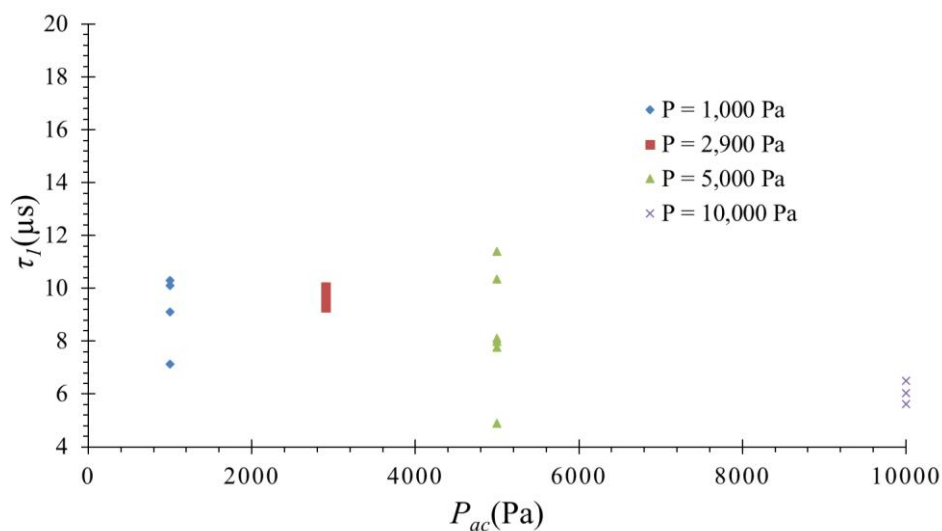


Figure 5.24. Fast decay time constants (τ_1) based on Gaussian peaks, data at $T = 298$ K.

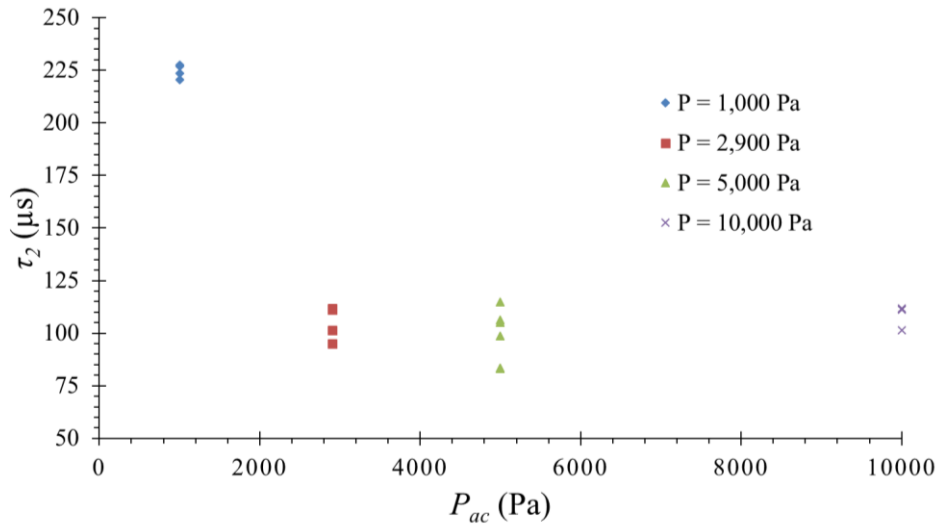


Figure 5.25. Slow decay time constants (τ_2) based on total counts, data is $T = 298$ K.

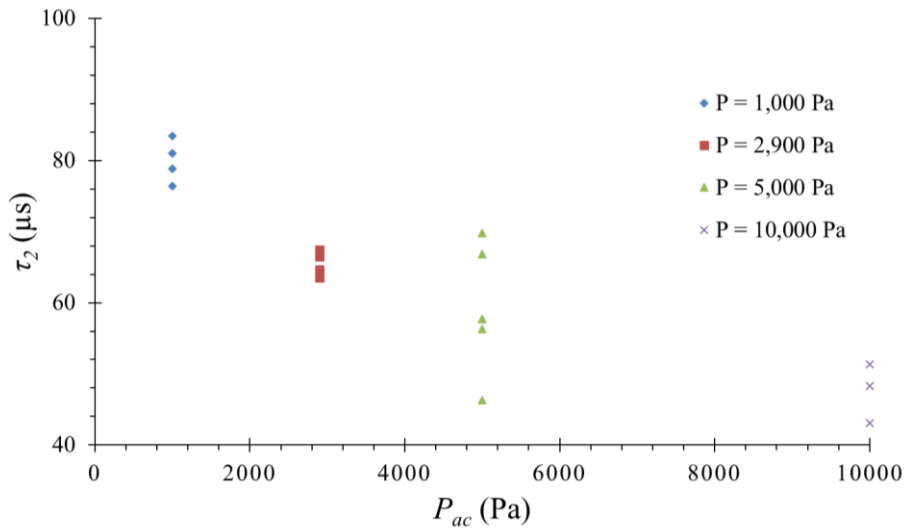


Figure 5.26 Slow decay time constants (τ_2) based on Gaussian peaks, data is at $T = 298$ K.

In this analysis, we present the time constants extracted based on two different ways. This approach of treating data has been presented in Section 5.4.2. The first approach is tracing the evolution of the total counts (S_T) in image(s) and the second approach is tracking the evolution of the Gaussian peaks intensity (S_P). As shown in Figure 5.11, these two approaches yield different slopes in the delayed phosphorescence, and this would imply that the estimation of the time constants should be different with these two approaches. Figure 5.23 shows the fast decay time constants τ_1 , which are fitted for the data based on analysis of total counts. On the other hand, Figure 5.24 shows τ_1 for the data based on Gaussian peaks. For the experimental data obtained in this study at room temperature, the smallest time constant (fast decay τ_1) is of the order of $10 \mu\text{s}$. Based on the two different approaches, we obtain similar values. Therefore,

if the interest is to study the early phosphorescence, it appears that both approaches of treating data are quite equivalent.

Table 5-6 Variation in the time constants for bi-exponential data based on S_T and S_p

P_{ac}	τ_1 variation based on S_T (%)	τ_1 variation based on S_p (%)	τ_2 variation based on S_T (%)	τ_2 variation based on S_p (%)
1,000	44.93	30.77	17.13	8.50
2,900	20.57	7.56	14.19	5.78
5,000	44.93	57.06	27.14	33.66
10,000	16.51	13.67	9.38	15.96

The variation of time constants (based on maximum value reference) for some experimental conditions as shown in Table 5-6. From this data, it can be inferred that the approach based on time constants cannot be used to predict the dependency on temperature, pressure or number density. Firstly, there is no strong dependency at different pressures. Secondly, even for the same experimental conditions, the variations in some cases ($P_{ac} = 5,000$) are as high as 57.06 %. This can be partly due to the fitting functions. The phenomenon of photoluminescence itself is based on the statistical nature of large number of molecules and their ensemble behaviour. Therefore, in a statistical mechanics approach, we have to study the average trend, and not place undue importance on every single variation of the time constants. Therefore, on average, we can see that τ_1 values at different pressures are rather close to each other and do not show any marked differences by variation of pressure in the system.

5.7 Modifications to the experimental chamber

5.7.1 Elements of the new chamber

For this section, the experimental chamber was changed by incorporating a heating element on a small plate inside the chamber as shown in Figure 5.27 and maintaining the chamber walls at a lower temperature. The temperature of the heating element was adjusted with the aid of a thermostat, which can control the temperature as it is coupled with a thermocouple placed on the heating element. The additional hardware required for regulating the temperature of the heating element is shown in Figure 5.28.

A local variation of temperature, and thereby density is expected, notably in the direction perpendicular to the heated element, i.e. in the direction of the laser beam. By tagging the region close to the heated element, it is possible to observe if the gradient of temperature – and consequently the gradient of density – generated along the laser beam influences the intensity captured. Due to the large volume of the chamber, the pressure is expected to stay constant during experiments.

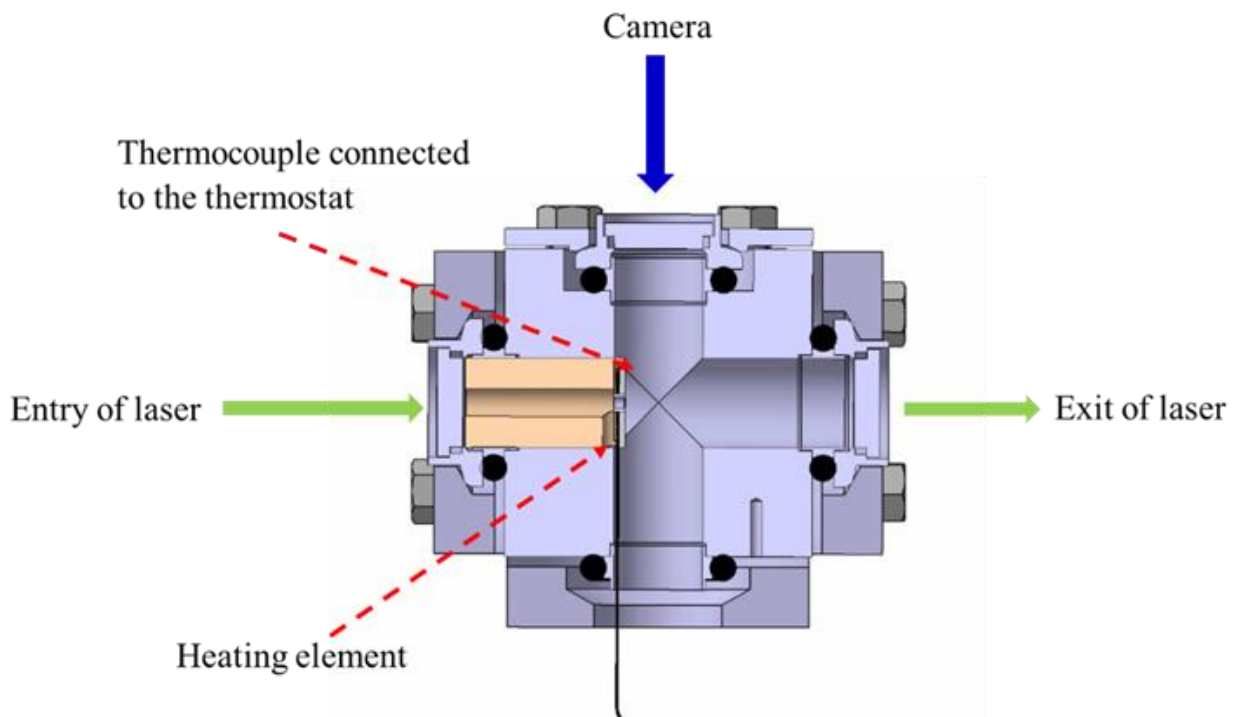


Figure 5.27. Cross sectional view of the experimental chamber showing the positions of the heating element and thermocouple, and the direction of laser beam.

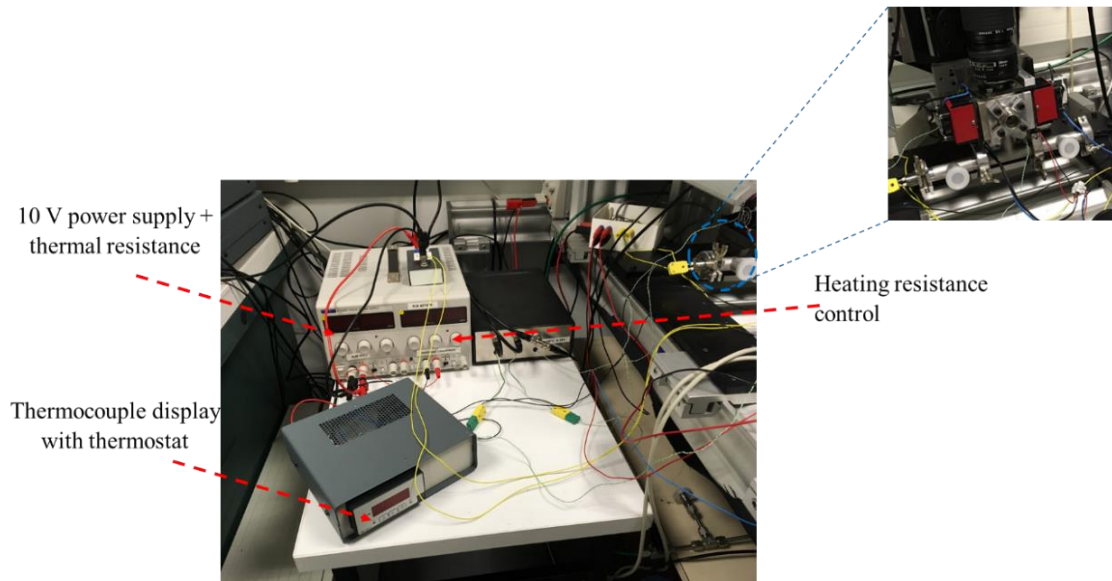


Figure 5.28. Additional heating and control equipment required for regulating the temperature of the heating element introduced in the chamber, shown on the top

5.7.2 Numerical simulations

Simple CFD simulations carried with Ansys Fluent 18.2 were performed in order to estimate the density and temperature gradients generated by the heating element in the chamber. The real experimental system was modelled as a four way cross as shown in Figure 5.29a, to simplify the numerical analysis. The heating element is positioned as shown in Figure 5.29b. Due to the symmetry involved in the design, only one half of the model was simulated. The heating element was modelled as a disk with a hole in the centre having a diameter of 2 mm, which corresponds to the access for the laser beam in the real experiments. The heated element was maintained at 348 K. The meshing option of inflation with progressive transition was employed. The geometry was meshed into 100,381 nodes and 312,086 elements. A viscous (laminar) based model with the fluid properties of acetone vapour was employed. A pressure based solver (including gravity) was used. For the solution methods, pressure–velocity coupling scheme was used. For the spatial discretisation, the following schemes were used: Gradient – least squares cell based, pressure – second order, for density, momentum and energy – second order upwind scheme.

Figure 5.30 shows the normalised variation of density, pressure and temperature along the line passing through the centre of the hole of the laser beam. It can be noted from this figure that there is a sharp drop in the density near the vicinity of the heating element. Based on the previous experimental results, CFD simulations, and modified experimental chamber, further

experiments were carried out to measure temperature gradients through the resulting gradient of number density, in an environment with controlled pressure.

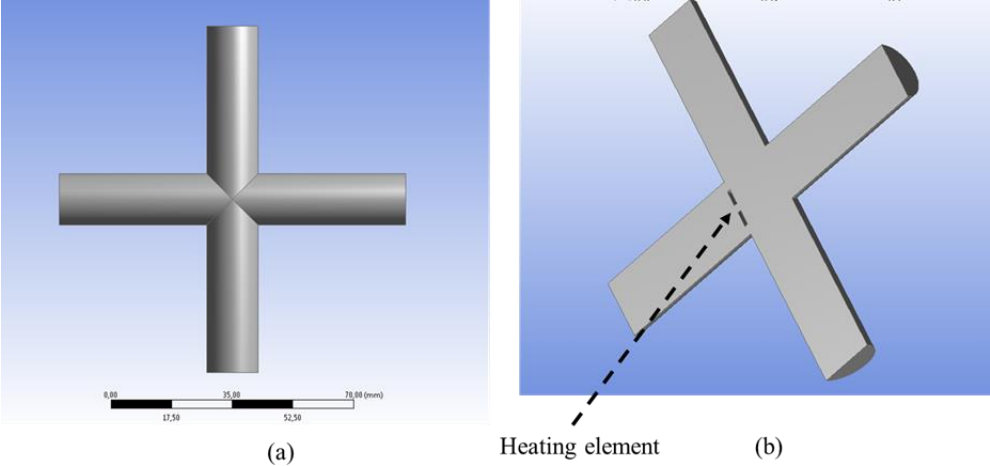


Figure 5.29. (a) Schematic of the simplified geometry used to model the experimental chamber. (b) Symmetry plane with the presence of heating element

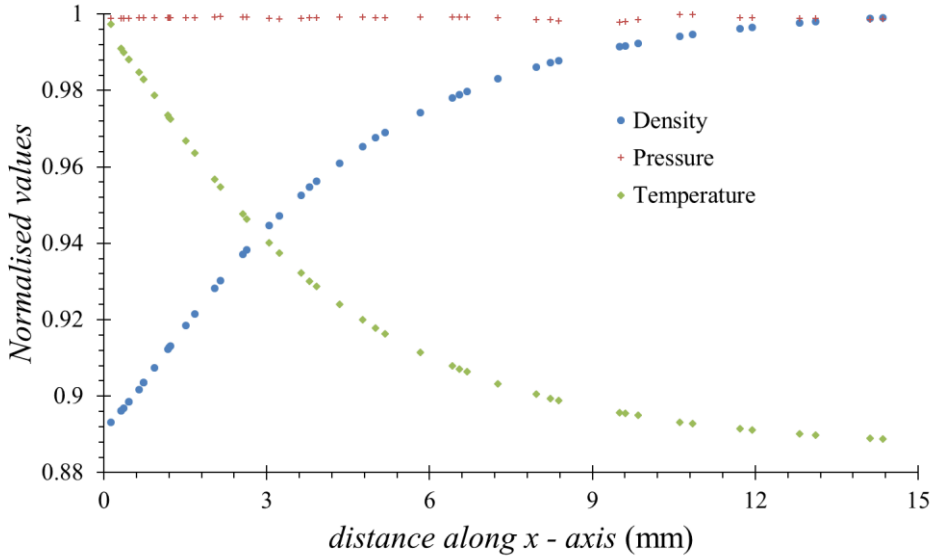


Figure 5.30 Normalised values of the variation of the density, pressure and temperature at the centre of the hole of laser beam, obtained from simulations. The heating element is located around $x = 0$ mm.

5.7.3 Experiments

The protocol for these experiments is as follows:

- The basic steps until the turning on the laser power supply and allowing the laser beam to stabilise is the same as in the previous sections.
- An image is taken with the laser beam turned on and without any acetone vapour in the chamber. This image is taken at $t = 5$ ns after the laser beam excitation, and this image serves as the background image. This image captures all the unwanted reflections and the possible fluorescence emitted by the optical access and reflected by other elements in the chamber. We captured fluorescent images at 5 ns to get the highest possible intensity.
- Then, acetone vapour is introduced in the chamber at room temperature. The pressure of acetone vapour is varied for different experiments. The details are presented in Table 5-7. Thereafter, fluorescent images are captured. These images are taken at room temperature (295 K).
- The acetone vapour is still present in the chamber. The power supply of the heating element is turned on and reaches a stable heated temperature. Thereafter, new fluorescent images are captured.

Table 5-7. Conditions of temperature and pressure for acetone vapour

Initial pressure (Pa) at $T = 295$ K	Temperature of heating element (K)
10,000	295; 348

5.7.4 Image processing

Figure 5.32 shows the details of the background image without covering the experimental chamber to avoid reflections from the surfaces. This background image is taken 5 ns after the laser pulse excitation without any acetone in the system. Based on the fluorescence of the glass window, we can locate the position of the suprasil® window and the heating element. Also, we can notice the screws placed on the top of the chamber. The reflection of the laser beam can also be observed in this image. Therefore, the experimental chamber was covered with a black sheet, exposing just the optical access to the camera. This resulted in the reduction of the reflections being captured by the chamber as shown in Figure 5.33.

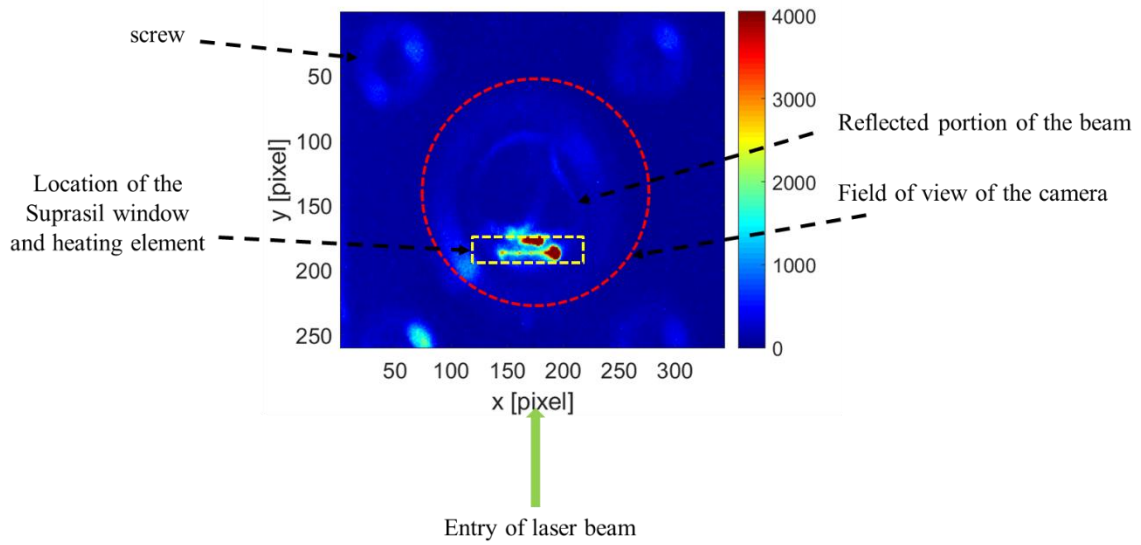


Figure 5.31. Background image taken at vacuum. This image is taken at a delay of 5 ns. The camera captures all the unwanted reflections of the laser beam.

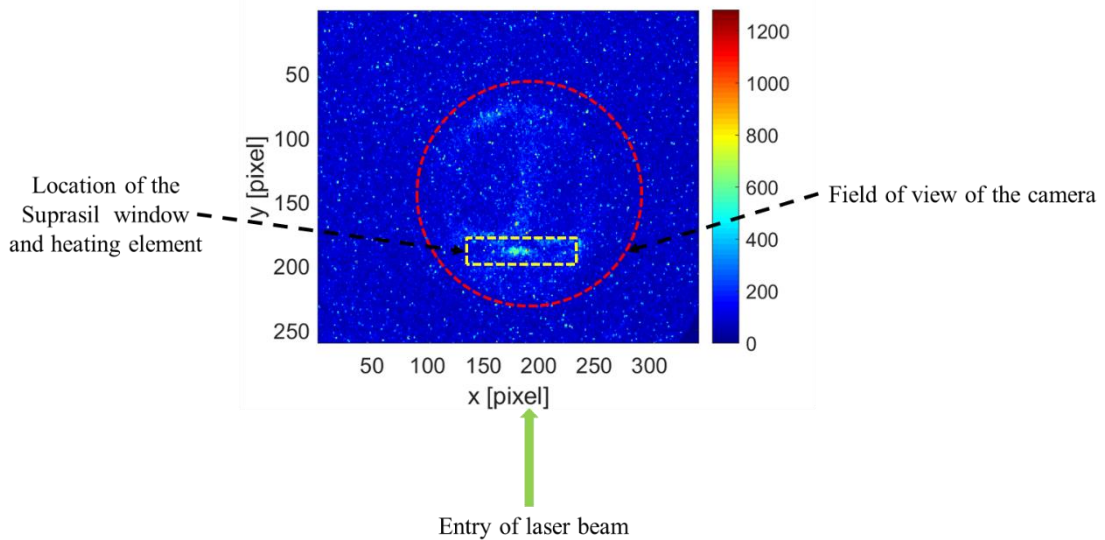


Figure 5.32. Background image taken at vacuum after reducing reflections. The image is taken at a delay of 5 ns. The camera captures all the unwanted reflections of the laser beam.

5.7.5 Experimental images with heated element at 348 K

For the purpose of the discussion in this section, we present the following result: Figure 5.33a shows the experimental image of acetone vapour at $P_{ac} = 10,000$ Pa and room temperature. Figure 5.33 (b) shows the image at $P_{ac} = 10,000$ Pa with the heating element turned

on and maintained at 348 K. Both images are obtained after subtraction of the corresponding background images.

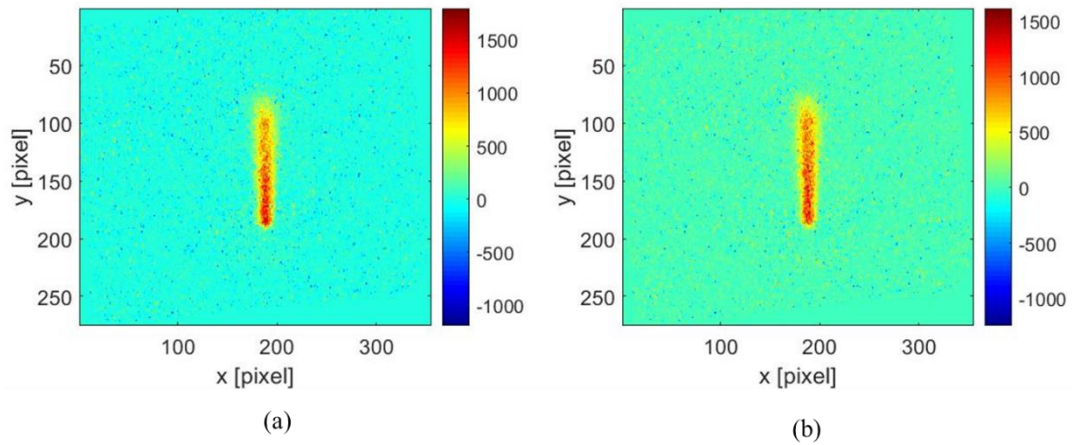


Figure 5.33 Experimental images of acetone vapour at $P_{ac} = 10,000$ Pa and $t = 5$ ns after subtracting corresponding background images. (a) chamber at room temperature, $T = 295$ K, (b) heated element maintained at $T = 348$ K

5.7.6 Treatment of experimental images

5.7.6.1 Integration of counts for every y-value

In this section, we present the different manners in which the experimental images shown in Figure 5.33 can be treated. The first method is to sum all counts along the x -direction for every pixel along the y -direction. Figure 5.34 shows the result for Figure 5.33a, which corresponds to acetone vapour at room temperature and at a pressure of 10,000 Pa. Due to the process of background subtraction, on average the intensity counts in regions far from the tagged region are close to zero, but for every pixel, the intensity counts can be either positive or negative. The next step is to identify the position of the heating element from Figure 5.34a. For this, we can observe the variation of the intensity counts in the y -direction. Around pixel number 185, when y decreases, the counts suddenly began to reduce back to zero. Therefore, pixel 185 is considered as the position of the heating element. It can be noticed that the region of interest is only between pixels 100 and 185 in the y -direction, and the rest of image is basically background with zero counts, which is of no relevance for the present study. The window of analysis is also limited between pixels 165 to 215 in the x -direction, to reduce the unnecessary information of the background pixels. Therefore, the signal is studied in the region

of interest (ROI) delimited by pixels 100 to 185 in the y -direction and pixels 165 to 215 in the x -direction.

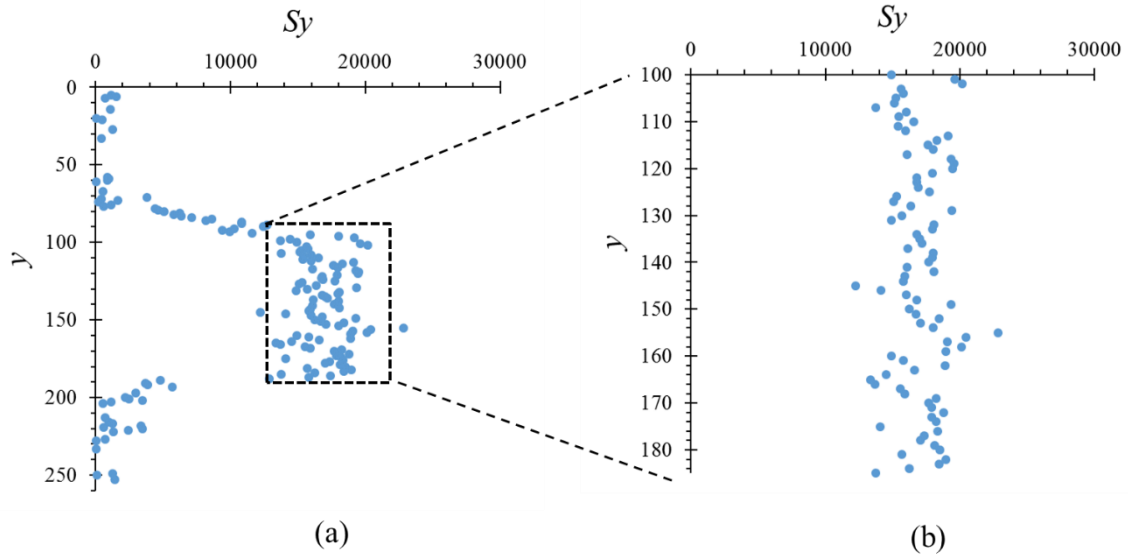


Figure 5.34. (a) The image of integrated counts along x -direction for every y value for image shown in Figure 5.33 a. (b) The zoomed portion shows the region of interest between $y = 100$ and 185.

Figure 5.35 demonstrate that this modification of ROI to a reduced window has improved the integrated signal. It can be clearly observed from this figure that the signal dispersion is lower and the quality of signal is better. The signal dispersions can be expressed in terms of RSD of the data, and are ~ 10.9 and $\sim 6.2\%$ without and with ROI, respectively. It can be noticed from Figure 5.35b that the signal intensity can be approximated with a straight and vertical line. As the heating element is turned off, the entire image is at room temperature and therefore, there is no variation of intensity along the y -direction of the laser beam. So, the equation representing the variation of intensity is expected to reduce to a constant value.

Fitting the curve for the data shown in Figure 5.35b leads to

$$S_y(y) = 4.70 y + 16,977.86 \quad y \in [100, 185] \quad (5.9)$$

At $y = 100$ and $y = 185$, we obtain, $S_y(100) = 17449$ and $S_y(185) = 17849$. The ratio $\frac{S_y(100)}{S_y(185)} = 0.98$. In the ideal case, this ratio should be equal to unity as the entire ROI is at uniform temperature $T = 295$ K. This also implies that there is no significant variation in the number density along the path of the laser beam. The slight deviation can be due to the fitting

function and the diffusion of the laser beam. Also, the laser beam is in the y – direction and this is a possibility of slight absorption by the acetone molecules in the ROI. Nevertheless, this demonstrates that without the heating element turned on, we do not observe any change in the number density, as expected.

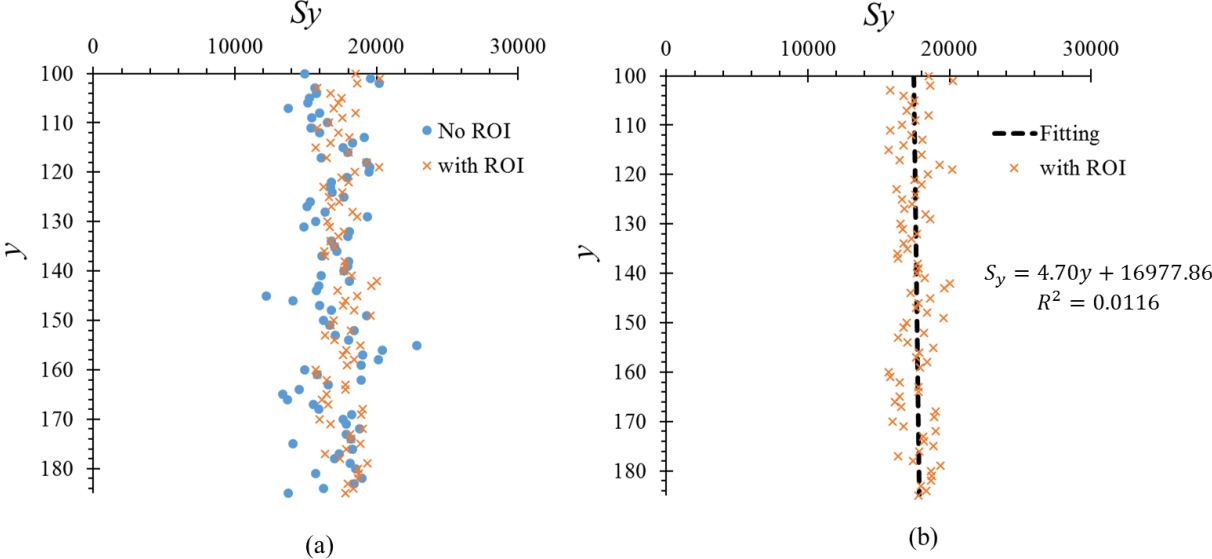


Figure 5.35. Variation of integrated counts for Figure 5.34(a);
 (a) with and without ROI, (b) with ROI and the fitting curve

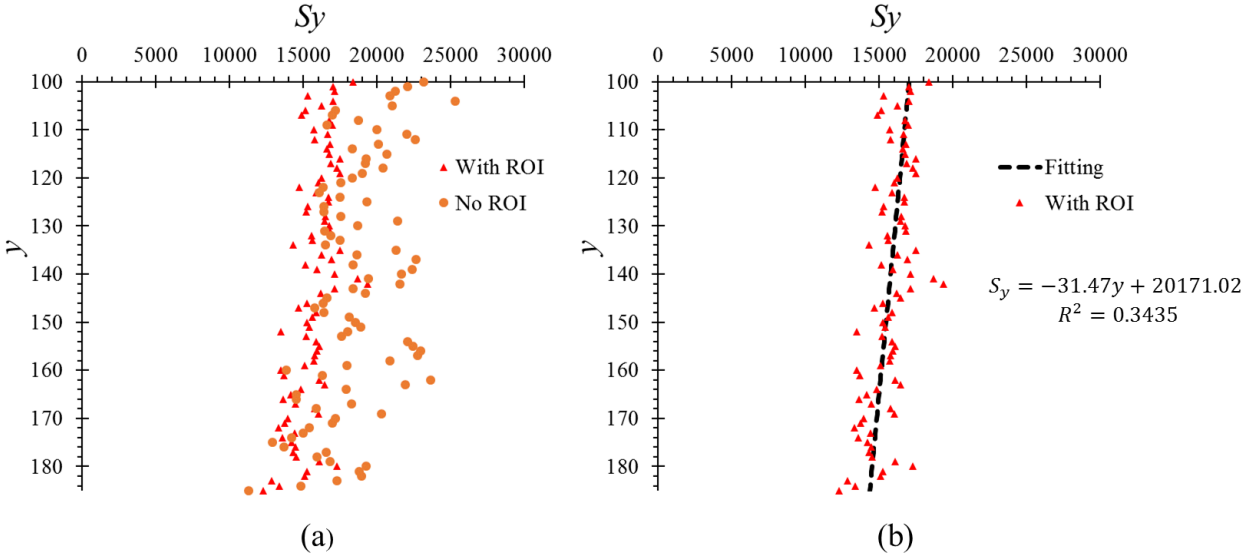


Figure 5.36. Variation of integrated counts of Figure 5.33b;
 (a) with and without ROI, (b) with ROI and the fitting curve

Figure 5.36 shows the variation of the integrated counts for the case with the heating element turned on (see Figure 5.33b). The signal dispersions expressed in terms of RSD of the data are ~ 14.8 and ~ 8.5 % without and with ROI, respectively. It can be noticed from Figure 5.36 that there is a decrease in the intensity counts as we are approaching the heating element. For this analysis, we can consider a linear approximation for the gradient in the observed intensity. With the heating element turned on, a linear approximation for the data shown in Figure 5.36b gives the following equation:

$$S_y(y) = -31.47 y + 20,171.02 \quad y \in [100, 185] \quad (5.10)$$

$S_y(100) = 17,024$ and $S_y(185) = 14349$. This gives $\frac{S_y(185)}{S_y(100)} \cong 0.84$.

It can be recalled from Equation (3.3) that the number of photons collected by a photo detector (S) from a volume ΔV of molecules excited by a laser beam of energy density I_{in} can be estimated as

$$S = \eta_p \frac{I_{in} \sigma_{abs}(\lambda, T)}{E_{ph}(\lambda)} n \phi(\lambda, T, P) \quad (5.11)$$

Where σ_{abs} is the absorption cross section, E_{ph} is the energy of a photon, λ is the wavelength of the light used for excitation, T is the temperature and P is the pressure, n is the molecular concentration or number density of the emitting molecules, and η_p is the capturing efficiency of the detecting optics. ϕ refers to the quantum yield.

In the present experiment, for both cases, with and without the heating element switched on, the optics is the same, the excitation of the wavelength is the same, and the laser energy is similar. S should then be proportional to S_y , which represents the number of counts and is an indirect measure of the number of photons. Consequently,

$$\frac{S_{y,295}}{S_{y,348}} = \frac{\eta_p \frac{I_{in} \sigma_{abs}(\lambda, T = 295 \text{ K})}{E_{ph}(\lambda)} n_{298} \phi(\lambda, T = 295 \text{ K}, P)}{\eta_p \frac{I_{in} \sigma_{abs}(\lambda, T = 348 \text{ K})}{E_{ph}(\lambda)} n_{348} \phi(\lambda, T = 348 \text{ K}, P)} \quad (5.12)$$

where $S_{y,298}$ and $S_{y,348}$ are the number of counts obtained without and with turning on the heating element, respectively. Based on the data shown in Figure 5.7, we notice that at 310 nm, the σ_{abs} at 295 K and 348 K are very close to each other. Therefore, we further make an assumption that the σ_{abs} are nearly the same at 298 K and 348 K, i.e., σ_{abs} are weakly dependent on temperature (see Figure 5.7).

This implies, we can further reduce the above equation to the following:

$$\frac{S_{y,295}}{S_{y,348}} = \frac{n_{295}\sigma_{abs}(\lambda, T = 295 \text{ K})\phi(\lambda, T = 295 \text{ K}, P)}{n_{348}\sigma_{abs}(\lambda, T = 348 \text{ K})\phi(\lambda, T = 348 \text{ K}, P)} \quad (5.13)$$

Now, we can estimate the ratio of $\frac{n_{298}}{n_{348}}$ based on the experimentally observed value of $\frac{S_{I,295}}{S_{I,348}}$, provided we know $\frac{\phi(\lambda, T=348, P)}{\phi(\lambda, T=295, P)}$. This ratio can be obtained from the data provided by Thurber et al.^{142,156} and it is ~ 0.95 .

As already mentioned, $S_{y,295}$ is the integrated signal obtained without turning the heating element on, and is approximately a constant. $S_{y,348}(100)$ would represent a pixel which is far away from the influence of the heating element, and at this location, we would expect that the temperature is the same as that of the case without the heating element turned on (see Figure 5.30). Therefore, $\frac{S_{y,295}(100)}{S_{y,348}(100)}$ should be equal to unity. On substituting the corresponding values, we obtain the ratio $\frac{S_{y,295}(100)}{S_{y,348}(100)} = 0.9756$. This value is very close to one, and the slight difference can be attributed due to the process of background subtraction. Even though the images with heating element turned on and turned off are obtained at different times, we subtracted the same background image to obtain the final images shown in Figure 5.33. This was due to the practical limitation to conduct the experiments. Having said this, this process of subtraction has no bearing on further analysis. We know from the simulations and the above analysis that the temperature at $y = 100$ is equal to 295 K. Therefore, instead of using $S_{y,295}(100)$, we can use $S_{y,348}(100)$ as these values should be identical, and this is also demonstrated by their experimental obtained ratio.

From the experimental data, $\frac{S_y(185)}{S_y(100)} = \frac{S_{y,348}}{S_{y,295}} = 0.84$. Therefore, on substituting the quantum yield ratio of 0.95 in equation (5.13), we obtain $\frac{n_{348}}{n_{295}} = 0.88$. Since the pressure in the ROI with and without heating element is relatively constant (see Figure 5.30), the expected number density ratio without and with heating element in ROI is the ratio of temperatures, i.e. $295/348=0.85$. The percentage deviation between experiment and prediction is about 3.4%, and this value can be improved if we are able to take other neglected terms, such as σ_{abs} and slight variations in I_{in} , into the analysis.

5.7.6.2 Gaussian fitting for every y

In this second approach, the intensity signal along x is fitted with a Gaussian function for every y value. Then, the variation of intensity of the peak (i.e. the maximum value) along the y -direction (i.e. direction of the laser beam) of these Gaussians curves are considered. Figure 5.37 shows the evolutions of the intensity S_p of the peaks along the y -direction obtained from images shown in Figure 5.33. Figure 5.37b shows the ROI with the heating element turned off ($T = 295$ K) and Figure 5.37c with the heating element turned on ($T = 348$ K). In both cases, we can notice a reduction of the intensity along the direction of the laser beam. In Figure 5.37 (b), this reduction is due to the diffusion of the laser beam as we move along the direction of the laser beam. Therefore, along the direction of propagation of the laser beam, it undergoes spreading, but the overall energy is almost conserved, as there is negligible absorption by acetone vapour. This has been verified from the image at room temperature by summing up the intensity counts along x -direction for every y -pixel in the ROI. Therefore, the variations of Gaussian peaks in Figure 5.37c is due to two factors: the first factor is the diffusion of the laser beam, and the second factor is due to the variation of the density along the y -direction.

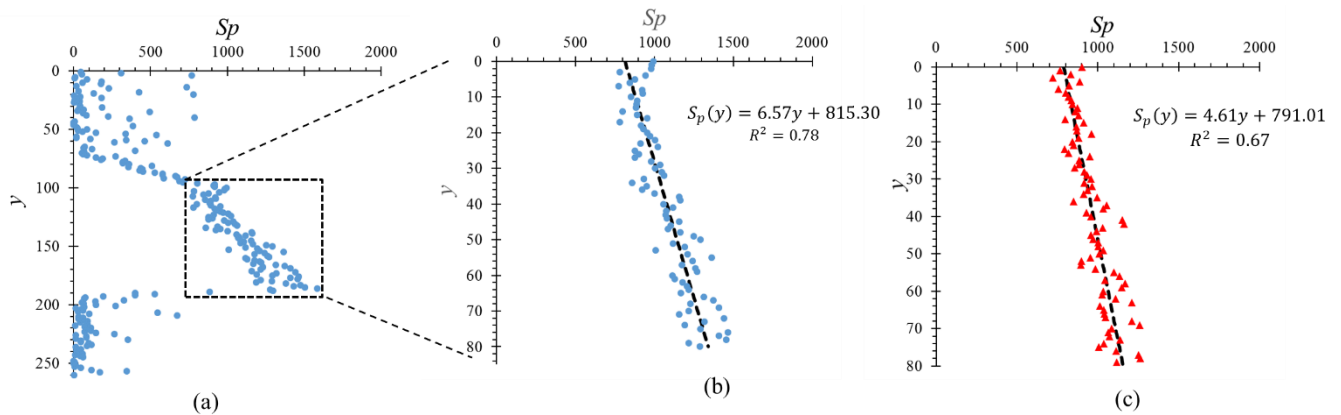


Figure 5.37 Variation of intensity counts along y -direction

- (a) for the whole the image from Figure 5.33(a),
- (b) the zoomed portion shows the ROI at $T = 295$ K (y -axis translated to zero)
- (c) in the ROI at $T = 348$ K (y -axis translated to zero)

To understand the influence of the heating element on the intensity value, we have to approximate its variation shown in Figure 5.37. In the ROI, a linear approximation is considered. The intensity value in the case of the heating element turned on should be slightly

lower when compared to the case where the heating element is turned off. Equations (5.14) and (5.15) show the linear approximations for the data shown in Figure 5.37b and c, respectively.

Without turning on the heating element,

$$S_{P,348}(y) = 4.26y + 798.48 \quad (5.14)$$

and with the heating element turned on and its temperature maintained at 348 K,

$$S_{P,295}(y) = 6.71y + 808.06 \quad (5.15)$$

Equations (5.13) and (5.14) have been obtained from a fit after translating values of y -pixels (0 to 85), the location of the heating element being now at $y = 85$. At $y = 0$, far away from the heating element, the temperature obtained should be same in both the cases, with heating element turned on and off. Since the pressure and temperature are same, the number density is same, and the quantum efficiency ratio for the pixels around this location is close to 1. This means that we would expect $\frac{S_{P,348}(y=0)}{S_{P,295}(y=0)}$ to be unity, and the measure gives

$$\frac{S_{P,348}(y = 0)}{S_{P,295}(y = 0)} = \frac{798.48}{808.06} = 0.99 \quad (5.16)$$

This ratio is close to 1, as expected. Near the heating element,

$$\frac{S_{P,348}(y = 85)}{S_{P,298}(y = 85)} = 0.84. \quad (5.17)$$

From equation (5.13) and after substituting the corresponding values of quantum efficiency ratio, we obtain $\frac{n_{348}}{n_{295}} = 0.88$, which provides the same result as with the first approach described in section 5.7.6.1.

5.8 Summary

In this chapter, we have conducted studies on acetone vapour photoluminescence. Based on the preliminary experiments conducted in Chapter 4, and the corresponding identification of the reasons for non-repeatability of the experimental data, we were able to design a new experimental chamber.

As this new chamber was free from leakages, we could introduce air (thereby, oxygen) in the system and establish the role played by oxygen molecules in quenching the luminescence

signal. It has been shown that the reduction in the intensity of acetone emission is strongly affected by the presence of oxygen in the system.

Absorption cross-sections experiments on acetone vapour were performed for a range of excitation wavelengths from 248 to 320 nm at different temperatures, 298 and 328.5 K. The procedure to conduct these experiments can be used to estimate these values with other potential tracer molecules. The values obtained in the present study were in close agreement with the values provided by other researchers in the literature¹²⁹.

A thorough study on the background signal effect was conducted. Different methods of image analysis, with and without the corrections for the background signal were performed. The experience gained through the experiments presented in Chapter 4 and the analysis of oxygen quenching, laser energy variations and background signal, allowed to experimentally understand the different factors which might influence the signal intensity. Therefore, a precise protocol to conduct the experiments and process images has been proposed. This protocol enabled us to improve the repeatability of the experimental data, which is vital in temperature measurements since the scale of intensity and its evolution at different temperatures would reveal the effect of temperature

A large number of experiments on acetone vapour at different pressures (1,000 to 10,000 Pa) and temperatures (298 to 343 K) has been performed. For the temperature range investigated in this study, the variation of intensity of acetone vapour with temperature has been shown to be weak. However, at different pressures, we were able to notice that the intensity was different, suggesting a dependency on the number density.

Further analysis was performed to evaluate the time constants and estimate their dependency with pressure. A bi-exponential fit seems to be a good choice and this fitting resulted in two time constants. One time constant was a representation of the rapid decay in the initial delays, and the other time constant indicates the slow decay in the later delays. The time constants estimated from our experimental data do not show any significant variation with pressures in the range 2,900 to 10,000 Pa. However, there is a slight variation on further lowering the pressure to 1,000 Pa. These time constants revealed the complex nature of the signal decay with time. Even though the scale of intensity varies from one pressure to another, there is no strong variation of the time constants with time. This implied that, at least for the experimental condition of this study, the raw intensities instead of its time evolution can provide a measure of pressure and consequently of number density.

To indirectly estimate the influence of temperature, the experimental chamber was modified by introducing a heating element. This localised heating resulted in the variation of the density along the direction perpendicular to the plane of the heating element, and experiments were performed to capture this variation. The experimental images were analysed in two different manners; firstly, by taking the integrated signal along every y -pixel, and secondly by fitting a Gaussian for every y -pixel. The influence of using a ROI was presented. These studies, though preliminary in nature, demonstrate that even for low temperature variations, of the order of a few tens of K, gas thermometry could be done through densitometry analysis, provided the pressure is uniform or known.

6 *Towards near wall measurements*

As presented in the previous chapters, the focus of this thesis is to explore the possibility of molecular tagging approach to measure temperature fields in gases at microscale. Our research group at Toulouse, France, had started to work on the technique of molecular tagging almost of decade ago with the objective to access the velocity profile near the wall, in other words, to experimentally observe the velocity slip at the wall. The preliminary work carried out in the first thesis on molecular tagging technique was majorly devoted to the assemblage and development of the hardware and software necessary to perform measurements with this approach. In the context of this thesis, Samouda et al¹⁴³. were able to carry out preliminary studies to demonstrate that molecular tagging could indeed provide information of velocity in flow fields. In the next work, Si Hadj Mohand et al¹⁴⁸. were able to improve the experiments to study the velocity profile in continuum conditions far from the wall. It was demonstrated that molecular tagging approach could faithfully reproduce the velocity profiles in gas flows. In this context, the latest thesis work from Fratantoni provided the preliminary results near the wall³³.

In this context, the ultimate goal of temperature measurements would be observe the temperature jump at the wall. Towards this goal, this is the first thesis in our research group dedicated to temperature measurements. Therefore, it was interesting to think about the future work that could be carried out to study temperature jump at the wall. In this chapter, we provide some of the ideas and the corresponding challenges that might be interesting to explore in the future. Many of the ideas presented in this chapter will be of preliminary nature, the goal being to provide different interesting strategies that lead to the ultimate step of measuring temperature jump at the wall.

The temperature measurements in this study were carried out in cases of thermodynamic equilibrium. Due to the nature of acetone's temperature behaviour, in the range investigated, we could not directly measure the temperature, but rather the changes in number density induced by the temperature gradient. This study provides a strict protocol to be followed to achieve repeatability of the experimental data. Therefore, in future, with another molecule or a combination of molecules, which might be more sensitive to temperature, similar experiments can be carried out. However, close to the wall, there would be thermodynamic non-equilibrium and further studies would be needed to really understand the manner in which the phosphorescence signal generated near the wall can be attributed to the temperature (or number density) at the wall. In this chapter, we will focus our attention on the aspect of generating

luminescence signal near the wall. In principle, this can be achieved with evanescent waves. Most of the work presented in this chapter has been carried out at Nokia Bell Labs in Dublin, Ireland, as a part of secondment within the framework of MIGRATE project.

6.1 Temperature prediction near the wall

In this section, we define Knudsen number and defined as $Kn = \frac{l}{a}$, where l is the equivalent free path defined as $\frac{\mu v_m}{P}$. Where μ is the viscosity, P is the pressure and v_m is the most probable speed at a temperature T defined as $\sqrt{\frac{2K_B T}{m}}$. These definitions are taken from the work of Sharipov⁴⁰.

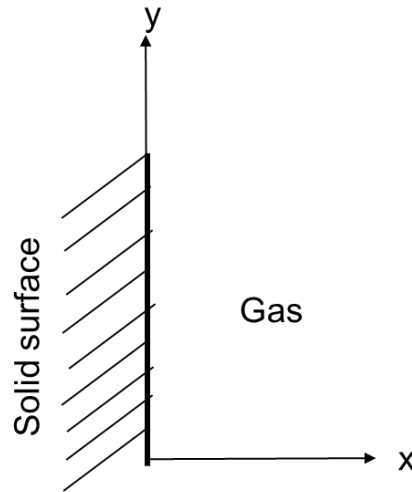


Figure 6.1 Schematic to define temperature jump coefficient⁴⁰

Consider a gas or mixture occupying a half of space occupying a half of space $x \geq 0$ as shown in Figure 6.1. Let us denote T_s as the temperature of the solid surface. Let T_g be the gas temperature, and assume a variation of it along the x . Next to the solid surface, the gas temperature is not equal to the surface temperature, but can be written in terms of a temperature jump condition at $x = 0$ as $T_g = T_s + \zeta_T l \frac{dT_g}{dx}$, where ζ_T is the temperature jump coefficient.

Based on the above definitions, the temperature profile of the gas in the region between the two parallel plates can be estimated. Consider an infinite parallel plate configuration, without flow, as shown in Figure 6.2. The bottom plate is at a location $x = -a/2$ and the top plate is at $x = +a/2$. The bottom and top plates (or walls) are maintained at a constant temperature

$T_0 - \frac{\Delta T}{2}$ and $T_0 + \frac{\Delta T}{2}$, respectively. Thus, ΔT represents the temperature difference between the two plates. The gap between the plates is occupied by a gas in the slip flow regime.

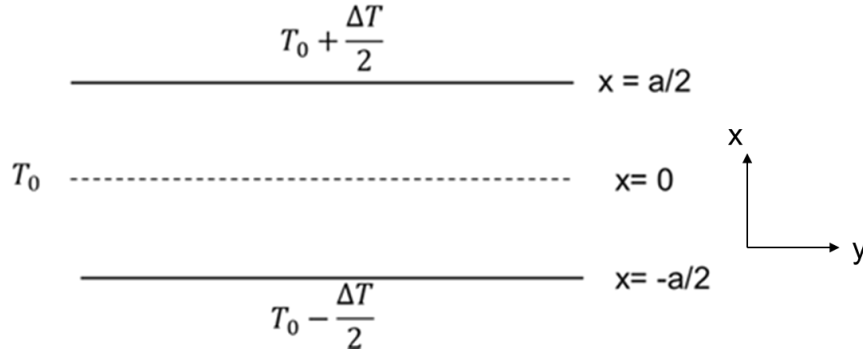


Figure 6.2 Schematic of the infinite parallel plate configuration

The temperature profile of the gas in the region between the two parallel plates can be obtained by solving the following heat conduction equation. On assuming a constant thermal conductivity k , the heat conduction equation is as follows:

$$\left(\frac{\partial^2 T}{\partial x^2} + \frac{\partial^2 T}{\partial y^2} + \frac{\partial^2 T}{\partial z^2} \right) + \frac{\dot{q}}{k} = \frac{1}{\alpha} \frac{\partial T}{\partial t} \quad (6.1)$$

Where T is the temperature, x , y , and z are the spatial variables, \dot{q} is the heat generation per unit volume and α is the thermal diffusivity. Under steady state conditions, no heat generation in the system, and assumption of one-dimensional heat transfer, the above partial differential equation reduces to an ordinary differential equation of the form

$$\frac{d^2 T}{dx^2} = 0 \quad (6.2)$$

To obtain the temperature profile of the gas between the plates, the above differential equation must be solved with the following boundary conditions:

$$T(x = 0) = T_0 \quad (6.3)$$

and slip boundary condition at the walls,

$$T = T_0 \pm \left(\frac{\Delta T}{2} - \zeta_T l \frac{dT}{dx} \right) \text{ at } x = \pm \frac{a}{2} \quad (6.4)$$

On solving Equation (6.2), with the boundary conditions (6.3) and (6.4), we obtain the temperature profile of the gas as

$$T(x) = T_o + \Delta T \frac{x}{a} (1 + 2\zeta_T Kn)^{-1} \quad (6.5)$$

Equation (6.5) represents the temperature profile of the rarefied gas between two parallel plates. For $Kn = 0$, the above equation reduces to the linear profile obtained for gas in continuous regime. To obtain the temperature profiles of a rarefied gas, the Knudsen range can be chosen between 0.1 and 0.001 (slip flow regime values). For a single gas exhibiting diffuse scattering (first approximation), the temperature jump coefficients are between 1.81 and 1.954⁴⁰. A value of 1.95 for the jump coefficient is recommended in practical applications⁴⁰.

A representative calculation for the difference in the gas and wall temperatures at $x = 0$ is as follows. It should be noted that the temperature profile of the gas has been generated by calculating the derivative of the profile in the region above the Knudsen layer and this slope is extrapolated in the Knudsen layer to estimate the temperature profile. The actual temperature exhibited by the gas molecules in the Knudsen layer will be different from the values obtained from Equation (6.5). However, we can get a ballpark estimation of the expected temperature difference between the gas and the wall.

For $Kn = 0.01$ and $\zeta_T = 1.95$, equation (6.5) reduces to

$$T(x) = T_o + \Delta T \frac{x}{a} (0.9624) \quad (6.6)$$

At the bottom wall, for gas at $x = \frac{-a}{2}$,

$$T(x) = T_o - \Delta T \frac{0.9624}{2}. \quad (6.7)$$

and at the top wall, for gas at $x = \frac{+a}{2}$,

$$T(x) = T_o + \Delta T \frac{0.9624}{2} \quad (6.8)$$

Assuming a temperature difference $\Delta T = 50 \text{ K}$ between the two walls and the bottom wall maintained at $T_{w,o} = 293 \text{ K}$, the gas molecules temperature at the same location, $x = \frac{-a}{2}$, can be estimated from Equation (6.7) as $T_g = 293.94 \text{ K}$. Based on this calculation, at the bottom wall, for $\Delta T = 50 \text{ K}$, the same temperature difference of about 0.94 K is expected

between the wall and gas molecules. By increasing the temperature difference $\Delta T = 100K$, a difference of almost 1.9 K is predicted between the wall and the gas molecules.

At $Kn = 0.1$ and with $\zeta_T = 1.95$, for $\Delta T = 50$ K, this difference increases to 7 K. For $\Delta T = 100$ K, it becomes 14 K.

At $Kn = 0.001$ and with $\zeta_T = 1.95$, for $\Delta T = 50$ K, this difference is only 0.1K. For $\Delta T = 100$ K, it becomes 0.2 K. These values show that at $Kn = 0.001$, we are almost at the threshold of continuum regime, and there is a negligible difference between the temperature of the wall and the gas molecules near the wall.

It would be interesting to see if a method can be developed to investigate these temperature differences between the wall and the gas molecules at the wall. We propose different ideas to develop an experimental setup that can be able to simultaneously measure the wall temperature by Infra-Red Thermography (IRT) and the near-wall fluid temperature by MTT. For this, it is necessary to illuminate only an extremely thin slice of molecules near the wall. In principle, this illumination can be done with so-called evanescent waves. The final goal of this approach is to experimentally determine the temperature jump when rarefied conditions are reached for an in-depth analysis of the domain of validity of the various temperature-jump models.

6.2 Total internal reflection and evanescent waves

The index of refraction, or refractive index, of a medium is defined as the ratio of the speed of light in that medium to the speed of light in vacuum. Consider Material ‘a’ with a refractive index α_a higher than the refractive index α_b of Material ‘b’. Let ‘A’ be a point source of light. When encountering the interface between the two materials, a part of the light from a perpendicular ray, such as Ray 1, is reflected at the interface and the rest travels through it without any directional change. For Ray 2, with an angle of incidence θ_a , there is a component of reflection, and the rest of the ray enters the other medium while undergoing refraction, with a refracted angle θ_b . For Ray 3, the angle of incidence is θ_{crit} and the refracted component has an angle of refraction $\theta_b = 90^\circ$. This implies that the refracted component is directly along the interface of the two materials. This angle of incidence, θ_{crit} , is referred to as a critical angle. For any beam with an angle of incidence greater than θ_{crit} there is no reflected component, and the light can be trapped inside Material ‘a’. This behaviour, shown in Figure 6.3, is called total internal reflection (TIR).

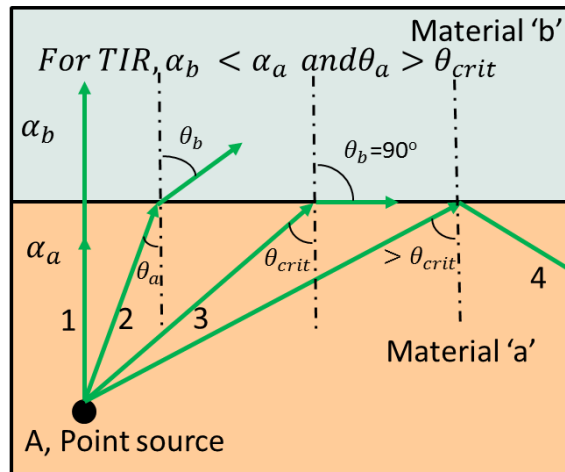


Figure 6.3 Schematic of total internal reflection (all reflected beams are not shown for clarity)

Snell's law of reflection gives the relation between the refractive indexes of the materials and the angles of incidence and refraction:

$$\alpha_b \sin \theta_b = \alpha_a \sin \theta_a \tag{6.9}$$

In the situation of critical angle, as $\theta_b = 90^\circ$, $\theta_{crit} = \arcsin \frac{\alpha_b}{\alpha_a}$ and it implies that α_b cannot be higher than α_a . In other words, TIR cannot occur if the incident light 'A' is originating from a medium of lower refractive index and entering into a medium of higher refractive index. In this scenario, at the interface, there is always a reflected and a refracted component of the ray.

From the above concept of TIR, it is interesting to study what occurs at the interface of the media. As discussed for TIR, only the reflected and the transmitted components of light wave remains, and the transmitted wave transforms into so-called evanescent waves, in the medium of lower refractive index. These evanescent waves exhibit an exponential decay in intensity with distance. The wave presence is felt within a layer with a width of a few hundred nanometres in the material of lower refractive index. Therefore, these evanescent waves can be employed to probe the regions very close to the wall, within the Knudsen layer. Evanescent waves are already employed in total internal reflection fluorescence (TIRF) microscopy, especially to study biological samples. At microscale, researchers have utilized this approach to study liquid flows and interfacial transport phenomena and to measure wall surface temperatures. The essence of the future work will be to apply this evanescent wave-based approach to study rarefied gases. This study seems to be more challenging as the signal

generated by gases, especially in rarefied conditions, will be considerably weaker than the signal achieved by liquids.

6.3 Calculations for our case

In our case, the interface for the evanescent wave could be between a layer of indium tin oxide, ITO, with higher refractive index and the region of acetone molecules with lower refractive index. Based on Snell's law (6.9), we can estimate the critical angle between the interface of ITO layer and acetone vapour. The manufacturer (Diamond coatings, UK) provides a coating of ITO layer on Sapphire and provided the refractive index of ITO layer, and the refractive index of acetone is estimated from empirical data presented in literature¹⁴⁴, and is close to unity. It should be noted that the exact refractive indexes may be a bit different from the values considered below in this section. However, these calculations give an estimate of the expected angles and penetration depth. The exact values must be confirmed experimentally.

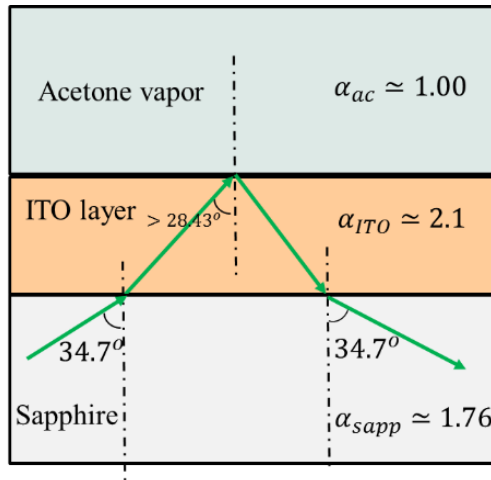


Figure 6.4. Bending angle calculations

Snell's law yields

$$\alpha_{ITO} \sin \theta_{ITO} = \alpha_{ac} \sin \theta_{ac} \quad (6.10)$$

where $\alpha_{ITO} \sim 2.1$ is the refractive index of ITO layer and $\alpha_{ac} \sim 1$ is the refractive index of acetone vapour. This results in the critical angle $\theta_{ITO} \sim 28.4^\circ$. Therefore, for this configuration, at the interface of ITO and acetone vapour, if the angle of incidence is close to 28.4° , TIR is

expected and evanescent waves are generated in the acetone molecules region. In a similar manner, at the interface between sapphire and ITO layer, the angle of incidence has to be 34.7° , so that the beam undergoes refraction and the angle of incidence will be 28.4° at the interface of ITO and acetone vapour. The corresponding bending angles are shown in Figure 6.4.

From the literature¹⁵⁷, the penetration depth d_p of the evanescent wave in the material of lower refractive index (acetone vapour) can be estimated as

$$d_p = \frac{\lambda}{4\pi\sqrt{\alpha_{ITO}^2 \sin^2\theta_{ITO} - \alpha_{ac}^2}} \quad (6.11)$$

where λ is the wavelength of light. Let us consider $\lambda = 310$ nm and 266 nm, as majority of our experiments were conducted at these wavelengths. Figure 6.5a shows the variation of the penetration depth of the evanescent waves for different incident (greater than critical) angles. For $\lambda = 310$ nm and 266 nm, at $\theta_{ITO} = 28.5^\circ$, we obtain $d_p \sim 385$ nm and ~ 330 nm, respectively. Even a slight increase of this angle by one degree reduces d_p to 90 nm and 80 nm for $\lambda = 310$ and 266 nm, respectively. This shows that the penetration depth is very sensitive to the angle of incidence, implying that the thickness of the region which can be probed by the evanescent wave will be highly sensitive to the critical angle.

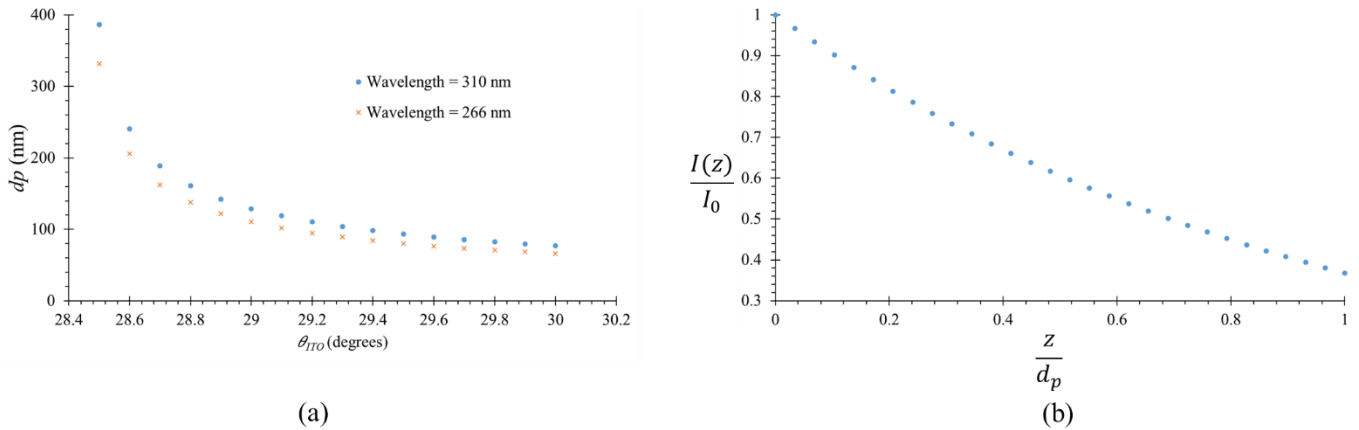


Figure 6.5. (a) Penetration depth of evanescent wave as a function of incident angle at the interface of ITO and acetone vapour, (b) Exponential decay of evanescent wave intensity

Further, it is interesting to note that the intensity of the evanescent wave in the region of the penetration depth is not constant, but undergoes an exponential decay with distance z :

$I(z) = I_0 e^{\frac{-z}{d_p}}$. This information is presented in Figure 6.5b. Thus, most of the light is captured by the molecules emitting in the first 50-100 nm nanometres near the wall.

6.4 Design ideas

In this section, we present the initial design ideas which can be of interest to generate evanescent waves and capture the photoluminescence signal in this illuminated region.

6.4.1 *First design idea*

To implement the idea of evanescent waves in a parallel plate configuration, we can proceed by different design ideas. The approach would be to commence with a simple version and then progress towards more complex situations. Figure 6.6 shows the first schematic envisaged. The upper wall where UV beam passes can be fabricated in pure sapphire or suprasil, both transparent to UV light, and the bottom wall can be made with metal or glass, depending on the ease of fabrication.

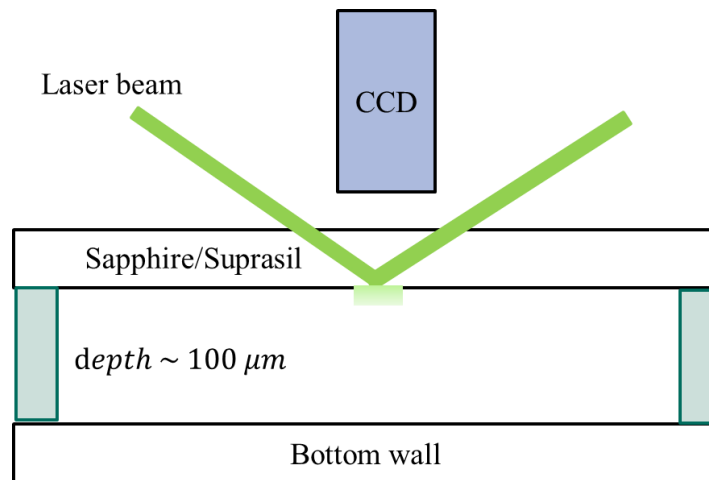


Figure 6.6. First envisaged schematic for evanescent wave study

The aim of this design is to generate evanescent waves within a close chamber with controlled acetone pressure and temperature and detect if an exploitable signal can be obtained. The experiments can be first carried out at isothermal conditions at room temperature. The study can be initiated with high-pressure acetone vapour, i.e. at low Kn . Thereafter, pressure can be reduced, thus Kn is increased, gradually. In this manner, with our existing optics, we can observe the pressure until which we are able to generate an exploitable signal. In addition, these

experiments can help understanding the effects of wall reflections and fluorescence. Based on this information, the temperature difference required between the walls to generate observable temperature difference between the wall and the gas near wall can be calculated.

6.4.2 Second design idea

Figure 6.7 shows the second modification in the design. The choice of suprasil or sapphire can be decided based on the experiments carried out with the previous cell. The goal of this second design will be to incorporate ITO layer, which can be heated and provide IR signal. We can calibrate the IR signal of ITO layer together with the phosphorescence signal of acetone molecules in isothermal conditions. With this information, preliminary measurements on the temperature difference between the wall and the gas near the wall in rarefied conditions can be started.

Further modifications are possible to enhance the sensitivity of the signal by incorporating a combination of optical filters, providing an optical path for phosphorescent signal, coupling with a single photon avalanche diode (SPAD). The optical path for the light can be an inverted microscope or a custom made caged device (see Figure 6.9).

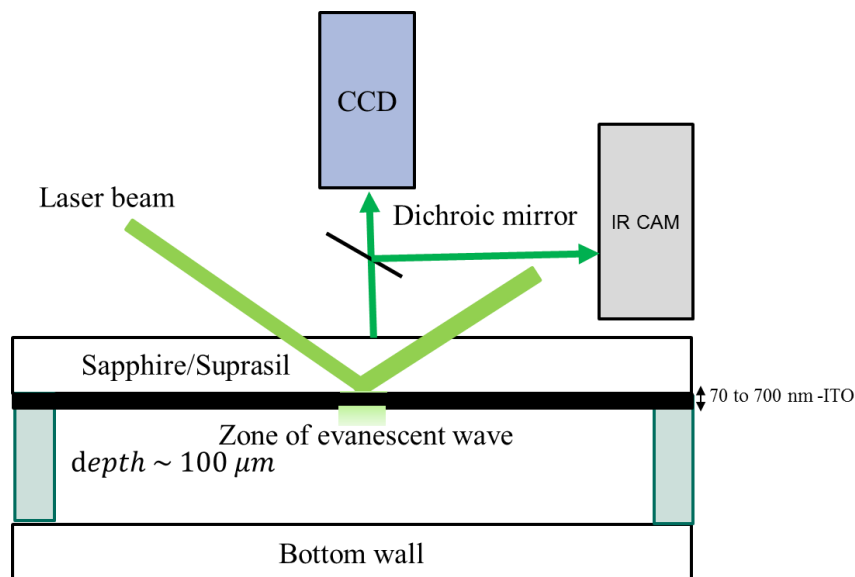


Figure 6.7. Second envisaged schematic for evanescent wave study

6.5 Fabricated cell

Figure 6.8 shows a cell designed for investigation of the evanescent waves. This cell, based on the first idea, has been fabricated and assembled. Preliminary leakage tests were performed. Due to a lack of time, we could not perform experiments during the thesis with this chamber.

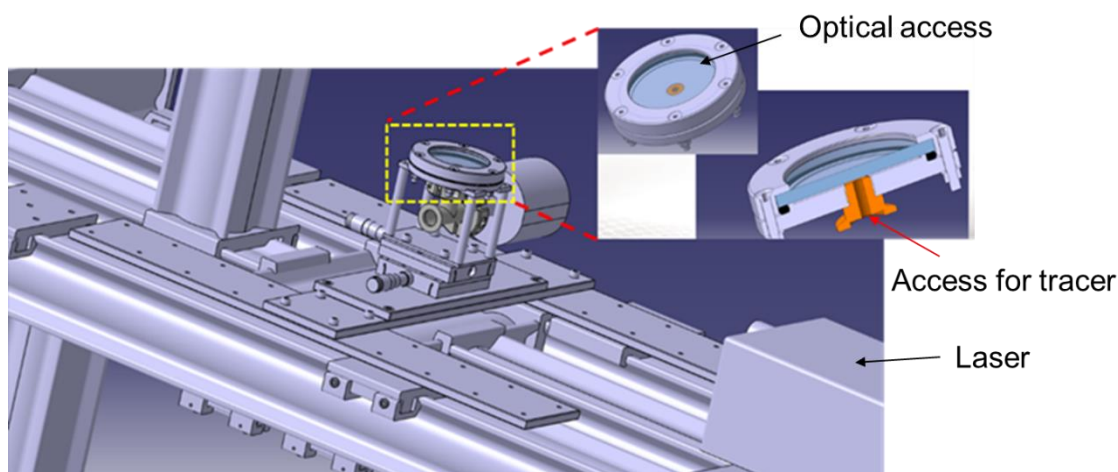


Figure 6.8. Experimental design for preliminary study on evanescent waves

Figure 6.8 shows the position of the envisaged chamber in the existing molecular tagging setup. In the figure, the position of the laser can also be seen. In the zoomed portion of the chamber, we see the optical access to capture images and there is one single access port, which will be used for both entry and exit of the tracer gas. A T- junction will be connected to this access port, and on one end, a pressure gauge would be placed and on the other end, the connections for tracer inlet and vacuuming would be placed. There are other components, which are not shown in the above schematic, such as optical fibre to introduce laser beam at an angle, sapphire prism to bend the beam, and the camera.

6.6 Further questions to be addressed

In this section, we present some questions which are of interest in the future to tackle this problem experimentally. The region probed is less than 200 nm with the intensity exhibiting an exponential decay. Moreover, the penetration depth is a very strong function of the incident angle. Therefore, the mechanical arrangement for guiding the laser beam in the system has to be very precise.

In general, in our experiments, the laser beam was illuminating a region of about 400 μm diameter and about 4 mm in length. With evanescent waves, length (d_p), is about 100 nm and the beam diameter will be still 400 μm diameter. This means that the signal volume investigation region will be about $10^4 - 10^5$ times lower than the signal which we were usually able to generate in this thesis. This implies that we would need a new detector, able to detect every single photon emitted by the acetone molecules. The experiment must be conducted in an environment of perfect darkness to reduce the influence of background sources of light.

For the fabrication of a wall of the microchannel, we would require an ITO layer deposited on sapphire or suprasil. This layer of ITO should be transparent enough to allow the signal of photoluminescence of the molecules. There are different grades and types of ITO, which can be broadly classified as hot and cold ITO¹⁵⁸. Therefore, it will be of interest to experiment with different kinds of ITO layers to observe the best combination that is able to transmit the emitted light.

Also, it will be interesting to fabricate a channel with a distance between the plates of the order of 100 μm . Moreover, within this small gap, the fluid should be subjected to a high temperature gradient, corresponding to a temperature difference of 50 to 100 K or a gradient of 0.5 to 1 K per μm . The work being carried out at ICA for the development of Knudsen pumps is of interest here to understand the manner in which high temperature gradients can be control in a relatively small domain. We have already demonstrated the dramatic role of leakages on the luminescent signal; it will then be vital to have an experimental chamber free from any leakages.

The physical components required will evolve according to the first experimental observations. There will be a need of new optical components, such as the Sapphire prisms (for light bending), dichroic mirror (for division of light beam), different kinds of optical filters to cut off the light reflections, UV immersion oil to achieve smooth bending of light. To enhance the signal capturing mechanics, we will need a combination of an optical path for light (can be an inverted microscope) coupled with a SPAD. In addition, an infrared camera is required to capture the wall temperature provided by the ITO layer. This will increase the complexity of the experimental setup, in terms of increasing the number of physical components and the exact alignment of all these components. One such possible complex arrangement is shown in Figure 6.9.

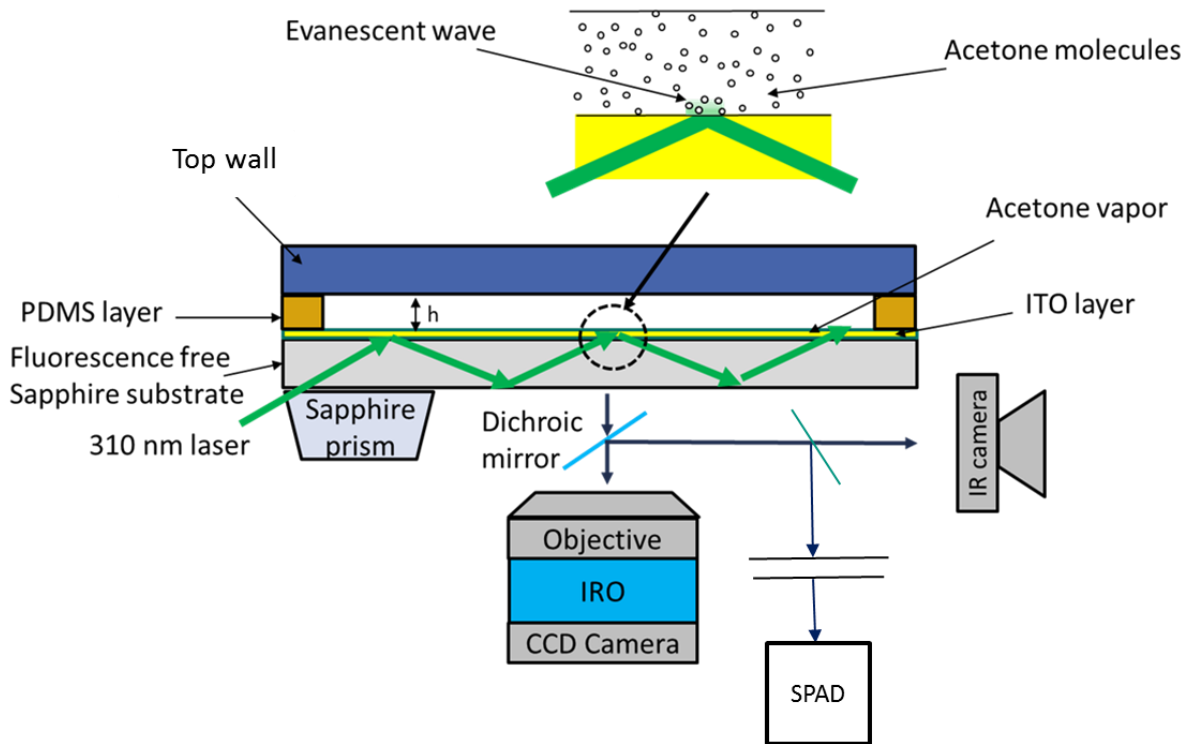


Figure 6.9 Envisaged complex schematic to realise temperature measurements with evanescent waves

To summarise, there seems to be many possibilities to further extend the work presented in this thesis towards the ultimate goal of being able to measure the temperature within the Knudsen layer near the wall. The preceding sections have tried to provide some directions in which the investigation can be performed with the objective of measuring the temperature jump at the wall.

6.7 Other research directions

In this section, we propose other directions in which future research can be carried out. It is worth mentioning here that it would be of great interest to obtain simultaneously the information of both pressure and temperature by capturing the lifetime curves of a gas. However, until this point of investigation, we understand that there can be a change in the intensity either due to variation in pressure or potentially due to variation in temperature. Therefore, to extract the information on one of these quantities, we would require that the other quantity is somehow already known.

Based on the experimental techniques developed in this thesis, at least in some special cases, as shown in Figure 6.10, we can get the information of temperature and pressure. In the channel to be built the optical windows should have a large size so that the laser can be shot at different locations. Assume a system in which there is a variation of pressure and temperature only along x – direction with a uniform condition of pressure and temperature along the z – direction. In such a scenario, at a particular location of (x, y, z) , we can measure σ_{abs} of the gas. Since this σ_{abs} is a function of only temperature, we can estimate the temperature along this region. Once we have the temperature, we can capture the intensities at different delays to get the lifetime curves. Therefore, as we already know the temperature, we can refer to our calibration curves to measure at which condition of temperature and pressure, this measured curve is expected. This process would give the temperature and pressure at a particular axial location. By adjusting the relative position of laser from the experimental chamber, repeating the experiment at a different locations would provide the data at these other locations. This thesis has successfully demonstrated the method to extract absorption cross-sections and to generate lifetime curves of decay. Therefore, based on these approaches, it is possible to carry out these experiments in the future.

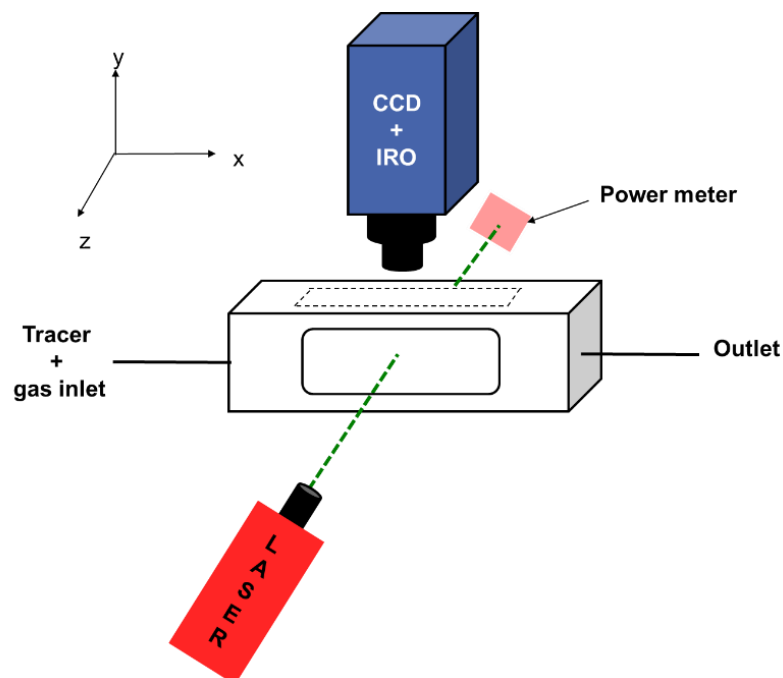


Figure 6.10 Schematic to show possible measurement of temperature and pressure with combination of σ_{abs} and lifetime curves.

In this thesis, focus has been on understanding the behaviour of acetone vapour phosphorescence excited at 310 nm for different conditions of temperature and pressure. The main reason for adopting 310 nm was the research of the highest luminescent intensity. But the point of interest is to understand the variations in intensities with temperature and pressure, and not necessary the absolute value of the signal, per se. As the absorption spectrum of acetone vapour is quite broad (see Section 5.3), there might be other possible excitation wavelengths where the emission signal might be low, but the dependency with temperature might be strong. Therefore, the experiments repeated in this study can be done by exciting acetone at different wavelengths, and to measure the time constants at different wavelengths for the same conditions of temperature and pressure. On choosing the time constant at a particular wavelength as a reference, we can normalise the time constants at other wavelengths with the chosen reference. Then, an analysis can be carried out to see the dependency of these time constants with temperature and pressure. If this ratio is independent (or weakly dependent) of the pressure in the system, then it will be possible to extract the information of temperature from the ratios of time constants, without bothering about the pressure in the system.

Basics of evanescent waves and the possible coupling of these waves with the technique of molecular tagging has been presented in the chapter. Also, it is interesting to note that with evanescent waves technique, in principle, we can try to understand the adsorption of acetone molecules at the walls. For a particular angle of incidence and wavelength of the beam, the depth of propagation of the evanescent waves is constant. We can introduce acetone at different conditions of pressure in the chamber and thereafter, immediately start capturing the variation of signal with time. Based on acquisition of the signal at different conditions of pressures, we can estimate the rate at which adsorption is occurring at the wall.

7 Conclusions

In this thesis, the molecular tagging technique has been studied with the objective of measuring temperature in gas microflows. We were interested to adapt and modify an existing MTV setup at ICA Toulouse to perform temperature measurements. These investigations could provide a new method of investigating gas microflows by simultaneous local measurements of temperature and velocity. Experiments were carried out on two different experimental chambers. In order to reproduce rarefied conditions encountered in fluidic microsystems, experiments have been done at low pressures, down to the order of 1,000 Pa with acetone vapour. The main findings in this thesis can be briefly summarised as follows:

- The preliminary experiments on acetone vapour luminescence excited at 266 nm, which corresponds to the peak of absorption of this tracer, demonstrated that the signal is no longer detectable after a few μs . Therefore, the behaviour of acetone vapour was investigated at different wavelengths. The highest intensity signal was found at 310 nm for acetone vapour, and experiments performed with another tracer, namely diacetyl vapour, showed a maximum luminescence at 410 nm.
- The initial experimental investigation with a first chamber on acetone vapour luminescence in the temperature range of 298 to 323 K and pressure range of 1,000 to 15,000 Pa seemed to indicate a weak temperature-dependency of luminescence. However, the experimental data were not reproducible, and this led us to investigate the factors leading to this non-repeatability. The intensity of signal was significantly due to laser energy uncontrolled fluctuations and was also altered by quenching due to small leakages in the system. The protocol of the experimental procedure was then refined to solve these issues.
- A detailed experimental investigation on the laser energy fluctuations led to an improved treatment of the data by taking energy normalisation into account. A new leak-free experimental chamber was designed with the ability to continuously monitor the laser energy.
- The strong quenching of the signal by the presence of a small amount of oxygen was experimentally demonstrated. The influence of repeated laser pulses on the acetone luminescent properties was studied. For the experimental conditions of the study, there was no observable photolysis of the acetone vapour.

- Fundamental experiments were performed to measure the absorption cross-sections of acetone vapour at different excitation wavelengths and temperatures. In future, a similar methodology can be applied to other tracer molecules which could be of interest for molecular tagging in gaseous environments.
- A detailed experimental investigation was carried on acetone vapour luminescence in the temperature range of 298 to 343 K and pressure range of 1,000 to 10,000 Pa at room temperature. The effect of the temperature was isolated by maintaining the number density constant. Analysis was carried out to extract the time constants of acetone vapour at different pressures. Different procedures for the analysis of the experimental images were developed. These experiments and the subsequent analysis showed that the effect of temperature itself on luminescence is negligible for the range investigated in this study. However, a dependency of intensity with the number density has been evidenced, showing the potentiality of the molecular tagging technique for indirect temperature measurement.
- The experimental chamber was modified to study the influence of a localized heating element, which induced a gradient of temperature and density along the direction of the heating element. Molecular tagging experiments were performed to capture this variation, with the heating element at a temperature of 348 K and a uniform pressure of 10,000 Pa in the chamber. The influence of the localized heating on the acetone vapour signal was analysed by various approaches, considering either the integrated signal or the variation of peaks of the Gaussians in different planes parallel to the heating surface. These experiments could experimentally demonstrate that the signal is function of the number density, itself induced by the temperature gradient.
- In the future, the final objective of this technique would be study the feasibility of measuring temperature jump at the wall. Therefore, theoretical ideas regarding the generation of luminescence signal near the wall, referred to as evanescent waves, were presented. In principle, with these waves, one can probe regions in a layer with a thickness in the order of 100 nm near the wall. Some setup design ideas were proposed to implement and exploit these evanescent waves. A chamber for preliminary investigation was designed and fabricated.

This research work seems to have opened up many promising lines of research that might be performed in the future months. The experimental procedure is now robust and the same approach can be applied to study other potential tracers, such as diacetyl and toluene. The

final objective will not only be to measure the temperature of tracer molecules, but rather use these molecules to estimate the temperature of the carrier gas, the presence of which can influence the signal intensity of the tracer gas. This factor has to be carefully studied by performing experiments at different concentrations of the tracer in the carrier gas. In a last step, it would be interesting to couple velocity and thermometry measurements and to evaluate them simultaneously, and to extend these measurements into 2D and 3D more or less complex configurations.

1 Appendix A

In this appendix, we present the experimental data on acetone vapour at other conditions presented in Table 4-13.

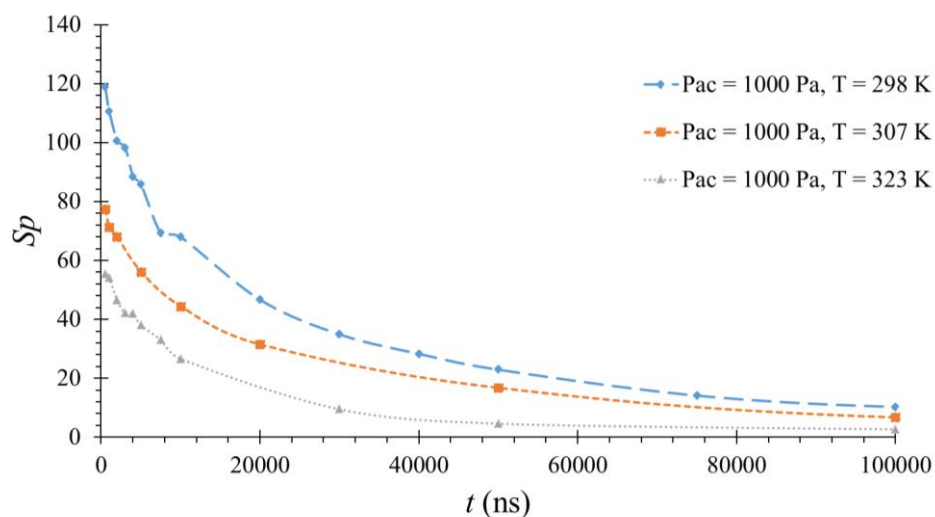


Figure 1.1 A1. Phosphorescence of acetone vapour at $P_{ac} = 1,000$ Pa at different temperatures

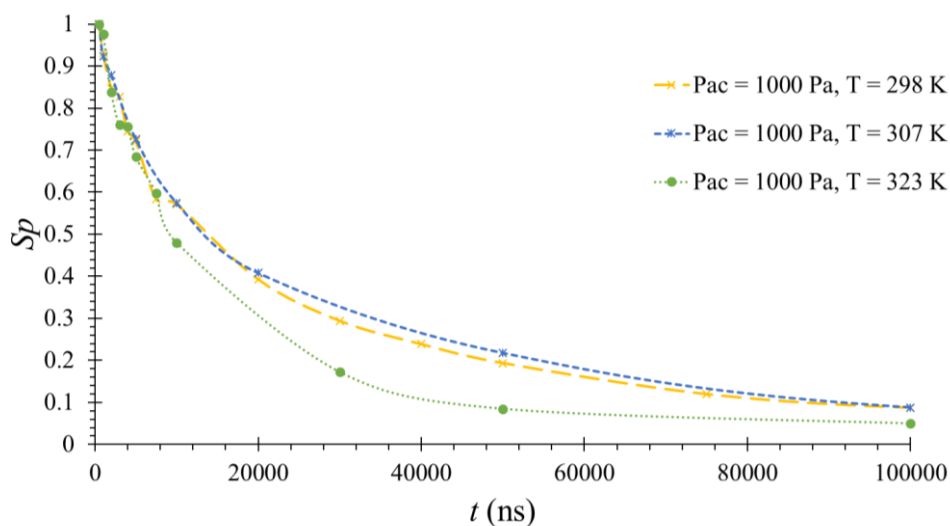


Figure 1.2.A1. Data shown in Figure 1.1 A1 normalised with the intensity value at 500 ns for every curve

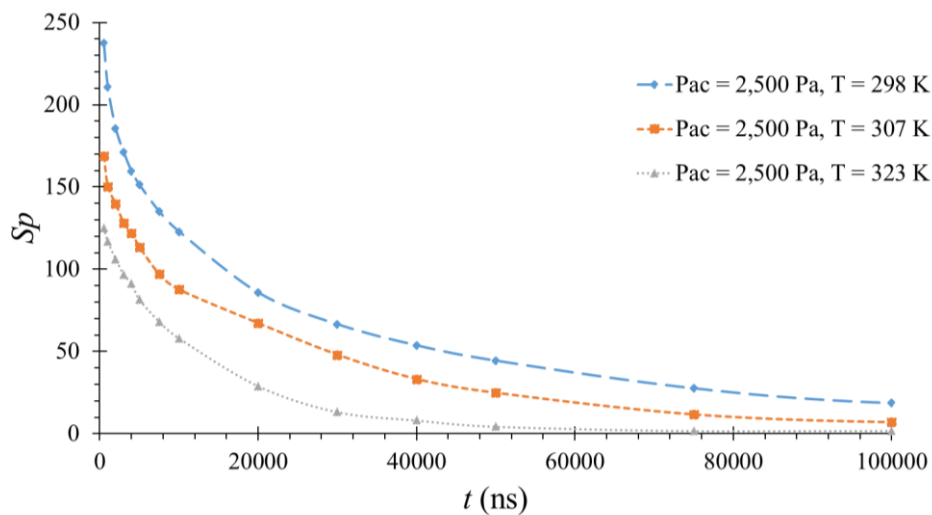


Figure 1.3.A1. Phosphorescence of acetone vapour at $P_{ac} = 2,500$ Pa at different temperatures

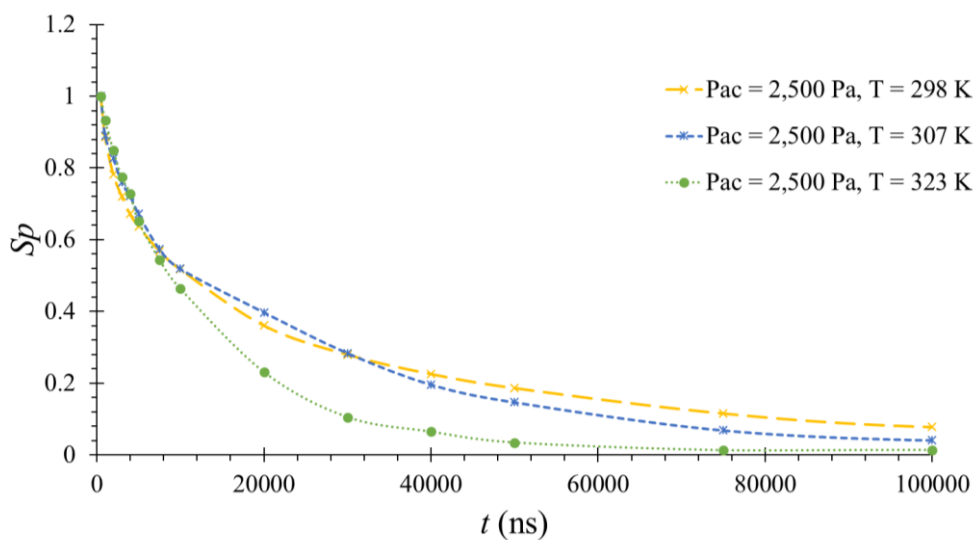


Figure 1.4.A1. Data shown in Figure 1.3 A1 normalised with the intensity value at 500 ns for every curve

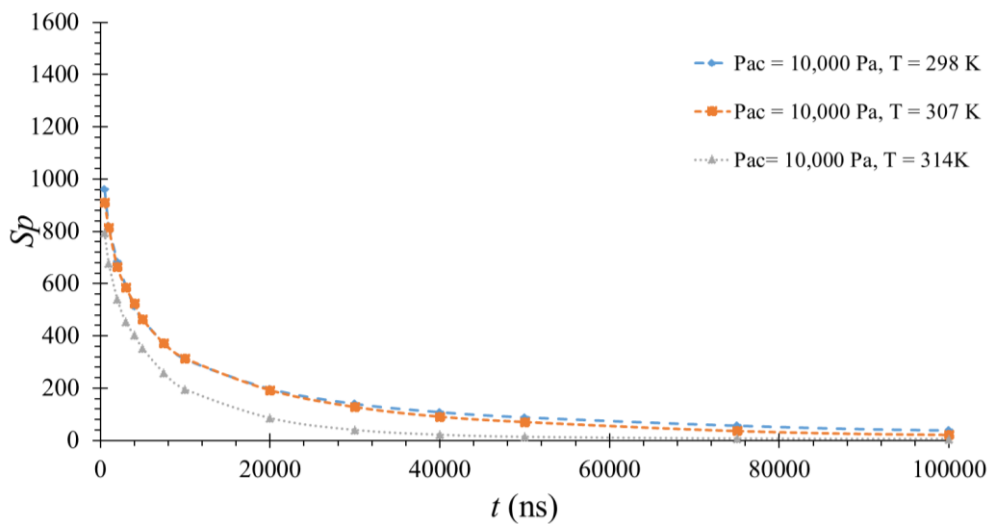


Figure 1.5.A1. Phosphorescence of acetone vapour at $P_{ac} = 10,000$ Pa at different temperatures

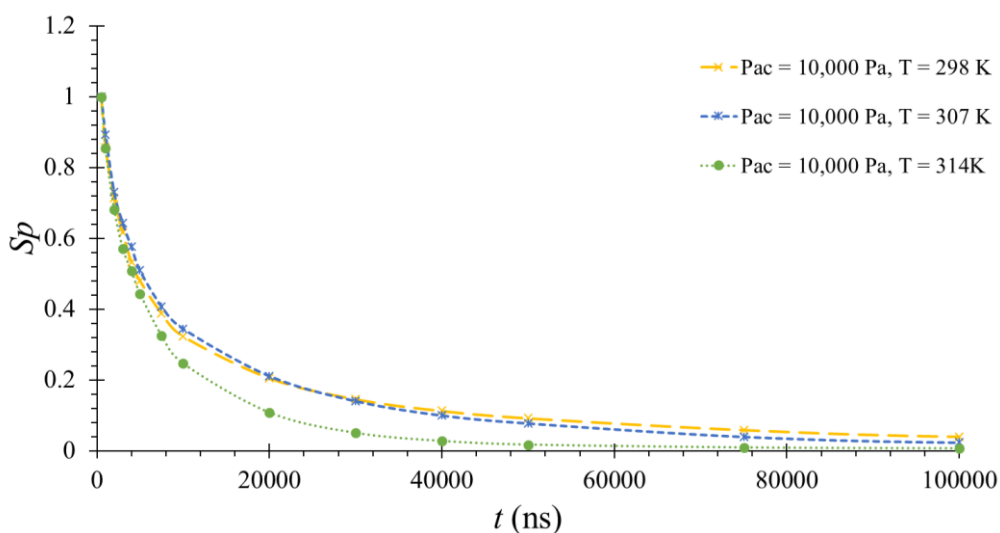


Figure 1.6.A1. Data shown in Figure 1.5 A1 normalised with the intensity value at 500 ns for every curve

2 Appendix B

In this appendix, we present the other details on laser energy fluctuations, discussed in Section 4.10.1.

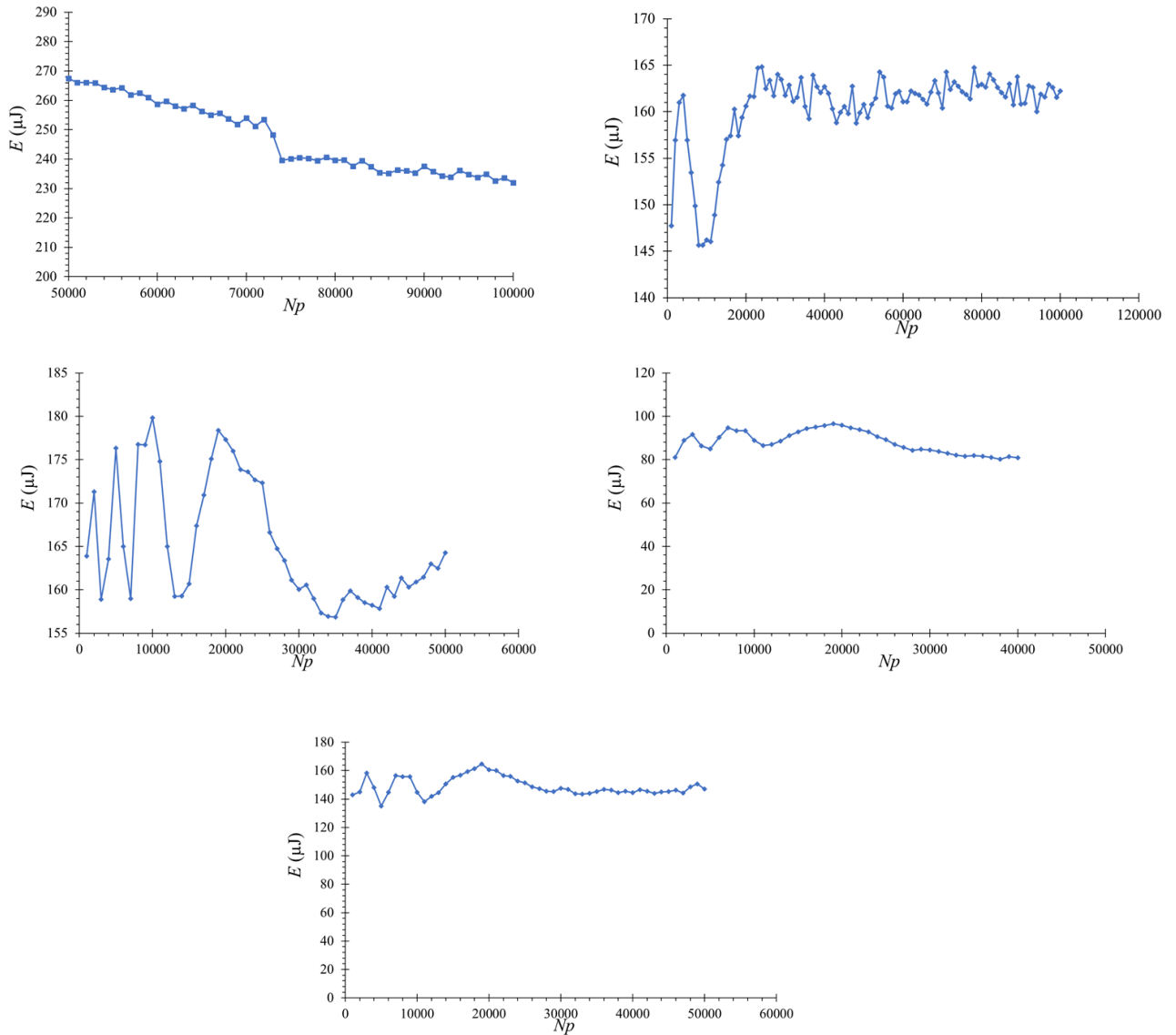


Figure 2.1.A.2 Laser energy fluctuations on operating at 100% energy

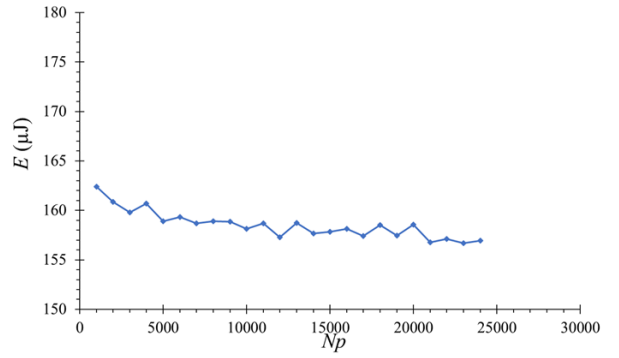
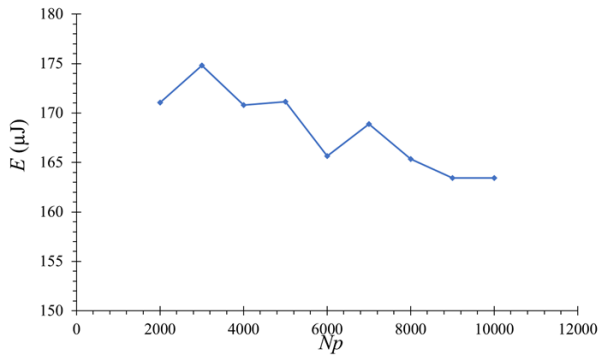
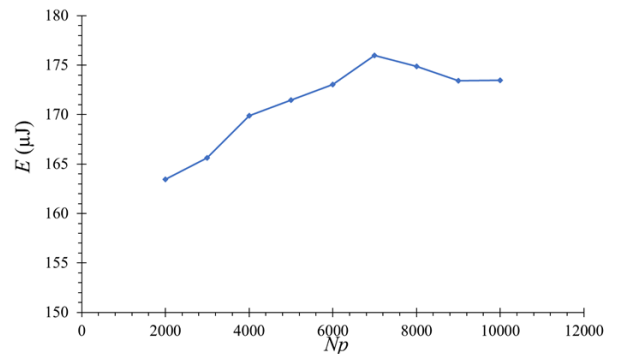
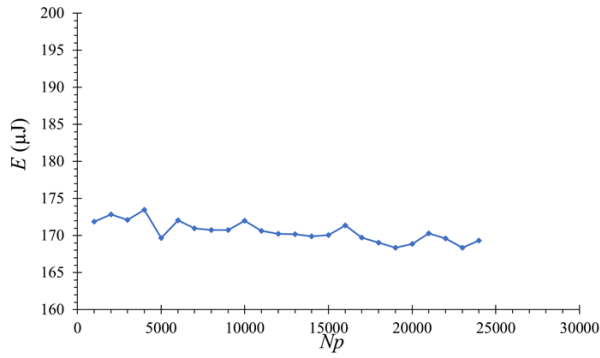


Figure 2.2.A.2 Laser energy fluctuations on operating at 91% energy

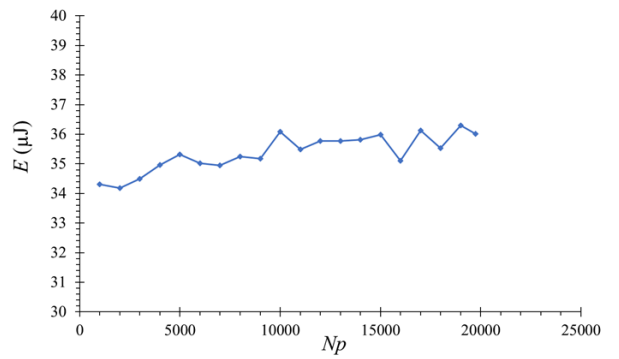
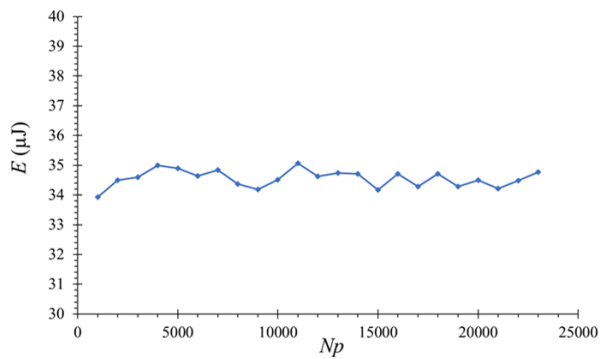
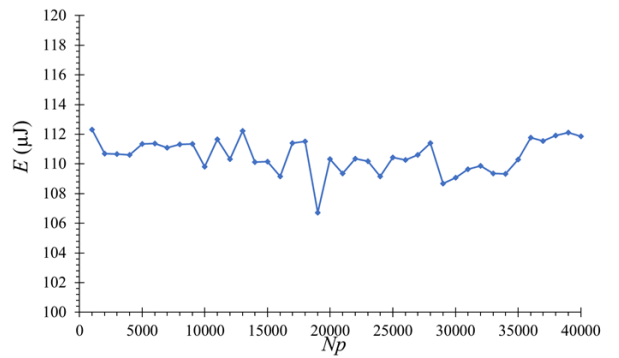
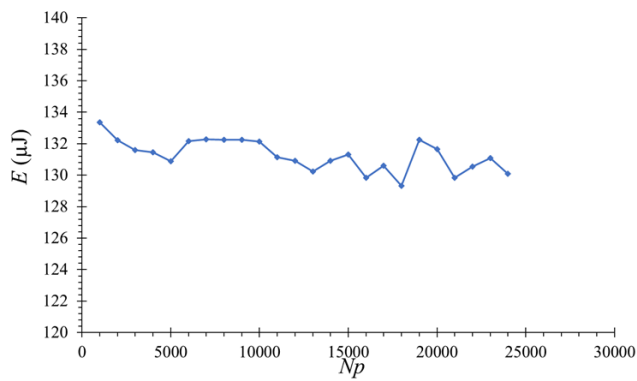


Figure 2.3 A.2 Laser energy fluctuations on operating at 87% energy

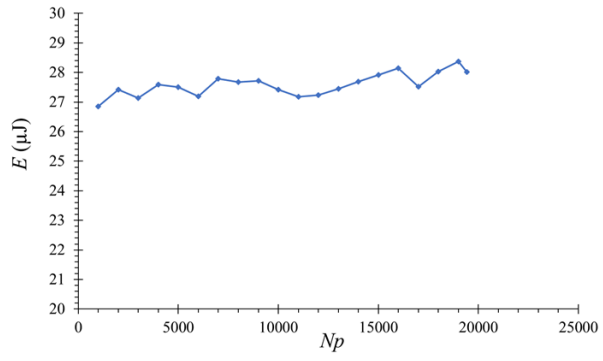
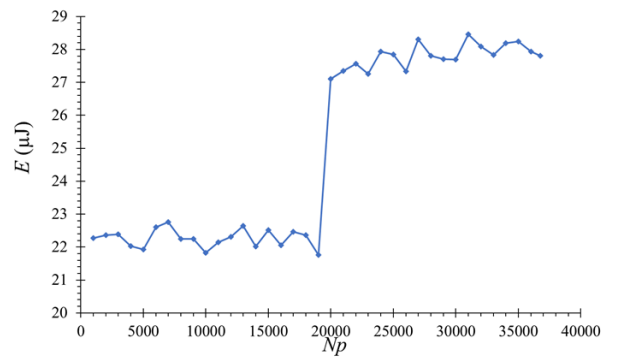
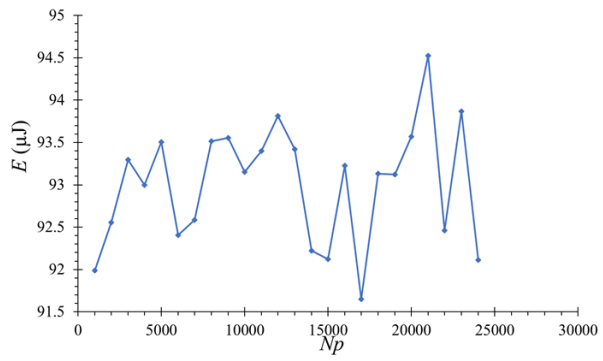


Figure 2.4 A.2 Laser energy fluctuations on operating at 83% energy

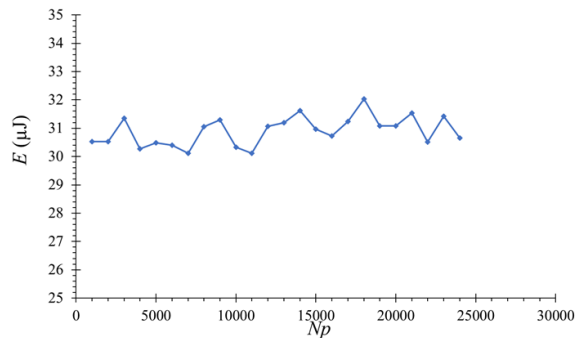
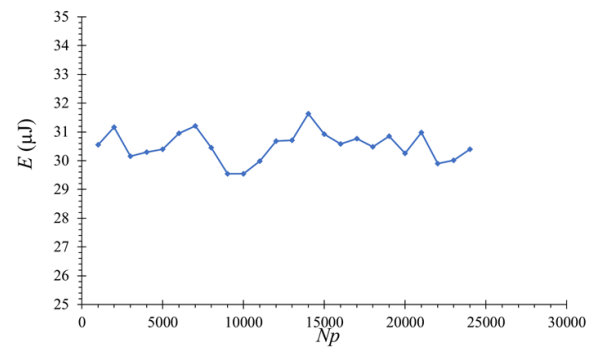
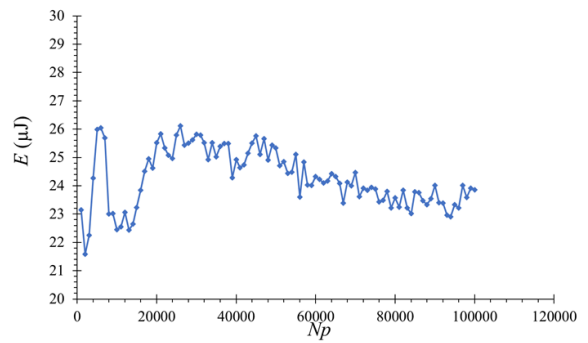
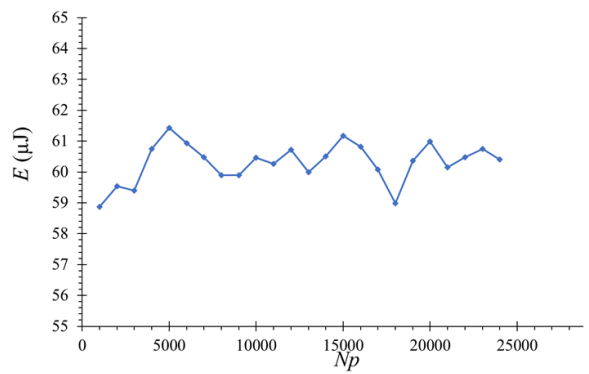


Figure 2.5.A.2. Laser energy fluctuations on operating at 79% energy

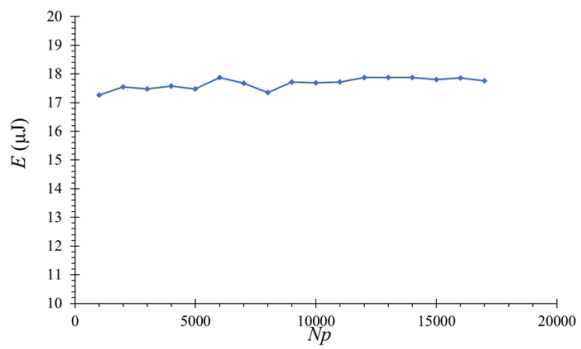
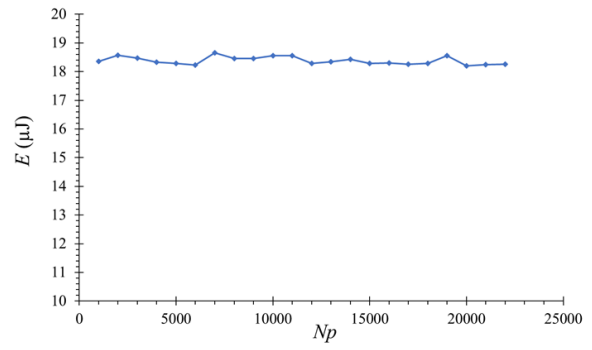
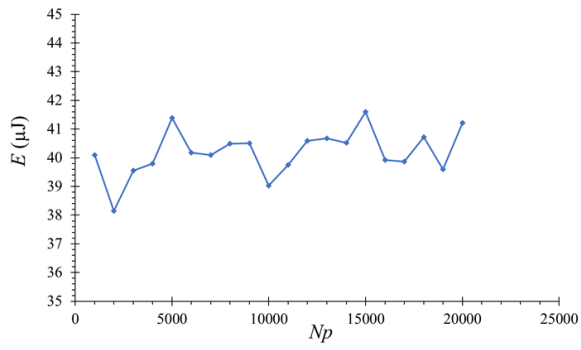


Figure 2.6.A.2. Laser energy fluctuations on operating at 79% energy (continued)

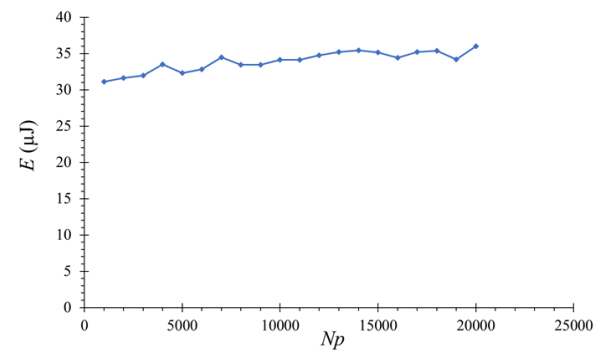
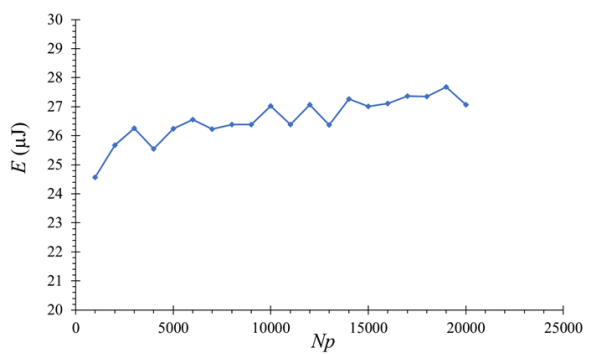
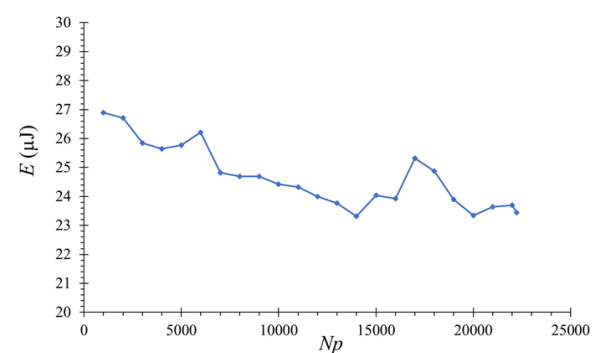
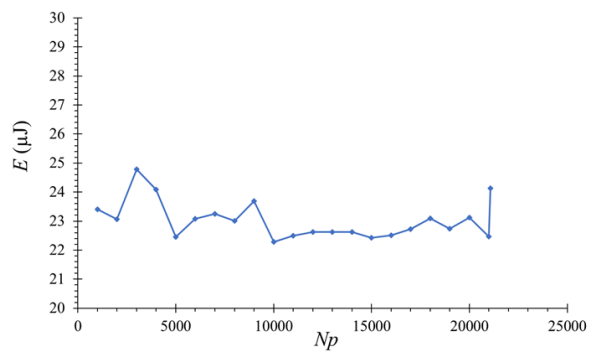


Figure 2.7.A.2. Laser energy fluctuations on operating at 77% energy

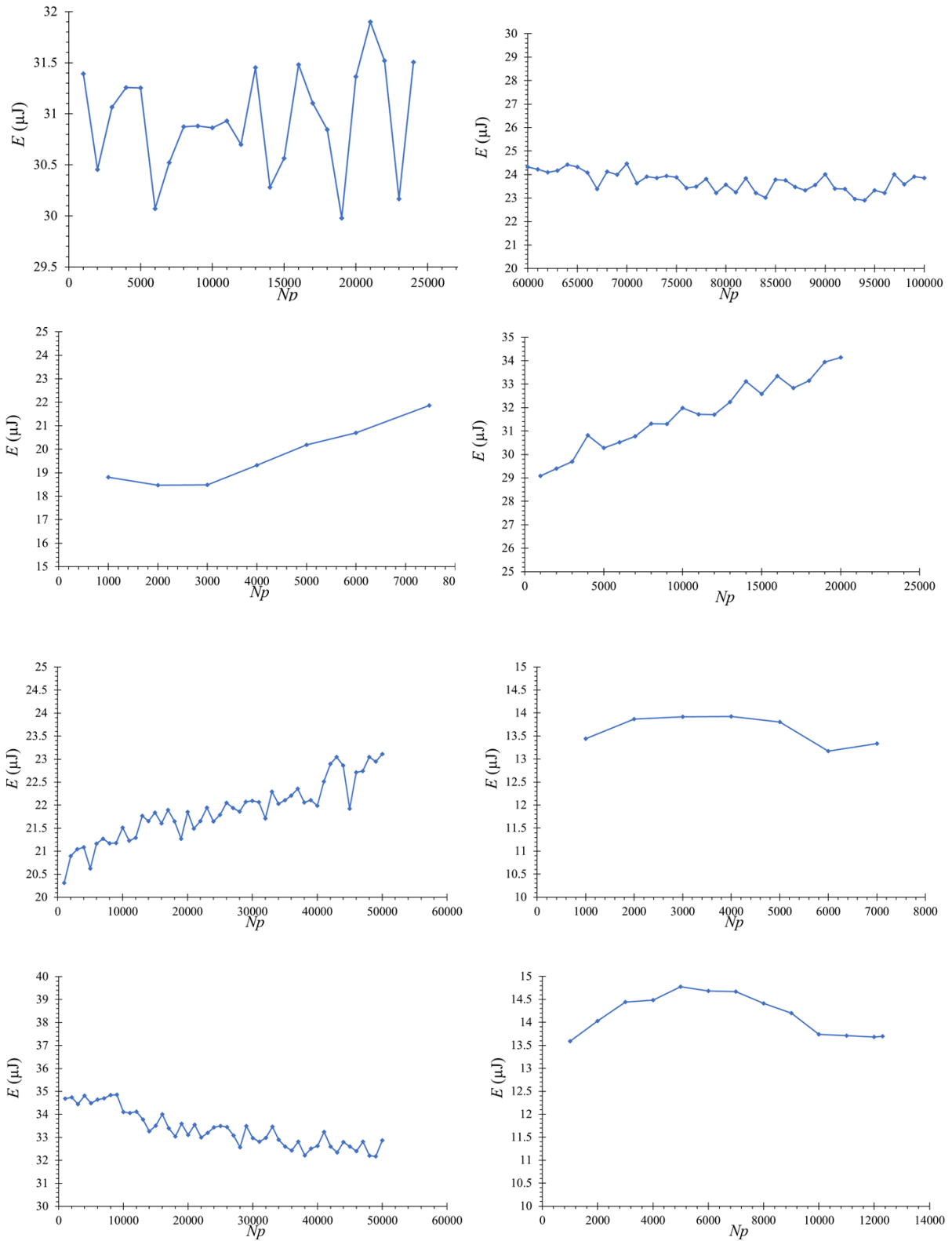


Figure 2.8.A.2. Laser energy fluctuations on operating at 75% energy

3 Appendix C

In this appendix, we present the additional results for the data conditions shown in Table 5-5.

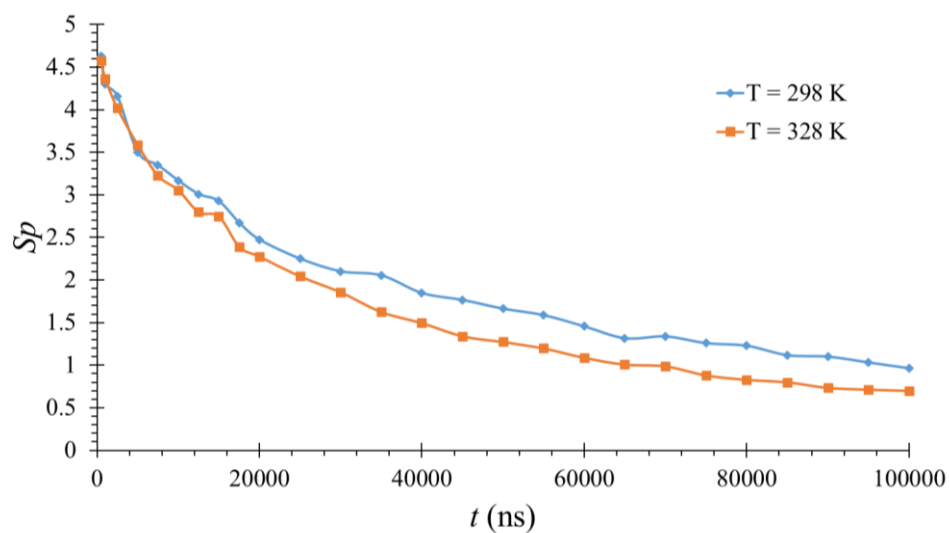


Figure 3.1.A3. Lifetime curve at initial conditions of $P_{ac} = 1,000$ Pa and $T = 298$ K. The same acetone vapour was heated to $T = 328$ K.

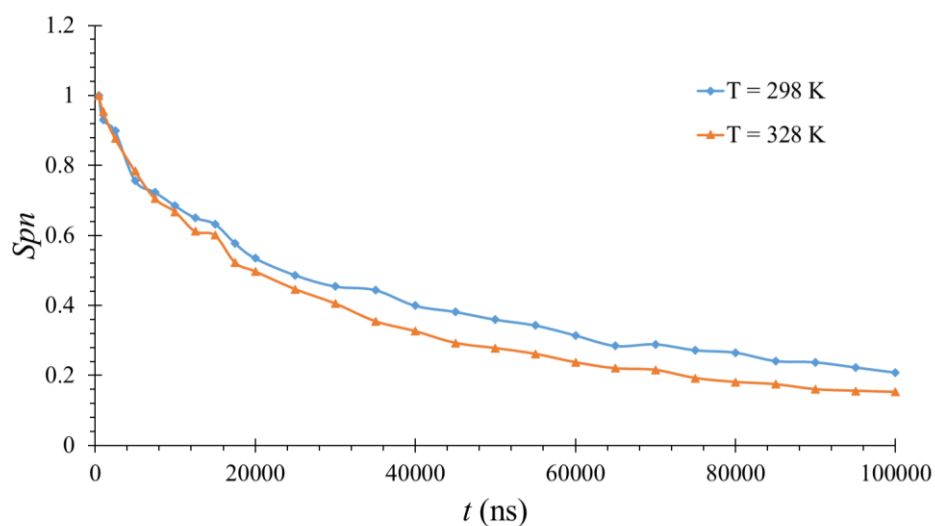


Figure 3.2 Data shown in Figure 3.1.A3 normalised with the intensity value at 500 ns for every curve

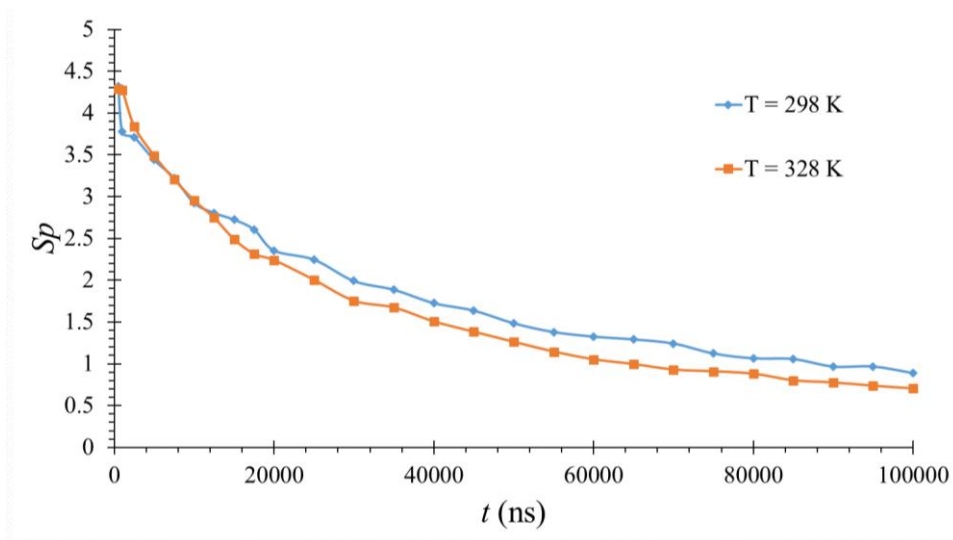


Figure 3.3 A3. Lifetime curve at initial conditions of $P_{ac} = 1,000$ Pa and $T = 298$ K. The same acetone vapour was heated to $T = 328$ K.

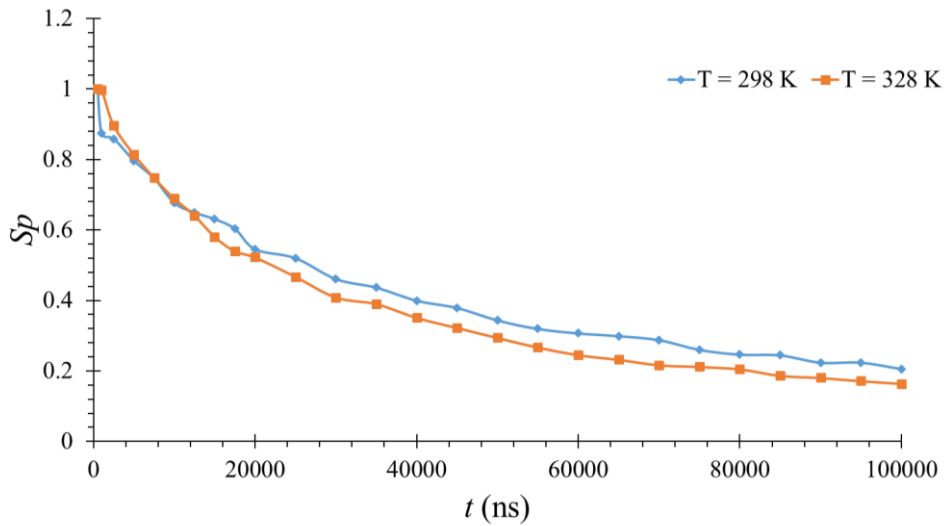


Figure 3.4 Data shown in Figure 3.3.A3 normalised with the intensity value at 500 ns for every curve

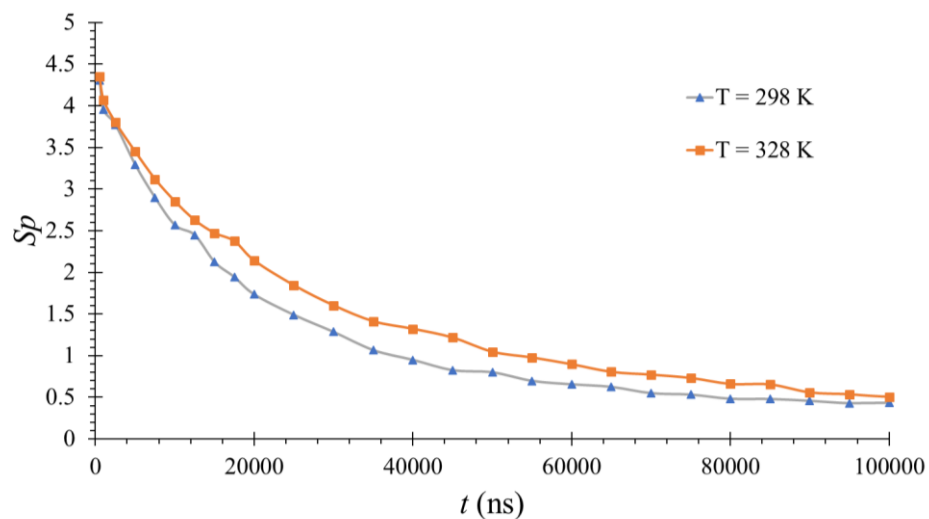


Figure 3.5 A3. Lifetime curve at initial conditions of $P_{ac} = 1,000$ Pa and $T = 298$ K. The same acetone vapour was heated to $T = 328$ K.

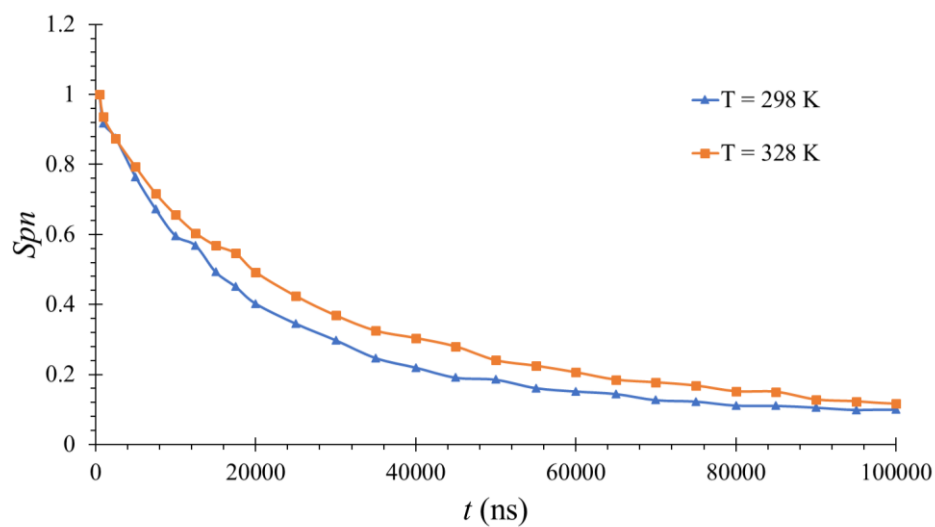


Figure 3.6 Data shown in Figure 3.5.A3 normalised with the intensity value at 500 ns for every curve

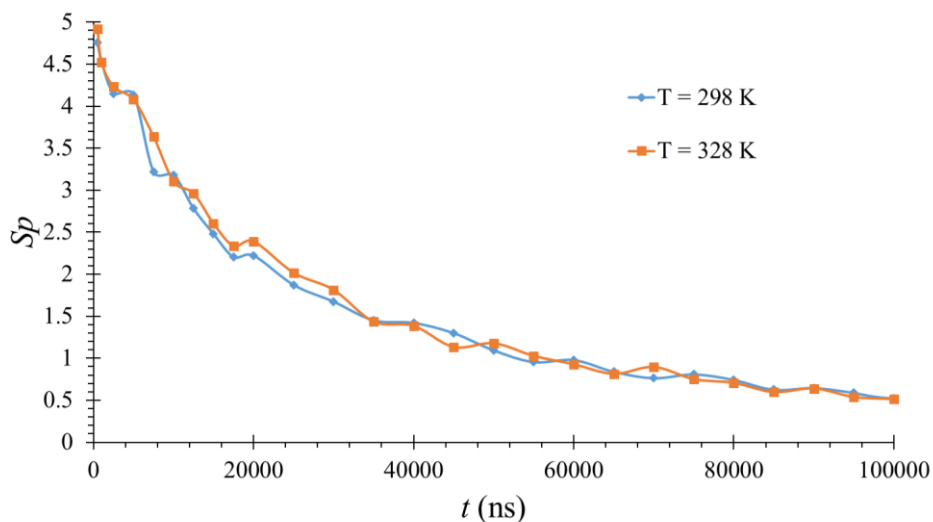


Figure 3.7 A3. Lifetime curve at initial conditions of $P_{ac} = 1,000$ Pa and $T = 298$ K. The same acetone vapour was heated to $T = 328$ K.

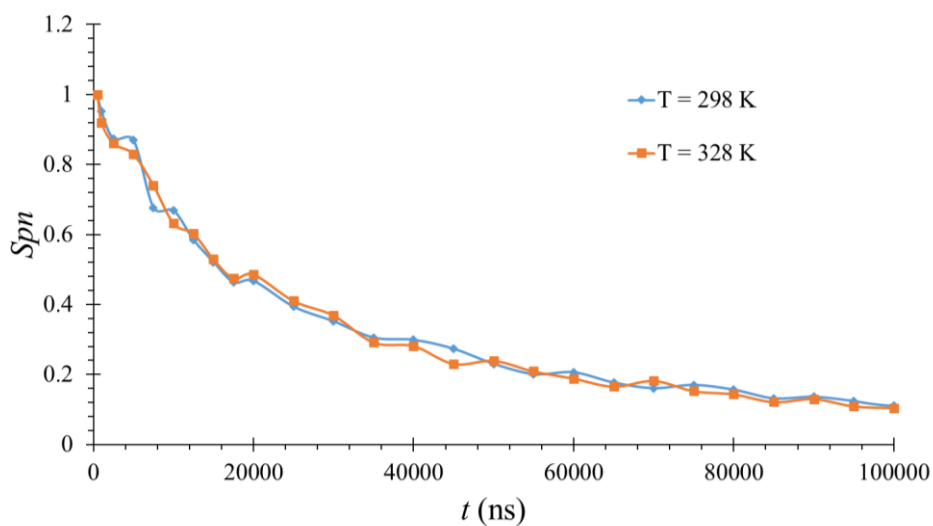


Figure 3.8 Data shown in Figure 3.7.A3 normalised with the intensity value at 500 ns for every curve

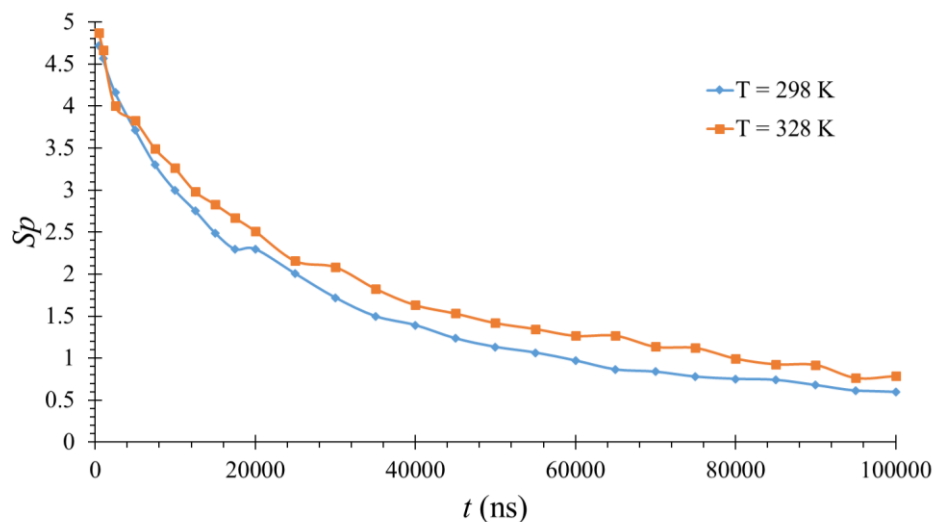


Figure 3.9 A3. Lifetime curve at initial conditions of $P_{ac} = 1,000$ Pa and $T = 298$ K. The same acetone vapour was heated to $T = 328$ K.

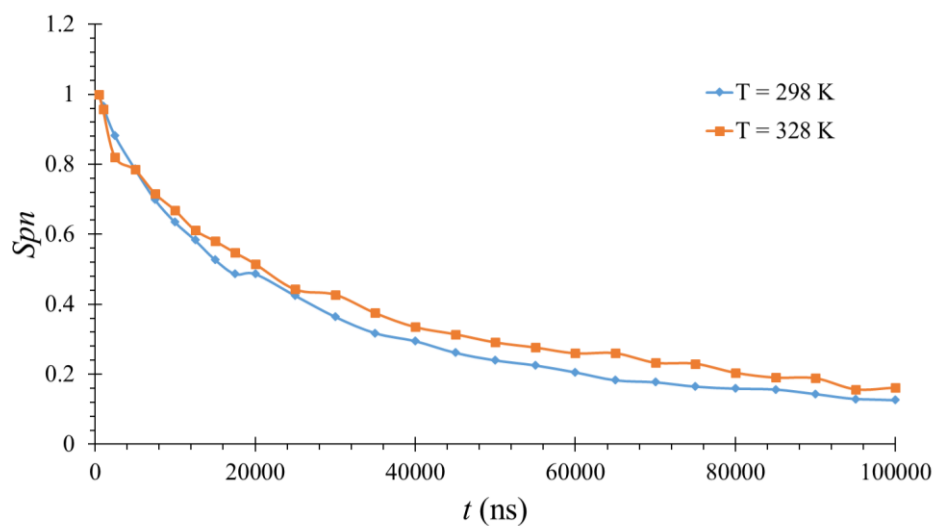


Figure 3.10 Data shown in Figure 3.9.A3 normalised with the intensity value at 500 ns for every curve

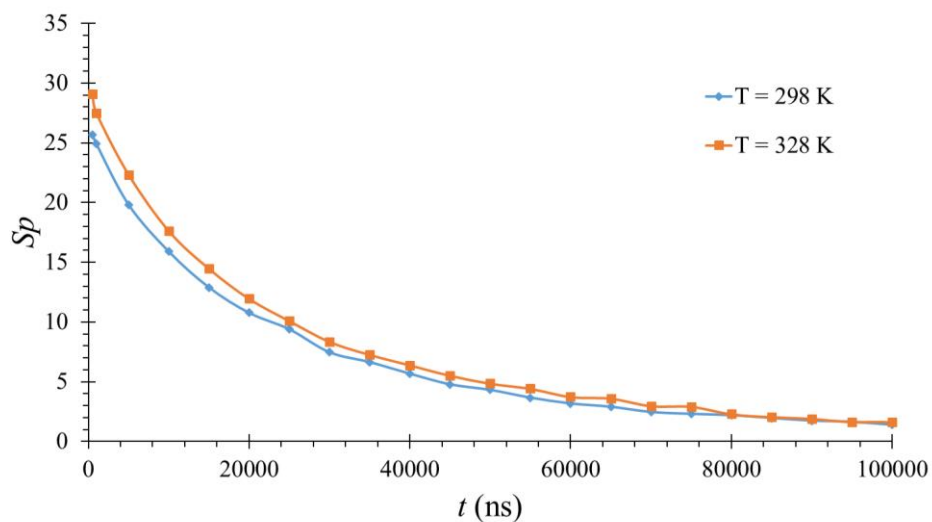


Figure 3.11 A3. Lifetime curve at initial conditions of $P_{ac} = 5,000$ Pa and $T = 298$ K. The same acetone vapour was heated to $T = 328$ K.

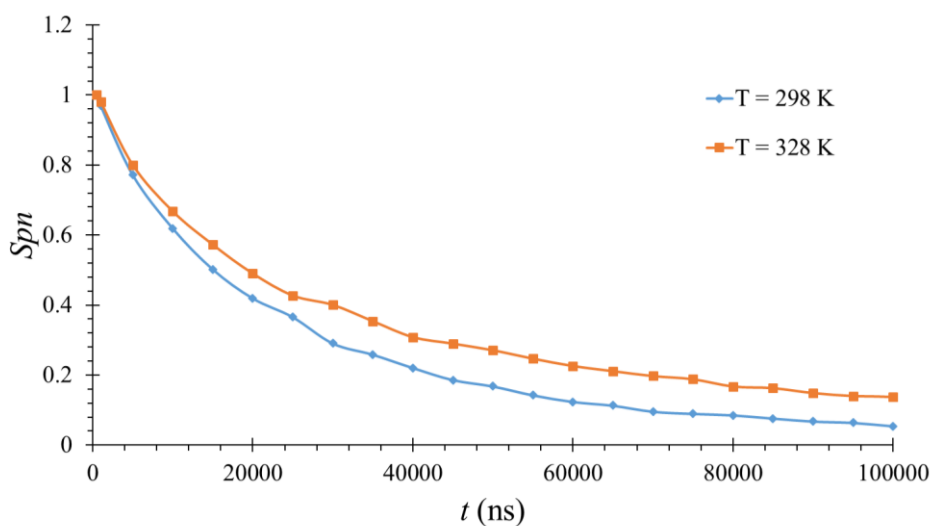


Figure 3.12 Data shown in Figure 3.11.A3 normalised with the intensity value at 500 ns for every curve

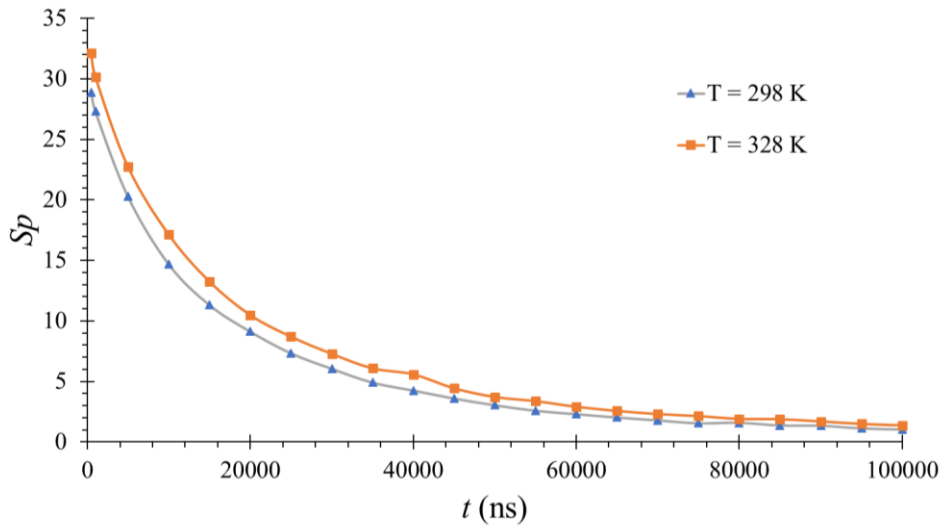


Figure 3.13 A3. Lifetime curve at initial conditions of $P_{ac} = 5,000$ Pa and $T = 298$ K. The same acetone vapour was heated to $T = 328$ K.

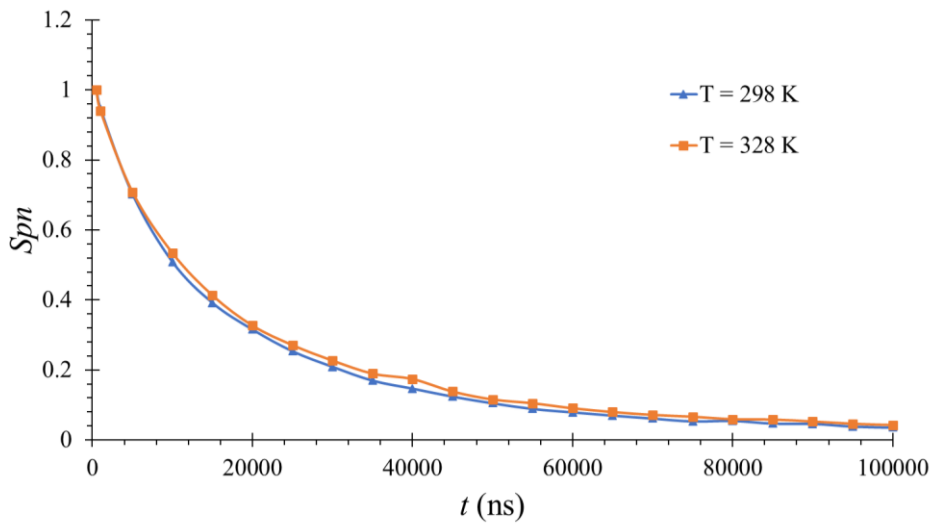


Figure 3.14 Data shown in Figure 3.14.A3 normalised with the intensity value at 500 ns for every curve

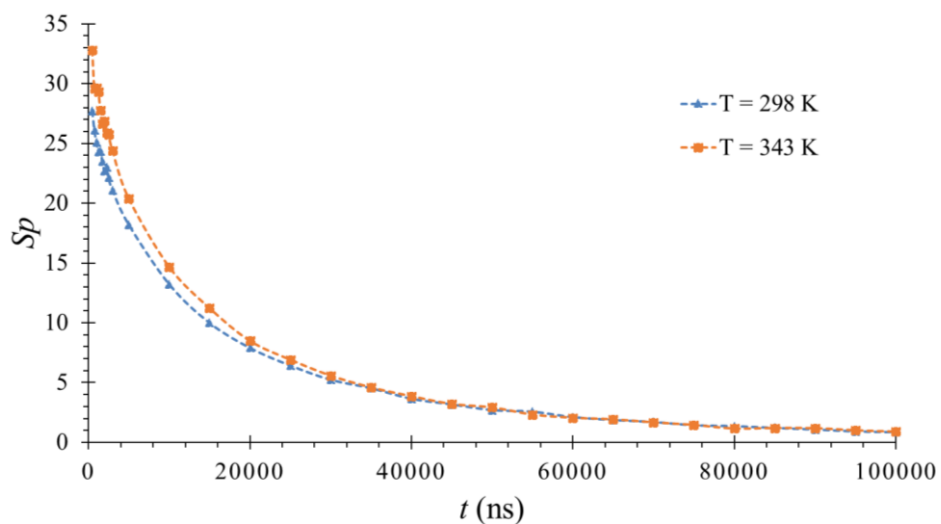


Figure 3.15 A3. Lifetime curve at initial conditions of $P_{ac} = 5,000$ Pa and $T = 298$ K. The same acetone vapour was heated to $T = 328$ K

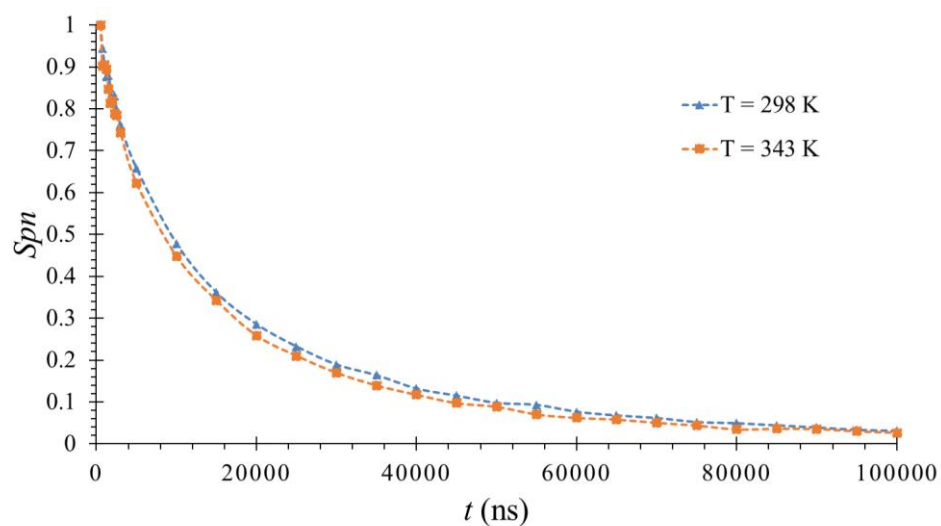


Figure 3.16 Data shown in Figure 3.16.A3 normalised with the intensity value at 500 ns for every curve

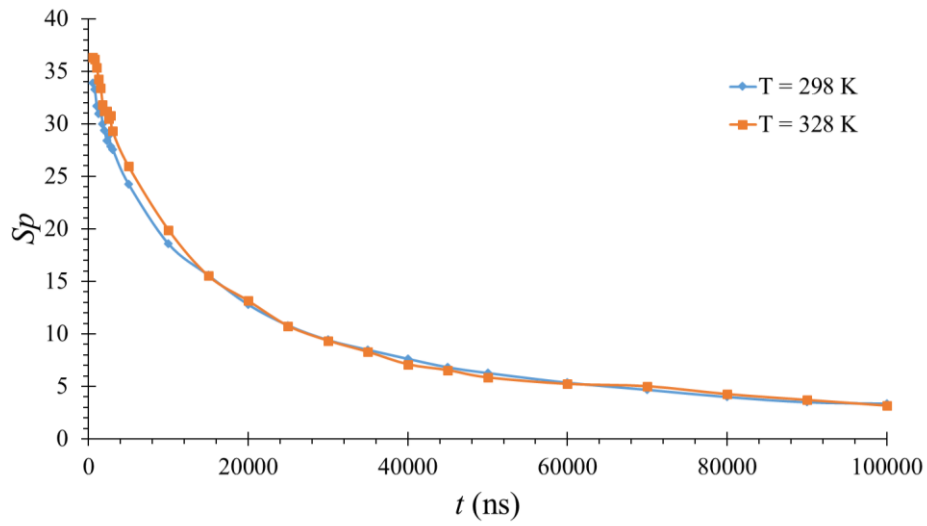


Figure 3.17 A3. Lifetime curve at initial conditions of $P_{ac} = 5,000$ Pa and $T = 298$ K. The same acetone vapour was heated to $T = 328$ K.

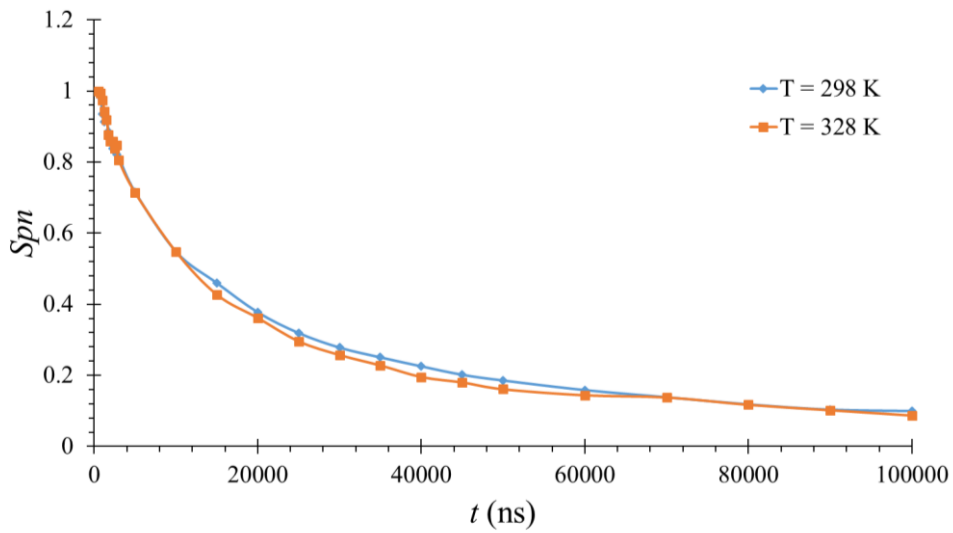


Figure 3.18 Data shown in Figure 3.18.A3 normalised with the intensity value at 500 ns for every curve

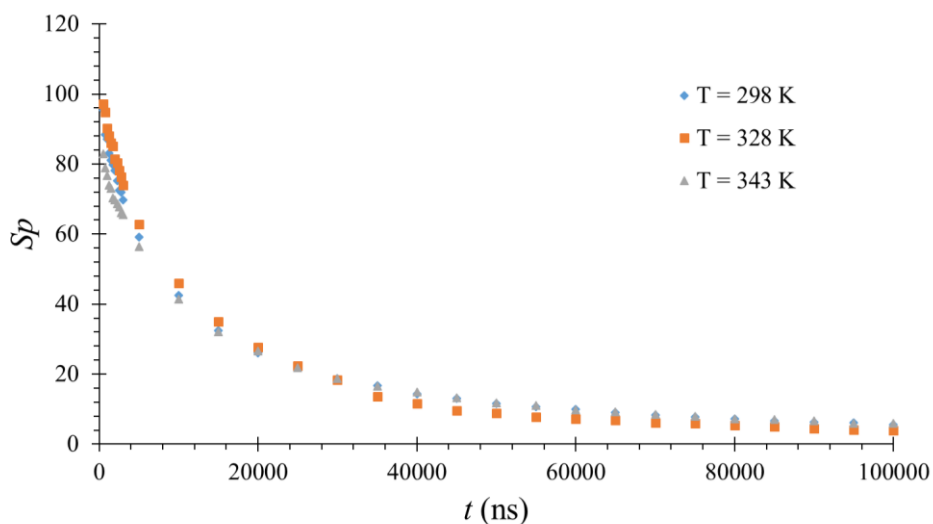


Figure 3.19 A3. Lifetime curve at initial conditions of $P_{ac} = 10,000$ Pa and $T = 298$ K. The same acetone vapour was heated to $T = 328$ K and 343 K.

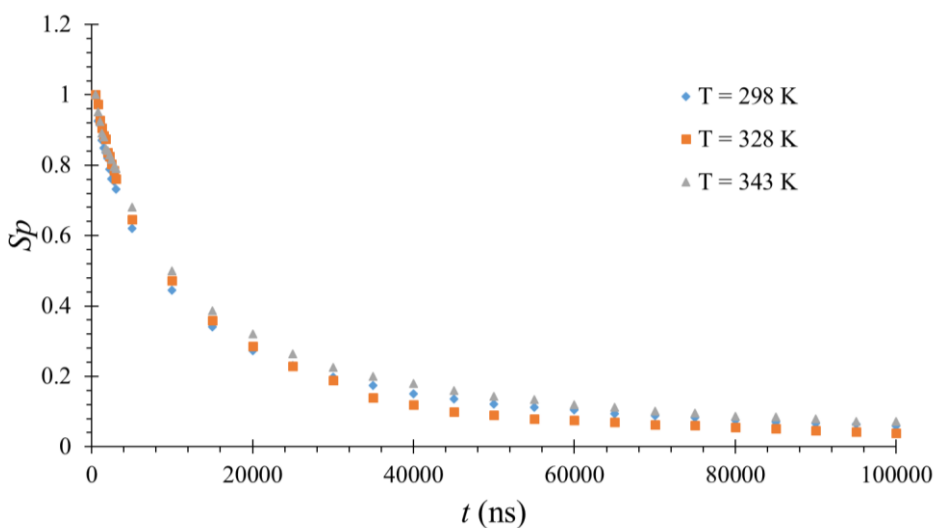


Figure 3.20 Data shown in Figure 3.20.A3 normalised with the intensity value at 500 ns for every curve

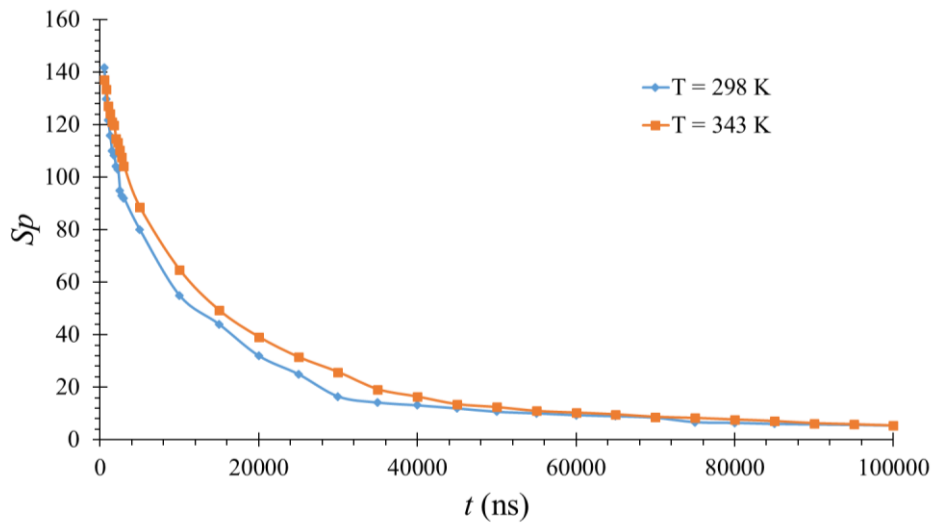


Figure 3.21 A3. Lifetime curve at initial conditions of $P_{ac} = 10,000$ Pa and $T = 298$ K. The same acetone vapour was heated to $T = 343$ K.

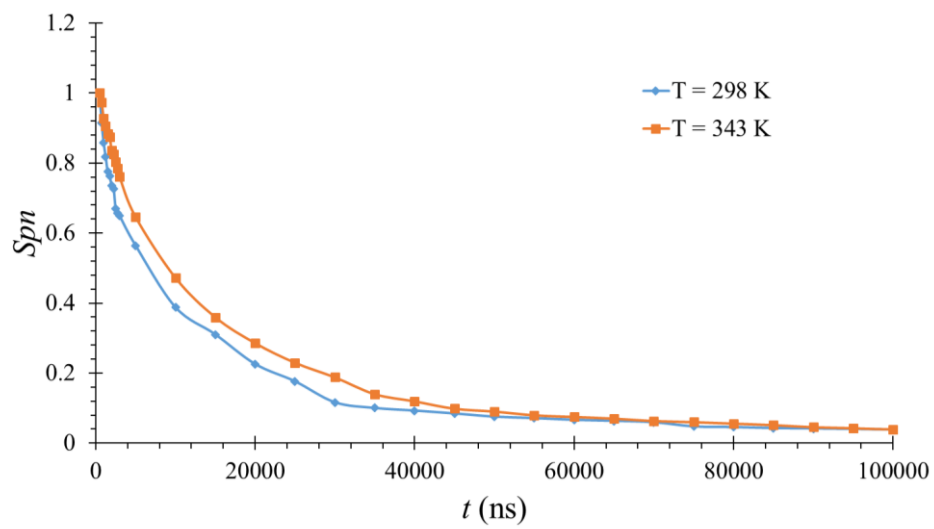


Figure 3.22 Data shown in Figure 3.22.A3 normalised with the intensity value at 500 ns for every curve

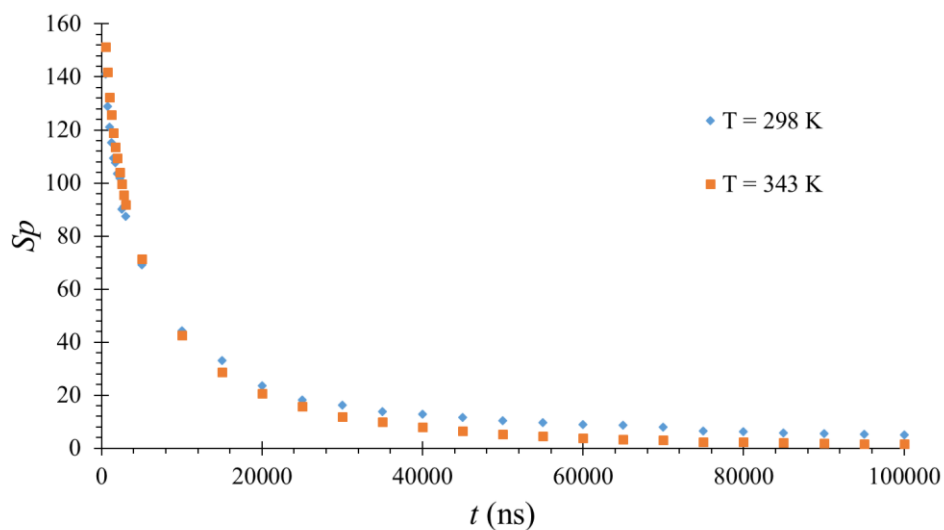


Figure 3.23 A3. Lifetime curve at initial conditions of $P_{ac} = 10,000$ Pa and $T = 298$ K. The same acetone vapour was heated to $T = 343$ K.

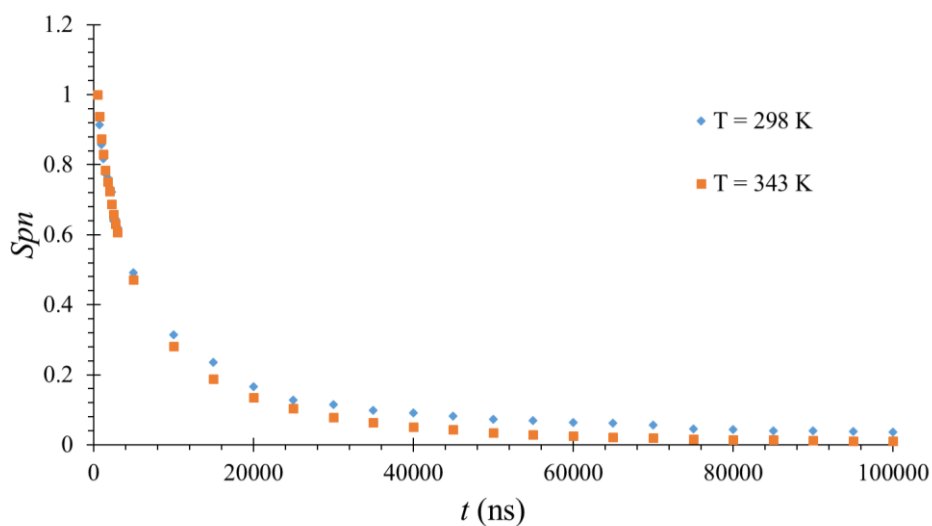


Figure 3.24 Data shown in Figure 3.24.A3 normalised with the intensity value at 500 ns for every curve

References

1. Feynman, R. P. Miniaturization. *Reinhold, New York* 282–296 (1961).
2. Tabeling, P. *Introduction to microfluidics*. (OUP Oxford, 2005).
3. Tripathi, S., Kumar, Y. B., Agrawal, A., Prabhakar, A. & Joshi, S. S. Microdevice for plasma separation from whole human blood using bio-physical and geometrical effects. *Scientific reports* **6**, 26749 (2016).
4. Nguyen, N. T. & Wereley, S. T. *Fundamentals and Applications of Microfluidics*, Artech House. Inc., Norwood, MA 292–337 (2002).
5. Karniadakis, G., Beskok, A. & Aluru, N. *Microflows and nanoflows: fundamentals and simulation*. vol. 29 (Springer Science & Business Media, 2006).
6. Li, S., Freidhoff, C. B., Young, R. M. & Ghodssi, R. Fabrication of micronozzles using low-temperature wafer-level bonding with SU-8. *Journal of Micromechanics and Microengineering* **13**, 732 (2003).
7. Gomez, J. & Groll, R. Pressure drop and thrust predictions for transonic micronozzle flows. *Physics of Fluids* **28**, 022008 (2016).
8. Bier, W. *et al.* Gas to gas heat transfer in micro heat exchangers. *Chemical Engineering and Processing: Process Intensification* **32**, 33–43 (1993).
9. Gerken, I., Brandner, J. J. & Dittmeyer, R. Heat transfer enhancement with gas-to-gas micro heat exchangers. *Applied Thermal Engineering* **93**, 1410–1416 (2016).
10. Lv, J. *et al.* Photocontrol of fluid slugs in liquid crystal polymer microactuators. *Nature* **537**, 179 (2016).
11. Cattafesta III, L. N. & Sheplak, M. Actuators for active flow control. *Annual Review of Fluid Mechanics* **43**, 247–272 (2011).
12. Chaalane, A. *et al.* A MEMS-based solid propellant microthruster array for space and military applications. in vol. 660 012137 (IOP Publishing, 2015).

13. Cen, J. & Xu, J. Performance evaluation and flow visualization of a MEMS based vaporizing liquid micro-thruster. *Acta Astronautica* **67**, 468–482 (2010).
14. Reddy, K. *et al.* Rapid, sensitive, and multiplexed on-chip optical sensors for micro-gas chromatography. *Lab on a Chip* **12**, 901–905 (2012).
15. Tian, W.-C., Chan, H. K., Lu, C.-J., Pang, S. W. & Zellers, E. T. Multiple-stage microfabricated preconcentrator-focuser for micro gas chromatography system. *Journal of Microelectromechanical systems* **14**, 498–507 (2005).
16. Gardner, J. W., Varadan, V. K. & Awadelkarim, O. O. *Microsensors, MEMS, and smart devices*. vol. 1 (Wiley New York, 2001).
17. Van Toan, N., Inomata, N., Trung, N. H. & Ono, T. Knudsen pump produced via silicon deep RIE, thermal oxidation, and anodic bonding processes for on-chip vacuum pumping. *Journal of Micromechanics and Microengineering* **28**, 055001 (2018).
18. Koplik, J., Banavar, J. R. & Willemsen, J. F. Molecular dynamics of Poiseuille flow and moving contact lines. *Physical review letters* **60**, 1282 (1988).
19. Koplik, J., Banavar, J. R. & Willemsen, J. F. Molecular dynamics of fluid flow at solid surfaces. *Physics of Fluids A: Fluid Dynamics* **1**, 781–794 (1989).
20. Gad-el-Hak, M. The fluid mechanics of microdevices—the Freeman scholar lecture. *Journal of Fluids Engineering* **121**, 5–33 (1999).
21. Li, D. *Encyclopedia of microfluidics and nanofluidics*. (Springer Science & Business Media, 2008).
22. Kandlikar, S., Garimella, S., Li, D., Colin, S. & King, M. R. *Heat transfer and fluid flow in minichannels and microchannels*. (elsevier, 2005).
23. Colin, S. Gas microflows in the slip flow regime: a critical review on convective heat transfer. *Journal of Heat Transfer* **134**, 020908 (2012).

24. Morini, G. L. The challenge to measure single-phase convective heat transfer coefficients in microchannels. *Heat Transfer Engineering* **40**, 695–710 (2019).
25. Hartmann, M. Minimal length scales for the existence of local temperature. *Contemporary Physics* **47**, 89–102 (2006).
26. Asheghi, M. & Yang, Y. Micro-and nano-scale diagnostic techniques for thermometry and thermal imaging of microelectronic and data storage devices. in *Microscale Diagnostic Techniques* 155–196 (Springer, 2005).
27. Childs, P., Greenwood, J. & Long, C. Review of temperature measurement. *Review of scientific instruments* **71**, 2959–2978 (2000).
28. Christofferson, J. *et al.* Microscale and nanoscale thermal characterization techniques. *Journal of Electronic Packaging* **130**, 041101 (2008).
29. Kim, M. M. *et al.* Microscale thermometry: A review. *Microelectronic Engineering* **148**, 129–142 (2015).
30. Samouda, F., Colin, S., Barrot, C., Baldas, L. & Brandner, J. J. Micro molecular tagging velocimetry for analysis of gas flows in mini and micro systems. *Microsystem Technologies* **21**, 527–537 (2015).
31. Mohand, H. S. H., Frezzotti, A., Brandner, J. J., Barrot, C. & Colin, S. Molecular tagging velocimetry by direct phosphorescence in gas microflows: correction of Taylor dispersion. *Experimental Thermal and Fluid Science* **83**, 177–190 (2017).
32. Frezzotti, A., Mohand, H. S. H., Barrot, C. & Colin, S. Role of diffusion on molecular tagging velocimetry technique for rarefied gas flow analysis. *Microfluidics and Nanofluidics* **19**, 1335–1348 (2015).
33. Fratantonio, D. *et al.* Molecular tagging velocimetry for confined rarefied gas flows: Phosphorescence emission measurements at low pressure. *Experimental Thermal and Fluid Science* **99**, 510–524 (2018).

34. Cercignani, C. The boltzmann equation. in *The Boltzmann equation and its applications* 40–103 (Springer, 1988).
35. Cercignani, C. *Mathematical methods in kinetic theory*. (Springer, 1969).
36. Sone, Y. *Kinetic theory and fluid dynamics*. (Springer Science & Business Media, 2012).
37. Karniadakis, G., Beskok, A. & Aluru, N. *Microflows and nanoflows: fundamentals and simulation*. vol. 29 (Springer Science & Business Media, 2006).
38. Bird, G. A. & Brady, J. *Molecular gas dynamics and the direct simulation of gas flows*. vol. 5 (Clarendon press Oxford, 1994).
39. Maxwell, J. C. VII. On stresses in rarified gases arising from inequalities of temperature. *Philosophical Transactions of the royal society of London* 231–256 (1879).
40. Sharipov, F. Data on the velocity slip and temperature jump on a gas-solid interface. *Journal of Physical and Chemical Reference Data* **40**, 023101 (2011).
41. Morini, G. L., Yang, Y., Chalabi, H. & Lorenzini, M. A critical review of the measurement techniques for the analysis of gas microflows through microchannels. *Experimental Thermal and Fluid Science* **35**, 849–865 (2011).
42. Kandlikar, S. G. *et al.* Heat transfer in microchannels—2012 status and research needs. *Journal of Heat Transfer* **135**, 091001 (2013).
43. Childs, P. R. N. *et al.* Review of temperature measurement. **2959**, (2012).
44. Kim, M. M. *et al.* Microscale thermometry: A review. *Microelectronic Engineering* **148**, 129–142 (2015).
45. Brites, C. D. S. *et al.* Thermometry at the nanoscale. *Nanoscale* **4**, 4799–4829 (2012).
46. Christofferson, J. *et al.* Microscale and Nanoscale Thermal Characterization Techniques (Reprinted from Thermal Issues in Emerging Technologies: Theory and Application, January, 2007). *Journal of Electronic Packaging* **130**, 1–6 (2008).

47. Quintanilla, M. & Liz-Marzán, L. M. Guiding Rules for Selecting a Nanothermometer. *Nano Today* **19**, 126–145 (2018).
48. Zhang, X., Choi, H., Datta, A. & Li, X. Design, fabrication and characterization of metal embedded thin film thermocouples with various film thicknesses and junction sizes. *Journal of Micromechanics and Microengineering* **16**, 900–905 (2006).
49. Thiery, L. *et al.* Temperature profile measurements of near-field optical microscopy fiber tips by means of sub-micronic thermocouple. *International Journal of Thermal Sciences* **39**, 519–525 (2000).
50. Balčytis, A., Ryu, M., Juodkazis, S. & Morikawa, J. Micro-thermocouple on nano-membrane: Thermometer for nanoscale measurements. *Scientific Reports* **8**, 8–13 (2018).
51. Schöler, L. *et al.* Monolithically integrated micro flow sensor for lab-on-chip applications. *Microelectronic Engineering* **78–79**, 164–170 (2005).
52. Wu, S., Lin, Q., Yuen, Y. & Tai, Y. C. MEMS flow sensors for nano-fluidic applications. *Sensors and Actuators, A: Physical* **89**, 152–158 (2001).
53. Wu, J., Cao, W., Wen, W., Chang, D. C. & Sheng, P. Polydimethylsiloxane microfluidic chip with integrated microheater and thermal sensor. *Biomicrofluidics* **3**, (2009).
54. Choi, H. & Li, X. Fabrication and application of micro thin film thermocouples for transient temperature measurement in nanosecond pulsed laser micromachining of nickel. *Sensors and Actuators, A: Physical* **136**, 118–124 (2007).
55. Rao, S. R. & Peles, Y. Development of an Experimental Method for Flow-Boiling Heat Transfer in Microchannels. *Interfacial Phenomena and Heat Transfer* **2**, 385–397 (2014).
56. Roth, R., Cobry, K., Lenk, G. & Woias, P. Micro process engineering of freestanding silicon fluidic channels with integrated platinum thermistors for obtaining heat transfer correlations. *8th Annual IEEE International Conference on Nano/Micro Engineered and Molecular Systems, IEEE NEMS 2013* **1**, 879–882 (2013).

57. Roth, R., Lenk, G., Kroener, M. & Woias, P. Silicon micro thermal sensor platform at high accuracy with back side contacts. *Sensors and Actuators, A: Physical* **201**, 450–457 (2013).
58. Roth, R., Lenk, G., Cobry, K. & Woias, P. Heat transfer in freestanding microchannels with in-line and staggered pin fin structures with clearance. *International Journal of Heat and Mass Transfer* **67**, 1–15 (2013).
59. Jiang, L., Wang, Y., Wong, M. & Zohar, Y. Fabrication and characterization of a microsystem for a micro-scale heat transfer study. *Journal of Micromechanics and Microengineering* **9**, 422–428 (1999).
60. Binslem, S. A. & Ahmad, M. R. Thermistor based nano-needle for single cell thermal characterization. *Proceedings - 2013 IEEE International Conference on Control System, Computing and Engineering, ICCSCE 2013* 590–595 (2013) doi:10.1109/ICCSCE.2013.6720034.
61. Bianchi, R. A. *et al.* CMOS-compatible smart temperature sensors. *Microelectronics Journal* 627–636 (1998).
62. Guha, P. K. *et al.* Novel design and characterisation of SOI CMOS micro-hotplates for high temperature gas sensors. *Sensors and Actuators, B: Chemical* **127**, 260–266 (2007).
63. Han, I. Y. & Kim, S. J. Diode temperature sensor array for measuring micro-scale surface temperatures with high resolution. *Sensors and Actuators, A: Physical* **141**, 52–58 (2008).
64. Chin, Y. L., Chou, J. C., Sun, T. P., Chung, W. Y. & Hsiung, S. K. A novel pH sensitive ISFET with on chip temperature sensing using CMOS standard process. *Sensors and Actuators, B: Chemical* **76**, 582–593 (2001).
65. Asheghi, M. & Yang, Y. Micro- and Nano-Scale Diagnostic Techniques for Thermometry and Thermal Imaging of Microelectronic and Data Storage Devices BT - Microscale Diagnostic Techniques. in (ed. Breuer, K. S.) 155–196 (Springer Berlin Heidelberg, 2005). doi:10.1007/3-540-26449-3_4.

66. Malacara, D., Servin, M. & Malacara, Z. Interferogram Analysis for Optical Testing. Marcel Decker. *New York* (1998).
67. Newport, D., Garvey, J., Dalton, T., Egan, V. & Whelan, M. Development of interferometric temperature measurement procedures for microfluid flow. *Microscale Thermophysical Engineering* **8**, 141–154 (2004).
68. Newport, D., Sobhan, C. B. & Garvey, J. Digital interferometry: Techniques and trends for fluid measurement. *Heat and Mass Transfer/Waerme- und Stoffuebertragung* **44**, 535–546 (2008).
69. Garvey, J., Newport, D., Lakestani, F., Whelan, M. & Joseph, S. Full field measurement at the micro-scale using micro-interferometry. *Microfluidics and Nanofluidics* **5**, 77–87 (2008).
70. Newport, D., Forno, C. & Whelan, M. Digital Moiré Subtraction Interferometry (DMS) for Electronics Cooling Applications in Enclosures. *Journal of Electronic Packaging* **132**, 031001 (2010).
71. Bon, P. *et al.* Three-dimensional temperature imaging around a gold microwire. *Applied Physics Letters* **102**, (2013).
72. Hariharan, P. *Basics of interferometry*. (Elsevier, 2010).
73. Forno, C. & Whelan, M. Digital moire subtraction applied to interferometers as a means of improving accuracy and extending field of view for engineering and optical measurement . **3745**, 49–57.
74. Tian, H., Fowler, B. & Gamal, A. E. Analysis of temporal noise in CMOS photodiode active pixel sensor. *IEEE Journal of Solid-State Circuits* **36**, 92–101 (2001).
75. Walsh, P. & Davies, M. Factors affecting temperature measurement using phase measurement interferometry in small scale devices. *Experimental thermal and fluid science* **30**, 853–862 (2006).

76. Asheghi, M. & Yang, Y. Micro-and nano-scale diagnostic techniques for thermometry and thermal imaging of microelectronic and data storage devices. in *Microscale Diagnostic Techniques* 155–196 (Springer, 2005).
77. Buffone, C. & Sefiane, K. IR measurements of interfacial temperature during phase change in a confined environment. *Experimental Thermal and Fluid Science* **29**, 65–74 (2004).
78. Hetsroni, G., Gurevich, M., Mosyak, A. & Rozenblit, R. Surface temperature measurement of a heated capillary tube by means of an infrared technique. *Measurement Science and Technology* **14**, 807–814 (2003).
79. Patil, V. A. & Narayanan, V. Spatially resolved temperature measurement in microchannels. *Microfluidics and Nanofluidics* **2**, 291–300 (2006).
80. Haber, J. *et al.* Infrared imaging of temperature profiles in microreactors for fast and exothermic reactions. *Chemical Engineering Journal* **214**, 97–105 (2013).
81. Safitri, A. Infrared Optical Imaging Techniques for Gas Visualization and Measurement. (2011).
82. Rothman, L. S. *et al.* The HITRAN 2008 molecular spectroscopic database. *Journal of Quantitative Spectroscopy and Radiative Transfer* **110**, 533–572 (2009).
83. Tourin, R. H., Henry, P. M. & Liang, E. T. Infrared Spectra of Nitrogen, Argon, and Helium Plasmajets. *Journal of the Optical Society of America* **51**, 800 (1961).
84. Tourin, R. H. & Krakow, B. Applicability of Infrared Emission and Absorption Spectra to Determination of Hot Gas Temperature Profiles. *Applied Optics* **4**, 237 (1965).
85. Abdullah, N., Talib, A. R. A., Jaafar, A. A., Salleh, M. A. M. & Chong, W. T. The basics and issues of thermochromic liquid crystal calibrations. *Experimental Thermal and Fluid Science* **34**, 1089–1121 (2010).
86. Hallcrest, L. TLC Products for Use in Research and Testing Applications. 1–18 (2009).
87. Sage, I. Thermochromic liquid crystals. *Liquid crystals* **38**, 1551–1561 (2011).

88. Stasiek, J. A. & Kowalewski, T. A. Thermochromic liquid crystals in heat transfer research. *10*, 374 (2002).
89. Wiberg, R. & Lior, N. Errors in thermochromic liquid crystal thermometry. *Review of Scientific Instruments* **75**, 2985–2994 (2004).
90. Segura, R. *et al.* Non-encapsulated thermo-liquid crystals for digital particle tracking thermography/velocimetry in microfluidics. *Microfluidics and Nanofluidics* **14**, 445–456 (2013).
91. Muwanga, R. & Hassan, I. Local Heat Transfer Measurements in Microchannels Using Liquid Crystal Thermography: Methodology Development and Validation. *Journal of Heat Transfer* **128**, 617 (2006).
92. Chaudhari, A. M., Woudenberg, T. M., Allin, M. & Goodson, K. E. Transient liquid crystal thermometry of microfabricated PCR vessel arrays. *Journal of Microelectromechanical Systems* **7**, 345–354 (1998).
93. Park, H., Dabiri, D. & Gharib, M. Digital particle image velocimetry/thermometry and application to the wake of a heated circular cylinder. *Experiments in Fluids* **30**, 327–338 (2001).
94. Parsley, M. The use of thermochromic liquid crystals in research applications, thermal mapping and non-destructive testing. in 53–58 (IEEE, 1991).
95. Noh, J. *et al.* In situ thermal diagnostics of the micro-PCR system using liquid crystals. *Sensors and Actuators, A: Physical* **122**, 196–202 (2005).
96. Hoang, V. N., Kaigala, G. V. & Backhouse, C. J. Dynamic temperature measurement in microfluidic devices using thermochromic liquid crystals. *Lab on a Chip* **8**, 484–487 (2008).
97. Basson, M. & Pottebaum, T. S. Measuring the temperature of fluid in a micro-channel using thermochromic liquid crystals. *Experiments in Fluids* **53**, 803–814 (2012).

98. Iles, A., Fortt, R. & De Mello, A. J. Thermal optimisation of the Reimer-Tiemann reaction using thermochromic liquid crystals on a microfluidic reactor. *Lab on a Chip* **5**, 540–544 (2005).
99. Wynberg, H. The Reimer-Tiemann Reaction. *Chemical Reviews* **60**, 169–184 (1960).
100. Nakashima, T. Membrane emulsification by microporous glass. *Key Eng. Mater.* **61**, 513–516 (1991).
101. Puccetti, G., Rossi, M., Morini, G. L. & Kähler, C. J. Sensitivity to shear stress of non-encapsulated thermochromic liquid crystal (TLC) particles for microfluidic applications. *Microfluidics and Nanofluidics* **20**, 19 (2016).
102. Segura, R., Rossi, M., Cierpka, C. & Kähler, C. J. Simultaneous three-dimensional temperature and velocity field measurements using astigmatic imaging of non-encapsulated thermo-liquid crystal (TLC) particles. *Lab on a Chip* **15**, 660–663 (2015).
103. Fujisawa, N. & Funatani, S. Simultaneous measurement of temperature and velocity in a turbulent thermal convection by the extended range scanning liquid crystal visualization technique. *Experiments in Fluids* **29**, S158–S165 (2000).
104. Ireland, P. T. & Jones, T. V. The response time of a surface thermometer employing encapsulated thermochromic liquid crystals. *Journal of Physics E: Scientific Instruments* **20**, 1195–1199 (1987).
105. Ireland, P. T. & Jones, T. V. Liquid crystal measurements of heat transfer and surface shear stress. **11**, 969–986 (2000).
106. Talib, A. R. A., Neely, A. J., Ireland, P. T. & Mullender, A. J. A Novel Liquid Crystal Image Processing Technique Using Multiple Gas Temperature Steps to Determine Heat Transfer Coefficient Distribution and Adiabatic Wall Temperature. *Journal of Turbomachinery* **126**, 587 (2004).

107. Wang, Z., Ireland, P. T. & Kohler, S. T. Gas temperature measurement in internal cooling passages. *ASME 1996 International Gas Turbine and Aeroengine Congress and Exhibition* **13**, V004T09A059--V004T09A059 (1996).
108. Picart, B. & Minguez, S. D. Test method in voltage contrast mode using liquid crystals. *Microelectronics Reliability* **32**, 1605–1613 (1992).
109. Wilson, E. B., Decius, J. C. & Cross, P. C. *Molecular vibrations: the theory of infrared and Raman vibrational spectra*. (Courier Corporation, 1980).
110. Smith, E. & Dent, G. *Modern Raman spectroscopy: a practical approach*. (John Wiley & Sons, 2013).
111. Lapp, M. & Penney, C. M. *Laser Raman gas diagnostics*. (Springer, 1974).
112. Phinney, L. M., Lu, W.-Y. & Serrano, J. R. Raman and Infrared Thermometry for Microsystems. *Journal of Thermal Science and Engineering Applications* **5**, 031011 (2013).
113. Chrimes, A. F., Khoshmanesh, K., Stoddart, P. R., Mitchell, A. & Kalantar-Zadeh, K. Microfluidics and raman microscopy: Current applications and future challenges. *Chemical Society Reviews* **42**, 5880–5906 (2013).
114. Kuriyama, R. & Sato, Y. Non-intrusive measurement of microscale temperature distribution by spontaneous Raman imaging. *Microfluidics and Nanofluidics* **14**, 1031–1037 (2013).
115. Thomas, O. & Burgess, C. *Uv-Visible Spectrophotometry of Water and Wastewater*. *Journal of Chemical Information and Modeling* (2013). doi:10.1017/CBO9781107415324.004.
116. Bagnall, K. R., Saadat, O. I., Joglekar, S., Palacios, T. & Wang, E. N. Experimental Characterization of the Thermal Time Constants of GaN HEMTs Via Micro-Raman Thermometry. *IEEE Transactions on Electron Devices* **64**, 2121–2128 (2017).

117. Beechem, T., Christensen, A., Graham, S. & Green, D. Micro-Raman thermometry in the presence of complex stresses in GaN devices. *Journal of Applied Physics* **103**, (2008).
118. Cai, S. C. and Q. L. and Q. Z. and Y. Q. and H. J. and R. S. R. and W. Thermal conductivity measurements of suspended graphene with and without wrinkles by micro-Raman mapping. *Nanotechnology* **23**, 365701 (2012).
119. Liu, X., Wu, X. & Ren, T. In situ and noncontact measurement of silicon membrane thermal conductivity. *Applied Physics Letters* **98**, 174104 (2011).
120. Kearney, S. P., Phinney, L. M. & Baker, M. S. Spatially resolved temperature mapping of electrothermal actuators by surface Raman scattering. *Journal of Microelectromechanical Systems* **15**, 314–321 (2006).
121. Beechem, T., Graham, S., Kearney, S. P., Phinney, L. M. & Serrano, J. R. Invited Article: Simultaneous mapping of temperature and stress in microdevices using micro-Raman spectroscopy. *Review of Scientific Instruments* **78**, (2007).
122. Kim, S. H. *et al.* Micro-Raman thermometry for measuring the temperature distribution inside the microchannel of a polymerase chain reaction chip. *Journal of Micromechanics and Microengineering* **16**, 526–530 (2006).
123. Ewinger, A., Rinke, G., Urban, A. & Kerschbaum, S. In situ measurement of the temperature of water in microchannels using laser Raman spectroscopy. *Chemical Engineering Journal* **223**, 129–134 (2013).
124. Kuriyama, R. & Sato, Y. An investigation of measurement condition for non-intrusive velocity determination based on thermal tracing by Raman imaging. *Journal of Thermal Science and Technology* **9**, JTST0014–JTST0014 (2014).
125. Kuriyama, R. & Sato, Y. Two-wavelength Raman imaging for non-intrusive monitoring of transient temperature in microfluidic devices. *Measurement Science and Technology* **25**, 095203 (2014).

126. Lucht, R. P., Roy, S., Meyer, T. R. & Gord, J. R. Femtosecond coherent anti-Stokes Raman scattering measurement of gas temperatures from frequency-spread dephasing of the Raman coherence. *Applied Physics Letters* **89**, 251112 (2006).
127. Schrötter, H. & Klöckner, H. Raman scattering cross sections in gases and liquids. in *Raman spectroscopy of gases and liquids* 123–166 (Springer, 1979).
128. Valeur, B. & Berberan-Santos, M. N. *Molecular fluorescence: principles and applications*. (John Wiley & Sons, 2012).
129. Thurber, M. C. Acetone laser-induced fluorescence for temperature and multiparameter imaging in gaseous flows. (1999).
130. Charogiannis, A. Development of a laser induced phosphorescence technique for the investigation of evaporating two-phase flows. (2013).
131. Thomson, S. L. & Maynes, D. Spatially Resolved Temperature Measurements in a Liquid Using Laser Induced Phosphorescence. *Journal of Fluids Engineering* **123**, 293 (2001).
132. Hu, H., Jin, Z., Nocera, D., Lum, C. & Koochesfahani, M. Experimental investigations of micro-scale flow and heat transfer phenomena by using molecular tagging techniques. *Measurement Science and Technology* **21**, (2010).
133. Fogg, D., David, M. & Goodson, K. Non-invasive measurement of void fraction and liquid temperature in microchannel flow boiling. *Experiments in Fluids* **46**, 725–736 (2009).
134. Chamarchy, P., Garimella, S. V. & Wereley, S. T. Non-intrusive temperature measurement using microscale visualization techniques. *Experiments in Fluids* **47**, 159–170 (2009).

135. Chamarchy, P., Garimella, S. V. & Wereley, S. T. Measurement of the temperature non-uniformity in a microchannel heat sink using microscale laser-induced fluorescence. *International Journal of Heat and Mass Transfer* **53**, 3275–3283 (2010).
136. Kim, M. & Yoda, M. Dual-tracer fluorescence thermometry measurements in a heated channel. *Experiments in Fluids* **49**, 257–266 (2010).
137. Hoera, C. *et al.* An integrated microfluidic chip enabling control and spatially resolved monitoring of temperature in micro flow reactors. *Analytical and Bioanalytical Chemistry* **407**, 387–396 (2015).
138. Chen, F., Li, H. & Hu, H. Molecular tagging techniques and their applications to the study of complex thermal flow phenomena. *Acta Mechanica Sinica* **31**, 425–445 (2015).
139. Hu, H. & Koochesfahani, M. Thermal effects on the wake of a heated circular cylinder operating in mixed convection regime. *Journal of Fluid Mechanics* **685**, 235–270 (2011).
140. Hu, H. & Jin, Z. An icing physics study by using lifetime-based molecular tagging thermometry technique. *International Journal of Multiphase Flow* **36**, 672–681 (2010).
141. Hu, H., Li, H. & Chen, F. Simultaneous Measurements of Droplet Size, Velocity and Temperature of “In-flight” Droplets in a Spray Flow by using a Molecular Tagging Technique. in 1224 (2015).
142. Thurber, M. C., Grisch, F., Kirby, B. J., Votsmeier, M. & Hanson, R. K. Measurements and modeling of acetone laser-induced fluorescence with implications for temperature-imaging diagnostics. *Applied optics* **37**, 4963–4978 (1998).
143. Samouda, F. Développement de la technique de vélocimétrie par marquage moléculaire pour l’étude expérimentale des micro-écoulements gazeux. (2012).
144. Howard, W. L. Acetone. *Kirk-Othmer Encyclopedia of Chemical Technology* (2000).

145. Lozano, A., Yip, B. & Hanson, R. Acetone: a tracer for concentration measurements in gaseous flows by planar laser-induced fluorescence. *Experiments in fluids* **13**, 369–376 (1992).
146. Tran, T. T. Acetone planar laser-induced fluorescence and phosphorescence for mixing studies of multiphase flows at high pressure and temperature. (2008).
147. Hiller, B., Booman, R., Hassa, C. & Hanson, R. Velocity visualization in gas flows using laser-induced phosphorescence of biacetyl. *Review of Scientific Instruments* **55**, 1964–1967 (1984).
148. Si Hadj Mohand, H. Micro-vélocimétrie par marquage moléculaire adaptée aux écoulements gazeux confinés. (2015).
149. Galbraith, D. A. & Weill, D. Diacetyl and bronchiolitis obliterans. *American journal of respiratory and critical care medicine* **178**, 313–313 (2008).
150. Myers, L. E., Eckardt, R., Fejer, M. M., Byer, R. L. & Bosenberg, W. R. Multigrating quasi-phase-matched optical parametric oscillator in periodically poled LiNbO₃. *Optics letters* **21**, 591–593 (1996).
151. Almy, G. & Gillette, P. The quantum yield of diacetyl fluorescence. *The Journal of Chemical Physics* **11**, 188–195 (1943).
152. Almy, G., Fuller, H. & Kinzer, G. The fluorescence of diacetyl. *The Journal of Chemical Physics* **8**, 37–45 (1940).
153. Heicklen, J. & Noyes Jr, W. A. The Photolysis and Fluorescence of Acetone and Acetone-Biacetyl Mixtures¹. *Journal of the American Chemical Society* **81**, 3858–3863 (1959).
154. Yip, B., Lozano, A. & Hanson, R. Sensitized phosphorescence: a gas phase molecular mixing diagnostic. *Experiments in fluids* **17**, 16–23 (1994).

155. Thurber, M. & Hanson, R. K. Pressure and composition dependences of acetone laser-induced fluorescence with excitation at 248, 266, and 308 nm. *Applied Physics B* **69**, 229–240 (1999).
156. Thurber, M. C., Grisch, F., Kirby, B. J., Votsmeier, M. & Hanson, R. K. Measurements and modeling of acetone laser-induced fluorescence with implications for temperature-imaging diagnostics. *Applied optics* **37**, 4963–4978 (1998).
157. Toomre, D. & Manstein, D. J. Lighting up the cell surface with evanescent wave microscopy. *Trends in cell biology* **11**, 298–303 (2001).
158. Kim, H. *et al.* Electrical, optical, and structural properties of indium–tin–oxide thin films for organic light-emitting devices. *Journal of Applied Physics* **86**, 6451–6461 (1999).